

2015-03-30

Understanding and Controlling Wettability of Carbon Powders for PEM Fuel Cell Applications

Li, Xiaoan

Li, X. (2015). Understanding and Controlling Wettability of Carbon Powders for PEM Fuel Cell Applications (Doctoral thesis, University of Calgary, Calgary, Canada). Retrieved from <https://prism.ucalgary.ca>. doi:10.11575/PRISM/28556
<http://hdl.handle.net/11023/2124>

Downloaded from PRISM Repository, University of Calgary

UNIVERSITY OF CALGARY

Understanding and Controlling Wettability of Carbon Powders for PEM Fuel Cell Applications

by

Xiaoan Li

A THESIS

SUBMITTED TO THE FACULTY OF GRADUATE STUDIES

IN PARTIAL FULFILMENT OF THE REQUIREMENTS FOR THE

DEGREE OF DOCTOR OF PHILOSOPHY

GRADUATE PROGRAM IN MECHANICAL AND MANUFACTURING ENGINEERING

CALGARY, ALBERTA

MARCH, 2015

© Xiaoan Li 2015

Abstract

The wettability of catalyst layers (CLs), especially of the cathode, is critical to enhancing the performance and lifetime of polymer electrolyte membrane fuel cells (PEMFCs). As the CLs are composed of Pt nanoparticles supported on carbon powders, bound together with Nafion[®], the main focus of this work was to understand and control the wettability of carbon materials for their use in PEMFCs.

The droplet impacting (DI) method was first used to study the wettability of conventional, microporous Vulcan[®] carbon (VC)/Nafion composites, showing that the wettability varies with VC content (from hydrophilic to superhydrophobic) and is significantly affected by the presence of Nafion. This is attributed primarily to the orientation and coverage of the Nafion molecular chains on the carbon surface, as well as the roughness of the composite surfaces.

Both contact angle kinetics (CAK) and water vapor sorption (WVS) measurements were then used to examine the relative wettability of several other types of carbon powders, but in the absence of Nafion, and using VC as a benchmark material. It was found that colloid-imprinted carbon (CIC) powders, synthesized using silica colloid templates of varying sizes, are much more hydrophilic than VC, due to their high surface oxygen group density. It was also shown that heat treatment at 1500 °C in N₂ makes the CICs much more hydrophobic by removing the surface oxygen groups.

Ordered mesoporous carbons (OMCs), synthesized using hexagonal mesoporous silica templates but with different carbon precursors, were also found to contain hydrophilic mesopores, but the anthracene-derived OMC contains more large mesopores and is more

hydrophilic than the sucrose-derived OMC, which may have a very thin carbon coating on its surface. These differences were explained as being due to the different formation mechanisms of the two OMCs.

Both CIC and VC surfaces were also surface modified with pentafluorophenyl groups, using an *in-situ* diazonium reduction reaction. The fluorination was confirmed to increase the hydrophobicity of these carbons, but the reaction was also found to introduce nitro groups onto the carbon surfaces.

Overall, this thesis work has demonstrated that the three methods used here for wettability assessment, DI, CAK and WVS, can all contribute to the understanding of the properties of carbon powder surfaces. The as-synthesized mesoporous carbons have been shown to be very hydrophilic, and either heat treatment or surface fluorination converts them to a hydrophobic state.

Acknowledgements

I owe many thanks to my supervisors, Dr. Daniel Y. Kwok and Dr. Viola Birss, for their endless guidance, support, and encouragement over the course of my Ph.D. degree. Particularly, the incredible patience and efforts of Dr. Viola Birss in advising and guiding me will never be forgotten. She is an excellent scientist and has been an outstanding mentor and a great example for me.

I extend my deep appreciation to Dr. Frank Cheng, Dr. Deyi Xue, Dr. Swavik Spiewak and Dr. Venkataraman Thangadurai (VT) for their advice, assistance, and suggestions. I would also like to thank Dr. Edward Roberts (internal external examiner) and Dr. Keryn K. Lian (external examiner) for their constructive suggestions on my thesis.

Special thanks also go to Dr. Fangxia (Felicia) Feng for her helpful guidance from the beginning of this research project to the subsequent years. I would also like to thank Dr. Dustin Banham, who was, in my eyes, a model Ph.D. student. He gave me great suggestions and instructions, especially in the synthesis of carbons. I also like to thank Dr. Abraham Joseph for his guidance in the functionalization of carbon surfaces. I am also grateful for Farisa Forouzandeh's help and discussions in the past years. Much appreciation is extended to Dr. Scott Paulson for his valuable technical support, suggestions, and discussions. I would also like to thank Dr. Holly (Bri) Campbell, Corie Horwood, Anusha Abhayawardhana, Beatriz Molero, Robert Mayall, Dr. Samar Gharaibeh, and Farisa Forouzandeh for their help with editing my thesis. Special thanks also go to Dr. Wang Hay (Jack) Kan, Dr. Min Chen, Hala T. Handal, Dr. Xia Tong, and Suresh Mulmi, for their great help and invaluable suggestions. Also, I would like to acknowledge the other members of the Birss and

Thangadurai research groups for their helpful assistance and for providing a wonderful working environment. Thank you all.

I extend my deep appreciation to Dr. Michael Schoel (Microscopy and Imaging Facility) and Dr. Max Anikovskiy (Faculty of Science) for their assistance with my SEM experiments, Dr. Johnson Li for elemental analysis, Dr. Pedro Pereira (Department of Chemical and Petroleum Engineering) and Samuel Aquino (Geoscience) for the porosity measurements, and Dr. Josephine Hill (Department of Chemical and Petroleum Engineering) for access to the die-pressor.

I am also very grateful for the financial support from the University of Calgary, the Natural Sciences and Engineering Research Council of Canada (NSERC), and Ballard Power Systems during my Ph.D. degree. I would like to especially thank Drs. Siyu Ye and Shanna Knights, from Ballard Power Systems, for their help in my work.

I would also like to thank Dr. Ke Zhang for his help in the past years. I also appreciate the help of Dr. Sudong Yin, Yutong Ruan, Qiran Li, and other friends in Calgary. I would like to give my thanks to Dr. Fuzhi Lu, Dr. Qinwen Yang, and other friends for helpful discussions regarding courses and research.

Acknowledgements are also extended to the administrative and technical staff in both the Department of Mechanical and Manufacturing Engineering and the Department of Chemistry, who have supported and helped me in overcoming many obstacles that I came across during my Ph.D. studies.

Finally, I gratefully thank my parents, sisters and other relatives in China for their spiritual and material support over the years here at the University of Calgary.

Dedication

For

my parents and other family members/relatives,

for my Master's Degree mentor (Prof. Zhenya Huang),

and for others who have taught, guided, and supported me in the past 30 years.

Table of Contents

Abstract	ii
Acknowledgements	iv
Dedication	vi
Table of Contents	vii
List of Tables	x
List of Figures	xi
List of Symbols	xvi
List of Abbreviations	xviii
 CHAPTER ONE: INTRODUCTION	 1
1.1 General background	1
1.2 Polymer electrolyte membrane fuel cells (PEMFCs)	2
1.3 Challenges for the development of PEMFCs	6
1.4 Catalyst supports for PEMFCs	8
1.4.1 Carbon blacks	8
1.4.2 Carbon nanotubes (CNTs)	9
1.4.3 Ordered mesoporous carbons (OMCs)	9
1.4.4 Colloid-imprinted carbons (CICs)	10
1.4.5 Other catalyst supports	11
1.5 Further treatment of carbon supports	12
1.5.1 Heat treatment	12
1.5.2 Surface modification	12
1.6 Wettability of components in PEMFCs	13
1.6.1 Wettability of gas diffusion layers (GDLs) and bipolar plates	13
1.6.2 Wettability of catalyst layers (CLs)	14
1.7 Wettability Measurements	16
1.7.1 Droplet impacting (DI) method	17
1.7.2 Contact angle kinetics (CAK)	17
1.7.3 Water vapor sorption (WVS)	18
1.8 Other characterization methods used for carbon powders	19
1.9 Research objectives of thesis	19
1.10 Thesis organization	20
 CHAPTER TWO: EXPERIMENTAL METHODS	 23
2.1 Preparation of carbon samples	23
2.1.1 Synthesis of colloid-imprinted carbons (CICs)	23
2.1.2 Synthesis of ordered mesoporous carbons (OMCs)	23
2.1.3 Heat treatment of carbons	25
2.1.4 Surface functionalization of carbons	25
2.2 Elemental analysis	25

2.3 Determination of carbon crystallinity	26
2.4 Surface morphology.....	26
2.5 Porosity determination	27
2.6 Wettability measurements.....	27
2.6.1 Water droplet experiments	27
2.6.1.1 Droplet impacting (DI) method	27
2.6.1.2 Contact angle kinetics (CAK) measurements	29
2.6.2 Water vapor sorption (WVS) measurements	31
2.7 Determination of electrochemical properties of carbons	32
2.8 Error analysis	33

CHAPTER THREE: WETTABILITY OF NAFION AND VULCAN CARBON/NAFION COMPOSITES..... 38

3.1 Introduction.....	38
3.2 Results and discussion	39
3.2.1 Water impacting behavior on 100% Nafion films	43
3.2.2 Water impacting behavior on VC/Nafion composite films	46
3.3 Summary	56

CHAPTER FOUR: WETTABILITY OF COLLOID-IMPRINTED CARBONS BEFORE AND AFTER HEAT TREATMENT..... 58

4.1 Introduction.....	58
4.2 Elemental composition of carbons before and after heat treatment.....	60
4.3 Crystallinity of carbons before and after heat treatment.....	61
4.4 Porous structure of carbons before and after heat treatment.....	63
4.5 Wettability of carbons before and after heat treatment.....	71
4.5.1 Contact angle kinetics (CAK) study	72
4.5.2 Water vapor sorption (WVS) study	77
4.6 Further efforts to understand the wettability differences of the carbon surfaces.....	88
4.7 Summary.....	91

CHAPTER FIVE: WETTABILITY OF ORDERED MESOPOROUS CARBONS BEFORE AND AFTER HEAT TREATMENT..... 93

5.1 Introduction.....	93
5.2 Elemental composition of OMCs before and after heat treatment	95
5.3 Porous structure of OMCs before and after heat treatment	96
5.4 Wettability of OMCs before and after heat treatment	108
5.4.1 Contact angle kinetics (CAK) study	109
5.4.2 Water vapor sorption (WVS) study	112
5.5 Electrochemical analysis of the wettability differences of OMC-S and OMC-A	121
5.6 Discussion of OMC-A and OMC-S wettability	124
5.7 Summary	130

CHAPTER SIX: WETTABILITY OF HIGH SURFACE AREA CARBON POWDERS AFTER SURFACE-MODIFICATION WITH PENTAFLUOROPHENYL GROUPS	132
6.1 Introduction.....	132
6.2 Porous structure of carbons before and after surface functionalization.....	133
6.3 Elemental composition of carbons before and after surface functionalization.....	139
6.4 Wettability of carbons before and after surface functionalization.....	142
6.4.1 Contact angle kinetics (CAK) study	142
6.4.2 Water vapor sorption (WVS) study	145
6.5 Further understanding of –PhF ₅ functionalized carbon surfaces	151
6.6. Summary	158
 CHAPTER SEVEN: CONCLUSIONS AND SUGGESTED FUTURE WORK	 159
7.1 Conclusions.....	159
7.1.1 Effect of Nafion on the wettability of carbon/Nafion composites	160
7.1.2 Wettability of synthesized and heat-treated carbons	161
7.1.3 Microstructure of mesoporous carbons and effect on wettability.....	161
7.1.4 Surface functionalization of carbons and effect on wettability	162
7.1.5 Conclusions related to wettability of carbons for PEMFC applications.....	163
7.2 Overview of novel contributions of this thesis work.....	164
7.3 Suggestions for future work.....	165
 REFERENCES.....	 169

List of Tables

Table 4.1 Elemental content (wt. %) of carbons before and after heat-treatment (HT).....	61
Table 4.2 Structural properties of carbons before and after heat-treatment (HT).....	69
Table 4.3. Water vapor sorption of carbons before and after heat-treatment (HT).....	81
Table 5.1 Elemental content (wt. %) of ordered mesoporous carbon (OMC) materials before and after heat-treatment (HT).....	96
Table 5.2 Structural properties of OMCs before and after heat-treatment.....	107
Table 6.1 Structural properties of VC and CIC-22 before and after surface functionalization.	137
Table 6.2 Element content (wt. %) of VC and CIC-22 before and after functionalization..	140

List of Figures

Figure 1.1. Cross section of a H ₂ –air polymer electrolyte membrane fuel cell (PEMFC).	3
Figure 1.2. Cartoon of triple phase boundary (TPB) in the cathode of PEMFCs where the oxygen reduction reaction (ORR, Reaction 1.2) occurs.	7
Figure 1.3. Schematic of a water droplet (blue) deposited on a flat sample surface (grey), showing the contact angle (θ) of water on the sample.	18
Figure 2.1. Schematic of the experimental setup used for the droplet impacting experiment.	29
Figure 2.2. Photograph of set-up used for contact angle kinetics (CAK) measurements.	30
Figure 2.3. (a) Photograph of a sealed dessicator containing carbon samples, used for water vapor sorption (WVS) measurements, where each sample was placed in a crucible. (b) Top-down photograph of the crucibles placed in the dessicator, where the empty crucible where the empty crucible was used as control experiments.	32
Figure 2.4. Visual Basic software used to measure the instantaneous spreading diameter (green arrow) of a water droplet on a sample surface.	34
Figure 2.5. Visual Basic software used to measure contact angles of water on a compacted carbon pellet.	35
Figure 3.1. Sequential images of a 2.4 mm dia water droplet impacting on (a) bare glass, (b) PMMA (poly(methyl methacrylate)), (c) Nafion, and (d) 10 – 90 wt. % Vulcan Carbon (VC)/Nafion composite thin films, coated on glass, all at an impacting height of 120 mm above the substrate.	40
Figure 3.2. Experimental spreading ratio (Equation 3.1) of a water droplet impacting on bare glass, poly(methyl methacrylate) (PMMA), and Nafion surfaces.	42
Figure 3.3. Scanning electron microscopy (SEM) images of the Pd/Au-sputtered (a) top-down surface and (b) the cross-section of a Nafion film, prepared by spin-coating a 1% Nafion/isopropanol solution onto a glass substrate. Note that the grey particle at the center of (a), likely a small piece of glass, was used to help with focusing. A schematic of the Nafion film surface (c) and cross-sectional structure (d) of the Nafion film formed in this work is also shown, with the dark spheres in (c) representing the openings of the nano-channels, shown as the dark vertical segments in (d).	45
Figure 3.4. Experimental spreading ratio of a water droplet impacting on spin-coated a thin Nafion film and on a series of Vulcan Carbon (VC)/Nafion composite surfaces (10–50 wt. %).	48

Figure 3.5. Experimental spreading ratio of a water drop impacting on a series of Vulcan Carbon (VC)/Nafion composite surfaces (50–90 wt. %). Inset figure shows the spreading ratios at $t = 16$ ms.	48
Figure 3.6. Schematic of Nafion, oriented on VC particle surface, with its hydrophobic backbone outwards, resulting in a hydrophobic outer surface.	49
Figure 3.7. Scanning electron microscopy (SEM) images of Pd/Au-sputtered (a–b) 20% VC/Nafion, (c–d) 40% VC/Nafion, (e–f) 60% VC/Nafion, (g–h) 80% VC/Nafion, and (i–j) 90% VC/Nafion.	51
Figure 3.8. Cartoons of a water droplet (blue) recoiling after impacting on the surface of (a) 30% VC/Nafion, (b) 40% VC/Nafion, (c) 60% VC/Nafion, and (d) 90% VC/Nafion, as seen at $t = 6.4$ ms in Figure 3.1, showing the interaction between the water droplet and the carbon/Nafion composite surfaces.	53
Figure 4.1. XRD patterns of the carbon samples (a) before and (b) after heat treatment (HT) at 1500 °C in a N ₂ atmosphere.	62
Figure 4.2. Field-emission scanning electron microscopy (FE-SEM) images (200,000 times magnification) of (a) VC, (b) VC-HT, (c) CIC-12, (d) CIC-12-HT, (e) CIC-22, (f) CIC-22-HT, (g) CIC-50, and (h) CIC-50-HT powders, all supported on carbon tape, at a high magnification.	64
Figure 4.3. Field-emission scanning electron microscopy (FE-SEM) images of (a) Vulcan carbon (VC), (b) VC-HT, (c) CIC-12, (d) CIC-12-HT, (e) CIC-22, (f) CIC-22-HT, (g) CIC-50, and (h) CIC-50-HT powders, all supported on carbon tapes, at low magnifications.	65
Figure 4.4. N ₂ adsorption (solid line) and desorption (dashed line) data for the carbons (a) before and (b) after heat-treatment (HT) for 2 h at 1500 °C in a N ₂ atmosphere. The corresponding pore size distributions (c) and (d) were calculated from the adsorption branch of the isotherm, using the Barrett-Joyner-Halenda (BJH) method, with the t -curve of carbon black used as the standard to determine the statistical thickness of the adsorbed nitrogen film.	67
Figure 4.5. Pore size distributions of the carbons (a) before and (b) after heat-treatment (HT) for 2 h at 1500 °C in a N ₂ atmosphere, calculated from the desorption branch of the N ₂ adsorption-desorption isotherms (Figure 3) using the Barrett-Joyner-Halenda (BJH) method, with the t -curve of carbon black used as the standard to determine the statistical thickness of the adsorbed nitrogen film.	68
Figure 4.6. Sequential images of a water droplet (diameter ≈ 2.7 mm) deposited onto flat carbon pellet surfaces, before and after heat-treatment at 1500 °C under a N ₂ atmosphere, showing the contact angle kinetics (CAK) of water on the pellet surfaces.	73
Figure 4.7. Contact angle kinetics (CAK) of water droplets after deposition onto carbon pellets (a) before and (b) after heat-treatment at 1500 °C under a N ₂ atmosphere.	75

Figure 4.8. Water vapor sorption (V_{WVS}) of carbons (a) before and (b) after heat-treatment at 1500 °C under a N_2 atmosphere, at room temperature.	78
Figure 4.9. Water vapor sorption data (from Figure 4.8) of carbons (a) before and (b) after heat-treatment at 1500 °C under a N_2 atmosphere, normalized to their corresponding surface area and pore volume (Tables 4.2 and 4.3), obtained from nitrogen sorption isotherms (Figure 4.4).	82
Figure 4.10. Cyclic voltammograms (CVs) of VC, VC-HT, CIC-22, and CIC-22-HT in N_2 -saturated 0.5 M H_2SO_4 aqueous solution at a scan rate of 10 mV/s.	89
Figure 5.1. Schematic illustration of ordered mesoporous carbon (OMC) synthesis using ordered mesoporous silica as the template.	94
Figure 5.2. Field-emission scanning electron microscopy (SEM) images of (a, b) OMC-S, (c, d) OMC-S-HT, (e, f) OMC-A, and (g, h) OMC-A-HT, supported on carbon tape.	98
Figure 5.3. (a) N_2 adsorption (solid line) and desorption (dashed line) analysis of OMCs before and after heat-treatment for 2 h at 1500 °C in a N_2 atmosphere, and (b) the corresponding pore size distributions obtained from the adsorption branch of the isotherm, obtained using the Barrett-Joyner-Halenda (BJH) method, with the t -curve of carbon black used as the standard to determine the statistical thickness of the adsorbed nitrogen film.	99
Figure 5.4. Schematic of the cross-sectional structure of a slit-like pore, potentially formed by the agglomeration of OMC-S particles, with its edges and mouth blocked by microporous carbon walls.	99
Figure 5.5. (a) Schematic of cross-sectional dimension of the pores (white circles) and pore walls of hexagonal mesoporous silica (HMS, grey), used as template for the synthesis of ordered mesoporous carbons (OMCs). (b) Schematic of cross-sectional dimension of the HMS pores filled with carbon nano-strings (black circles), after the carbon precursor-filled HMS (a) has been heat-treated at high temperature (900 °C). (c) Schematic of cross-sectional dimension of the pores of OMCs after removal of silica from (b).	102
Figure 5.6. Schematic of the cross-sectional dimensions of (a) the carbon/HMS composite after heating at 900 °C and before the removal of silica, with the circles (black: carbon strings, white: non-filled pores) having the same dimensions as those in Figure 4b.	103
Figure 5.7. Cartoon showing a possible mechanism of the development of the microstructure of anthracene-based ordered mesoporous carbon (OMC-A).	106
Figure 5.8. Sequential images of water droplets (diameter ≈ 2.7 mm) deposited on compressed OMC pellets, before and after heat-treatment at 1500 °C under a N_2 atmosphere, showing the contact angle kinetic (CAK) behavior of water on the pellet surfaces.	110
Figure 5.9. Contact angle kinetics (CAK) of water droplets deposited onto the OMC pellets, before and after heat-treatment at 1500 °C under a N_2 atmosphere (data from Figure 5.8).	111

Figure 5.10. Water vapor sorption (V_{WVS}) data for OMCs, before and after heat-treatment at 1500 °C under a N_2 atmosphere, all at room temperature.	114
Figure 5.11. Water vapor sorption data (V_{WVS} , from Figure 5.10) of OMCs (a) before and (b) after heat-treatment at 1500 °C under a N_2 atmosphere, normalized to their corresponding (a) surface area and (b) pore volume (Tables 5.2), obtained from nitrogen sorption isotherms (Figure 5.3a).	116
Figure 5.12. (a) Partial pressure (P/P_o) required to condense N_2 (Figure 5.3a) to fill the same pore volume as water vapor did at each stage in Figure 5.10. (b) Estimated size of the pores that have been fully filled by water with time, corresponding to the points in Figure 5.10, calculated using the Kelvin equation (5.2) and the statistical thickness of an adsorbed N_2 film on a carbon black surface (Equation 5.3).	119
Figure 5.13. Cyclic voltammograms (CVs) of OMCs, before and after heat treatment, in N_2 -saturated 0.5 M H_2SO_4 at a scan rate of 10 mV/s.	122
Figure 5.14. Cartoon of the cross-sectional microstructure of (a) OMC-A and (b) OMC-S.	125
Figure 5.15. Cartoon showing a possible mechanism of the development of the microstructure of sucrose-based ordered mesoporous carbon (OMC-S).	127
Figure 6.1. N_2 adsorption (solid line) and desorption (dashed line) isotherms for VC and CIC-22, before and after surface functionalization with pentafluorophenyl ($-PhF_5$) groups using the diazonium reduction reaction (Scheme 6.1).	134
Figure 6.2. Pore size distribution of carbons before and after surface functionalization, calculated from the (a) adsorption and (b) desorption branches of the N_2 sorption isotherms (Figure 6.1) using the Barrett-Joyner-Halenda (BJH) method, with the t -curve of carbon black used as the standard to determine the statistical thickness of the adsorbed nitrogen film.	135
Figure 6.3. Sequential images of water droplets deposited on carbon pellets before and after surface functionalization with pentafluorophenyl groups.	143
Figure 6.4. Contact angle kinetics (CAK) of water droplets after deposition onto carbons pellets before and after surface modification with $-PhF_5$ groups.	144
Figure 6.5. Water vapor sorption (WVS) data of VC and CIC-22, before and after surface functionalization with pentafluorophenyl ($-PhF_5$) groups, in a water vapor atmosphere at room temperature.	146
Figure 6.6. Water vapor sorption data (V_{WVS} , from Figure 6.5) of VC and CIC-22 before and after surface functionalization, normalized to their corresponding (a) surface area and (b) pore volume (S_{BET} and S_{NSI} in Table 6.1, respectively), obtained from nitrogen sorption isotherms (Figure 6.1).	148

Figure 6.7. (a) Partial pressure (P/P_o) required to condense N_2 (Figure 6.1) to fill the same pore volume as water vapor did at each stage in Figure 6.5. (b) Estimated size of the pores that have been filled by water with time, corresponding to the points in Figure 6.5, obtained by using the Kelvin equation (5.2) and the statistical thickness of an adsorbed N_2 film on a carbon black surface (Equation 5.3) at the corresponding partial pressures in (a), as described in Chapter 5.150

Figure 6.8. Cyclic voltammograms (CVs) of (a) VC, (b) VC- PhF_5 , (c) CIC-22, and (d) CIC-22- PhF_5 in N_2 -saturated 0.5 M H_2SO_4 solution at a scan rate of 10 mV/s.155

Scheme 1.1. Molecular structure of Nafion.5

Scheme 3.1. Molecular structure of PMMA.39

Scheme 4.1. Model of zig-zag edge configuration (top side) of graphene layers.90

Scheme 6.1. Functionalization of carbon surfaces with pentafluorophenyl ($-PhF_5$) groups.132

Scheme 6.2. Suggested C-C single bonds between $-PhF_5$ groups and carbon surfaces: (a) a planar graphene surface and (b) a surface composed of graphene edges (top side).141

Scheme 6.3. Possible reactions of carbon surfaces with amyl nitrite during the functionalization reaction (Scheme 6.1).154

List of Symbols

Symbol	Value	Units	Definition
C_g		F/g	gravimetric capacitance
C_s		F/m ²	specific capacitance
d		nm	Pore diameter
d_{002}		nm	Interlayer spacing of graphitic structure
l		nm	Length
L_c		nm	Crystallite length in the c -direction
m		g	Mass
M		g/mol	Molar mass
M_w		g/mol	Molecular mass
N_A	6.022×10 ²³	mol ⁻¹	Avogadro's constant
P		Pa	Pressure
P_o		Pa	Saturated pressure
P/P_o			Partial pressure
R	8.31451	J/K mol	ideal gas constant
r		nm	Pore radius
S_{BET}		m ² /g	BET surface area
S_{BJH}		m ² /g	BJH surface area
$S_{external}$		m ² /g	External surface area
S_{micro}		m ² /g	Micropore surface area
T		K, °C	Temperature
t		ms, h	Time
t		nm	Thickness (used with subscripts, e.g., t_{ads})
T_g		°C	Glass transition temperature

V_m	L/mol	Molar volume
V_{micro}	mL/g	Micropore volume
V_{mono}	mL/g	Volume of one monolayer of water
V_{NSI}	mL/g	Pore volume
V_{WVS}	mL/g	Volume of adsorbed/condensed water vapor
γ	J/m ² , N/m	Surface tension
θ	°	Contact angle
λ	nm	Wavelength
π	3.14159...	
ρ	g/cm ³	Density
σ	nm ²	Cross-sectional area of molecule

List of Abbreviations

Abbreviation	Definition
A	Anthracene
ACL	Anode catalyst layer
BET	Brunauer-Emmett-Teller
BJH	Barrett-Joyner-Halenda
CAK	Contact angle kinetics
CIC	Colloid-imprinted carbon
CCL	Cathode catalyst layer
CL	Catalyst layer
CNT	Carbon nanotubes
CS	Colloidal silica
CV	Cyclic voltammetry
DI	Droplet impacting
DMFC	Direct methanol fuel cell
FC	Fuel cell
FESEM	Field-emission scanning electron microscopy
GC	Glassy carbon
GDL	Gas diffusion layer
HMS	Hexagonal mesoporous silica
HT	Heat-treated, Heat-treatment
HR-TEM	High-resolution transmission electron microscopy
MEA	Membrane electrode assembly
MP	Mesophase pitch
MPL	Microporous layer
N	Naphthalene

ND	Not detectable
NSI	Nitrogen sorption isotherms
OMC	Ordered mesoporous carbon
ORR	Oxygen reduction reaction
PEMFC	Proton exchange/electrolyte membrane fuel cell
-PhF ₅	Pentafluorophenyl group
PMMA	poly(methyl methacrylate)
PTFE	Polytetrafluoroethylene
RHE	Reversible hydrogen electrode
S	Sucrose
SEM	Scanning electron microscopy
TEM	Transmission electron microscopy
TGA	Thermogravimetric analysis
TPB	Triple-phase boundary
VC	Vulcan carbon
WVS	Water vapor sorption
XRD	X-ray diffraction

Chapter One: Introduction

1.1 General background

It is well-known that the population (estimated to be 7.2-7.3 billion by January 2015 [1, 2]) of this resource-limited planet is continuously growing at a rate of ca. 1.1 % annually. Inevitably, this dramatic increase in population will result in a significant increase in the already great energy demand required to support the everyday activities of the human race, despite fluctuations in the global energy market. Currently, fossil fuels (e.g., natural gas, raw oil and coal) are the dominant energy sources. However, the combustion of these fuels to form a usable form of energy (e.g., electric power and heat) produces a huge amount of carbon dioxide, nitrogen oxides, sulfur oxides, air-borne particulates, etc., which are blamed for their role in global warming, ozone depletion, acid rain, and air pollution. Because of these negative impacts of traditional industrial development, sustainability of the relationship between human beings and the natural environment is currently a world-wide area of focus [3].

In order to reach the goal of sustainable development, governments, institutions, and individuals are seeking advanced materials and techniques to improve the utilization efficiency of traditional energy resources, and to increase the use of renewable energy sources (e.g., solar, wind, hydropower). Because of the ability to convert chemical energy to electricity with very high efficiency and without pollutant emissions [4-8], fuel cells are one of the most promising techniques for reaching the goal of sustainable development, and thus this technology has been extensively studied in recent decades.

Fuel cells (FCs) include alkaline fuel cells, polymer electrolyte membrane fuel cells (PEMFCs), direct methanol fuel cells (DMFCs), phosphoric acid fuel cells, molten carbonate fuel cells, and solid oxide fuel cells, listed in order of their operating temperatures [9]. In addition to their high energy conversion efficiencies and very low emissions, FCs are normally quiet and can be easily maintained, since they do not involve any moving parts, as is the case in combustion engines. These advantages make FCs a promising alternative power source for cell phones, vehicles, stationary electricity, and so on.

1.2 Polymer electrolyte membrane fuel cells (PEMFCs)

PEMFCs are also known as proton exchange membrane fuel cells, devices that are able to convert the chemical energy of H_2 and O_2 to electricity with electrical efficiencies up to 60% in practice. H_2 is used as the fuel for PEMFCs because of its high energy density of 33 kWh/kg and one possible environmentally friendly regeneration method (by the electrolysis of water, using renewable energy). As shown in Figure 1.1, a PEMFC consists of two catalyst layers (CLs), separated by a polymer electrolyte membrane (PEM) and each attached to a gas diffusion layer (GDL) and two flow/bipolar plates (bipolar plates are used when multiple fuel cells are stacked in series). Without including the flow/bipolar plates, these components are collectively referred to as the membrane electrode assembly (MEA), which is the core component of a PEMFC (Figure 1.1).

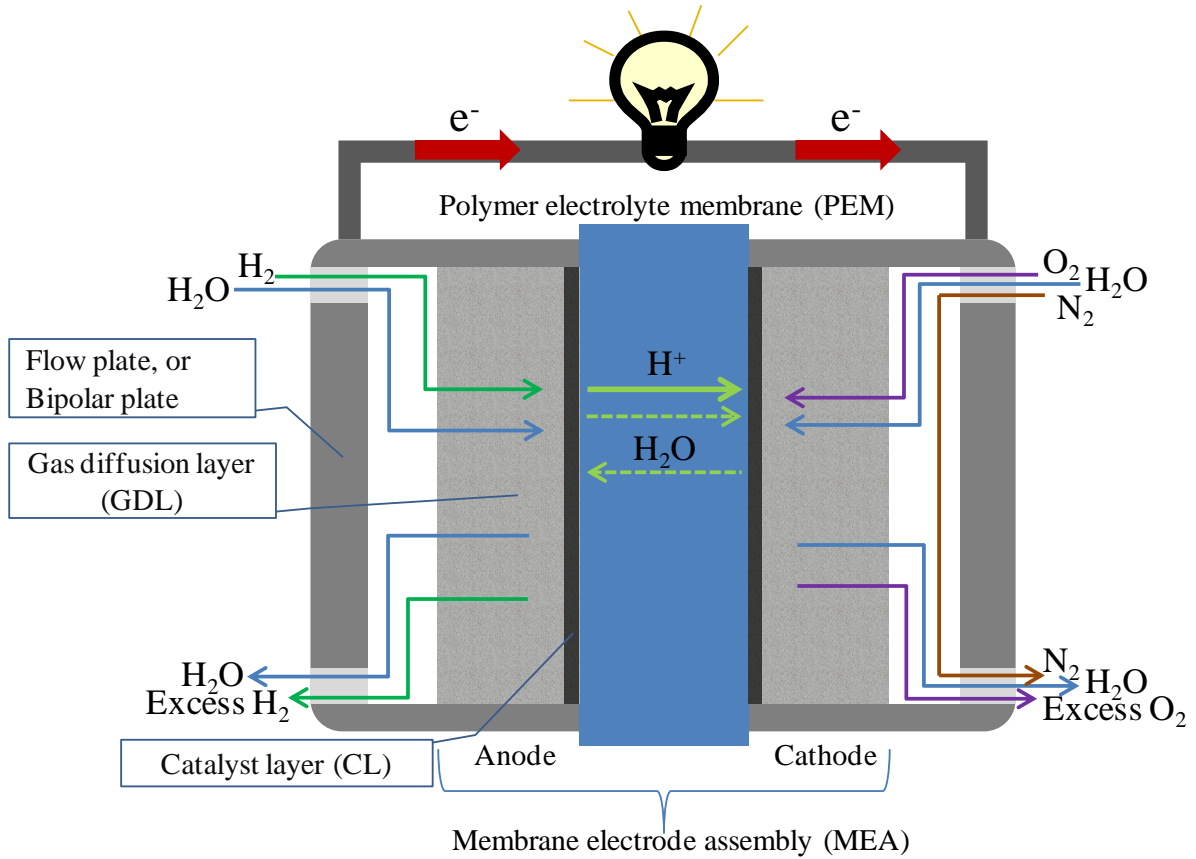


Figure 1.1. Cross section of a H₂–air polymer electrolyte membrane fuel cell (PEMFC).

At the anode catalyst layer (ACL), hydrogen is oxidized following the electrochemical half reaction given in Reaction 1.1,



The generated protons are transported through the electrolyte membrane to the cathode catalyst layer (CCL), where they react with oxygen (Figure 1.1) and the electrons that are transported via the external circuit to form water, as shown in Reaction 1.2.



Hence, in this process, while H₂ and O₂ are consumed, electrical power and pure water are generated, with the overall reaction given in Reaction 1.3,

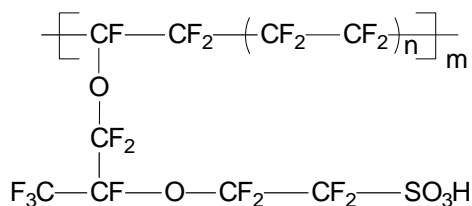


At both CLs, Pt nanoparticles are typically used to catalyze the redox reactions (Reactions 1.1 and 1.2). In order to decrease the cost and to increase their utilization, the Pt nanoparticles are deposited on a carbon support, which has a relatively low cost as well as a high electronic conductivity, surface area, and porosity. Carbon black, such as Vulcan carbon XC-72R (VC), is currently the most widely used catalyst support [10-12]. Due to the high price of Pt, non-noble-metal catalysts are also being developed in order to cut down the cost of manufacturing PEMFCs [13]. However, this is out of the scope of this thesis, which is focused mainly on the carbon materials using to support the catalytic Pt nanoparticles. Even so, the findings of this work would also be relevant to non-noble-metal catalyst development, which also involve the use of carbon powders as supports.

A polymer electrolyte (ionomeric phase, Figure 1.1), normally a poly(perfluorosulfonic acid) (PFSA), e.g., Nafion[®] (Scheme 1.1), functions as an ion selective separator between the anode and the cathode, and also serves as a critical component of both the anode and cathode CLs, where its primary role is to facilitate H^+ transport to/from the catalytic sites [14-19]. The proton conductivity of Nafion is significantly dependent on temperature and water content, which depends on the relative humidity [20], i.e., the operating parameters of PEMFCs. It is known that the activity towards the oxygen reduction reaction (ORR, Reaction 1.2) increases with the addition of Nafion in the CCL [14, 15]. It has also been reported that the specific Nafion content in the CL has a significant impact on the ORR activity and thus on the fuel cell performance [16-19]. In addition to Nafion, other commercially available PFSA materials are also available, such as Flemion[®] and Aciplex[®]. In addition, a number of new proton conducting polymer

electrolytes are also being developed, e.g., sulfonated poly(ether ether ketone), sulfonated polyimide [21], and metal-organic framework materials [22], such as Na₃(2,4,6-trihydroxy-1,3,5-benzenetrisulfonate) [23], but none of these have shown better properties than Nafion. Since Nafion[®] is the most widely used ionomer in PEMFCs, it was also employed in Chapter 3 of this thesis work.

Normally, carbon fiber paper or carbon fiber cloth is used as the GDL material (Figure 1.1) to support and protect the catalyst layer coated membrane and to collect the current generated from the electrochemical reactions (Reactions 1.1 and 1.2) [24, 25]. These carbon fiber based materials contain micrometer size pores, which facilitate the mass transport of humidified gases (Figure 1.1), and provide good conductivity for current collection. Recently, a microporous layer (MPL), composed of carbon black and Teflon[®] beads (or Nafion, used as the binder), was placed between the carbon fiber paper and catalyst layer in order to improve the mass transport and current collection between these two layers. The MPL is also considered to be a critical component of the GDL, and thus the carbon fiber paper/cloth is sometimes called a macroporous layer [26].



Scheme 1.1. Molecular structure of Nafion.

The bipolar plates (Figure 1.1) are typically composed of polymeric graphite or metal, e.g., stainless steel, containing flow channels to provide the desired flow field of hydrogen and air at the anode and cathode, respectively [27, 28]. The bipolar plate also functions as a current collector and mechanical support for the MEA. The sealing material is also an important component of a PEMFC, as it is essential for the prevention of reactant gas leakage and is also critical for performance stability and enhanced lifetime of PEMFCs [29, 30].

1.3 Challenges for the development of PEMFCs

The challenges involved in the development and commercialization of high-performance PEMFCs include reducing the manufacturing cost and enhancing long-term durability [5, 8, 31-36]. In a PEMFC (Figure 1.1), the Pt catalyst is much more costly than all other components. Therefore, it is essential to cut down the usage of Pt in the CLs while also maintaining high power density, with the goal being to lower the Pt loading to 0.15 mg per cm^2 MEA and also simultaneously increase its power density to 0.8-0.9 W/cm^2 at a cell voltage of ≥ 0.65 V [37]. The US Department of Energy (DOE) has established 2017 technical targets for the reduction of the total Pt group metal (PGM) loading to 0.125 mg_{PGM} per cm^2 of the MEA or 0.125 $\text{g}_{\text{PGM}}/\text{kW}$ (the same as the 2020 targets [38]), a significant decrease over the current Pt loading of 0.4–1.0 mg/cm^2 in PEMFCs [39]. These targets can be realized only by enhancing the utilization of the Pt active surface area at high current densities.

In a CL, the electrochemical reactions (1.1 and 1.2) occur only when the three phases are present in the same location, i.e., the gas (H_2 or O_2), liquid (water, for H^+ transport), and

solid (Pt and carbon, catalysis and conducting e^-), called the triple-phase boundary (TPB) [16, 19, 32, 33]. For example, Figure 1.2 shows the TPB in a PEMFC cathode, which should have as long a length as possible.

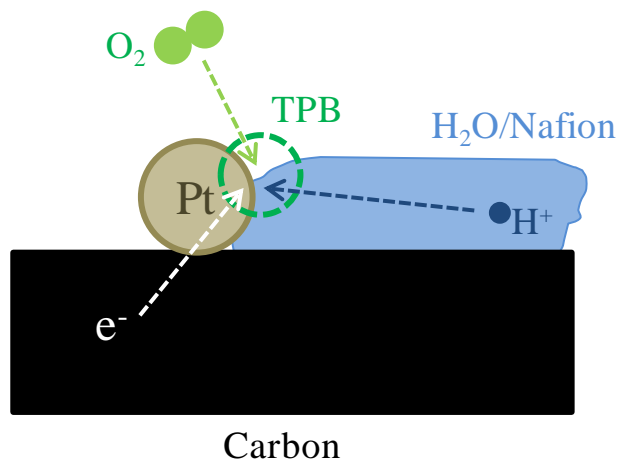


Figure 1.2. Cartoon of triple phase boundary (TPB) in the cathode of PEMFCs where the oxygen reduction reaction (ORR, Reaction 1.2) occurs.

In order to achieve high utilization of the Pt nanoparticles, the number of TPB sites must be maximized, realized through high dispersion of Pt on the carbon support and of Nafion in the pores to conduct the protons. Optimal water management is also required within the CLs, especially in the CCL. As explained above, too much water in the CLs could block the pathways of gases (O_2 in CCL), while too little is harmful for proton conductivity of Nafion. Thus, the surface wettability of the carbon supports used in PEMFC CLs is critical to all of these objectives.

Another goal is to enhance the stability of PEMFCs, i.e., to increase their lifetime while retaining good performance [30]. One problem is the corrosion of carbon catalyst

supports, which is thermodynamically feasible even at very low potentials, and is thus a serious problem at the cathode, where potentials of up to 1.4 V vs. SHE can be reached [40]:



The corrosion of the carbon supports is believed to be accelerated in the presence of Pt and, in turn, carbon corrosion causes a loss of active Pt nanoparticle surface area, thus decreasing the ORR activity in the CCL [41]. Therefore, it is also important to enhance the corrosion resistance of the carbon supports, which is proposed in this thesis work to be tied to carbon wettability.

1.4 Catalyst supports for PEMFCs

1.4.1 Carbon blacks

As mentioned in Section 1.2, carbon blacks (e.g., VC) are widely used as catalyst supports in PEMFCs, due to their low cost and high availability. Carbon blacks are normally produced by the pyrolysis of hydrocarbons and have been used almost exclusively as catalyst supports in low-temperature fuel cells up to the 1990s [42]. VC is a typical example of a carbon black and has a relatively high surface area, but it is microporous (< 2 nm pore size) in nature. Thus the loaded Pt nanoparticles are only present on the outer surface of the VC particles (size: ~ 30 nm), as also found in the previous work of the Birss group [43]. As there are likely to be a wide range of textural pores between the VC particles, any aggregation of the VC particles may bury some of the Pt nanoparticles and also block the pathways of gases and protons to/from them [44]. This will inevitably result in low utilization of the loaded Pt nanoparticles.

1.4.2 Carbon nanotubes (CNTs)

Due to their higher graphitic nature, carbon nanotubes (CNTs) are more stable and conductive than are carbon blacks. Wang, et al. compared the electrochemical surface oxidation of Pt-loaded Vulcan carbon XC-72 (VC) to that of Pt-loaded multiwalled CNTs, and found that CNT-supported Pt is more stable than VC-supported Pt [45]. However, CNTs may also exhibit some disadvantages in other respects. For instance, CNTs may not be as good for the binding of the Pt nanoparticles due to the non-polar CNT surfaces [42]. For this reason, the surface of the CNTs can be modified to improve the bonding to Pt [42], while ideally not affecting the conductivity and corrosion resistance of the CNTs [46]. In 2013, Jha, et al. used chemically modified single-wall CNTs to support Pt for use in both CLs of PEMFCs, resulting in a decrease in Pt loading to 0.06 mg/cm^2 MEA, in accordance with the US DOE 2017 targets [39]. In addition, due to their unique shape, it may be difficult to control the characteristics of the pores between individual CNTs and retain optimal pathways for gas diffusion through the CLs, a problem this still needs to be overcome [46].

1.4.3 Ordered mesoporous carbons (OMCs)

Because of their high surface areas as well as their controllable and ordered pore structures, OMCs have also been considered as a potential alternative to commercially used carbon black supports in PEMFCs [43, 44, 47, 48]. The high surface area of the OMCs promotes good dispersion of the Pt nanoparticles, and ordered mesopores (2-50 nm in size) could be a benefit to electrochemical reaction rates, such as the ORR. Using hexagonal mesoporous silica (HMS) with different pore sizes, Banham, et al. synthesized a series of sucrose-based OMCs with different thicknesses of the carbon ‘nano-strings’, also

determining the ORR activity of OMC-supported Pt nanoparticles [49]. They found that the thicknesses of the ‘nano-strings’ (or the carbon ‘wall thickness’) influences the ORR activity. Specifically, the thinner the nano-string, the poorer the ORR activity, which was attributed to the lower electronic conductivity of the OMC-based films (ohmic loss).

However, when compared to carbon black (VC) supported Pt catalysts (Pt/VC), Banham et al. found that the OMC supported catalysts (Pt/OMC) showed better ORR performance at lower overpotentials due to the smaller particle size of Pt on the OMCs, while, at higher overpotentials, the ORR performance of Pt/OMC was worse than Pt/VC, due to significant mass transport losses through the CL [43]. It was reported that OMC pores 3-8 nm in size may allow for the diffusion of reactants, but restrict ionomer access to the Pt nanoparticles contained in the pores [42]. Therefore, for use of the OMCs as catalyst supports in PEMFCs, larger pores and more conductive carbon walls would be required.

1.4.4 Colloid-imprinted carbons (CICs)

There are various methods used to fabricate mesoporous carbons [50-53], including colloid imprinting [48, 54]. In this approach, mesophase pitch (MP) is used as the carbon precursor, as it has a high conversion efficiency (up to 85%) to carbon [55], while colloidal silica (CS) is normally used as the templating material. CS suspensions are commercially available and have a narrow particle size distribution. In the synthesis of colloid-imprinted carbon (CIC), MP is imprinted at its softening temperature by dried silica colloids and is then carbonized at high temperatures (e.g., 900 °C). Thus, a reverse porous carbon structure is obtained after the removal of the silica template.

It has been shown that CICs formed in this way have a uniform pore size distribution and dense (thus very conductive) pore walls, making them promising catalyst supports, compared to widely used carbon black and other recently developed ordered mesoporous carbons [43, 48]. CICs have also been employed as catalyst supports in fuel cells, giving quite promising results [56, 57]. Banham, et al. have extensively studied the ORR activity of Pt catalyst-supported CICs that had a range of pore sizes (15 - 80 nm) and varied pore depths [43, 48, 58, 59], in acidic solutions, showing that Pt/CICs are promising materials for PEMFC cathodes, due to their thick and crystalline walls, as well as relatively large pore sizes.

1.4.5 Other catalyst supports

In addition to the high surface area carbons discussed above, there are also other types of catalyst supports, such as carbon nanofibers [60, 61], carbon gels [42], metal oxides [61, 62], and so on [61]. Each of them has been shown to have advantages and disadvantages for PEMFC applications [42, 61, 63-65]. For example, compared to carbonaceous supports, metal oxides are thermodynamically more corrosion resistance than carbon samples [62]. At the same time, metal oxides normally have a lower electric conductivity than carbon supports. Therefore, hybrid composite are being considered in order to obtain a property-optimized catalyst support. For example, CeO₂ nanocubes-graphene oxide composites have been investigated as catalyst supports in PEMFCs [66], where CeO₂ serves as the radical scavenger to enhance the stability of the CLs.

1.5 Further treatment of carbon supports

1.5.1 Heat treatment

The carbon precursors used to produce mesoporous carbons (e.g., OMCs and CICs) are normally carbonized at a temperature lower than 1000 °C. Especially for those obtained by using a hard templating method, too high a carbonization temperature may result in reactions between the carbon and the template material. As a result, the as-synthesized carbons are amorphous (low degree of crystallinity or graphitization) and thus prone to electrochemical oxidation when used as a catalyst support in PEMFCs. Therefore, these carbons are often further heat treated at high temperatures (e.g., 2600 °C) to enhance their crystallinity, which will increase their electric conductivity and their resistance to electrochemical oxidation, as presented in the literature [41, 67-69]. This is very important for the long-term stability of PEMFCs.

1.5.2 Surface modification

Surface modification is also widely carried out to extend the applications of carbons [51, 70, 71], including for catalyst supports [64]. For example, carbon nanotubes have been treated with HNO₃ solution to increase their surface polar group density, which, in turn, was shown to improve the dispersion of Pt nanoparticles on the carbon surface [42]. In other work, a polymer layer was physically adsorbed on heat treated mesoporous carbons in order to enhance the bonding between Pt nanoparticles and the carbon surface [68].

Of the various surface modifications employed in the literature, fluorination has often been used to increase the hydrophobicity of carbon surfaces. A simple reaction involves fluorination of a carbon sample with diluted F₂ in N₂ at temperatures lower than 200 °C [72].

Sansotera, et al. thermally treated a mixture of fluorinated peroxides and carbon black (VC) to allow the covalent linkage of fluorinated radicals to the polycyclic aromatic structure of the carbon black, giving very hydrophobic carbon surfaces [73]. Xu, et al. used an *in-situ* diazonium reduction reaction to functionalize 20% Pt/VC with pentafluorophenyl (-PhF₅) groups in order to increase the hydrophobicity of the catalyst for use in a PEMFC, which prevented local flooding in the catalyst layer [74].

1.6 Wettability of components in PEMFCs

As explained in Section 1.3, reducing the manufacturing cost and enhancing the long-term durability are the two main goals in the development and commercialization of high-performance PEMFCs [5, 8, 31-36]. The wettability of all of the components of a PEMFC is critical to reaching these goals [8, 26, 75-77].

1.6.1 Wettability of gas diffusion layers (GDLs) and bipolar plates

The wettability of the GDLs and bipolar plates significantly influences the mass transport of gases through these regions. Particularly at the cathode side, water accumulation (due to Reaction 1.2) will take place in hydrophilic GDLs as well as in the bipolar plate, which can block the air flow channels and thus decrease the performance of the fuel cell [8, 34, 35, 78]. More importantly, water accumulation has also been found to negatively influence the stability of the cathode GDL [30]. However, at the same time, hydrophilic pathways in the GDL are required to facilitate the removal of liquid water from the CCLs [77]. Therefore, an optimum balance between hydrophilicity and hydrophobicity of the GDLs and also of the bipolar plates will enhance the performance and durability of PEMFCs

significantly, thereby decreasing the production cost and enhancing the marketability of these devices.

1.6.2 Wettability of catalyst layers (CLs)

It is still unclear how to balance and precisely control the wettability of the CL and hence the performance of PEMFCs, especially for the cathode CL (CCL), as the ORR (Reaction 1.2) is very sluggish relative to the hydrogen oxidation reaction (Reaction 1.1) in the anode CL (ACL) [43, 79]. Water is critical to enhancing the diffusion of H^+ in the CLs (Figure 1.2) [19, 32] and yet too much water accumulation in the cathode CL decreases O_2 transport, resulting in “flooding” [8, 32, 33]. Normally, flooding can be minimized by making the CCL hydrophobic. However the CLs must also be sufficiently wettable in order to transport H^+ and H_2O to/from the reaction sites (TPB, Figure 1.2) [16, 19, 32, 33]. The control of the wettability of CCLs is also believed to be important to the stability (or life time) of PEMFCs, such as dissolution/dislodgement of Pt nanoparticles and corrosion of the carbon support [30, 63], but there are few reports on the correlation between the wettability and stability of CCLs. For example, it is expected that hydrophobicity could protect carbon surfaces from attack by water (Reaction 1.4) and thus from electrochemical corrosion, beneficial for the durability of a PEMFC [63].

Prior to the startup of this project, investigations of the wettability of CLs mainly relied on modeling [8, 26], which suggested that an optimum balance between hydrophilicity and hydrophobicity in the CLs should be reached in order to maximize the performance of PEMFCs, as explained above. Some work has recommended the addition of hydrophobic components to the CL to increase the density of hydrophobic domains or phases [33, 77], so

as to improve the mass transport of gases. Even so, the wettability of CLs still needs more study in order to fully understand the underlying mechanism, which is essential for the precise control of the wetting of CLs and to optimize the utilization of all of the components.

The wettability of the components of the CLs, i.e., Pt, carbon, and Nafion, has been studied in depth in the past decades, primarily in relation to PEMFC applications [73, 80-85]. A clean Pt surface has been shown to be hydrophilic (almost zero contact angle) [80, 86], while the wettability of carbon surfaces varies, depending on the type and density of the surface functional groups [73, 83, 84, 87]. A dry Nafion film shows a very high advancing contact angle ($\sim 110^\circ$) for water, but a very low receding contact angle ($\sim 30^\circ$), and thus Nafion exhibits a significant contact angle hysteresis [81, 82, 85]. Wood et al. used neutron reflectometry to study the interaction between Pt surfaces and Nafion molecules [88], finding that the polar groups of Nafion (Scheme 1.1) attach to an oxidized Pt surface, while the hydrophobic backbones of Nafion attach to the reduced Pt surface.

The wettability of carbon/Nafion composites, such as those found in the CL, has been studied by only a few research groups [89-91]. Volkovich et al. used the method of standard contact porosimetry to determine the wettability of carbon/Nafion composites [89, 90], finding it to be a function of pore size and also of the nature of the carbon surface functional groups, which are different from those found at bare carbon. In recent years, some researchers have also studied the interaction between carbon and Nafion through molecular dynamic calculations and experiments [88, 92-94]. It was found that the interaction varies, depending on the carbon surface polarity, relative humidity, thickness of the Nafion layer on carbon, etc.

Yu et al. studied the contact angle of water on a catalyst layer using both the conventional sessile drop method and environmental scanning electron microscopy [91]. They found the results to be time-dependent, largely due to the presence of Nafion, which has a high contact angle hysteresis [81, 82, 85], as mentioned above, and a swelling problem during long-time contact with water [82, 88]. These factors make it difficult to study the wettability of the catalyst layers with static contact angle measurements.

In most applications, the surface properties of carbon materials, especially their surface polarity (or wettability), significantly impact on their performance. For example, surface polarity influences the selectivity if carbon is used as an adsorbent [95]. The surface wettability of the carbon materials used in PEMFCs can affect the size distribution and stability of the Pt nanoparticles loaded on them, influence the distribution of Nafion clusters in the catalyst layers [43, 49, 58, 89, 96], and thus play a crucial role in the formation of the TPB (Figure 1.2) in the CLs. Therefore, understanding and controlling the surface wettability of carbon catalyst supports is essential to understanding and controlling the overall performance of PEMFCs because of the critical issue of water balance in the catalyst layers [8, 32, 33].

1.7 Wettability Measurements

The methods available to determine the wettability of a sample surface include contact angle measurements [97-99], capillary penetration (or Washburn method) [98, 100], adsorption/desorption methods [101-103], etc. Application of these methods is always associated with some requirements regarding the size, morphology, surface stability, and mechanical strength of the samples to be tested. Considering the limitations of sample size

and the availability of relevant testing systems, only some of the methods have been employed in this project.

1.7.1 Droplet impacting (DI) method

The droplet impacting (DI) method has been widely used to examine the wettability of surfaces [104-108]. In this approach, the dynamics of the impacting droplet on the sample surfaces are recorded in a sequence of high speed images in order to examine the surface properties. Due to the fast impacting velocity, the interaction behavior of a droplet on the surface must be recorded with a high speed camera, and the interactions only at short times (e.g., 20 ms) are used to determine the wettability of the sample surface [108]. By studying the dynamic behavior of the droplets, the relative wettability of a sample surface can be obtained. However, this method requires that the surface is mechanically robust enough to survive the high kinetic energy impact associated with the falling water droplet.

1.7.2 Contact angle kinetics (CAK)

Contact angle measurements are one of the methods widely used to evaluate the surface wettability of materials [97, 109-111]. Generally, a water droplet is deposited on the surface of a material and the profile of the drop is then captured, from which the water contact angle on the surface can be obtained (Figure 1.3). However, in order to obtain consistent contact angles, these methods require the surface to be as smooth, nonreactive, and homogeneous as possible. These requirements cannot be fulfilled by carbon powders, such as the colloid-imprinted carbons (CICs) and ordered mesoporous carbons (OMCs) mentioned above. This is because the interaction between the carbon particles is relatively weak and

thus the particles can move under an external force. Therefore, it is not possible to employ common contact angle measurements to determine the wettability of carbon powders.

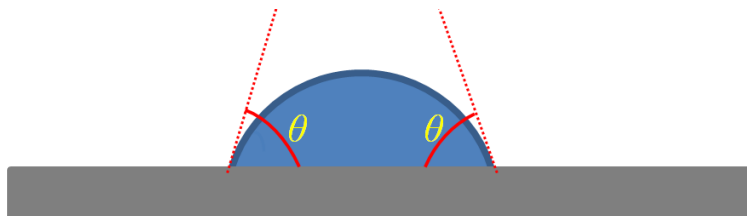


Figure 1.3. Schematic of a water droplet (blue) deposited on a flat sample surface (grey), showing the contact angle (θ) of water on the sample.

Even so, contact angle kinetics (CAK) measurements were recently used to examine the wettability of powder samples [112, 113]. In this method, the contact of water droplets on the powder was recorded with a camera. The sequential contact angles of the water droplet on the sample surface were then compared with those on another sample at a range of times [112-114], instead of at an arbitrary time, as is the case in normal contact angle measurements [97, 109-111]. The relative wettability of the powder samples can then be determined by comparing the contact angles at each instant time after the water droplet contacts and by considering the contribution of the interactions between the sample particles [111-113]. Additionally, CAK studies of carbon powders using water droplets is expected to give more information than a single contact angle measurement, since the contact process is examined dynamically and in more detail.

1.7.3 Water vapor sorption (WVS)

Water vapor sorption (WVS) has also been widely used to determine the hydrophilic/hydrophobic properties of powder/porous samples [111, 115, 116], with WVS of

carbon samples having been studied in depth by many researchers [117-122]. WVS isotherms can provide important information regarding the suitable relative humidity for the storage of powders and also to help understand the intrinsic surface/interfacial properties of materials [102, 103, 122]. A dedicated and well-designed WVS testing system can even reveal the polarity of heterogeneous surfaces [102, 115, 122].

1.8 Other characterization methods used for carbon powders

Other techniques can also be used to determine the wettability of surfaces, such as carbon. For example, elemental analysis and energy-dispersive X-ray spectroscopy has been used to obtain chemical composition information, while X-ray photoelectron spectroscopy can be used to determine the chemical composition of their surfaces [123]. Fourier transform infrared spectroscopy has also been used to analyze for the chemical groups present on carbon surfaces [124]. Cyclic voltammetry (CV) can also be used to examine the electrochemical response of their surfaces [125-127]. Scanning electron microscopy (SEM) and nitrogen sorption isotherms (NSI) of the samples could also be collected to analyze their outer surface morphology and internal porous structures [128]. These data are all very critical to helping to interpret the wetting of carbon surfaces.

1.9 Research objectives of thesis

Collectively, this project has been focused on the study of the wettability of various carbon samples (Vulcan carbon black (VC), colloid-imprinted carbons (CICs) and ordered mesoporous carbons (OMCs)) and carbon/Nafion composites for their applications in the cathode catalyst layer (CCL) of PEMFCs. Specifically, the focus of this project is:

- a) To examine the wettability of Nafion and carbon/Nafion composites and to understand the origins of the wetting properties of these materials.
- b) To measure the relative wettability of as-synthesized and heat-treated colloid-imprinted carbon (CIC) materials.
- c) To correlate the relative wettability of CICs with their elemental and microstructural properties.
- d) To determine the relative wettability of as-synthesized and heat-treated ordered mesoporous carbons (OMCs).
- e) To understand the origin of the different microstructures of OMCs derived from different carbon precursors.
- f) To study the relative wettability of carbon samples after surface functionalization with pentafluorophenyl (-PhF₅) groups and the related surface chemistry.

The findings in this project are also applicable to direct methanol fuel cells (DMFCs), ethanol and formic acid fuel cells (all of which utilize catalyst-supported carbon), capacitors, biosensors, solar cells and other technologies in which the wettability of carbon and carbon/polymer composites plays an important role in their performance.

1.10 Thesis organization

The present chapter provides a general introduction to the research background, including the challenges in PEMFC development, especially related to wettability, and also covering some common wettability measurement methods. Chapter 2 presents the experimental methods used in this project, such as sample preparation and wettability

measurements. Chapters 3-6 are focused on the results obtained in this thesis work, along with a discussion of these results. A short introduction is presented at the start of each of these results chapter to place the chapter in context with the previous one.

Chapter 3 was published in *Langmuir* [96]. In this work, the wettability of Nafion and Nafion/Vulcan carbon (VC) composites was studied using the droplet impacting method. This chapter confirms the surface heterogeneity of the Nafion surface, resulting in different wetting behavior before and after water contact, and it also shows that the wettability of carbon/Nafion composites is very strongly influenced by their composition. The discussion in this chapter provides a basic understanding of the complex factors influencing the surface wettability of composites, such as surface roughness and chemical heterogeneity.

Chapter 4 was published in *Carbon* [129]. This work involves the measurement of the wettability (using contact angle kinetics (CAK) and water vapor sorption (WVS) methods) of the colloid-imprinted carbons (CICs) vs. VC, both before and after heat treatment, where the CICs have a range of pore sizes, derived from the use of colloidal silica of various diameters. Chapter 4 explains how the CAK and WVS results were interpreted, also correlating them with other properties of the carbons. It was found that the CICs are much more hydrophilic than commercial carbon black (VC) and that heat treatment makes all of the carbon samples more hydrophobic, which is consistent with the expectations based on the literature [125, 126]. This, in turn, indicated that both the wettability measurements and the data interpretation methods used are reliable.

In Chapter 5, the wettability and microstructures of ordered mesoporous carbons (OMCs), derived from different carbon precursors but using the same silica template, were investigated. The experimental results show that the carbon precursors significantly affect the

wettability of the final product, which was not expected prior to this thesis work. In this chapter, we further improved the wettability evaluation methods from those used in Chapter 4 in order to better understand the relative wettability of the OMCs before and after heat treatment. Based on these results, some formation mechanisms for the OMCs are suggested in Chapter 5.

Based on the knowledge gained from the work described in Chapters 3-5, the wettability of surface functionalized VC and CIC samples was then evaluated, as presented in Chapter 6. It was found that surface modification with pentafluorophenyl ($-\text{PhF}_5$) groups makes the hydrophilic CIC sample become much more hydrophobic, demonstrated by both the CAK and WVS methods. However, these two methods offer conflicting findings regarding the wettability change of VC after surface functionalization. Based on the results obtained using other characterization methods, it was suggested that the conflicting results arise from differences in surface wetting using water droplets vs. water vapor, especially when micropores are present, as well as side reactions during the surface functionalization process, which left some polar (e.g., nitro) groups on some of the carbon surfaces.

Finally, Chapter 7 summarizes the overall conclusions from this thesis and also provides suggestions for future work, based on the findings obtained in this project.

Chapter Two: Experimental Methods

This chapter summarizes the experimental methods that were used for the work presented in this thesis.

2.1 Preparation of carbon samples

2.1.1 Synthesis of colloid-imprinted carbons (CICs)

The synthesis of colloid-imprinted carbons (CICs) followed the procedures published previously [43, 48, 54, 130, 131]. Briefly, 1 g of mesophase pitch (MP, Mitsubishi Gas Chemical Company, Inc.) was dispersed in 20 mL of ethanol/H₂O (60:40 v/v), and then a colloidal silica suspension (Ludox-HS-40, Ludox-AS-40, or NanoSol-5050S with an estimated average colloid size of 12 nm, 22 nm, and 50 nm, respectively), containing 10 g of silica, was added drop-wise with vigorous stirring under room conditions. After removing the solvent at elevated temperatures (50 - 100 °C), the dried SiO₂/MP composite was heated at 400 °C for 2 h and then cooled down to room temperature, followed by carbonization at 900 °C for 2 h, all under N₂ and using a heating rate of 5 °C min⁻¹. The solid product was refluxed in 3 M NaOH solution for at least 24 hours to remove the SiO₂ template and to form mesopores, and was then washed with water until it remained neutral. The obtained carbons (~ 0.7 g) were named CIC-12, CIC-22, and CIC-50, corresponding to the colloid sizes (in nanometers) used to form their pores.

2.1.2 Synthesis of ordered mesoporous carbons (OMCs)

Hexagonal mesoporous silica (HMS) was used as the template for the synthesis of ordered mesoporous carbon (OMC) materials. The preparation of HMS-16 followed the

procedure reported previously by the Birss group [43, 48, 132], using $C_{16}H_{33}NH_2$ as the soft template and tetraethyl orthosilicate as the silica precursor. Here, “16” in the name of HMS-16 represents the number of carbon atoms in the molecular chain of the surfactant, which determines the HMS pore size (~ 3 nm). Sucrose- and anthracene-based ordered mesoporous carbons (OMC-S and OMC-A, respectively) were synthesized also following previous reports [43, 48, 132], using HMS as the hard template, and sucrose and anthracene as the carbon precursors, correspondingly.

Briefly [43, 48, 132], for the synthesis of OMC-S, 1 g of calcined HMS-16 was mixed with an aqueous sucrose/ H_2SO_4 solution (composed of 1.25 g of sucrose, 0.14 g of 98% H_2SO_4 , and 5 g of water), and the mixture was dried at 100 °C for 6 h and then heated at 160 °C for another 6 h in air. The mixture was impregnated with another sucrose/ H_2SO_4 aqueous solution (composite of 0.8 g of sucrose, 0.09 g of 98% H_2SO_4 , and 5 g of water) and heated again, following the same procedure as before. The carbon precursor-silica composites were carbonized at 900 °C for 2 h in N_2 , using a heating rate of 5 °C/min. OMC-S (~ 0.6 g) was obtained after removing the silica template with NaOH solution and drying at 120 °C for 12 h.

The synthesis procedure used for OMC-A was almost the same as that of OMC-S, except for replacing the sucrose/ H_2SO_4 aqueous solution with the anthracene/ H_2SO_4 acetone solution (0.44 g of anthracene dissolved in 50 mL of 0.14 M H_2SO_4 /acetone solution). The impregnation of 1 g of HMS-16 with the anthracene solution was repeated several times until the solution was fully consumed [43, 48, 132]. The carbon yield when anthracene was used in the synthesis of OMC-A was about 70 %.

2.1.3 Heat treatment of carbons

The synthesized CICs, OMCs, and Vulcan XC-72R carbon black (VC, Cabot, used as received) powders were treated at 1500 °C under a nitrogen atmosphere for 2 h at a heating rate of 5 °C min⁻¹, and the heat-treated carbons were labelled as CIC-12-HT, CIC-22-HT, CIC-50-HT, OMC-S-HT, OMC-A-HT, and VC-HT, correspondingly. All of the carbon samples were dried at 100 °C overnight prior to carrying out any further analysis.

2.1.4 Surface functionalization of carbons

The as-prepared CIC-22 and the as-received VC were dried in air at 100 °C overnight before surface functionalization with pentafluorophenyl groups. 1.0 g of the carbon powder, 5.6 g of 2,3,4,5,6-pentafluoroaniline (Sigma-Aldrich), and 150 mL of acetonitrile were placed into a 250 mL flask, and the mixture was then sonicated for 1 hour under the flow of N₂. After that, 6.2 mL of amyl nitrite was added drop-wise into the mixture in the flask under sonication and N₂ protection. The new mixture was then heated to reflux for 24 hours under N₂. The surface functionalized carbon was then filtered and rinsed with 25 mL of dimethylformamide and 50 mL of acetonitrile. Any reaction residues in the functionalized carbon powders were further removed by Soxhlet extraction with acetonitrile for more than 4 days. Finally, the samples were dried at 100 °C in air overnight. The functionalized carbons were denoted as CIC-22-PhF₅ and VC-PhF₅, respectively.

2.2 Elemental analysis

The carbon, hydrogen and nitrogen content of VC and of the prepared carbons was determined using combustion analysis (PerkinElmer 2400, Chemistry Instrumentation

Facility, Department of Chemistry, University of Calgary). The fluorine content of the surface-functionalized carbons was determined using a classical wet chemistry method (potentiometric titration with $\text{La}(\text{NO}_3)_3$ [133]), conducted by Micro-Analysis (Wilmington, U.S.). The content of inorganic residue (e.g., silica) of the carbons was determined using thermogravimetric analysis (TGA, Mettler-Toledo TGA/DSC 1) by heating each carbon sample at 2 °C/min up to 800 °C under air.

2.3 Determination of carbon crystallinity

A Rigaku Multiflex X-ray diffractometer (Department of Geosciences, University of Calgary) was used to collect the X-ray diffraction (XRD) patterns of the carbon samples, using an XRD angle range of 10 - 90 °. $\text{CuK}\alpha$ radiation ($\lambda = 0.15406 \text{ nm}$) was selected as the X-ray source, with an accelerating voltage and current of 40 kV and 20 mA, respectively.

2.4 Surface morphology

The surface morphology of the carbon powder samples was determined by field emission scanning electron microscopy (FE-SEM) using a Zeiss Sigma VP instrument at an accelerating voltage of 2 kV (for the VC and CIC samples) or 4 kV (for the OMC samples), with an InLens detector used to collect the electronic signals. The sample powders were supported on conductive, adhesive carbon tapes for the imaging experiments.

For the spin-coated films, scanning electron microscopy (SEM) analysis (Philips/FEI instrument, Microscopy and Imaging Facility, University of Calgary) was carried out at an accelerating voltage of 20 kV to image their surfaces and to examine the cross-sections,

especially before the droplet impacting experiments (Section 2.6.1.1). All surfaces and cross-sections were sputter-coated with 20%/80% Pd/Au prior to SEM imaging.

2.5 Porosity determination

The carbons samples were also examined with nitrogen gas adsorption/desorption analysis, with the data collected at ca. 77 K using a Micromeritics Tristar 3020 analyzer (Department of Chemical and Petroleum Engineering, University of Calgary). The samples were out-gassed in N₂ at 250 °C for 4 h, and were then degassed again at a vacuum lower than 10⁻³ Torr, prior to gas sorption analysis. The specific surface area was obtained using the Brunauer-Emmett-Teller (BET) plot [134] in the range of $0.05 < P/P_o < 0.30$, where P and P_o are the equilibrium pressure and the vapour-saturated pressure of nitrogen, respectively. The pore sizes were determined from the adsorption branch of the isotherms using the Barrett-Joyner-Halenda (BJH) method [135], and the total pore volumes were then calculated at $P/P_o = 0.98$.

2.6 Wettability measurements

2.6.1 Water droplet experiments

2.6.1.1 Droplet impacting (DI) method

All of the materials evaluated here for their wettability using the droplet impacting (DI) method (Chapter 3) were deposited as thin films via the spin-coating method [88, 136], with microscopic glass slides used as the substrate in each case. Each glass slide (Microscope Slide) was cut into 2.5 cm × 2.5 cm square pieces. They were subsequently cleaned by

soaking in chromic acid overnight, rinsing with distilled water, and drying in an oven at 120 °C for 2 hours.

As a reference, poly(methyl methacrylate) (PMMA) powder ($M_w = 350,000$ g/mol, $T_g = 122$ °C (midpoint), Aldrich) was dissolved in chloroform (CHCl_3 , $\geq 99.8\%$, Sigma-Aldrich) to form a 1 wt. % PMMA/ CHCl_3 solution for spin-coating. A 5 wt. % Nafion/alcohol stock solution (DuPont) was diluted with isopropanol ($\geq 99.8\%$, Sigma-Aldrich) to form a 1 wt. % Nafion/isopropanol solution. This 1% solution was then mixed with Vulcan carbon (VC, dried overnight at 120 °C) to form VC suspensions (inks), with VC:Nafion mass ratios of 1:9, 2:8, 3:7, 4:6, 5:5, 6:4, 7:3, 8:2, 8.5:1.5, and 9:1. The dispersion of VC in Nafion solution was facilitated by sonication at 20-30 °C for 2 hours.

The prepared solutions of 1% Nafion/isopropanol and 1% PMMA/ CHCl_3 , as well as the varying weight percentage VC/Nafion/isopropanol inks, were spin-coated onto the cleaned microscopic glass slides. A Photo-Resist Spinner (Laurell Technologies Corp.) was employed, with the spin coater set to 100 rpm during the first 5 seconds, 1000 and 3000 rpm in the next 10 and 5 seconds, respectively, and with a final speed of 3000 rpm maintained for another 20 seconds. The coated glass slides were then placed onto a 120 °C hot plate for 10 minutes to minimize any solvent residuals.

The prepared film surfaces were characterized via the DI technique using the experimental setup shown schematically in Figure 2.1. Deionized ultra-filtered water (Fisher Scientific) was selected as the testing liquid in all experiments. Water droplets of about 7 μL volume (approximately 2.4 mm dia) were generated from a 1 mL glass syringe (Hamilton) together with a 25 G steel needle (Precision Glide). The impacting height was set at 120 mm above the substrate.

A high speed camera (DRS Technologies) was used to capture the dynamics of the droplets during their impact onto the prepared surfaces. A frame rate of 5000 frames per second (fps), with a resolution of 256×100 pixels, was selected. All DI experiments were performed at the same magnification and distance away from the camera. In order to capture the details of reflection of each droplet as it impacted onto a surface, the camera was positioned at an angle of inclination of approximately 15° from the horizontal (Figure 2.1). Sequences of these images were recorded by computer via a video card.

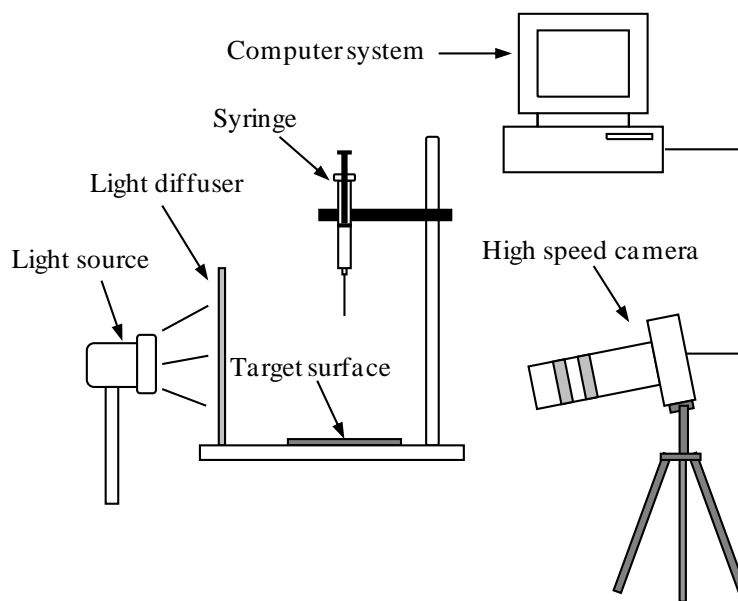


Figure 2.1. Schematic of the experimental setup used for the droplet impacting experiment.

2.6.1.2 Contact angle kinetics (CAK) measurements

This method was used when the sample was considered to be in danger of damage from the high energy associated with the DI method. For the CAK measurements, carbon powder samples (~ 0.1 g) were pressed into pellets (25 mm in diameter) using a stainless steel die under a pressure of 36 MPa for 4 minutes, with the testing system otherwise the

same as that used for the DI method (Section 2.6.1.1, Figure 2.1), but using some different operating parameters, as follows. For the CAK experiments, a 10 μL water droplet (2.7 mm in diameter) was allowed to impinge on the carbon pellets from a height of only ~ 1 mm. These larger water droplets (2.7 vs. 2.4 mm) were generated from a 25 G steel needle with a flattened tip. The droplet behavior was captured by the high speed camera at a frame rate of 1000 fps and with a shutter time of 0.25 ms, and the camera was placed in line with the top surface of the carbon pellets to allow focus on the water droplet contacting the pellet, as shown in Figure 2.2. The magnification of the camera and of the image of the droplets was fixed during the CAK experiments and data analysis for all of the carbons in order to allow an accurate comparison of their wettability to be made.

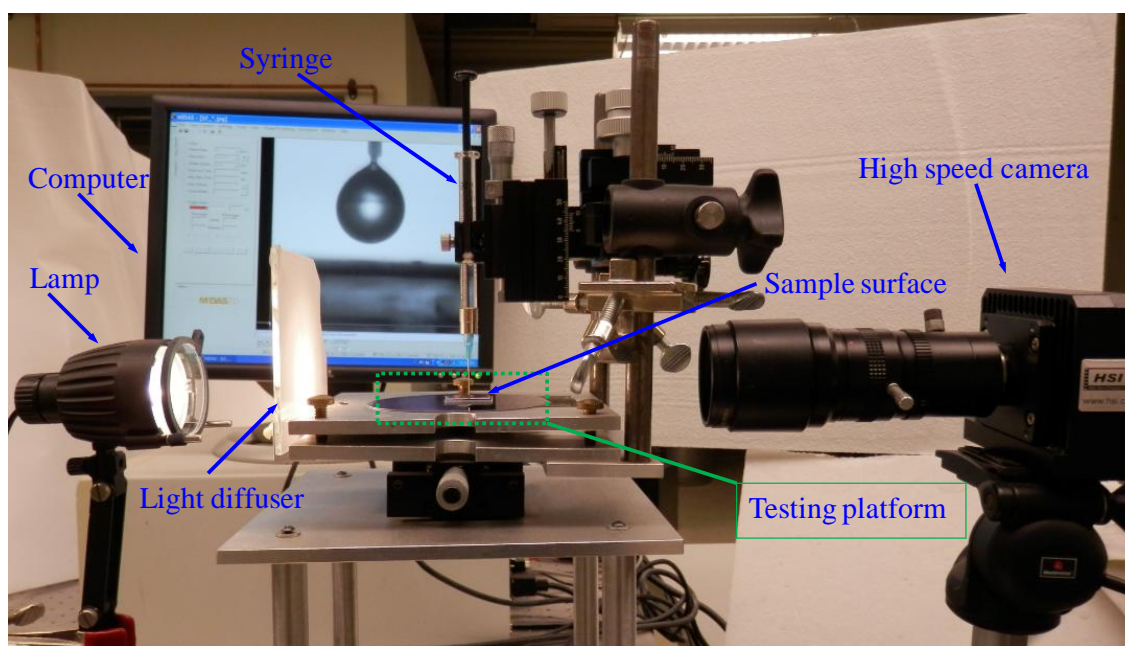


Figure 2.2. Photograph of set-up used for contact angle kinetics (CAK) measurements.

2.6.2 Water vapor sorption (WVS) measurements

0.1 g of each carbon sample was placed into a porcelain crucible, located in a sealed desiccator containing 100 mL of distilled water at room temperature (23 ± 2 °C). Distilled water was placed in the bottom of the desiccator, while the crucible was supported on a grid above the liquid (Figure 2.3). The sample was periodically removed from the desiccator to measure the mass of the crucible plus the carbon sample as a function of time, and then placed back in the desiccator, repeating this sequence until the mass no longer changed. All of the carbon specimens that were to be compared directly with each other in terms of their WVS results were placed in one desiccator (Figure 2.3). For example, all of the OMC samples before and after heat treatment were placed in one desiccator at the same time. This allowed the accurate determination of the relative wettability of the carbons. The mass change of each group of samples (in the same desiccator) was tracked at the same time. The amount of water vapor sorbed by each carbon was obtained by normalizing the mass increase of the carbon to its original mass and to the density of water.

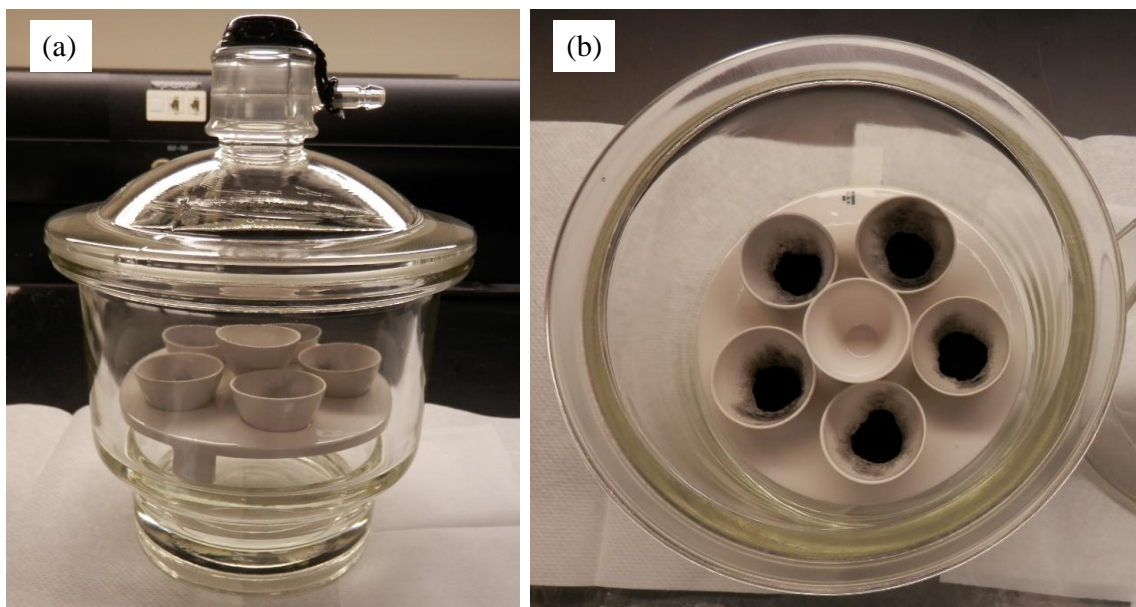


Figure 2.3. (a) Photograph of a sealed dessicator containing carbon samples, used for water vapor sorption (WVS) measurements, where each sample was placed in a crucible. (b) Top-down photograph of the crucibles placed in the dessicator, where the empty crucible was used as a control experiment. 100 mL of distilled water was added into the bottom of the sealed dessicator one day before placing the samples into the dessicator.

2.7 Determination of electrochemical properties of carbons

The surface properties of the carbon samples were determined using electrochemical methods in a 3-electrode cell containing N_2 -saturated 0.5 M H_2SO_4 , a Pt mesh counter electrode, and a reversible hydrogen (RHE) reference electrode [137]. The working electrode was prepared by adding 0.01 g of carbon powder to a vial, followed by the addition of 0.1 g of 12 wt. % H_2SO_4 /ethanol solution. The mixture was sonicated for 5 min and then 0.4 g of 1 wt% Nafion/ethanol solution was added. After sonication for 1 hour, 14 μL of this mixture (ink) was deposited onto the polished end of a glassy carbon (GC) rod and left to dry under room conditions, forming a carbon/ H_2SO_4 /Nafion film. The cyclic voltammetric (CV) response of the film on the GC rod was obtained using an EG&G 173 potentiostat combined

with an EG&G PARC 175 function generator, with the data collected and analyzed by Chart 5 (PowerLab).

2.8 Error analysis

The error in the C, H, N, and F content of carbon samples was estimated according to what is reported by the instrument (PerkinElmer 2400) or the examiner (Micro-Analysis), which is ≤ 0.3 wt. %, while the error in the weight of solid residue of the carbons, synthesized via the hard templating method, is estimated to be < 2 wt. %, based on the information provided by Mettler-Toledo. Since the oxygen content of each carbon sample investigated in this thesis was obtained based on the assumption that the samples are composed only of C, H, N, O, and solid residue (for the synthesized carbons), as well as F for the fluorinated carbons, the error in the oxygen content (δ_O) was thus estimated using Equation 2.1.

$$\delta_O = \left(\sum \delta_i^2 \right)^{\frac{1}{2}} \quad (2.1)$$

where δ_i is the error in the content of each element or solid residue of a carbon sample.

For the droplet impacting experiments (Section 2.6.1.2) presented in this thesis, the diameter of water droplets was ~ 2.4 mm, with a variation of < 3 %, according to the sizes measured in the images of the droplets before contacting the sample surfaces. The instantaneous spreading diameter of the water droplets on the sample surfaces was measured using in-house software coded using Visual Basic, as shown in Figure 2.4. Due to the limited number of image pixels, the measured spreading diameter of the water droplets has an error

of $\pm 5\%$, relative to their sizes before impacting on the sample surface (spreading ratio, Section 3.2).

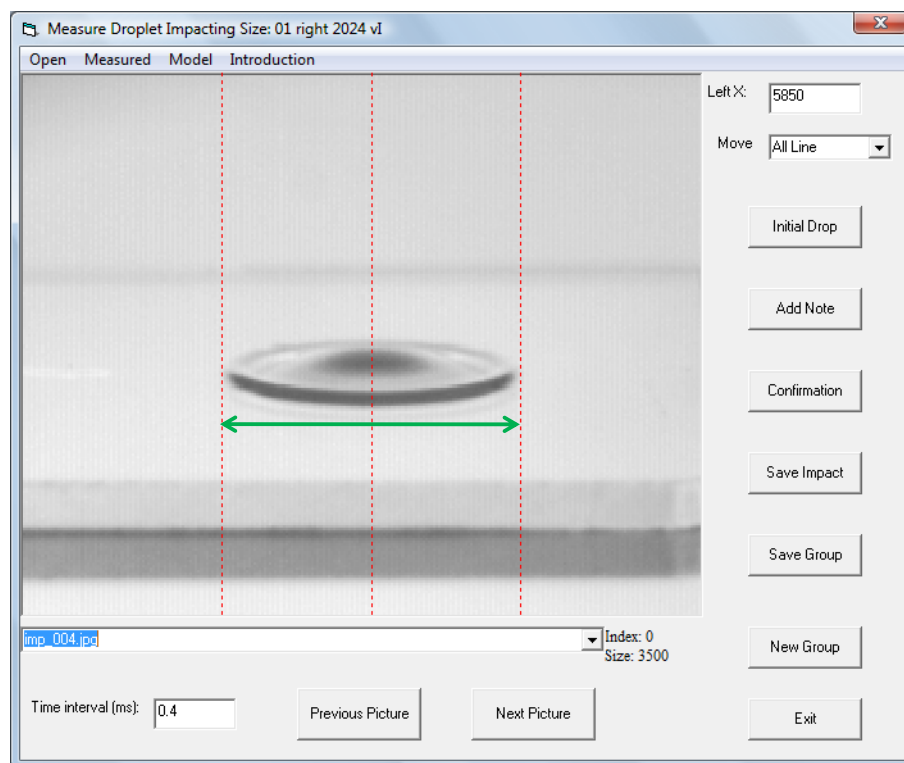


Figure 2.4. Visual Basic software used to measure the instantaneous spreading diameter (green arrow) of a water droplet on a sample surface.

The contact angle of the water droplets on the compressed carbon pellets (Section 2.6.1.2) were measured using software coded using Visual Basic, as shown in Figure 2.4. The error associated with each measured contact angle was about $\pm 2^\circ$. For each carbon sample, the CAK measurements were conducted at least three times, while each image shows two contact angles (left and right, Figure 2.5). The contact angles (vs. time) of the water droplets on the carbon surfaces were obtained by averaging the three groups of CAK results

(≥ 6 contact angles at each time). The deviation in the CAK values for the carbon samples was thus estimated at about $\pm 5^\circ$.

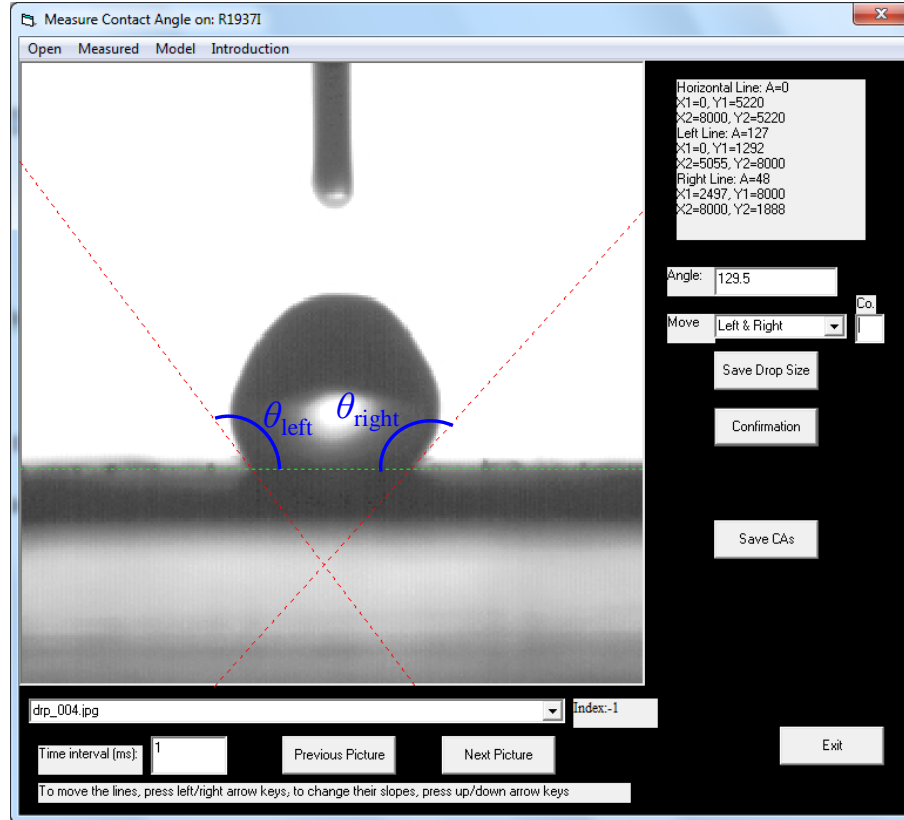


Figure 2.5. Visual Basic software used to measure contact angles of water on a compacted carbon pellet.

During the CAK experiments, the time that it takes for a carbon pellet to fully absorb the impinging water droplet is referred to as “Time to 100% dryness” in this thesis. This parameter was obtained by averaging the time required for at least three water droplets to be taken up by a carbon pellet, with an error of $\pm 10\%$. If a water droplet was not fully absorbed by a carbon pellet in a time shorter than 10 min after deposition, the time to 100% dryness was not specifically monitored during that experiment, because the water droplet may have

rolled off the pellet surface when the carbon sample was removed from the testing platform (Figure 2.2). After a long time on the carbon pellet surface, the water droplet may also have shrunk due to evaporation, which is significantly affected by the surrounding conditions (e.g., relative humidity and air flow). Therefore, only approximate times to 100% dryness were given in these cases, e.g., > 10 min, indicating that the water droplets were still stable on the sample surface after 10 min of observation. These approximate ‘time to dryness’ values of larger than some number of minutes were never used in comparison with each other in this thesis work.

During the WVS experiments, the mass of each carbon sample along with the crucible was tracked with a normal lab balance (AB204, Mettler-Toledo), having an error of ± 0.1 mg. At each time of weighing, the dessicator has to be opened and then the sample (the crucible) was transferred from the dessicator to the balance. During this process, some of the sorbed water evaporated due to the low relative humidity in the lab, resulting in a mass loss. In order to obtain the value of this mass loss, the first sample was measured again after weighing all of the samples in sequence (Figure 2.3), and the mass of each sample was adjusted based on the mass loss of the first sample. This adjustment was verified for each group of WVS measurements by weighing the samples in different sequences, showing that the mass of sorbed water has an error of ± 1.0 mg. Therefore, the WVS data in this thesis have an error of ± 0.01 mL/g, after normalizing to the original sample mass (0.100 g) and the density of water.

In order to assure the precision of the WVS experiments, each crucible and sample was weighed at least twice before placing them into the dessicator to sorb water. The difference between the values obtained from these two-time measurements was at about 0.2

mg. The WVS experiments were stopped only when the weight of the samples in the same dessicator reached a steady state (mass changes smaller than 1.0 mg in three successive measurements).

The as-synthesized or treated carbons obtained from different batches may have had slightly different microstructural properties, e.g., pore size and surface area. However, the relative wettability of the carbons was always found to be the same, i.e., CIC-22 vs. VC, or CIC-22 vs. CIC-50, even though the CAK and WVS results of each carbon may have varied somewhat from one batch to another, due to slight variances in the synthesis procedure or testing conditions.

The cyclic voltammetry (CV) data, shown in this thesis, was obtained by averaging the results obtained for at least three working electrodes, coated with the same carbon material (Section 2.7). The error in the gravimetric current (or capacitance) is estimated at less than $\pm 5\%$. The use of a 12 wt. % H_2SO_4 /alcoholic solution for ink preparation, as described in Section 2.7, has been found to greatly enhance the reproducibility of the CV data shown in this work.

Chapter Three: Wettability of Nafion and Vulcan Carbon/Nafion Composites

The results of this chapter have been published: *Langmuir*, 2012, 28 (16), 6698–6705.

3.1 Introduction

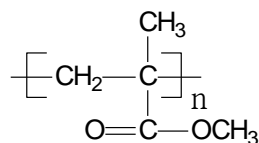
In Chapter 1, it was indicated that understanding the wettability of catalyst layers (CLs, made of Pt/carbon/Nafion composites) used in polymer electrolyte membrane fuel cells (PEMFCs) is critical to managing the water balance within CLs [5, 31, 36], which is also closely related to their durability [5, 8, 31-36]. This is especially important for the cathode catalyst layer (CCL), where water is generated as the product of oxygen reduction.

While there has been some prior work on the wettability of CLs or of carbon/Nafion composites [89-91], as stated in Chapter 1, this chapter represents the first-time investigation of the wettability of carbon/Nafion composites having a wide range of carbon contents. This chapter is also aimed at understanding the wetting properties as well as on the controlled modification of the wettability of CLs for future purposes. Notably, Nafion serves as both the ionomer in the CL, thus extending the electrochemically active area within the CL (Figure 1.2), and as a binder for the Pt-loaded carbon powder. Therefore, it was considered important to determine how the presence of Nafion, as a binder, influences the wettability of carbon itself.

Because carbon black, e.g., Vulcan carbon (VC), is widely used as the catalyst support in the CLs and in the microporous layers (MPLs) in PEMFCs, VC was considered as a good choice for this wettability study. In this chapter, the wettability of a series of VC/Nafion composites with different carbon contents (10-90%) was therefore studied using

the droplet impacting method [104-108]. As described in Section 2.6.1.1, this method only examines the first ~20 ms of water droplet contact with a sample surface. This short-time characterization should avoid the influence of the swelling of Nafion after water absorption on the morphology and wettability of the carbon/Nafion composites.

To achieve a complete understanding of the wettability of the composites, a pure Nafion surface was also examined using the droplet impacting method. In addition, poly(methyl methacrylate) (PMMA, Scheme 3.1) and glass were also employed as reference surfaces to help with the interpretation of the dynamic water droplet impacting data, and thus to understand the relative wettability of all of these surfaces, especially that of pure Nafion. All surfaces (except glass) examined in this study were prepared by casting a solution/suspension of the material onto a solid substrate by spin-coating [88, 136], as described in Section 2.6.1.1, in order to prepare a uniform surface.



Scheme 3.1. Molecular structure of PMMA.

3.2 Results and discussion

Figure 3.1 shows the sequential images of deionized ultra-filtered water droplets impacting onto the surfaces of (a) bare glass, (b) poly(methyl methacrylate) (PMMA, Scheme 3.1), (c) Nafion (Scheme 1.1), and (d) 10–90% VC/Nafion composite films. Given the constant water droplet size and impacting height in all cases, any apparent variation in the impacting behavior arises from differences in the intrinsic surface energetic properties. For example, a water droplet colliding on a glass surface spreads quickly to a contact diameter

that represents the maximum spreading, as seen at 6.4 ms in Figure 3.1 (a). The droplet then behaves essentially like a pancake, without recoil, as a result of very strong adhesion at the water/glass interface. In terms of the PMMA (Figure 3.1 (b)), a water droplet of the same size and impacting height exhibits a relatively smaller maximum spreading diameter (seen at 3.2 ms) with rapid recoil, due to the more hydrophobic PMMA surface (Scheme 3.1).

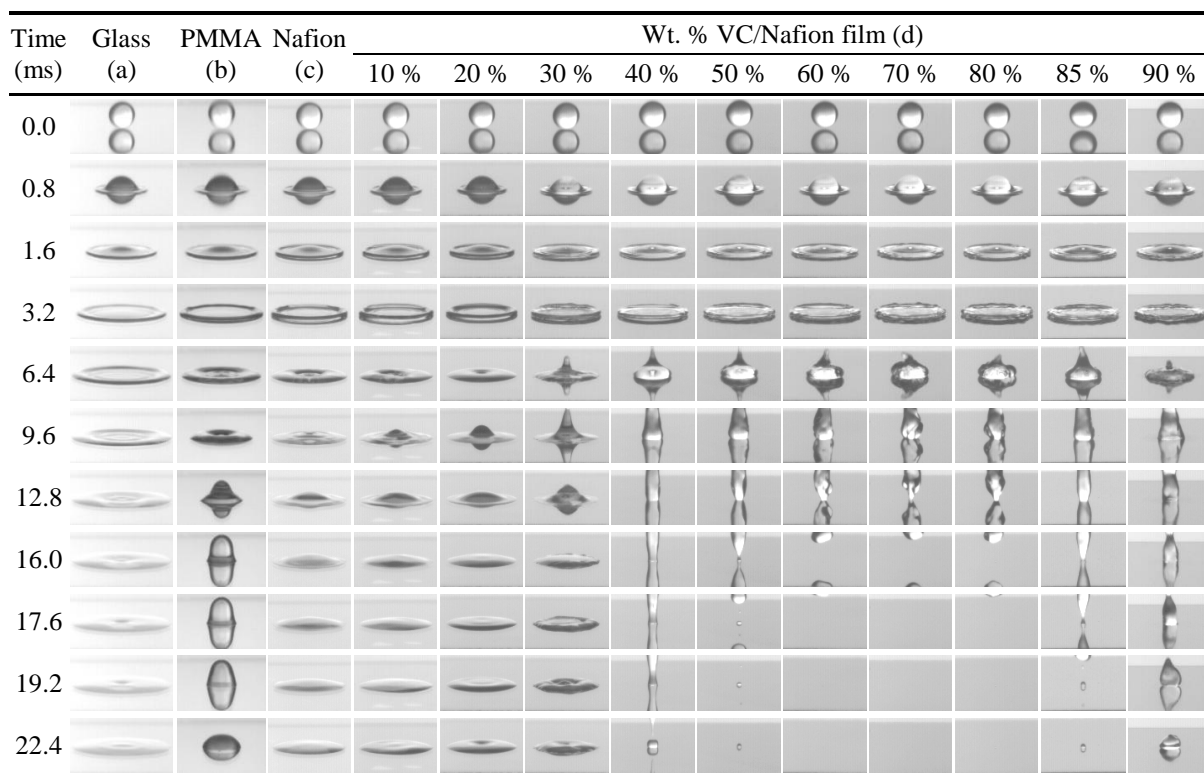


Figure 3.1. Sequential images of a 2.4 mm dia water droplet impacting on (a) bare glass, (b) PMMA (poly(methyl methacrylate)), (c) Nafion, and (d) 10 – 90 wt. % Vulcan Carbon (VC)/Nafion composite thin films, coated on glass, all at an impacting height of 120 mm above the substrate. The differences in the behavior of the water droplets are due to surface energetics.

Figure 3.1 (c) also shows the impacting behavior of a water droplet onto the 100% Nafion film, which is very similar to that on glass except that a smaller maximum spreading

diameter is reached. The gradual addition of VC content, from 0 to 30%, to Nafion (shown in Figure 3.1 (d)) causes the water droplets to increase their recoil, as shown clearly for times between 6.4–12.8 ms. Increasing the VC content to 40% causes a dramatic change, with both recoil and rebound of the water droplet seen (Figure 3.1 (d)), suggesting that the 40% VC/Nafion surfaces are much more hydrophobic than those at 30% VC content. The successive addition of more VC (> 40%) to Nafion results in moderate further accelerated recoiling and fully rebounding characteristics after 16 ms, showing superhydrophobicity starting at ca. 60% VC. At above 80% VC, these recoiling effects are seen to be somewhat slower, leaving some water stuck on the surface, as is explained more fully below.

It is instructive to more closely examine the behavior shown in Figure 3.1. In general, the spreading and recoiling behavior of a droplet on a dry surface results from a balance between inertial and surface forces [104, 106-108]. Given the same water droplet size and impacting height, the inertial force, as calculated from the Weber number [108], is expected to be constant in all cases studied here. This inertial force dominates the initial spreading behavior of the water droplet, while the surface tension of the solids and liquids causes a minimization in their interfacial area, thus interfering with droplet deformation. Therefore, the surface tension (surface hydrophobicity) determines the maximum spreading diameter and the entire recoil process when interfacial and inertial forces are of the same order of magnitude.

One parameter used to characterize the dynamic process of water droplets impacting onto solid surfaces is the so-called ‘spreading factor’ or ‘spreading ratio’ [104, 105, 108], given in Equation (3.1).

$$\text{Spreading ratio} = \frac{\text{Instantaneous droplet contact diameter}}{\text{Initial droplet size before impacting}} \quad (3.1)$$

In Figure 3.2, we plot the spreading ratio of water droplets on glass, PMMA, and Nafion surfaces, calculated by averaging at least 4–5 measurements, vs. time, using the data in Figure 3.1. Error in the calculated spreading ratio arises from error in droplet size estimation via limited image pixels and is estimated to be about ± 0.05 . Another experimental uncertainty lies in the actual time calculation from the different image frames. Since the exact instant of droplet impact can only be estimated between two image frames, the best estimate of the error in time (t) along the x -axis in Figure 3.2 is ± 0.2 ms. As a result, the experimental instantaneous spreading ratios do not necessarily equal zero at $t = 0$ ms.

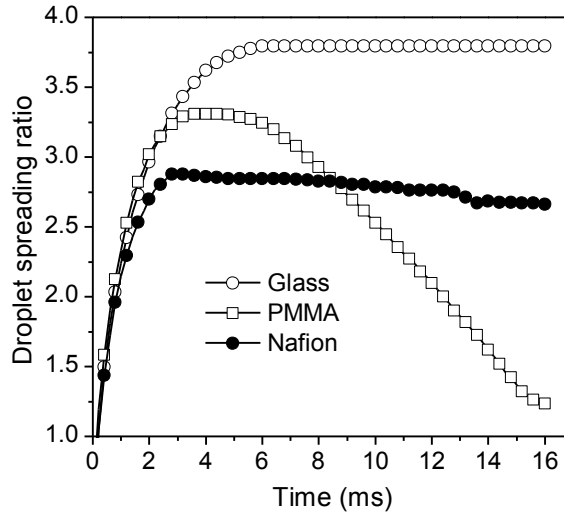


Figure 3.2. Experimental spreading ratio (Equation 3.1) of a water droplet impacting on bare glass, poly(methyl methacrylate) (PMMA), and Nafion surfaces.

In Figure 3.2, it is clearly seen that the maximum spreading ratio of water droplets on a glass surface is larger than that on PMMA. This is as expected, as glass is more hydrophilic than PMMA, and hence, the resistance to droplet deformation due to inertial force is weaker.

Compared to PMMA, the smaller maximum spreading ratio of Nafion indicates that the Nafion surface has a higher resistance to droplet deformation. This confirms the fact that Nafion is more hydrophobic than PMMA, as expected, because of its polytetrafluoroethylene (PTFE) backbone (Scheme 1.1).

Since surface forces dominate the recoil behavior [106, 108], we also examine here the droplet recoil process, which occurs after reaching its maximum spreading. It can be seen in Figure 3.2 that the spreading ratio of water on glass remains roughly constant after reaching its maximum spreading diameter. This is understood to be the result of the hydrophilic nature of the glass surface and hence the strong adhesion between the water and glass surfaces. PMMA is relatively more hydrophobic [108] and, after the water droplet reaches its maximum spread, the instantaneous spreading ratio decreases sharply due to the recoil and rebound of the water as a result of the high surface tension of water and the weaker adhesion between water and PMMA surfaces. Based on our understanding of Nafion, it is expected to have an even more hydrophobic character than PMMA and glass surfaces because of its PTFE backbone. Therefore, one would expect water to recoil faster on Nafion and for its instantaneous spreading ratio to decrease more sharply after reaching its maximum spread. This is contrary to the results shown in Figure 3.2, where the instantaneous spreading ratio of the water droplet on Nafion decreases slightly after reaching its maximum.

3.2.1 Water impacting behavior on 100% Nafion films

The key question therefore arises as to why water droplets on Nafion do not show significant recoil behavior, even though Nafion is expected to have a more hydrophobic surface than PMMA or glass surfaces, as suggested by the smaller maximum spreading ratio

for Nafion in Figure 3.2. However, it is worth pointing out that the hydrophobicity of Nafion is normally associated with the interpretation of a Nafion/air interface. If the exposed functional groups on Nafion are flexible enough to allow re-orientation when in contact with water, the Nafion/water interface will be different from the Nafion/air interface. Indeed, it appears that there is strong “adhesion” at the water/Nafion interface that resists water droplet recoil. Therefore, preferential re-orientation of the sulfonic acid group (Scheme 1.1) towards water may occur, causing the unexpectedly strong adhesion observed in Figure 3.2. Such phenomena have been described as “sticking” effects in the literature [138], observed from static contact angle measurements at some combinations of liquid and solid surfaces.

We also note in Figure 3.2 that, after reaching its maximum spreading, the spreading ratio of water on Nafion has a tendency to decrease only slowly over time, rather than maintaining a constant value, as seen on glass. This could be due to some unknown and complex phenomena at the water/Nafion interface. For this reason, we examined the top-down and cross-sectional morphologies of the Nafion film on glass substrates, as shown in Figure 3.3. The surface of the Nafion film (Figure 3.3a) is very smooth, while its cross-section (Figure 3.3b) shows the presence of parallel nano-channels normal to the substrate.

Rubatat et al.[139] and Schmidt-Rohr et al.[140] recently proposed an elongated parallel water-channel model for hydrated Nafion, which seems to explain the properties of Nafion very well. In this model, Nafion has long cylindrical water-filled nano-channels (e.g., ~ 2.5 nm diameter for a 20% water content), separated by regions composed of the PTFE backbone, with the surface of the channels occupied by sulfonic acid terminates. Figure 3.3b (dry Nafion film) may indicate its good agreement with this model, showing parallel ca. 20 nm channels, which were probably formed by the packing of several inverted-micelle nano-

channels [139, 140] and are expected to be hydrophilic in nature and separated from each other by hydrophobic PTFE zones. All of the channels in Figure 3.3b have an opening at the outer surface at which the water droplet would impinge, as shown by the schematic in Figures 3.3c and 3.3d. The size of these openings on the Nafion surface (20-50 nm, Figure 3.3b) are similar to that of the proton conductive domains of hydrated Nafion membrane, measured with electrochemical atomic force microscopy [4, 141]. As it is not certain whether the vertical channels seen in Figure 3.3b are the same as those proposed in the literature [139, 140], more work will be done to verify this in the future.

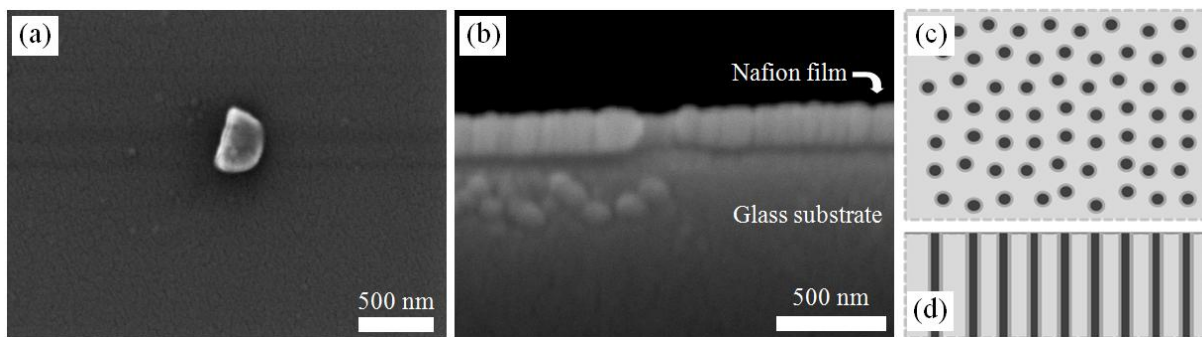


Figure 3.3. Scanning electron microscopy (SEM) images of the Pd/Au-sputtered (a) top-down surface and (b) the cross-section of a Nafion film, prepared by spin-coating a 1% Nafion/isopropanol solution onto a glass substrate. Note that the grey particle at the center of (a), likely a small piece of glass, was used to help with focusing. A schematic of the Nafion film surface (c) and cross-sectional structure (d) of the Nafion film formed in this work is also shown, with the dark spheres in (c) representing the openings of the nano-channels, shown as the dark vertical segments in (d).

Using the structural data and model of Figure 3.3, we can now explain the water droplet impacting behavior on the Nafion film. As the water droplet spreads, the hydrophobic PTFE surface will initially resist it from moving forward so that a very small maximum spreading ratio is seen (Figure 3.2). As the water droplet increasingly contacts the Nafion

surface, as well as the openings of the hydrophilic nano-channels, the sulfonate groups re-orient themselves towards the water droplet. During recoil, this strong interaction between water and the sulfonate groups will prevent the water droplet from recoiling. At the same time, some water may penetrate into the hydrophilic channels due to capillary action. This small decrease in water volume would have a strong effect on near the three-phase contact edge, causing the spreading ratio to decrease slowly. Our suggested behavior of water on Nafion also explains the phenomena, described in the literature [81, 82, 85], that the advancing contact angle of water on dry Nafion membranes is about 110° (Teflon-like), while the receding contact angle is only about 30° . A similar interpretation has been offered for hydrated Nafion membranes by other researchers, based primarily on atomic force microscopy results [4, 141-144].

3.2.2 Water impacting behavior on VC/Nafion composite films

The wettability of the VC/Nafion composites, which is discerned from the water droplet behavior in Figure 3.1 (d), is shown more quantitatively by the droplet spreading ratios in Figures 3.4 and 3.5. In Figure 3.4, it can be seen that, at low VC contents (from 0 to 30 %), the surface is only slightly less hydrophilic than Nafion alone and causes slightly more recoil to occur, as shown from the development of a dip (after the maximum spreading ratio). This is thought to reflect, at least in part, the fact that the sulfonate groups on Nafion will preferentially orient towards the polar VC surface [73], thus exposing more of the Teflon-like backbone to the impacting water droplet, generating a hydrophobic surface and minimizing the overall surface energy (Figure 3.6). This orientation of Nafion on carbon was also proposed recently by other researchers, using similar conditions, including from contact

angle measurements [145], porosimetry [89, 90], and from molecular dynamics studies [146, 147]. It should be noted that all of the films examined here were annealed at 120 °C during preparation, which is higher than the glass transition temperature (T_g , 109 °C) of Nafion [148]. The annealing can facilitate the distribution and orientation of Nafion to decrease the overall surface energy of the composites, hence generating a hydrophobic surface.

When the VC content is increased to 40% and above, however, the recoil increases dramatically (Figure 3.4), indicative of the development of a very poorly wetting surface. Even though pure Nafion does not show a significant recoiling of the water droplet and although the VC particles have a hydrophilic surface [73], their composites display hydrophobic behavior at these ratios of VC to Nafion. As still more VC is added to Nafion (60–80% VC), a superhydrophobic surface is obtained, seen visually in the images in Figure 3.1 (d) and also from the recoil behavior (a spreading ratio of zero at long times) in Figure 3.5.

From an energetic perspective and within the context of the water/composite film interface, the phenomenological contact angles are expected to arise not only from the effect of the three interfacial tensions at the solid-liquid, solid-air, and liquid-air interfaces, but also from surface roughness effects. Therefore, it is possible that our results (Figure 3.5), showing that the water/composite film interface suddenly behaves very differently when the VC content is increased from 30% to 40% and that the “sticking” phenomenon, seen for Nafion alone and for the < 30% VC/Nafion composites, is no longer apparent (Figure 3.1 (d)), may arise from surface roughness contributions.

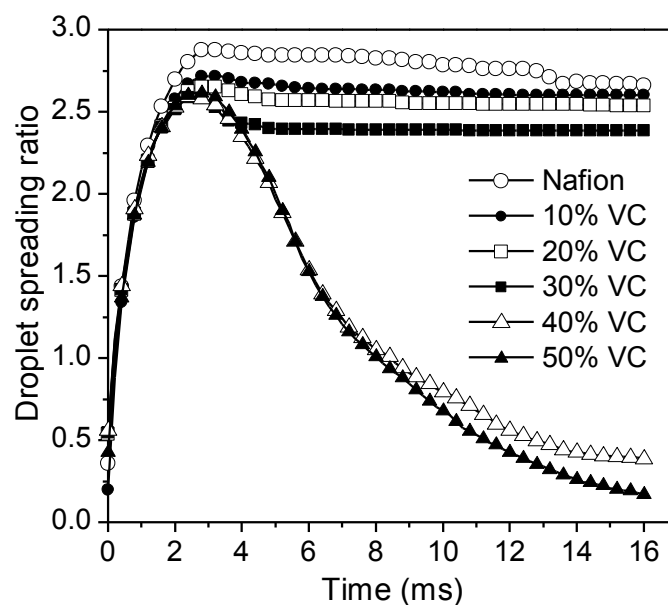


Figure 3.4. Experimental spreading ratio of a water droplet impacting on spin-coated a thin Nafion film and on a series of Vulcan Carbon (VC)/Nafion composite surfaces (10–50 wt. %).

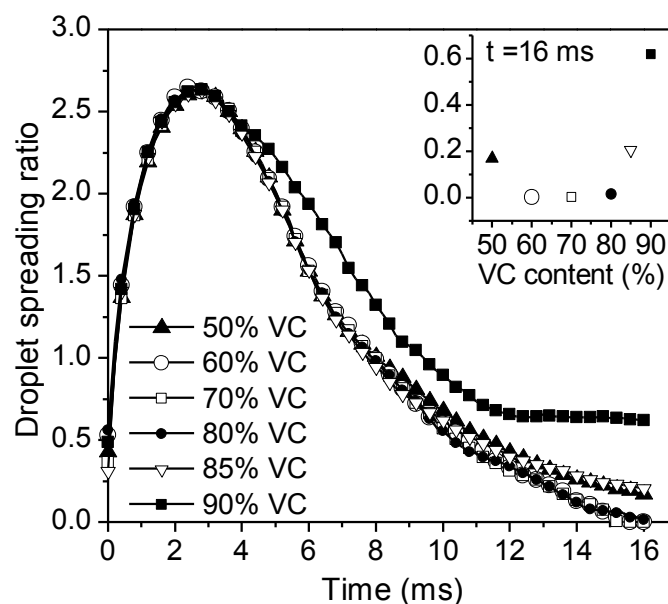


Figure 3.5. Experimental spreading ratio of a water drop impacting on a series of Vulcan Carbon (VC)/Nafion composite surfaces (50–90 wt. %). Inset figure shows the spreading ratios at $t = 16$ ms.

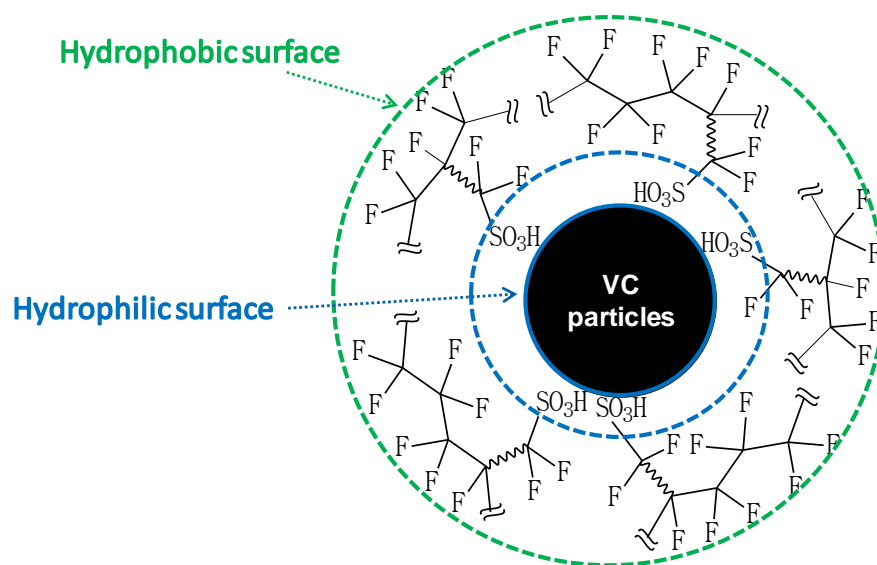


Figure 3.6. Schematic of Nafion, oriented on VC particle surface, with its hydrophobic backbone outwards, resulting in a hydrophobic outer surface.

To verify this, SEM analyses were carried out to determine the surface morphology of a selection of the composite Nafion/VC films. Figure 3.7 shows that the increasing VC content (the brighter regions) in the VC/Nafion films causes a significant increase in the overall roughness, especially in the transition from 20 to 40% VC, when compared to the smoothness of the 100% Nafion film in Figure 3.3. This is the same composition range at which the sudden change in surface wetting characteristics is seen in Figure 3.4. The decreasing extent of “sticking” seen for the 0 to 30% VC/Nafion mixtures (smaller maximum spreading ratio and the small dip after the maximum) in Figure 3.4 is therefore also likely partly due to contributions from surface roughness effects. While surface roughness does add complications to the data interpretation, and although there are a wide range of length scales involved in this work (large water droplet size relative to the smaller size of the carbon particles, the inter-particle pores, and the Nafion film thickness), this should not affect the overall trends observed, which will be dominated by the interfacial energies present.

At higher than 40% VC, when superhydrophobicity is seen (Figure 3.5), the surface roughness remains high for the 60 and 80% VC contents (Figure 3.7). In fact, it is known that a superhydrophobic surface can arise from a combination of hydrophobicity and surface roughness effects [149-154], also reported earlier as the ‘Lotus effect’, seen on plant leaves [149] and various artificial surfaces [150, 153] in contact with water. The surface roughness affects the phenomenological contact angle of water on a superhydrophobic surface by two mechanisms, as described by the Wenzel and Cassie models [151, 152, 154]. In the latter case, tiny air pockets are proposed to form beneath the droplet, which lower the friction and increase the degree of droplet mobility on a hydrophobic surface. This contributes to the observed full rebound of the water droplets from a superhydrophobic surface [152], as shown in the case of the 60-80% VC/Nafion composite films (Figure 3.1(d)).

As the VC content increases from 80 to 90%, it is interesting to note in Figures 3.1 (d) and 3.5 that the rebound behavior decreases again, reflecting a decrease in the superhydrophobicity of the films. Especially for the 90% VC/Nafion film, the dynamic receding contact angle at 9.6 ms is smaller than 90° , indicative of slightly more wettable surface characteristics. This decrease in surface hydrophobicity cannot be explained by an altered surface roughness, as Figure 3.7 shows that the degree of roughness is very similar at these high VC contents. Instead, this behavior indicates that there is now insufficient Nafion available to fully cover all of the VC particles, leaving some of the VC surfaces, which are hydrophilic [73] relative to the non-polar PTFE backbone of Nafion, exposed to the impacting water droplet.

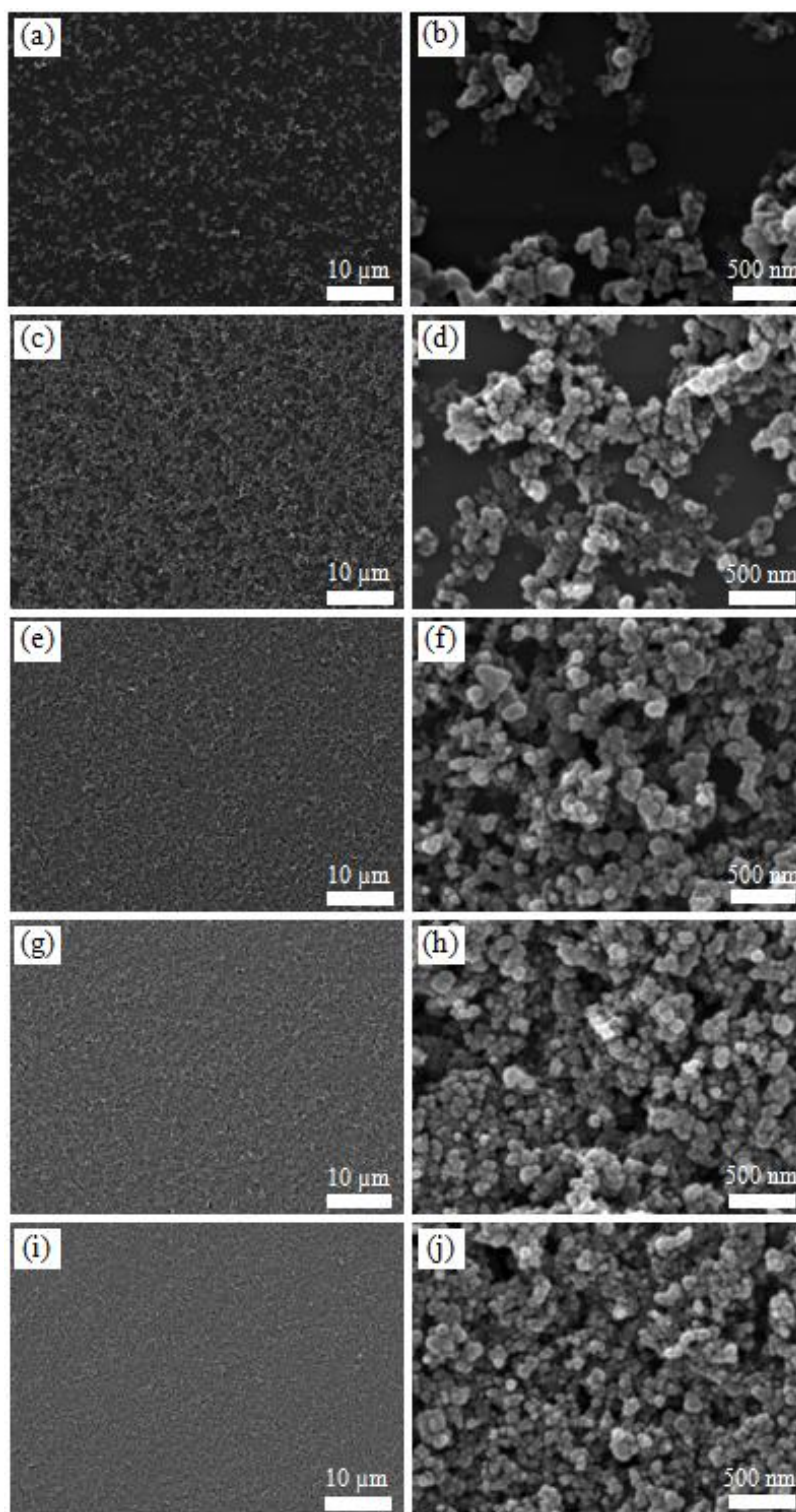


Figure 3.7. Scanning electron microscopy (SEM) images of Pd/Au-sputtered (a–b) 20% VC/Nafion, (c–d) 40% VC/Nafion, (e–f) 60% VC/Nafion, (g–h) 80% VC/Nafion, and (i–j) 90% VC/Nafion. The first and second columns represent the low and higher magnification images of the surfaces, respectively.

In order to clarify the discussion above, Figure 3.8 shows a schematic of the surface structure of some of the VC/Nafion composites, deposited on glass substrates, as well as the interaction of these composite surfaces with recoiling water droplets (in blue), as seen at $t = 6.4$ ms in Figure 3.1. In Figure 3.8, the black structures with the green outline represent the VC particles coated with Nafion, respectively, while the dashed green outline in Figure 3.8d indicates that there is insufficient Nafion present to fully cover the VC particles in the case of the 90% VC/Nafion composite. The light green regions on the glass substrate in Figures 3.8a and 3.8b indicate that excess Nafion is present for the 30% and 40% VC/Nafion composites, as is also seen in the SEM images (Figures 3.7b and 3.7d).

As shown in Figure 3.8a, when the VC content is low (≤ 30 wt %), an impacting water droplet will contact primarily the Nafion domains on the glass substrate, between the carbon particles, and thus cannot easily rebound from the surface (Figure 3.1d). As the carbon content increases (Figure 3.8b), the center of the impacting water droplet surface will be able to contact the Nafion domains on the underlying substrate, due to the high vertical impacting velocity. However, the outer edges of the water droplet will not penetrate between the hydrophobic Nafion-covered carbon particles, resulting in the droplet being unable to completely rebound from the surface (40 % and 50 % VC in Figure 3.1d). When the carbon content is ≥ 60 % (Figure 3.8c), the majority of the Nafion surrounds the carbon particles (Figure 3.7), and thus the water droplets will interact primarily with the hydrophobic Nafion-covered carbon particles (Figure 3.6) as well as the air pockets between the particles (Figure 3.8c), resulting in a superhydrophobic surface.

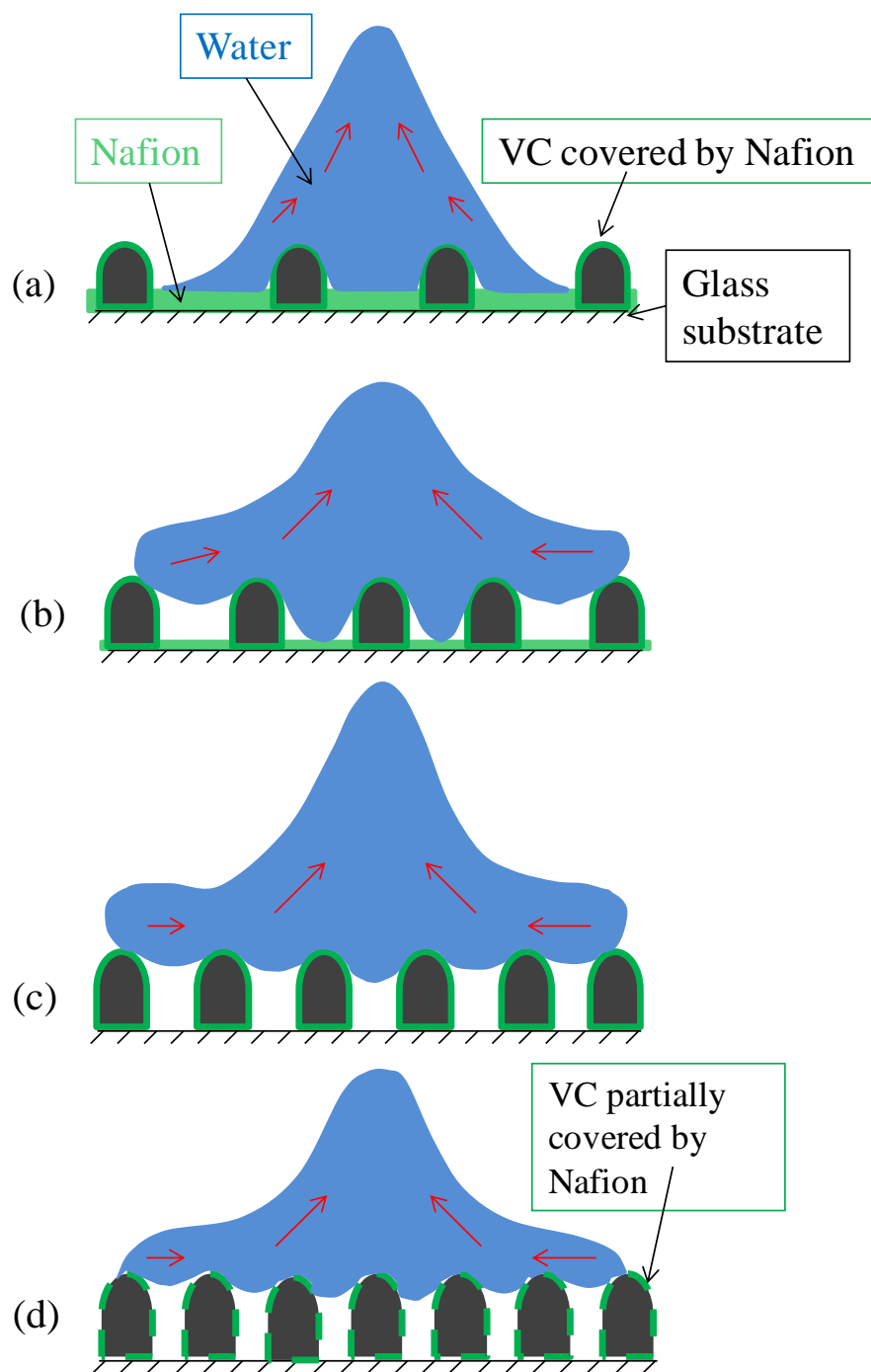


Figure 3.8. Cartoons of a water droplet (blue) recoiling after impacting on the surface of (a) 30% VC/Nafion, (b) 40% VC/Nafion, (c) 60% VC/Nafion, and (d) 90% VC/Nafion, as seen at $t = 6.4$ ms in Figure 3.1, showing the interaction between the water droplet and the carbon/Nafion composite surfaces. The red arrows represent the direction of movement of the water droplets.

However, when the carbon content is too high (Figure 3.8d), there is insufficient Nafion to fully cover the carbon particles and thus the impacting water droplets also contact the hydrophilic carbon surfaces, resulting in incomplete rebounding from the surfaces of the 85% and 90% VC/Nafion composites in Figure 3.1d, for example. In turn, the complete rebound of the water droplets from the surface of the 80% VC/Nafion composite (Figure 3.1d) indicates that there may be just enough Nafion present to fully cover the VC particles at this particular composition, as also explained above.

From this, the minimum amount of Nafion (m_{\min}) needed to fully cover 1 m² of the VC surface can be estimated (Equation 3.2), using a surface area of 130 m²/g for VC (excluding the micropores, which are not accessible to Nafion) [155]. It is also assumed that the 80% VC/Nafion mixture (mass ratio of VC to Nafion of 8:2) is the critical composition below which superhydrophobicity is observed and above which Nafion no longer fully covers all of the VC particles. The thickness of Nafion film on VC in the 80% VC/Nafion mixture ($t_{80\% \text{ VC/Nafion}}$) can also be estimated (Equation 3.3), assuming that Nafion is homogeneously distributed with the density of 2.0 g/cm³ as its bulk state [148] and that the VC:Nafion mass ratio in the films is the same as the ratio of these components in the ink. The latter assumption is reasonable because the inks were sonicated for 2 hours prior to their deposition to ensure that they were well-mixed. Furthermore, the 70-90% VC/Nafion composite inks are quite viscous and thus it is probable that the mass ratio of VC:Nafion will be maintained during the spin-coating process. Similarly, the thickness of Nafion in 70% VC/Nafion composites ($t_{70\% \text{ VC/Nafion}}$) is estimated to be about 1.6 nm (Equation 3.4), in good agreement with that obtained from molecular dynamics simulations for a layer of Nafion film on graphite [92]. This supports our speculation that the hydrophobicity of VC/Nafion

composites arises from a layer of Nafion with its sulfonate groups attached to VC and its PTFE backbones exposed to air.

$$m_{\min} = \frac{2}{8 \times 130 \text{ m}^2/\text{g}} \approx 1.9 \text{ mg/m}^2 \quad (3.2)$$

$$t_{80\% \text{ VC/Nafion}} = \frac{1.9 \text{ mg/m}^2}{2.0 \text{ g/cm}^3} \approx 1.0 \text{ nm} \quad (3.3)$$

$$t_{70\% \text{ VC/Nafion}} = \frac{\frac{3}{7 \times 130 \text{ m}^2/\text{g}}}{2.0 \text{ g/cm}^3} \approx 1.6 \text{ nm} \quad (3.4)$$

The findings of this work are expected to be very helpful in understanding the wetting characteristics, and the future design, of PEMFC catalyst layers, where the VC content (relative to Nafion) is commonly 55–65% [16–18]. Our results indicate that this is in the range of hydrophobic, and potentially superhydrophobic, surface conditions, although it is understood that the presence of Pt nanoparticles will likely influence these results, as will the temperature. In 3-electrode catalyst evaluation work carried out in acidic media using a rotating disc electrode, the thickness of the ink layer and the carbon content are both variables [43, 48, 79]. The carbon content can range from 60% to 70%; the present work suggests that these ink layers would have similar wetting characteristics. In other recent PEMFC work [156], a VC/Nafion mixture was used in the microporous layer (MPL), which is located between the CL and the carbon fiber paper of the GDL, to enhance the oxygen reduction performance. It was found that a 90% VC content was the best [156], with our current results suggesting that the MPL would then be in a hydrophobic state, but with the carbon particles not fully covered by Nafion, thus facilitating oxygen transport as well as electronic conductivity through the layer.

Collectively, our results clearly demonstrate that the percentage of VC in the VC/Nafion composites has a strong impact on the preferential configuration of Nafion on VC support in terms of wettability when exposed to water. The VC/Nafion composites must be as hydrophobic as possible to avoid flooding at the cathode, at which water is generated during oxygen reduction. Surface roughness also affects the wettability phenomenologically. The relative percentage of Nafion, in turn, influences the surface coverage of Nafion on VC and indirectly influences the effect of roughness on hydrophobicity. It is these complex relationships between the interfacial properties that directly affect the anticipated fuel cell performance. In actual PEMFC operation, the catalyst layers are expected to have a more complex microstructure than the dried VC/Nafion composites studied here. This is caused by the different fabrication methods employed, the presence of Pt, and the higher humidity and temperatures under PEMFC operating conditions, all of which could have a significant effect on the orientation of Nafion on carbon. These studies need to be moved forward in the future using the experimental methodology and approaches described here.

3.3 Summary

We have performed dynamic impacting droplet experiments on spin-coated pure Nafion and composite Vulcan Carbon (VC)/Nafion films, showing that there exist complicated inter-relationships between Nafion, VC, surface coverage, and surface roughness, all of which influence the phenomenologically observed wettability. 100% Nafion films have a hydrophobic PTFE backbone, but exposure to water causes the re-orientation of the sulfonate groups towards the water droplet, making the surface hydrophilic. SEM imaging has shown the presence of vertically aligned nano-channels in the Nafion film

structure, suggested to be hydrophilic in nature, also contributing to the large contact angle hysteresis observed in the water droplet impacting experiments on 100% Nafion films.

For the VC/Nafion composites, at low VC contents, the Nafion-rich surfaces behave just like Nafion alone, being hydrophilic after droplet impact and exhibiting significant hysteresis, as reported previously by others. However, as the VC weight percentage increases to 40% and above, the surface becomes more hydrophobic. This is because Nafion has a preferential orientation, with its sulfonic acid groups pointing towards the polar VC surface and thus exposing more of its hydrophobic Teflon-like backbone. Also, the increasing VC content causes significant surface roughness to be introduced, resulting in higher contact angles, even exhibiting superhydrophobicity at a 60–80% VC content. The phenomenological contact angles are therefore affected by the balance between geometrical surface roughness and intrinsic hydrophobicity.

It is also found in our work that, at above 80% VC content, insufficient Nafion is present to fully cover all of the VC particle surfaces, and thus these carbon-rich films begin to show a less hydrophobic character. Based on the 80% VC content at which this turn-around occurs, we calculated the minimum amount of Nafion required to fully cover the VC surface used in our work to be about 1.9 mg/m^2 with an estimated minimum thickness of 1.0 nm.

Chapter Four: Wettability of Colloid-Imprinted Carbons Before and After Heat Treatment

The results of this chapter have been published: *Carbon*, 2015, 87, 44–60.

4.1 Introduction

As explained in Chapter 1, understanding the surface wettability of carbons is essential to achieving the optimum dispersion of Pt nanoparticles on carbon supports, a high stability of the catalyst layers (CLs), a good distribution of ionomeric Nafion[®] clusters in the CLs, and to improve water management in polymer electrolyte membrane fuel cells (PEMFCs). Therefore, Chapters 4-6 are focused specifically on measuring and modifying the wettability of several different carbon support materials.

As found in Chapter 3, the wettability of composites of Nafion and Vulcan carbon (VC, a commercially available microporous carbon black) is very dependent on the relative VC and Nafion content and the surface roughness of the composites. Also, because the VC surface is normally covered by the Nafion phase, the wettability of the composites is dominated by the wettability of Nafion. As Nafion contains both hydrophobic and hydrophilic segments (Scheme 1.1), this results in major challenges in determining the inherent wettability of the VC surface. Therefore, in the following chapters, the carbons under study here were not mixed with Nafion, but were rather investigated on their own.

Due to the high kinetic energy of water droplets falling on to a surface, the droplet impacting (DI) method (Section 2.6.1.1), used in Chapter 3, was found to be unsuitable for the determination of the wettability of carbon powder alone, as it is relatively loosely packed together in pellet form in this work. Even so, the kinetic behavior of water droplets

contacting a sample surface can still provide useful knowledge about the wetting behavior of carbon powders. Therefore, in this chapter, the water droplets were released from only from only a short height (~ 1 mm), generating contact angle kinetic (CAK) data (Section 2.6.1.2), in order to avoid the high energy impact associated with the method used in Chapter 3.

Water vapor sorption (WVS) properties of the carbon powders were also determined using a simple method (Section 2.6.2), in order to verify the wettability results obtained from the CAK studies. The focus of this chapter is therefore specifically on understanding these CAK and WVS results, as well as the development of reliable data analysis methods. These approaches then serve as the cornerstones of the following two chapters.

As introduced in Chapter 1, colloid-imprinted carbons (CICs), with pore diameters ranging from ca. 15-80 nm, are promising catalyst support materials for use in PEMFCs due to their narrow pore size distribution, ordered porous structure, high conductivity, controllable pore sizes, etc. As mentioned in Chapter 1, the ordered mesopores are also considered to be important for the distribution of Pt nanoparticles, shown [43, 58] to be readily deposited inside the CIC mesopores. However, since the first report of the synthesis of CICs in 2001 [54, 157], there have been no publications focused on the wettability of these carbons, even though they are widely applicable for uses other than PEMFC catalyst supports, such as in lithium batteries, biosensors, capacitors, adsorption systems, etc. [158-162]. Therefore, CICs with different pore sizes were synthesized and examined particularly for their wettability for the first time in this chapter.

As also explained in Section 1.5.1, heat treatment is known to enhance the crystallinity of carbons, thus improving their stability in the harsh oxidation conditions found in PEMFCs. In this study, the as-synthesized CICs were thus heat treated at 1500 °C in a N₂

atmosphere, and then examined by using the CAK and WVS methods, for the first time, in order to determine their wettability for future application in PEMFCs. To serve as a benchmark, VC was also treated and examined using the same approaches. This work thus helps to understand the surface chemistry of carbons synthesized via hard templating methods [50, 51, 71] while also paving the way for understanding the wettability of the ordered mesoporous carbons (OMCs) examined in Chapter 5 and the surface-modified carbons studied in Chapter 6.

4.2 Elemental composition of carbons before and after heat treatment

Table 4.1 shows the elemental composition of the synthesized CIC samples and VC (as a reference) before and after heat-treatment (HT) at 1500 °C in N₂. The carbon, hydrogen and nitrogen contents, obtained by combustion analysis, have an error of < 0.3 % for each element, while the solid residue was determined by burning out the carbon under an air atmosphere using thermogravimetric analysis (TGA). VC and VC-HT were burned out completely, while the CICs and CICs-HT left some visible solid residues (Table 4.1). The residues are likely related to the silica templates, which were not removed completely during the CIC synthesis. The mass of the residue was too low to be detected by TGA, and thus the data are estimated to have an error of ± 2.0 % (Table 4.1). The oxygen content in Table 4.1 was obtained by difference, assuming that each of these carbon samples is composed only of C, H, N, and O, as well as the solid residue. The error in the oxygen content in Table 4.1 is thus estimated at about ± 0.5 %, or ± 2.1 % for those samples containing solid residues.

As indicated in Table 4.1, heat treatment of all of the carbons at 1500 °C in a N₂ environment resulted in a notable decrease in the oxygen content. In general, the exposure of

a carbon sample to high temperatures in an inert atmosphere removes its oxygen-containing functional groups, such as carboxylic acid and phenolic groups, from the carbon surface, producing H₂O, CO₂, CO, etc. [125, 126], and thus decreasing the oxygen content (Table 4.1). At 1500 °C, the small amount of silica remaining in the CICs may react with carbon to form volatiles, such as CO and SiO [163], which were removed by the flowing nitrogen gas. A small part of the SiO could react further and form a thin layer of SiC on the carbon surface [163]. This is likely the reason why the heat-treated CICs contain so little solid residue (Table 4.1).

Table 4.1 Elemental content (wt. %) of carbons before and after heat-treatment (HT)

Sample ^a	C (%)	H (%)	N (%)	Solid residue (%) ^b	O (%) ^c
VC	98.4	0.8	0.1	-	0.7
VC-HT	99.0	0.7	0.3	-	0.0
CIC-12	93.9	1.0	0.2	ND	4.9
CIC-12-HT	98.8	0.8	0.5	ND	0
CIC-22	90.7	1.2	0.1	1.7	6.3
CIC-22-HT	98.6	0.5	0.7	ND	0.2
CIC-50	92.5	0.8	0.0	2.3	4.4
CIC-50-HT	98.8	0.6	0.4	ND	0.2

^a The numbers in the sample names reflect the particle size (in nanometers) of the colloidal silica template used in the colloid-imprinted carbon (CIC) synthesis. HT: these samples were heat treated at 1500 °C in a N₂ atmosphere.

^b The solid residues in the CICs were determined via thermogravimetric analysis (TGA) in air. ND = not detectable.

^c The oxygen content was obtained by subtracting the C+H+N+solid residue mass from the original sample mass.

4.3 Crystallinity of carbons before and after heat treatment

Figure 4.1 shows the X-ray diffraction (XRD) patterns of the VC and CIC powders, before and after heat treatment, and the corresponding interlayer spacing (d_{002}) and crystallite

length in the c -direction (L_c), based on Bragg's law and the Scherrer equation [164]. It is seen that all of the as-synthesized CICs exhibit a similar crystallinity to commercial carbon black (Vulcan carbon, VC), with an L_c value of ca. 1 nm. After heat treatment, these peaks became sharper (Figure 4.1b), confirming an enhancement in the crystallinity of all of the carbons after heat treatment, with the average L_c having increased to ca. 2 nm.

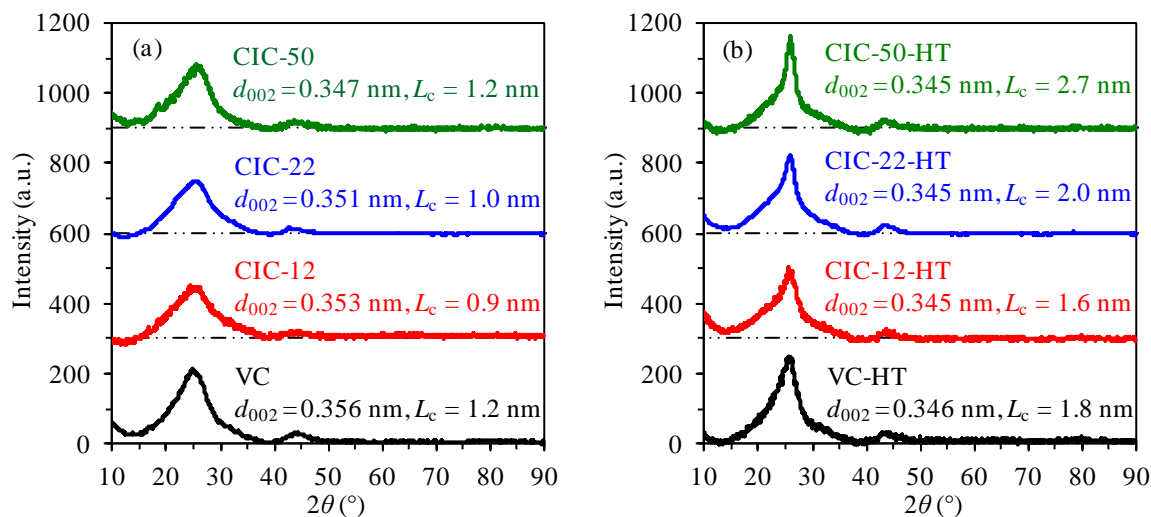


Figure 4.1. XRD patterns of the carbon samples (a) before and (b) after heat treatment (HT) at 1500 °C in a N_2 atmosphere. The dash-dot-dot lines beneath the curves show the baseline for the corresponding pattern. The interlayer spacing (d_{002}) and crystallite length in the c -direction (L_c) of each carbon was obtained using Bragg's law and the Scherrer equation for the peak at $2\theta \approx 25^\circ$ in the corresponding pattern [164].

In Figure 4.1, it is also seen that the CIC with the larger pore size has a slightly higher degree of crystallinity, i.e., lower d_{002} and larger L_c values. According to the literature [165-170], the mesophase pitch (MP, composed of polycyclic aromatic hydrocarbons), used to synthesize the CICs, may align in an ordered, vertically oriented fashion on the silica surfaces at the imprinting stage of the synthesis. After carbonization and removal of the silica template, packed planar graphene sheets, produced by the nucleation of MP, may form the

internal walls of the carbon pores and leave the sheet edges exposed [165, 168, 170]. Due to their lower curvature, larger silica colloids will facilitate tighter packing of the MP molecules on the spherical silica particles, resulting in a CIC with a lower d_{002} and a larger L_c value, as seen for CIC-50 vs. CIC-12. After heat treatment, the increase in the CIC L_c values is seen to vary with pore size (e.g., 1.5 nm for CIC-50-HT vs. 0.7 nm for CIC-12-HT in Figure 4.1), indicating that larger pores facilitate carbon crystallite growth.

4.4 Porous structure of carbons before and after heat treatment

As discussed above, heat treatment in an inert atmosphere made the CIC samples more carbonaceous (Table 4.1) and also more crystalline (Figure 4.1). However, at the same time, some mass was lost ($\sim 20\%$) in the form of volatiles. All of these changes may have altered the original surface morphology and the porous structure of the carbons. In order to further clarify this, scanning electron microscopy (SEM) analysis of the carbons, before and after heat-treatment, was carried out, with the images shown in Figure 4.2. The low-magnification SEM images of these carbons are shown in Figure 4.3, revealing the particle sizes of the CICs before and after heat treatment.

From Figure 4.2a, it is seen that the small VC particles, each ca. 20-50 nm in diameter, are agglomerated together. This was also seen in our previously reported transmission electron microscopy (TEM) images of VC [43]. After heat treatment, no significant change in the size of the individual VC particles is seen (Figure 4.2b), with the particles having remained in an agglomerated form. These minor changes are consistent with the small mass loss (about 5%) and the small changes in their elemental content (Table 4.1) observed after heat treatment.

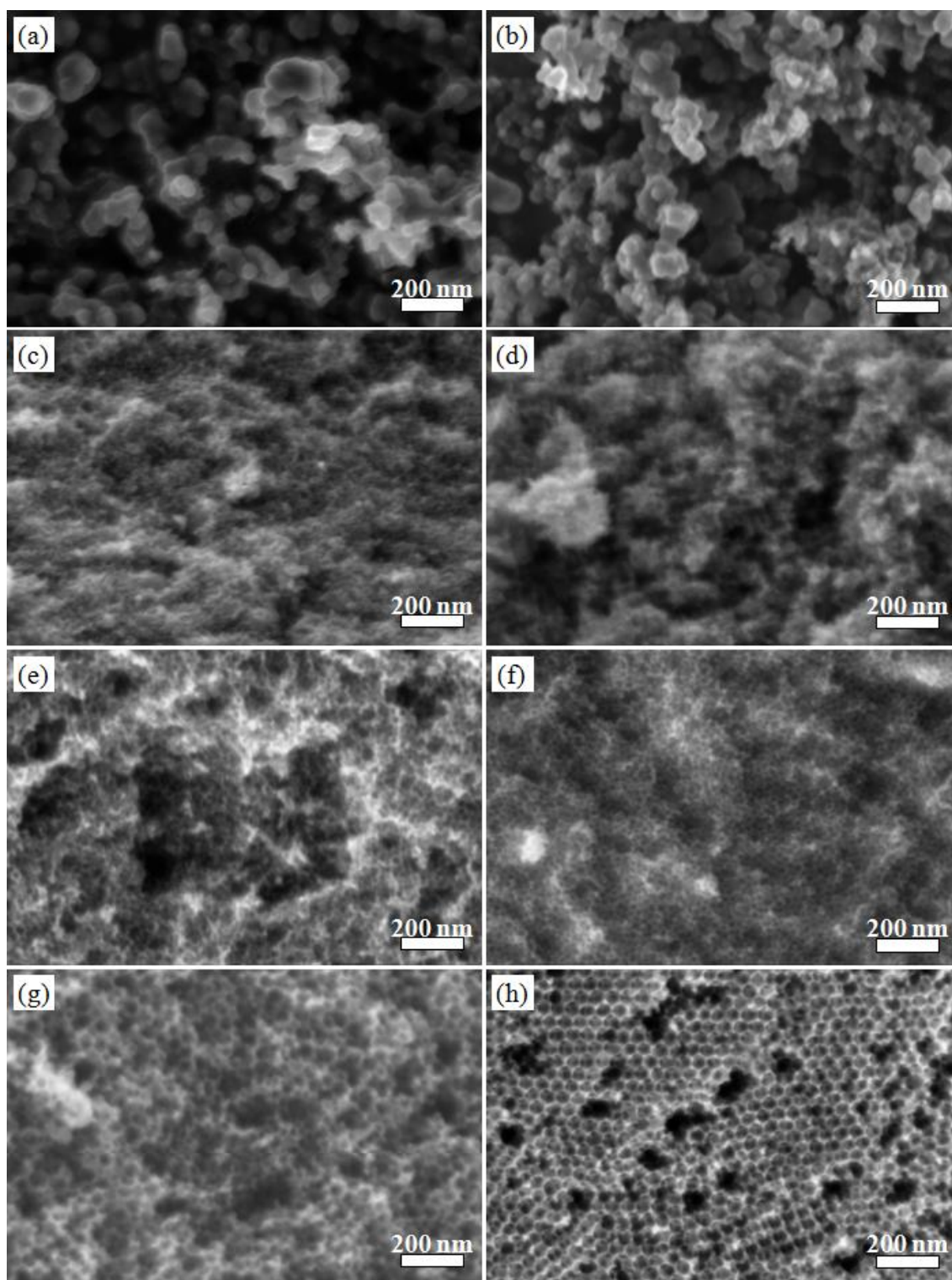


Figure 4.2. Field-emission scanning electron microscopy (FE-SEM) images of (a) VC, (b) VC-HT, (c) CIC-12, (d) CIC-12-HT, (e) CIC-22, (f) CIC-22-HT, (g) CIC-50, and (h) CIC-50-HT powders, all supported on carbon tape, at a high magnification.

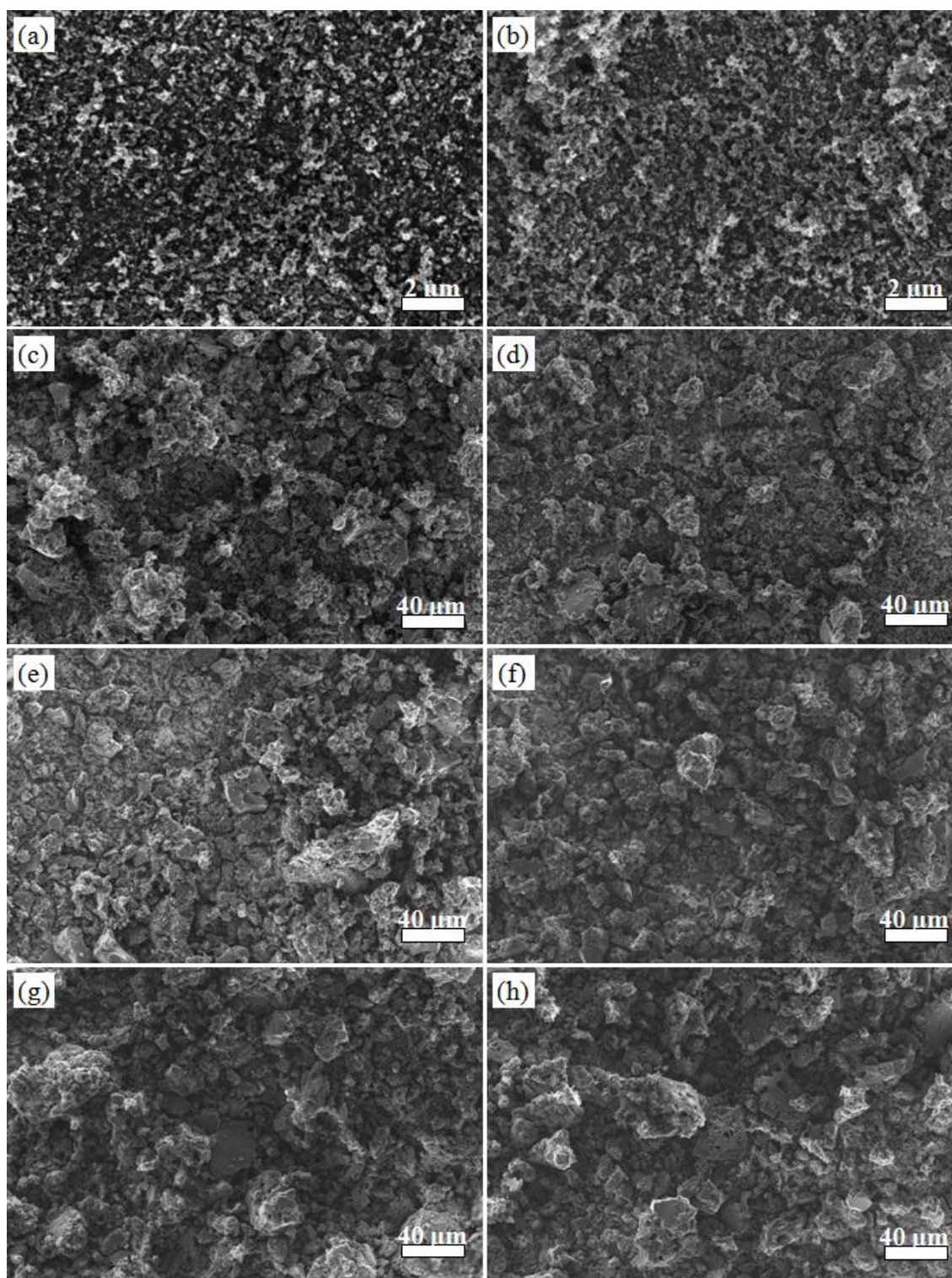


Figure 4.3. Field-emission scanning electron microscopy (FE-SEM) images of (a) Vulcan carbon (VC), (b) VC-HT, (c) CIC-12, (d) CIC-12-HT, (e) CIC-22, (f) CIC-22-HT, (g) CIC-50, and (h) CIC-50-HT powders, all supported on carbon tapes, at low magnifications.

As shown in Figures 4.2c, 4.2e, and 4.2g, the as-synthesized CICs all have different nanopore sizes, corresponding to the size of the imprinting colloid used, as expected. Furthermore, heat treatment at 1500 °C did not significantly change the pore sizes of the CICs, according to the SEM images (Figure 4.2).

In order to more quantitatively characterize the porous structure, particularly the internal porosity, the N₂ sorption isotherms (NSI) of the CICs vs. VC, both before and after heat treatment, were collected, with the results shown in Figures 4.4a and 4.4b. As seen in Figures 4.4a and 4.4b, all of the carbons exhibit Type IV isotherms [171], with adsorption/desorption hysteresis seen at high relative pressures, indicating the presence of nanopores within the samples (Figures 4.4c and 4.4d).

The large hysteresis shown in the gas sorption data for the CIC and CIC-HT samples, particularly for CIC-22 and CIC-50 both before and after heat treatment (Figures 4.4a and 4.4b), is attributed to the ink-bottle-shaped pores (and thus pore necks) connecting adjacent spherical pores, arising from the close packing of the spherical silica particles during CIC synthesis. The pore necks of the CIC and CIC-HT samples constrain the evaporation of condensed nitrogen during the desorption process until a low relative pressure is reached, sufficient for the condensed nitrogen in the necks to evaporate. The CIC pore sizes, estimated from the desorption branches, are shown in Figure 4.5, where the maximum in the pore size distribution plot reflects the pore neck size of the corresponding carbon.

Therefore, the adsorption branches of the isotherms were selected to estimate the pore size distribution of the CICs in Figures 4.4c and 4.4d. The TEM images of the CICs, previously reported by our group, have shown that the pore sizes of the CICs are best estimated by applying the BJH method to the adsorption branch of the corresponding

isotherms [48, 58]. Additionally, the adsorption branches are the most comparable to the process of water vapor sorption, discussed later in this chapter. A summary of the structural properties (pore size, surface area, and pore volume) of these carbons, obtained from the N₂ sorption data in Figure 4.4, are given in Table 4.2 to facilitate comparison.

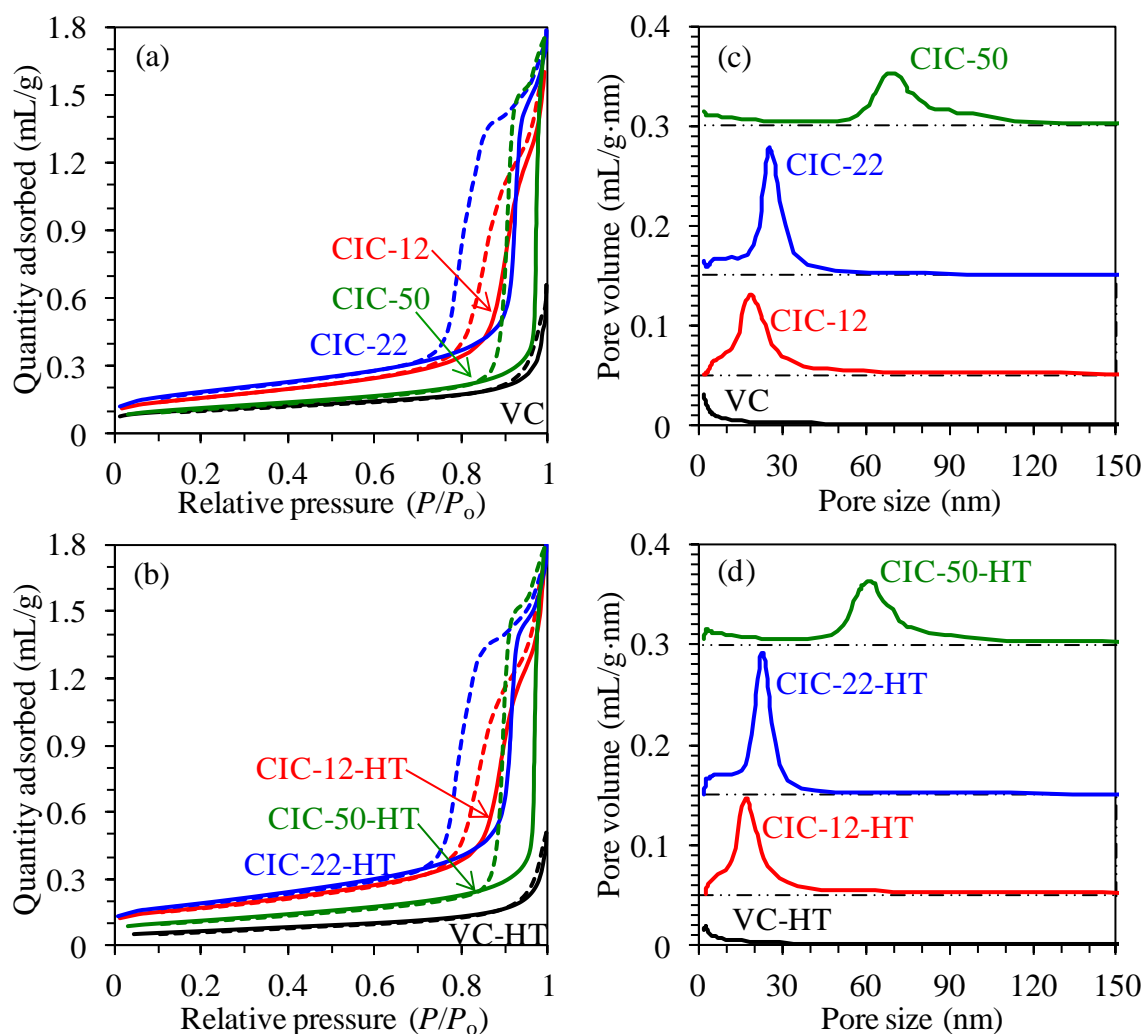


Figure 4.4. N₂ adsorption (solid line) and desorption (dashed line) data for the carbons (a) before and (b) after heat-treatment (HT) for 2 h at 1500 °C in a N₂ atmosphere. The corresponding pore size distributions (c) and (d) were calculated from the adsorption branch of the isotherm, using the Barrett-Joyner-Halenda (BJH) method, with the *t*-curve of carbon black used as the standard to determine the statistical thickness of the adsorbed nitrogen film [172]. The dash-dot-dot lines beneath the curves (c and d) show the baseline for the corresponding distribution plot.

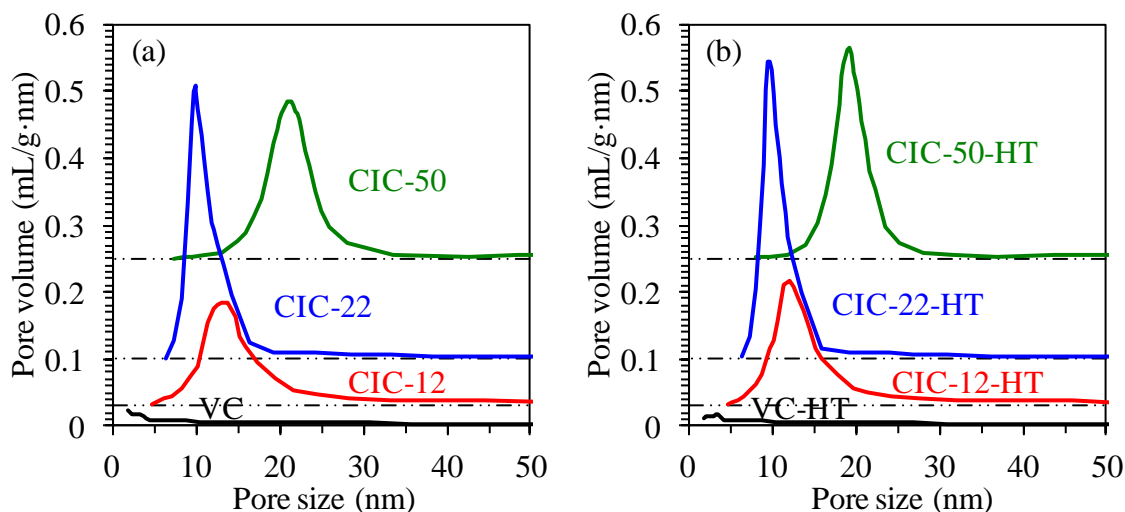


Figure 4.5. Pore size distributions of the carbons (a) before and (b) after heat-treatment (HT) for 2 h at 1500 °C in a N₂ atmosphere, calculated from the desorption branch of the N₂ adsorption-desorption isotherms (Figure 3) using the Barrett-Joyner-Halenda (BJH) method, with the *t*-curve of carbon black used as the standard to determine the statistical thickness of the adsorbed nitrogen film [172]. The dash-dot-dot lines beneath the curves show the baseline for the corresponding distribution plot.

The fact that the pore size of CIC-12 (Table 4.2) is larger than expected can be attributed to a range in the particle size distribution of the silica colloids, to occasional incomplete imprinting during CIC synthesis, and to the collapse of some of the thin walls. These factors would then also contribute to the wide pore size distribution (Figure 4.4c) and the narrower hysteresis of the N₂ sorption isotherms (Figure 4.4a) of CIC-12, compared to CIC-22 and CIC-50. Larger pores, compared to the corresponding colloids, are also observed in the FESEM images of CIC-12 and CIC-12-HT (Figures 4.2c and 4.2d), consistent with the literature [43, 48, 131].

Table 4.2 Structural properties of carbons before and after heat-treatment (HT)^a

Sample	Pore size (nm) ^b	S_{BET} (m ² /g) ^c	S_{external} (m ² /g) ^d	S_{micro} (m ² /g) ^e	$S_{\text{micro}}/S_{\text{BET}}$ (%)	V_{NSI} (mL/g) ^f	V_{micro} (mL/g) ^d	$V_{\text{micro}}/V_{\text{NSI}}$ (%)
VC	< 2	220	130	90	40	0.38	0.05	10
VC-HT	< 2	150	130	20	10	0.30	0.01	3
CIC-12	19	340	280	60	20	1.4	0.03	2
CIC-12-HT	17	380	340	40	10	1.5	0.02	1
CIC-22	25	410	320	90	20	1.6	0.04	3
CIC-22-HT	23	420	370	50	10	1.6	0.02	2
CIC-50	48 ^b	240	180	60	30	1.4	0.03	2
CIC-50-HT	46 ^b	250	220	30	10	1.6	0.02	1

^a Heat treated at 1500 °C for 2 h under a N₂ atmosphere.

^b Pore size obtained from the maximum in the pore size distribution plots in Figure 4.4, except for CIC-50 and CIC-50-HT, where the pore diameter was estimated directly from the FE-SEM images (e.g., Figures 4.2g and 4.2h).

^c S_{BET} = total surface area, obtained using the Brunauer-Emmett-Teller (BET) plot in the partial pressure range of $0.05 < P/P_0 < 0.30$.

^d S_{external} = external surface area and V_{micro} = micropore volume, both obtained using the t -plot method in the partial pressure range of $0.2 < P/P_0 < 0.5$, with carbon black used as the reference [172].

^e S_{micro} = micropore surface area, obtained by subtracting the external surface area (S_{external}) from the total surface area (S_{BET}).

^f V_{NSI} = pore volume, acquired from N₂ sorption isotherms at $P/P_0 = 0.98$.

However, the pore sizes of CIC-50 and CIC-50-HT (68 nm and 61 nm, respectively), obtained from gas sorption analysis (Figures 4.4c and 4.4d), are also significantly larger than what is seen in the FESEM images for these two materials (Figures 4.2g and 4.2h) and what is expected based on the silica colloid size. This may be attributed to limits to the BJH analysis method [173], which requires very precise control of the higher pressures ($P/P_0 \sim 0.96$ for 50 nm pores) in order to obtain an accurate estimation of the size of large nanopores in the range of 50 nm. Therefore, the pore sizes of CIC-50 and CIC-50-HT were obtained

from their SEM images (e.g., Figures 4.2g and 4.2h). For each of these two carbons, more than 100 pores were analyzed, with the average value given in Table 4.2. In general, heat treatment causes only a minor decrease in the pore size of the CICs (Table 4.2). This is likely due to the sintering of their pore walls at high temperature (1500 °C), consistent with the increased degree of crystallinity seen from the XRD analysis (Figure 4.1).

As indicated in Table 4.2, the total surface area (S_{BET}) of VC decreased by ca. 30% after heat-treatment, while the area of the CICs was much more stable. The decrease in the surface area of VC after heat treatment is attributed primarily to the loss in its micropore surface area (S_{micro} , Table 4.2), likely due to the sintering of the VC particles at 1500 °C. The only minor change seen in the external surface area of VC after heat treatment is consistent with the SEM images (Figure 4.2), where essentially no change is seen in the VC particle size. The sintering of the particles also contributes to the decrease in both the micropore volume and the total pore volume of VC after heat treatment (V_{micro} and V_{NSI} , Table 4.2).

Similar to VC, the CICs also exhibit a decrease in their micropore surface area and micropore volume after heat treatment (S_{micro} and V_{micro} , Table 4.2), which may be caused by the sintering of the CIC pore walls. At the same time, however, the CICs experienced an increase in their external surface area, but little change in their pore volume (S_{external} and V_{NSI} , Table 4.2). The increase in external surface area is partially related to the decrease in pore size, as a CIC with a smaller pore size is expected to have a larger surface area [58].

Additionally, the S_{micro} and V_{micro} values of the as-synthesized CICs, estimated using t-plot analysis (Table 4.2), may also be affected by the polar groups on their surfaces, because the polar groups exhibit a similar adsorption behavior as micropores do [172]. Thus, the removal of the surface polar groups, reflected by the decrease in oxygen content (Table

4.1), resulted in a decrease in the estimated S_{micro} and V_{micro} values, with an increase in S_{external} and little change in V_{NSI} . This is what is seen in Table 4.2 for the changes in the porosity of the CICs after heat treatment. Comparatively, VC experienced little change in S_{external} but a significant decrease in S_{micro} , resulting from the loss of micropores due to sintering under heat treatment, as discussed above. However, it is not clear how much the presence of polar surface groups is influencing the S_{micro} and V_{micro} values of the CICs before heat treatment. As this is out of the scope of this work, we do not further address this issue here.

Compared to VC, the CICs show little change in their S_{BET} , V_{NSI} , and pore sizes with heat-treatment, while exhibiting a decrease in S_{micro} but an increase in S_{external} (Table 4.2). This suggests that the pore walls of the CICs are more stable to high temperatures than are the microporous VC particles. These results, along with the lack of morphology change seen in the SEM images (Figures 4.2 and 4.3), are consistent with what has been reported by others and also verified by our recent TEM studies [43, 48, 131, 174]. The dense, highly carbonaceous walls may be linked to the properties of the mesophase pitch (MP) carbon precursor (C wt. % = 94 %, or H/C \approx 0.65, atom/atom), which has a high mass conversion efficiency to carbon, relative to other carbon precursors. Overall, these results show that the CICs are highly promising nanoporous materials for applications in which a thermally stable nanoporous structure is required [174].

4.5 Wettability of carbons before and after heat treatment

In the above work, the CICs were shown to exhibit little change in their porous structure (Table 4.2), but did undergo a significant change in their elemental composition (Table 4.1) after heat treatment, while VC showed only a minor change in its elemental

content but an obvious decline in its micropore surface area (Tables 4.1 and 4.2). To better understand these results, the wettability of the carbons, before and after heat-treatment, was determined using both contact angle kinetics (CAK) and water vapor sorption (WVS) methods.

4.5.1 Contact angle kinetics (CAK) study

Figure 4.6 shows the sequential images obtained during the water droplet kinetics experiments using the compressed VC and CIC powder pellets. The estimated time to 100% dryness in Figure 4.6 (last row) was obtained when the water droplet was fully taken up by a porous pellet. The water droplet deposited on VC behaves quite differently from that on the CICs, and it takes much longer to be absorbed by VC than the CICs. The water droplet kinetics of the heat-treated carbons are also quite different from those on the fresh carbon samples, and it also takes less time for VC-HT to absorb the water droplets than for the CIC-HT samples (Figure 4.6).

Given the constant water droplet volume and negligible impacting height (~ 1 mm) in these experiments, the differences in the water droplet behavior in Figure 4.6 could result from differences in the surface properties of carbon pellets. For example, there are two possible mechanisms during the water droplet kinetic measurements on the VC pellet, hydrodynamics and surface energies. Initially, the water droplet quickly spreads due to hydrodynamics, causing the contact angle to change with time. Secondly, given the constant volume of each droplet, the water up-take by the pellet causes the contact angle to decrease slowly ($t > 100$ ms, Figure 4.6). The water droplet was fully absorbed by the VC pellet after ca. 9 s. This phenomenon can be attributed to the hydrophilic surface of VC and the porous

structure of the pellet, as was also observed by other researchers [73]. The porous structure of these pellets includes both the internal pores of each particle and the void space between the individual particles that constitute the pellets.



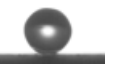
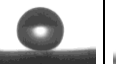

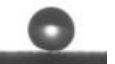

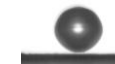
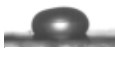



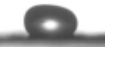


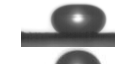
























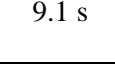
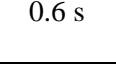
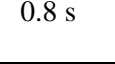
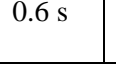
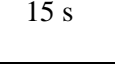
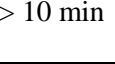
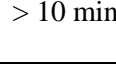
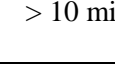
Time (ms)	<i>Before</i> heat-treatment				<i>After</i> heat-treatment at 1500 °C in N ₂			
	VC	CIC-12	CIC-22	CIC-50	VC-HT	CIC-12-HT	CIC-22-HT	CIC-50-HT
0								
8								
25								
100								
250								
1000								
Time to 100% dryness	9.1 s	0.6 s	0.8 s	0.6 s	15 s	> 10 min	> 10 min	> 10 min

Figure 4.6. Sequential images of a water droplet (diameter ≈ 2.7 mm) deposited onto flat carbon pellet surfaces, before and after heat-treatment at 1500 °C under a N₂ atmosphere, showing the contact angle kinetics (CAK) of water on the pellet surfaces. The estimated time to 100% dryness refers to the time that it takes for the pellet to fully absorb the water droplet deposited on it.

In comparison, a water droplet impacting on the VC-HT pellet shows a larger contact angle than on the non-heat-treated VC pellet at all stages, requiring a longer time (~ 15 s) to be taken up by the heat-treated carbon sample as compared to the fresh sample (Figure 4.6). VC and VC-HT have similar particle sizes, as seen from their SEM images (Figure 4.2), and thus they are expected to have a similar pellet surface roughness. If this is the case, then the contact angle kinetics of water droplets on VC and VC-HT can be qualitatively compared, showing that heat-treatment causes the VC samples to become more hydrophobic.

Compared to the fresh VC, water droplets deposited on the pellets of the as-synthesized CICs show much higher contact angles at the early stages of contact ($t = 25$ ms, Figure 4.6), but they subsequently show a more rapid drop in both their volume and contact angle. In general, the rapid up-take of water by the pellets suggests that the CICs are more hydrophilic than VC. After heat treatment, all of the CICs exhibit a higher water contact angle ($> 90^\circ$) for a longer time period than does VC-HT (Figure 4.6), suggesting that the heat-treated CICs are very hydrophobic.

In order to compare the wetting dynamics of water on the carbon pellets more quantitatively, we also plot the contact angles of the water droplets vs. time in Figure 4.7 after deposition onto the carbon surfaces, using the data shown in Figure 4.6. Each plot was obtained by averaging at least three independent measurements, having a standard deviation of about $\pm 6^\circ$ in the contact angles and an estimated ± 1 ms error in the time axis in Figure 4.7. A contact angle of 180° shows that the water droplet has fully rebounded from the CIC-HT surfaces, as seen at $t = 25$ ms in Figure 4.6, indicative of its extreme hydrophobicity.

It is seen that water droplet kinetics experiments at both VC (Figure 4.7a) and VC-HT (Figure 4.7b) reveal a declining contact angle, but with dissipating oscillations within the first 200 ms of contact. The oscillations arise from the balance between hydrodynamics and the interfacial energy of the water/substrate system, including dissipation due to water viscosity and the interaction between carbon and water. The number of oscillation cycles seen in Figure 4.7 depends on the rate of dissipation, which could be caused primarily by the interfacial energy between water and carbon (i.e., the hydrophilicity of the carbon) for the same hydrodynamics. The more hydrophilic a carbon is, the fewer times the water droplet will oscillate on it. Figure 4.7 shows clearly that the water droplets exhibit a higher contact

angle on VC-HT and take a longer time to reach equilibrium, as compared to those on VC, confirming that VC-HT is more hydrophobic than VC.

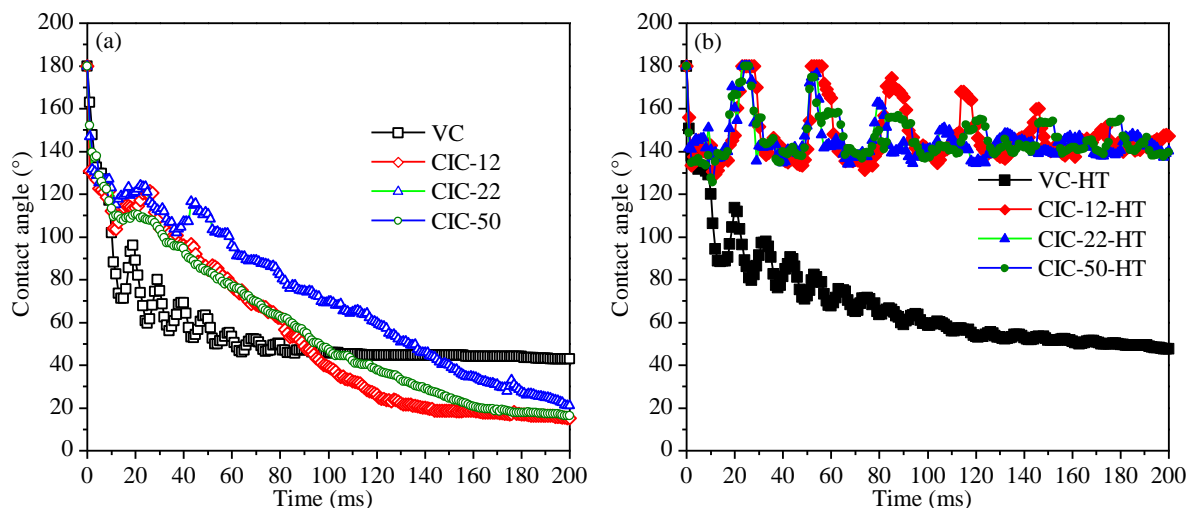


Figure 4.7. Contact angle kinetics (CAK) of water droplets after deposition onto carbon pellets (a) before and (b) after heat-treatment at 1500 °C under a N₂ atmosphere.

In the case of the non-heat-treated CICs, all of the pellets exhibit a larger water contact angle (10-90 ms in Figure 4.7a) than does VC. Since the CIC particles are larger (0.5-50 μm) and more irregular in shape as compared to VC (20-50 nm), as seen in Figures 4.2 and 4.3, the CIC pellets will be rougher than the VC pellets, resulting in a larger observed contact angle. This could explain the relatively large contact angles ($> 90^\circ$) displayed by the water droplets on the CICs within the first 40 ms in Figure 4.7a. However, water sorption by the CIC pellets rapidly decreases the droplet volume (25-250 ms, Figure 4.6) as well as the contact angle (30-200 ms, Figure 4.7a) of the droplets. All of these phenomena indicate that the CIC powders are intrinsically much more hydrophilic than VC.

In terms of the contact angle differences between CICs of varying pore size, observed in Figure 4.7a, the underlying causes could be complicated. One possible reason could be that the CIC particle surfaces are different from each other in terms of their pore properties. For example, CIC-22 may have smaller or less open pores than the other two CICs, or the outer surface of the CIC particles may be less hydrophilic than the internal pore surfaces, thus leading to slower water uptake.

When the water droplets deposit on the heat-treated CIC pellets, they show a similar behavior to those on the as-synthesized CIC pellets at short times (Figures 4.6 and 4.7), although they still show higher contact angles than VC-HT. As concluded from the SEM images (Figure 4.3), the CIC particle sizes did not change significantly after heat treatment. Thus, the surface roughness of the heat-treated carbon pellets should be similar to the non-treated samples. Compared to the as-synthesized CICs, water droplets rebound on the heat-treated CICs ($t = 25$ ms, Figure 4.6), show larger dynamic contact angles ($> 130^\circ$) within the first 200 ms (Figure 4.7b) and higher static contact angles ($t = 1$ s, Figure 4.6), and also take a longer time to be fully absorbed (> 10 min, Figure 4.6). This significantly different behaviour indicates that all of the CICs have become much more hydrophobic as a result of heat treatment. As discussed above, all of the CICs appear to have similar particle sizes and thus their pellets should have similar surface roughness, in both the as-synthesized and heat-treated states. Hence, the water droplet behavior in Figures 4.6 and 4.7 strongly suggests that the heat-treated CICs all have similar intrinsic hydrophobicity.

As mentioned earlier, heat-treatment can remove the active polar groups from the surface of carbons by the loss of oxygen and other elements (Table 4.1). It can also increase the graphitic nature (i.e., crystallinity) of carbon by re-organizing/sintering the graphene

sheets (Figure 4.1). For example, it has been reported that a highly graphitized carbon exhibits a water contact angle of close to 90° [124, 175-177]. The high contact angles ($> 130^\circ$) of water on the heat-treated carbons examined in this work thus likely arise from both the intrinsic hydrophobicity of the sintered carbon surfaces and the roughness of the pellets.

The significantly smaller particle size of the heat-treated VC (~ 40 nm) vs. the heat-treated CICs (~ 10 μ m) results in the VC-HT pellets having a much smoother surface and smaller gaps between particles, thus giving a smaller water contact angle. At the same time, VC-HT contains more micropores (~ 3 %, Table 4.2) than do the CIC-HT samples, which could cause water to penetrate through the VC-HT inter-particle spaces. This could be the reason why the water droplets were quickly absorbed by VC-HT but were absorbed more slowly by the CIC-HT samples (Figure 4.6).

Overall, the CAK experiments (Figures 4.6 and 4.7) show that a single equilibrium contact angle does not exist for water droplets on the powdered carbon samples being investigated here. A very hydrophilic porous sample can absorb the water droplet deposited on it in a very short time, as seen for the as-synthesized CICs (Figure 4.6). This makes it difficult to identify a stable and static contact angle, and also makes it unreasonable to obtain the relative wettability of the samples by comparing the contact angles at an arbitrary time, as is commonly performed in the literature [87, 128, 178-180].

4.5.2 Water vapor sorption (WVS) study

As discussed above, the behavior of water droplets when deposited on pelletized carbon powders is not only affected by the surface wettability of the carbon particles that constitute the pellet, but also by the surface roughness of the pellet and the interactions between the particles.

Water vapor sorption (WVS) experiments were thus used to help evaluate the relative hydrophilicity of the carbons, before and after heat-treatment, primarily to verify the conclusions derived from the CAK experiments (Figures 4.6 and 4.7). Figure 4.8 shows the WVS results as a function of the exposure time of dry non-heat-treated and heat-treated VC and CIC samples to water vapor. The volume of water vapor absorbed by the carbons was calculated from the mass increase of the samples when they were exposed to water vapor at room temperature, with an uncertainty in the mass of ca. 0.01 mL/g.

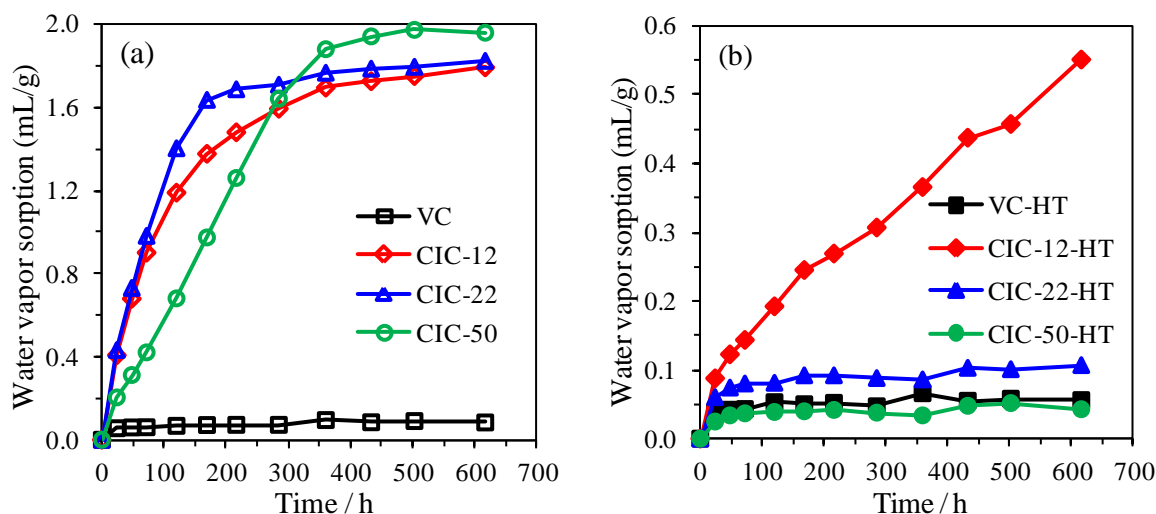


Figure 4.8. Water vapor sorption (V_{WVS}) of carbons (a) before and (b) after heat-treatment at 1500 °C under a N_2 atmosphere, at room temperature.

It can be seen in Figure 4.8a for the non-heat-treated carbons that, compared to VC, all of the CICs absorb significantly more water vapor than can be held by their pore volumes alone, as determined by N_2 sorption testing (Table 4.2). This suggests that the CICs are intrinsically more hydrophilic than VC, consistent with the CAK data. After heat-treatment (Figure 4.8b), the amount of water vapor absorbed by each carbon, except VC, decreases substantially. These

results are also fully consistent with the contact angle data in Figures 4.6 and 4.7, confirming the significant decrease in the hydrophilicity of the CICs after heat treatment, while the wetting properties of VC hardly change.

In this work, all of the carbons (before heat treatment) were placed in the same chamber at the same time and thus exposed to the same water vapor partial pressure, so that their sorption curves (Figure 4.8a) can be compared fairly against each other. Similarly, the heat-treated samples were placed together in another chamber, so that their sorption behavior can also be directly compared or their curves (Figure 4.8b) can be compared with one another.

Contrary to nitrogen gas adsorption (Figure 4.4), water vapor tends to adsorb at polar sites at low partial pressures (or low relative humidity), and form clusters surrounding polar sites at higher partial pressures [181], instead of forming a statistical monolayer, as assumed in BET theory [134]. This is due to the high interaction forces between water molecules (i.e., hydrogen bonds). With increasing water vapor partial pressure, the size of the clusters will increase, eventually forming a film of water (> monolayer thick) if the polar group density (or hydrophilicity, reflected in water contact angles) of the surface is sufficiently high. A hydrophilic pore surface will accelerate the condensation of water vapor, as indicated by the Kelvin equation:

$$\ln \frac{P}{P_o} = -\frac{2\gamma V_m}{rRT} \cos \theta \quad (4.1)$$

where P is the real-time water vapor pressure, P_o is the saturated water vapor pressure at temperature T , γ is the surface tension of water in contact with air, V_m is the molar volume of

water, r is the radius of the pore, R is the universal gas constant, and θ is the contact angle of water on the surface.

According to the Kelvin equation, it is clear that, at a certain partial pressure, vapor condensation into a pore depends on its size (r in Equation 4.1) and surface wettability. A completely hydrophobic pore ($\theta > 90^\circ$) does not favor water vapor condensation at all, while the smaller a hydrophilic pore, the faster the condensation into it (capillary condensation [182, 183]). Assuming that all of the samples have a homogeneous surface polarity (constant θ), water vapor will condense initially in the small pores and will then fill the larger pores at a constant relative humidity (P/P_o), if the surface is hydrophilic ($\theta < 90^\circ$). At equilibrium, the more hydrophilic a sample surface, the larger are the pores that are filled by condensed water, resulting in larger water vapor sorption (WVS) values.

However, the WVS results are also influenced by the total surface area and the pore volume of the samples, because a more porous material, normally with a higher surface area, can absorb more water than a less porous material, both having the same intrinsic hydrophilic surfaces. Therefore, for a fair comparison of the relative wettability of these carbons, the WVS data (V_{WVS} , Figure 4.8) were normalized to both their surface area and pore volume (S_{BET} and V_{NSI} , Table 4.2), obtained from the nitrogen sorption isotherms, to obtain the sorption ratios, V_{WVS}/V_{mono} and V_{WVS}/V_{NSI} (Table 4.3 and Figure 4.9). Here, V_{mono} represents the volume of one monolayer of water adsorbed on the sample surface (Table 4.3), in order to facilitate the comparisons. The one monolayer of water adsorbed on a sample surface is based on the simplified assumption that, after placing a sample in the water vapor environment, the molecules will firstly pack closely on the sample surface with a cross-sectional area of 0.106 nm^2 [184, 185], if the surface is sufficiently hydrophilic. After adsorbing several monolayers, the water

vapor starts to condense in the hydrophilic pores, following the Kelvin equation (4.1), as discussed above.

Table 4.3. Water vapor sorption of carbons before and after heat-treatment (HT)

Sample	$V_{WVS,1d}$ (mL/g) ^a	$V_{WVS,st}$ (mL/g) ^b	V_{mono} (mL/g) ^c	$V_{WVS,1d}/V_{mono}$	$V_{WVS,st}/V_{mono}$ ^d	$V_{WVS,st}/V_{NSI}$ ^e
VC	0.06	0.09	0.063	0.9	1.4	0.22
VC-HT	0.04	0.06	0.042	0.9	1.3	0.19
CIC-12	0.41	1.76	0.097	4.2	(18) ^d	1.2
CIC-12-HT	0.09	0.55	0.106	0.8	(5.2) ^d	0.37
CIC-22	0.43	1.80	0.115	3.8	(16) ^d	1.1
CIC-22-HT	0.06	0.10	0.120	0.5	0.9	0.07
CIC-50	0.20	1.96	0.069	3.0	(29) ^d	1.4
CIC-50-HT	0.02	0.05	0.076	0.3	0.7	0.03

^a $V_{WVS,1d}$ = Water vapor sorbed after exposure to water vapor for ~24 hours (Figure 4.8).

^b $V_{WVS,st}$ = Water vapor sorbed after reaching steady-state, obtained from the average of the last three points of the water vapor sorption isotherms of all the carbons in Figure 4.8 ((a) non-heat-treated and (b) heat-treated), except CIC-12-HT, where only the last point was selected, as water vapor sorption on CIC-12-HT did not reach a steady-state within the designated experimental time (Figure 4.8b),.

^c V_{mono} = one monolayer of water molecules closely packed on sample surfaces, using the equation: $V_{mono} = S_{BET} M_{H_2O} / \sigma_{H_2O} N_A \rho_{H_2O}$, where S_{BET} is the specific surface area of samples shown in Table 4.2, M_{H_2O} = molar mass of water, σ_{H_2O} = cross-sectional area of water molecules (0.106 nm²) [184, 185], N_A = Avogadro's constant, and ρ_{H_2O} = water density at 23°C.

^d The numbers in the parentheses cannot be compared directly with others in this column.

^e V_{NSI} = Pore volume, shown in Table 4.2.

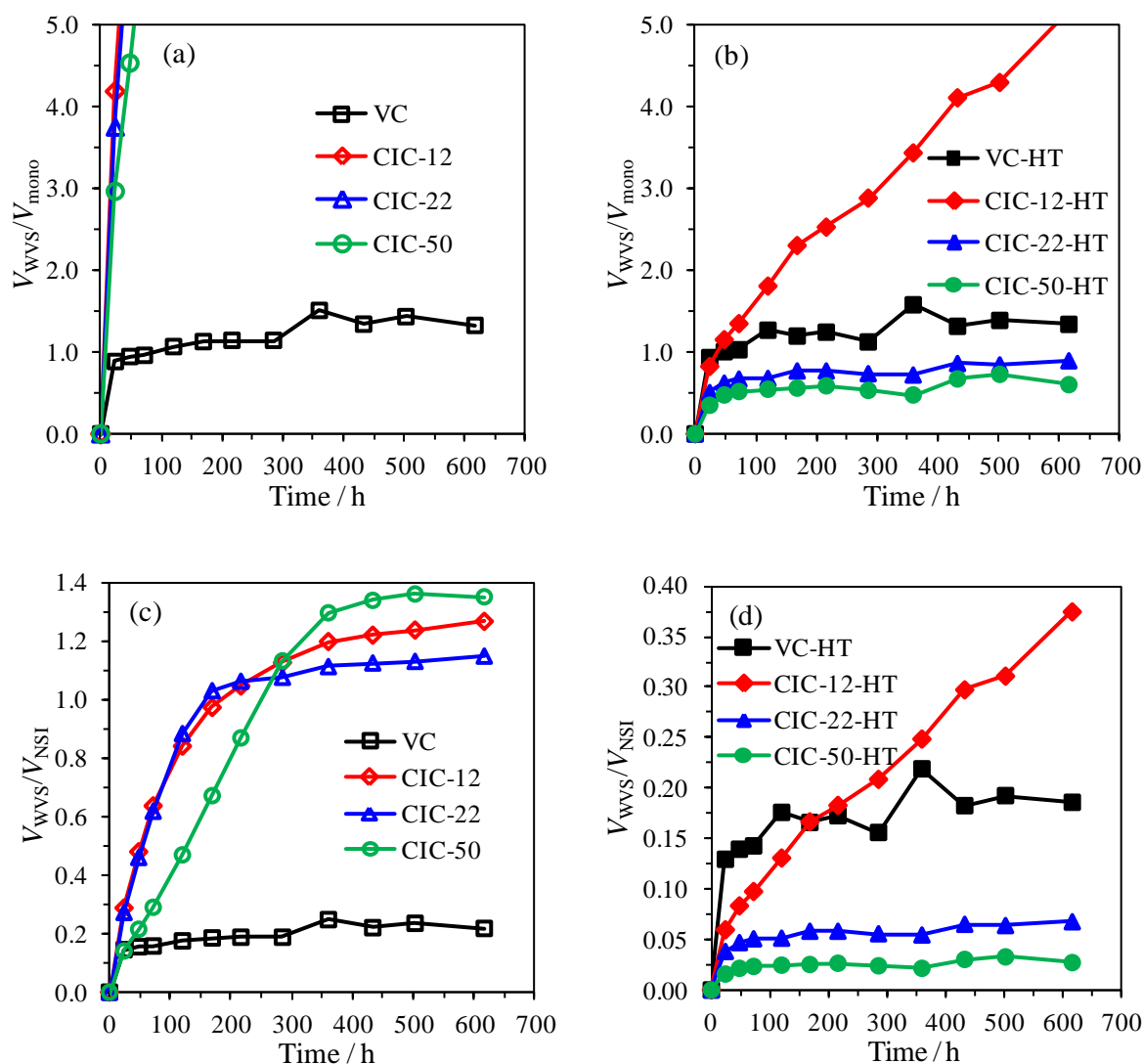


Figure 4.9. Water vapor sorption data (from Figure 4.8) of carbons (a) before and (b) after heat-treatment at 1500 °C under a N₂ atmosphere, normalized to their corresponding surface area and pore volume (Tables 4.2 and 4.3), obtained from nitrogen sorption isotherms (Figure 4.4).

It has been reported that a polar solid surface strongly interacts with water when fully immersed, causing restructuring in up to five molecular layers of water, with each layer having a thickness of ca. 0.25 nm [186, 187]. Assuming that water vapor will behave similarly to bulk water, only V_{WVS}/V_{mono} ratios lower than 5 were plotted in Figures 4.9a and 4.9b, with

$V_{\text{WVS}}/V_{\text{mono}}$ ratios greater than 5 listed in Table 4.3 only for general interest. However, on a hydrophobic surface, water vapor cannot form a water monolayer under the experimental conditions ($P/P_o < 1$) used here and thus cannot condense into the pores, giving a $V_{\text{WVS}}/V_{\text{mono}} < 1$. A more hydrophobic surface will thus result in an even smaller $V_{\text{WVS}}/V_{\text{mono}}$ ratio. It should be clarified that these $V_{\text{WVS}}/V_{\text{mono}}$ values do not actually represent the molecular coverage of water on these sample surfaces, since water molecules tend to form clusters on a hydrophobic surface, as discussed above. Instead, these numbers can reveal the relative polar group density, or polarity, of the sample surfaces. Thus, a surface with a lower polar group density will take up less water after exposure to the same vapor conditions, showing its more hydrophobic nature.

According to the first-day sorption ratios, shown in Table 4.3 ($V_{\text{WVS},1d}/V_{\text{mono}}$) and in Figure 4.9a ($t = 24$ h), more monolayers of water have adsorbed on the as-synthesized CICs than on the as-received VC, indicating that the CICs are more hydrophilic than VC. The increase in the $V_{\text{WVS},1d}/V_{\text{mono}}$ ratio for CICs with smaller pore sizes suggests that the hydrophilicity of the CICs increases with the decrease in pore size.

After reaching steady-state (Figure 4.9c), all of the CICs have a very high sorption ratio, compared to VC ($V_{\text{WVS},st}/V_{\text{NSI}}$: ~ 1.2 vs. 0.22, Table 4.3), suggesting that the condensed water vapor filled all of the CIC pores detected by N_2 sorption at $P/P_o = 0.98$. In the nitrogen sorption experiment (Figure 4.4), the condensed N_2 can only fill the cylindrical pores having a diameter smaller than ca. 100 nm at $P/P_o = 0.98$, estimated by using the statistical thickness of an adsorbed N_2 layer and the Kelvin radius at the relative pressure of 0.98 [172]. Thus, the pore volumes shown in Table 4.2 do not include pores larger than 100 nm in diameter. The statistical N_2 layer thickness was calculated here using carbon black as the reference material

[172], while the Kelvin radius of 47 nm was obtained using the Kelvin equation (4.1), where $\gamma = 8.88 \text{ mJ/m}^2$, $V_m = 34.68 \text{ cm}^3/\text{mol}$, and $\theta = 0^\circ$ for liquid nitrogen at $T = 77 \text{ K}$ [188].

Therefore, the high sorption ratios of the non-heat-treated CICs indicate that they contain very hydrophilic nanopores, as well as very hydrophilic macropores (pore size $> 100 \text{ nm}$), clearly favoring water vapor condensation inside the pores. CIC-50 has a higher sorption ratio than does CIC-12 and CIC-22 ($V_{\text{WVS,st}}/V_{\text{NSI}}$, Table 4.3), which is attributed to the fact that CIC-50 has a larger number of pores larger than 100 nm in diameter, as compared to CIC-12 and CIC-22 (Figure 4.4c).

It should be noted that the rate of water vapor sorption of the carbon samples, before reaching steady-state (e.g., for the as-synthesized CICs after 400 h in Figure 4.9c), depends on the pore size, pore curvature, accessible surface area, and surface wettability of the carbon samples, as well as on the evaporation rate of the water source. It has been mentioned above that smaller pores should accelerate the condensation of water vapor vs. the larger pores if they are all hydrophilic, and that CIC-12 is more hydrophilic than CIC-22, which is more hydrophilic than CIC-50. Therefore, the condensation rate of water vapor into the CIC pores should be in this order: $\text{CIC-12} > \text{CIC-22} > \text{CIC-50}$. However, this trend is not seen, with the water vapor sorption data for CIC-12 almost overlapping with that of CIC-22 in the first 100 h (Figure 4.9c). The slower condensation rate seen at CIC-12 vs. CIC-22 after 100 h is probably due to the fact that CIC-12 has a disordered pore structure [48] and a wider pore-size distribution than the other CICs, as shown in Figures 4.4c and 4.5. This disordered pore structure is clearly not favorable for water vapor transport into the pores. Also, the wider pores within CIC-12 (up to 130 nm, Figure

4.4c) will be less likely to condense water vapor than are the smaller pores of CIC-22 (Figure 4.4c), according to the Kelvin equation (4.1).

CIC-22 has a narrow pore size distribution (Figure 4.4c), centered at around 25 nm, as shown by both the N₂ sorption isotherms and TEM analysis [48]. The pore volume of CIC-22 (Table 4.2) should thus arise mainly from the 25 nm diameter pores. Compared to the other CICs, CIC-22 sorbs water vapor with a V_{WVS}/V_{NSI} ratio that increases linearly in the first 120 h (Figure 4.9c), then reaching a sorption ratio of 1.0. This is likely due to the uniform pore structure of CIC-22 and its hydrophilic pore surfaces. CIC-50 also exhibits a linearly increasing V_{WVS}/V_{NSI} ratio before reaching an equilibrium state, but with a slower rate of increase vs. CIC-22 because of its larger pore size. These results also confirm that CIC-50 has a hydrophilic pore surface and a narrow pore size distribution, as shown in Figure 4.4c.

All of the CICs, prior to heat treatment, exhibit a sorption ratio > 1 at long exposure times (Figure 4.9c and $V_{WVS,st}/V_{NSI}$ in Table 4.3). This may indicate that these carbons have hydrophilic pores with diameters larger than 100 nm, also seen in their SEM images (Figure 4.2). These large pores likely formed due to the aggregation of the silica colloidal particles during synthesis, so that the CIC pores were not completely imprinted. Alternatively, these large pores formed by the collapse of the CIC porous structure during synthesis. However, these large pores still have intrinsically hydrophilic surfaces, similar to those of the nanopores (< 100 nm) originating from contact with the silica templates. It should be noted that these large water-filled pores may also include the external pores between the CIC particles, but it is not clear how much the external pores contribute to the water vapor sorption data.

After heat-treatment, VC-HT exhibits a similar sorption ratio to fresh VC ($V_{WVS,st}/V_{mono}$: 1.3 vs. 1.4, $V_{WVS,st}/V_{NSI}$: 0.19 vs. 0.22, Table 4.3), with only a slight increase in the hydrophobicity. However, the large decrease in the sorption ratios of the CICs (Table 4.3 and Figure 4.9) indicates that the CIC surfaces underwent a significant change during heat treatment, becoming significantly more hydrophobic. Based on the maximum sorption ratios of the heat-treated carbons ($V_{WVS,st}/V_{mono}$ and $V_{WVS,st}/V_{NSI}$, Table 4.3), they exhibit the following hydrophilicity sequence: CIC-12-HT > VC-HT > CIC-22-HT > CIC-50-HT. This is slightly different from what was seen in the CAK experiments (Figures 4.6 and 4.7), where VC-HT was shown to be more hydrophilic than all of the CIC-HT samples. As discussed in Section 4.5.1, the more hydrophilic nature of VC-HT is attributed to its smaller particle size (Figure 4.2), giving a smoother pellet surface and showing a smaller water contact angle (Figures 4.6 and 4.7), as compared to CIC-12-HT.

However, it should be noted that, in the initial stages, all of the CIC-HT samples exhibited smaller sorption ratios than the VC-HT specimen ($t = 24$ h in Figure 4.9b and $t < 150$ h in Figure 4.9d), showing that, the wider the carbon pores, the less likely that they will wet. As discussed above, heat-treatment at 1500 °C decreases the oxygen content of carbon by removing polar groups from its surface, also increasing its crystallinity. Ideally, this should make all of the carbon surfaces similar to graphite [67]. Even so, according to the Kelvin equation (4.1), the smaller pores will favor the condensation of water vapor into them. This is exactly what was seen by the initial water adsorption behavior of the heat-treated carbons in the first 24 h (Figure 4.9b).

After 24 h of exposure to water vapor, CIC-12-HT still shows a nearly linearly increasing sorption ratio with time, while the other heat-treated carbons reached a steady state (Figures 4.9b and 4.9d). As mentioned above, a fully graphitic carbon normally has a water contact angle of ca. 90° (after long-time exposure to air [124, 177]), but this form of carbon can be obtained only by heat-treatment in Ar at 2000°C or higher [51, 68]. In this work, the carbon powders were heat-treated only up to 1500°C in N_2 , so their surfaces are expected to be less hydrophobic than graphite, with a water contact angle of $< 90^\circ$. In the WVS experiments (quasi-equilibrium, $P/P_o < 1$), water vapor can only condense into the small carbon pores, such as the micropores ($< 2\text{ nm}$) of VC-HT, and condense slowly in the mesopores ($\sim 17\text{ nm}$) of CIC-12-HT. This confirms that these carbon surfaces should exhibit a water contact angle smaller than 90° , according to the Kelvin equation (4.1).

However, due to the relatively hydrophobic surface of the CICs after heat treatment, water vapor cannot condense inside the larger pores of CIC-22-HT and CIC-50-HT (23 nm and 46 nm, respectively). In fact, water vapor sorption on the heat-treated carbons may occur as clusters in the hydrophobic micropores, as suggested by others [102, 181]. Importantly, the relatively hydrophobic properties of the heat-treated CICs, containing mesopores ranging from 23 to 46 nm in size, should lead to good resistance to corrosion [63] and flooding [8, 32] in PEMFC cathode layers, with parallel work currently underway to test these predictions. Compared to the extreme hydrophobicity of the CIC-HT samples observed in this work, it is possible that CIC samples exhibiting less hydrophobicity could be prepared by heat-treatment at a temperature $< 1500^\circ\text{C}$, or by loading them with catalytic nanoparticles, e.g., Pt, for use in PEMFCs.

4.6 Further efforts to understand the wettability differences of the carbon surfaces

Collectively, Figures 4.6-4.9 and Table 4.3 show that the as-synthesized CICs have very hydrophilic surfaces, in contrast to as-received VC, and that heat treatment makes the CICs much more hydrophobic than before. It was also found that heat treatment causes a significant decrease in the oxygen content of the CICs (Table 4.1), consistent with the loss of polar surface groups, as also suggested by others [125, 126]. This, in turn, indicates that there is a high density of polar O-containing groups (e.g., C-OH, C=O, COOH, etc.) on the as-synthesized CIC surfaces.

In order to augment the elemental analysis shown in Table 4.1, the surface oxygen content of the CICs was semi-quantitatively compared by examining their cyclic voltammetry (CV) response. Here, the CV of CIC-22 (before and after heat-treatment) is shown in Figure 4.10 as an example, with the CVs of VC and VC-HT given for comparison. Additionally, the relative surface area of the carbons can be estimated from the magnitude of the double layer capacitance currents [189].

Compared to VC (Figure 4.10), which is known to contain very few surface oxygen groups [190], the CV of CIC-22 shows a very large pseudo-capacitance peak, centered at ca. 0.55 V, typically attributed to the redox chemistry of quinone (C=O) and hydroquinone (C-OH) groups on the carbon surface (Reaction 4.2) [40, 132]. These large peaks are consistent with the relatively high oxygen content of CIC-22 before heat treatment, as also seen by elemental analysis (Table 4.1). Figure 4.10 also shows that VC lost its very small pseudo-capacitance peak after heat treatment (VC-HT, Figure 4.10), reflecting the loss of its surface oxygen groups (also consistent with Table 4.1).

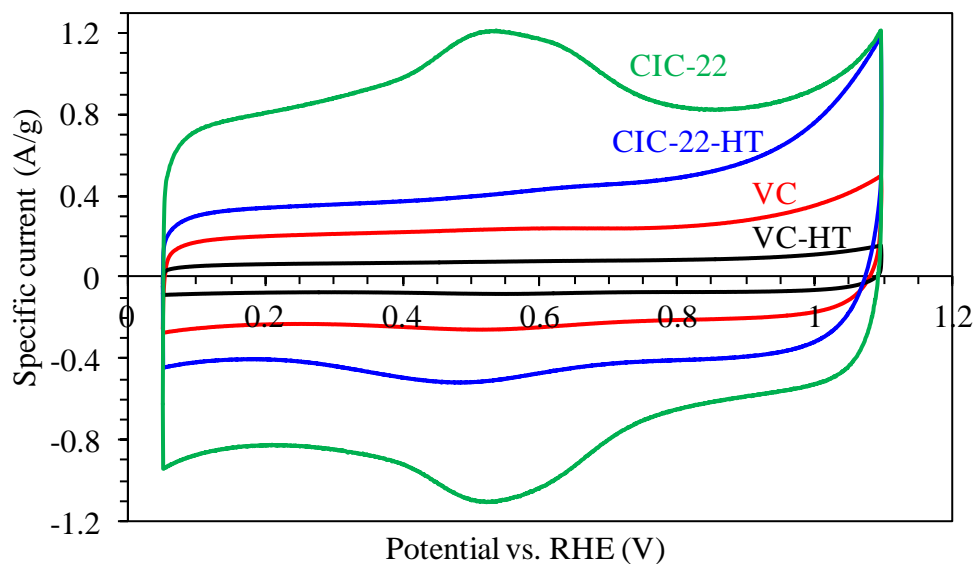
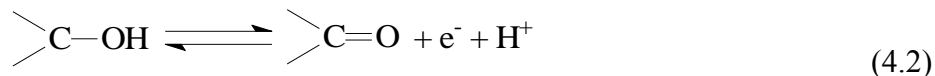
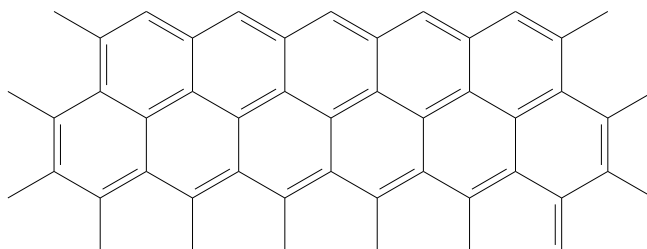


Figure 4.10. Cyclic voltammograms (CVs) of VC, VC-HT, CIC-22, and CIC-22-HT in N₂-saturated 0.5 M H₂SO₄ aqueous solution at a scan rate of 10 mV/s.



Notably, the double layer capacitance current of VC-HT is much smaller than that of VC, attributed to the loss of surface area of VC after heat treatment (Table 4.2). In addition to the disappearance of the pseudo-capacitance peak, CIC-22-HT shows a smaller capacitive current than does CIC-22 (Figure 4.10), although they have a similar surface area (Table 4.2). The significant change in the CV of CIC-22 after heat treatment is likely attributed to the loss of oxygen-containing groups from its surface after high-temperature treatment. Although it is not clear how much the oxygen-containing groups contribute to the charging current of the CICs before heat treatment, Figure 4.10 clearly indicates that there is a high density of oxygen groups on the as-synthesized CIC surfaces.

As discussed in Section 4.3, the pore walls of the CICs are composed of closely packed planar graphene sheets with their sheet edges exposed, according to the literature [165-170]. This suggests that the as-synthesized CIC surfaces are composed mainly of graphene edges, and thus they should have an area-specific active site density of ca. 20 $\mu\text{mol}/\text{m}^2$, assuming that all of the graphene edges are in the zig-zag edge configuration (Scheme 4.1) [191].



Scheme 4.1. Model of zig-zag edge configuration (top side) of graphene layers [191].

If it is also assumed that all of the oxygen content of the CICs (Table 4.1) is in the form of $-\text{OH}$ groups, the CICs should have an area-specific $-\text{OH}$ group density of 9 - 11 $\mu\text{mol}/\text{m}^2$, obtained by normalizing the oxygen content to the corresponding surface area in Table 4.2. Therefore, the surface functional groups will take up roughly 50 % of the surface area of the CICs. This high fraction of polar group coverage on the CIC surfaces is believed to contribute to the high hydrophilicity found in this work. This also explains why Pt nanoparticles can be dispersed so well on the CIC surfaces, as was shown in our previous work [43, 48].

It should be noted that the functional group coverage is based on elemental analysis and the N_2 sorption results, as well as on the literature [165-169, 191]. More advanced

techniques, such as high resolution transmission electron microscopy (HR-TEM), Raman spectroscopy, temperature programmed deposition/oxidation (TPD/TPO), and X-ray photoelectron spectroscopy, are needed to confirm the nature of the surface structures (i.e., oriented graphene layers) and of the functional groups attached to the surface of the as-synthesized CICs, vs. the heat-treat carbons. The Boehm titration could also be used to determine the specific concentration of some of these surface functional groups [192, 193], such as phenols and carboxylates. Additionally, mercury porosimetry and water vapour isotherm determination could enhance the understanding of the surface wettability of these carbons, especially those with larger pores (width > 50 nm).

4.7 Summary

Contact angle kinetics (CAK) and water vapor sorption (WVS) methods were used to determine the wettability of in-house synthesized colloid-imprinted carbons (CICs), having a range of pore sizes of 19 - 50 nm, before and after heat treatment at 1500 °C in a N₂ atmosphere. The CICs exhibited little change in their mesoporous structure but did show a significant decrease in their surface oxygen content after heat treatment.

The CAK and WVS tests demonstrated that the CICs have a much more hydrophilic pore surface, compared to commercial carbon black, while heat-treatment at 1500 °C made them much more hydrophobic. The high hydrophilicity of the as-synthesized CICs is attributed to the high oxygen-containing surface functional group density, $\sim 10 \mu\text{mol}/\text{m}^2$, with a coverage of up about 50 %, based on the assumption that the oxygen atoms are present in the form of –OH groups on the CIC surfaces. The existence of a high surface density of oxygen-containing groups

on the as-synthesized CICs, and their removal by heat treatment, was also confirmed by their cyclic voltammetric response in acidic solutions.

Chapter Five: Wettability of Ordered Mesoporous Carbons Before and After Heat Treatment

This work is not published yet.

5.1 Introduction

As mentioned in Chapter 1, ordered mesoporous carbons (OMCs) are an alternative catalyst support for use in polymer electrolyte membrane fuel cells (PEMFCs), and thus it is essential to understand their wettability in order to further evaluate their advantages/disadvantages. In recent years, a wide variety of OMC materials has been synthesized using various templating materials and a range of carbon precursors (or carbon sources) [51, 53, 71, 194].

The templates used to control the porous structures of OMCs are normally divided into two types, soft and hard [71, 194]. A soft template decomposes before the solidified carbon precursor is carbonized at high temperature, forming mesopores [194]. A hard template (e.g., mesoporous silica) is removed by dissolution after the precursor has been carbonized, leaving mesopores in the carbon structure [71, 195]. Compared to the soft-template method, the hard-template approach is applicable for a wider variety of carbon precursors, including carbohydrates and hydrocarbons [53, 196, 197], e.g., sucrose and anthracene. Of these, sucrose has been the most widely used for the synthesis of OMCs with various porous structures [47, 132, 198, 199].

A commonly accepted formation mechanism of hard-template synthesis of OMCs is shown in Figure 5.1 [71]. Briefly, the carbon precursor is infiltrated into the pores of mesoporous silica, followed by carbonization at a high temperature and then removal of the

silica in base or acid (e.g., aqueous NaOH or HF solutions), forming carbon frameworks with mesopores having the same shape and size as the silica template. It is also believed that the carbon framework is inter-connected, as shown schematically in Figure 5.1 by the thin carbon ‘nanowires’ (dark) between the carbon ‘nanorods’ (grey). This three-dimensional connection constrains the microstructure of OMCs from deformation so that the structure can survive heat-treatment even at high temperatures [200].

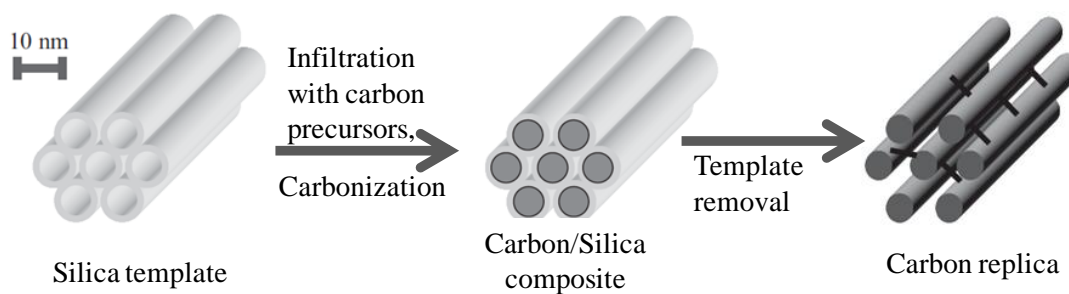


Figure 5.1. Schematic illustration of ordered mesoporous carbon (OMC) synthesis using ordered mesoporous silica as the template [71].

Hexagonal mesoporous silica (HMS), which has a worm-hole structure [49, 132, 197] vs. the rod-like structure (e.g., of SBA-15) shown in Figure 5.1, is one of the silica templates used for the synthesis of OMCs. HMS-templated OMC is thus believed to be composed of interconnected “nano-strings”, rather than rigid carbon nanowires, as illustrated in Figure 5.1. These differences in mesopore shape are attributed to the different synthesis conditions employed, such as temperature and the type of surfactants used as templates to form the silica framework. With HMS as a template, sucrose and anthracene have both been used to synthesize OMCs [49, 132, 197].

Despite the many reports about their properties and applications [49, 51, 71, 132], including in PEMFCs, as discussed in Section 1.4.3, OMCs have not been studied yet for their wettability characteristics. In this work, we used HMS as the hard template to synthesize OMCs, with sucrose (S) and anthracene (A) employed as the carbon precursor, producing OMC-S and OMC-A, correspondingly. These OMCs were then heat treated at 1500 °C under a N₂ atmosphere to increase their carbonaceous nature. The OMCs were also examined with elemental and porosity analysis in order to understand their wettability and microstructure. The relative wettability of the OMCs, before and after heat treatment, was then determined using contact angle kinetics (CAK) and water vapor sorption (WVS) methods, also used in Chapter 4. The mechanism of formation of the microstructure of the OMCs, derived from different carbon precursors, is also discussed in this chapter.

5.2 Elemental composition of OMCs before and after heat treatment

Table 5.1 shows the elemental content of the ordered mesoporous carbon (OMC) samples, before and after heat treatment. It is seen that OMC-A has a slightly higher oxygen content than OMC-S does. Heat treatment at 1500 °C in a N₂ environment enhances the carbonaceous nature of both OMCs (i.e., increases their carbon content) and significantly decreases their oxygen content. These changes after heat treatment are well understood, with the exposure of a carbon sample to high temperatures in an inert atmosphere removing the volatile oxygen-containing surface groups [125, 126].

The solid residue of the as-prepared OMCs (Table 5.1) likely arises from some silica templating material that was not removed completely during the synthesis. At 1500 °C, silica may react with carbon to form volatiles, such as CO and SiO [163], which could be removed

by flowing nitrogen gas, resulting in a decrease in the amount of solid residue obtained from OMC-HT vs. OMC (Table 1). Some of the SiO could react further with carbon and form SiC in the carbon samples [163], which is seen as a grey (slightly green) solid residue after burning the OMC-HT samples in air. Similar phenomena were also observed for colloid-imprinted carbons (CICs), as presented in Chapter 4, where colloidal silica particles were used as the template.

Table 5.1 Elemental content (wt. %) of ordered mesoporous carbon (OMC) materials before and after heat-treatment (HT)

Sample ^a	C (%) ^b	H (%) ^b	N (%) ^b	Solid residue (%) ^c	O (%) ^d
OMC-S	86.6	1.4	0.1	4.6	7.3
OMC-S-HT	96.5	0.4	0.1	2.2	0.8
OMC-A	84.9	1.2	0.0	4.2	9.7
OMC-A-HT	97.4	0.6	0.5	2.3	-0.8

^a ‘S’ and ‘A’ represent the carbon precursors, sucrose and anthracene, respectively, used in ordered mesoporous carbon (OMC) synthesis. HT indicates that the samples were heat treated at 1500 °C in a N₂ atmosphere.

^b The carbon, hydrogen and nitrogen contents were obtained by combustion analysis, with an error of ca. ± 0.3 % for each element.

^c Solid residue from the OMCs was obtained by thermogravimetric analysis (TGA) in air, with an estimated error of ± 2.0 %.

^d Assuming O% = 100% – (C% + H% + N% + solid residue%), with an estimated error of ca. ± 2.1 %.

5.3 Porous structure of OMCs before and after heat treatment

Scanning electron microscopy (SEM) analysis of the ordered mesoporous carbons (OMCs) was also carried out in order to detect any differences in the microstructures of the two as-synthesized OMCs and also to determine if there are any changes in their structure after heat treatment, with the images shown in Figure 5.2. Both OMC-S and OMC-A consist of particles having both spherical and plate-like shapes (Figures 5.2a and 5.2e) in a similar

size range (0.5-5 μm), as expected, since they were prepared using the same silica template (hexagonal mesoporous carbon, HMS). Compared to the as-prepared OMCs, heat treatment at 1500 $^{\circ}\text{C}$ did not change the OMC particle size, according to the SEM images (Figure 5.2).

Two distinct surface morphologies are seen for both OMC-S and OMC-S-HT in Figures 5.2b and 5.2d. Some particles contain mesopores (2-50 nm) with sharp (or thin) edges, such as those shown in the dashed red circles in Figure 2. Other particles have a smoother, less porous surface. Most of the OMC-S and OMC-S-HT particles exhibit the latter morphology (Figures 5.2a and 5.2c), while more porosity is seen for the OMC-A and OMC-A-HT powders (Figures 5.2e and 5.2g).

N_2 sorption isotherms (NSIs) of the OMCs, both before and after heat treatment, were also collected, as shown in Figure 5.3a. Based on these results, more quantitative information about the porous structures of the OMC and OMC-HT samples was obtained, such as specific surface area, pore volume, and pore size distribution, particularly about the internal pores and the pores smaller than 10 nm, which cannot be distinguished in the SEM images (Figure 5.2). OMC-A shows a steep hysteresis at a partial pressure (P/P_0) > 0.8 , which suggests the presence of mesopores > 10 nm in diameter (Figure 5.3b). This is also seen in the SEM images (Figure 5.2f). In comparison, OMC-S exhibits hysteresis up to $P/P_0 = 0.45$ (*Type H4* hysteresis), normally attributed to narrow slit-like pores associated with micropores [171, 201]. This may be due to the agglomeration of the OMC-S particles (Figure 5.2a), blocked by microporous carbon walls, thus forming slit-like pores between the agglomerated particles (Figure 5.4).

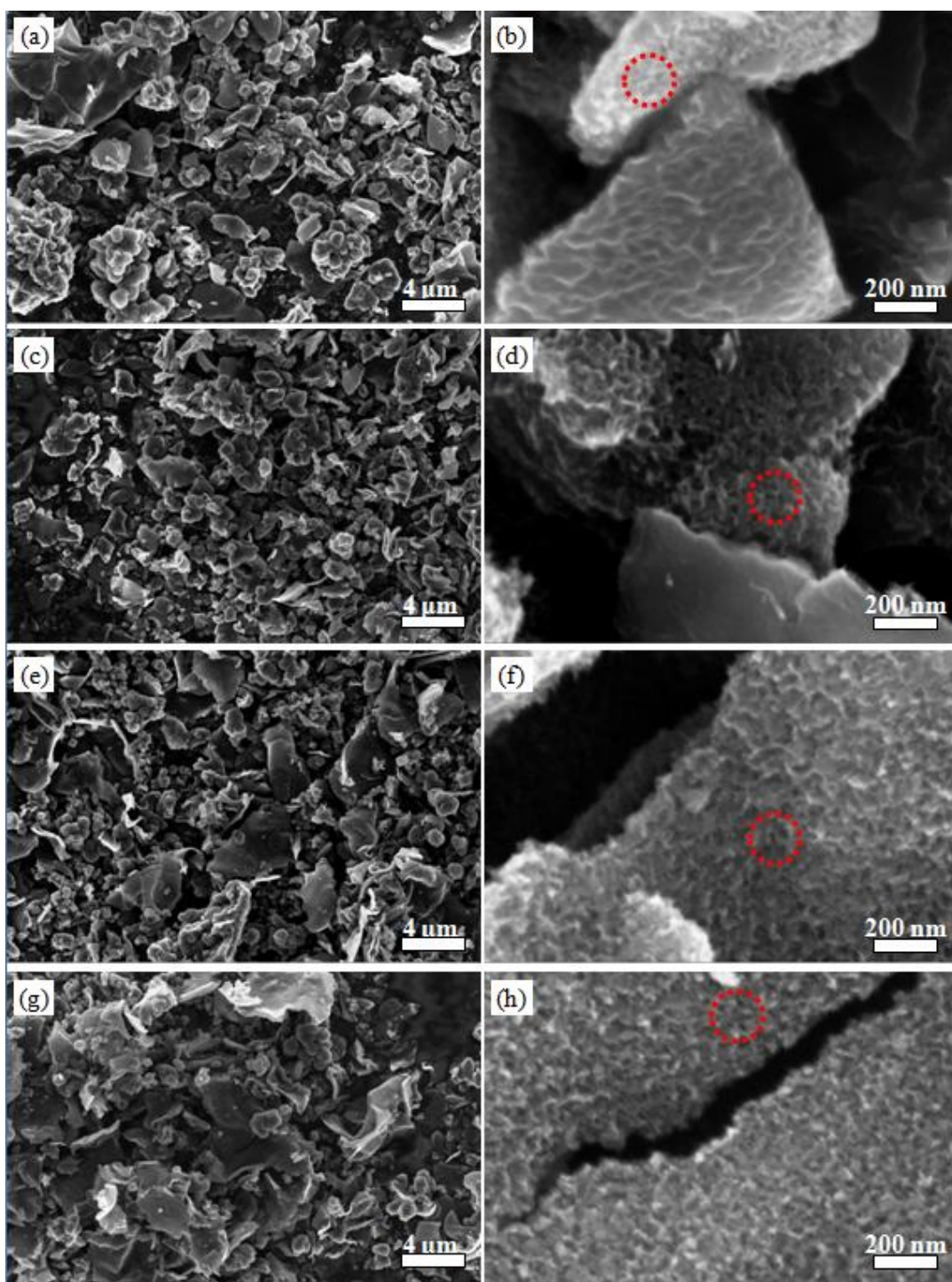


Figure 5.2. Field-emission scanning electron microscopy (SEM) images of (a, b) OMC-S, (c, d) OMC-S-HT, (e, f) OMC-A, and (g, h) OMC-A-HT, supported on carbon tape. The first and second columns represent lower and higher magnifications, respectively. Some mesopores (size ≤ 50 nm) in the OMC particles are circled with a dashed red line.

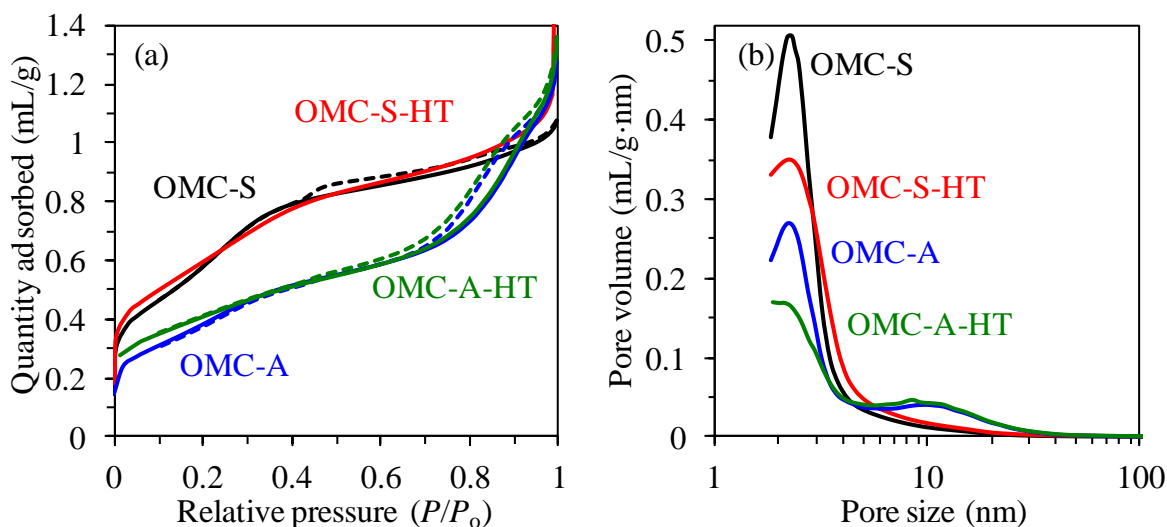


Figure 5.3. (a) N_2 adsorption (solid line) and desorption (dashed line) analysis of OMCs before and after heat-treatment for 2 h at 1500 °C in a N_2 atmosphere, and (b) the corresponding pore size distributions obtained from the adsorption branch of the isotherm, obtained using the Barrett-Joyner-Halenda (BJH) method, with the t -curve of carbon black used as the standard to determine the statistical thickness of the adsorbed nitrogen film [172].

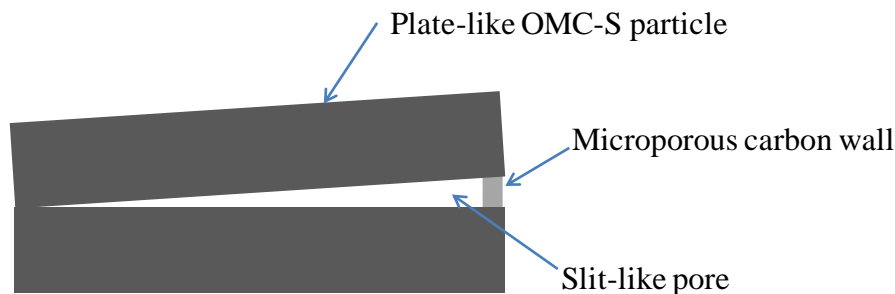


Figure 5.4. Schematic of the cross-sectional structure of a slit-like pore, potentially formed by the agglomeration of OMC-S particles, with its edges and mouth blocked by microporous carbon walls.

During the synthesis of OMC-S, the HMS particles may aggregate, forming slit-like pores between adjacent HMS particles, with the outlet of these pores potentially blocked by the sucrose/ H_2SO_4 mixture. Slit-like pores may also develop after carbonization and the

removal of silica, with the pore mouths blocked by microporous carbon (derived from the pyrolysis of sucrose).

The slit-like pores could have a width of up to 100 nm or larger, but they can still be completely filled by condensed N₂ at a high partial pressure (e.g., $P/P_o = 0.98$, Chapter 4) during the nitrogen adsorption process (Figure 5.3a for OMC-S). If the outlets of the slit-like pores are all < 5 nm [201, 202], evaporation of the condensed nitrogen will be constrained during the desorption process. When P/P_o is lower than 0.45, cavitation phenomena can occur [201, 202], i.e., a bubble that develops in the liquid nitrogen can accelerate the evaporation of the liquid nitrogen in the blocked pores. This is seen by a sudden decrease in the amount of nitrogen present in the desorption branch of the nitrogen sorption isotherms (NSI) at $P/P_o \approx 0.45$ (Figure 5.3a), producing an *H4*-type hysteresis in the NSI data (Figure 5.3a, for OMC-S). A similar hysteresis has been reported in the literature for other OMCs [132, 199, 200]. It should also be pointed out that the slit-like pores referred to here may have shapes other than what is shown schematically in Figure 5.4, due to different formation mechanisms, such as incomplete infiltration of the HMS template by the precursor.

After heat treatment at high temperatures (1500 °C in this work), the thin microporous carbon walls (Figure 5.4) may be broken down, leaving the slit-like pores open and freely accessible for N₂, resulting in the loss of the *H4* type hysteresis, as shown in Figure 5.3a (OMC-S-HT vs. OMC-S). In comparison, after heat treatment, OMC-A-HT exhibits only a slightly larger hysteresis than OMC-A, perhaps due to the formation of new larger mesopores (Figure 5.3b).

The pore size distribution of each carbon in Figure 5.3b was obtained by applying the Barrett-Joyner-Halenda (BJH) analysis method to the N₂ adsorption branch of the corresponding

isotherms. The adsorption branch was used because it is most comparable to the water vapor sorption experiments (Section 5.4.2), as also discussed in Chapter 4. The adsorption branch should also avoid the misleading effect of the slit-like pores of OMC-S (Figure 5.4) on the apparent pore size distribution. This is because, during the desorption process, the evaporation of condensed N_2 from the slit-like pores can be affected by the cavitation effect [201, 202], as discussed above. Compared to OMC-S, OMC-A shows a smaller peak at ca. 2-2.5 nm, but it has a higher specific pore volume arising from pores between 5 and 50 nm in width (Figure 5.3b). Heat treatment results in a decrease in the volume of the 2-2.5 nm pores for both OMCs, but an increase in the volume of the pores that are larger than 5 nm in diameter (Figure 5.3b).

In order to understand the origin of the 2-2.5 nm pores of the as-synthesized OMCs and also of the heat-treated OMCs (Figure 5.3b), as well as the 5-50 nm pores of OMC-A and OMC-A-HT, it is necessary to take into account the dimensions of the porous structure of the hexagonal mesoporous silica (HMS) template [49, 132], used for the synthesis of the OMCs. We show only a repeatable group of four adjacent pores of the HMS template in Figure 5.5a as an example to illustrate the size evolution of the OMC pores. The wall thickness within each group of three adjacent pores of HMS is defined by the diameter of the dashed circle (Figure 5.5a), which is shown as tangential to these pores.

After the pores are filled with carbon precursor and catalyst (H_2SO_4), HMS is heat treated at a high temperature (900 °C in this work) to convert the precursors to carbon (Figure 5.5b). The carbon then fills the worm-hole shaped channels of the HMS mesopores [49, 132], producing carbon nano-strings, as mentioned in Section 5.1. After heating at 900 °C, the silica framework shrinks by about 10 % in each dimension [199], due to skeletal

densification (polymerization and structural relaxation of amorphous silica) [203], and thus the silica wall thickness between two adjacent carbon nano-strings should also decrease from 2.2 to 2 nm, and the silica wall thickness surrounded by three adjacent carbon nano-strings decreases from 3 to 2.7 nm (Figures 5.5b vs. 5.5a).

After the removal of silica, the distance between two adjacent nano-strings should be 2 nm, and the pores between three adjacent carbon nano-strings should have a diameter of 2.7 nm (Figure 5.5c). Therefore, the equivalent cylindrical pores, obtained by using the BJH method to fit the nitrogen adsorption isotherms of these carbons (Figure 5.3), should exhibit a pore size in the range of 2 - 2.7 nm. This is exactly what is seen in the pore size distributions of both OMC-S and OMC-A (Figure 5.3b).

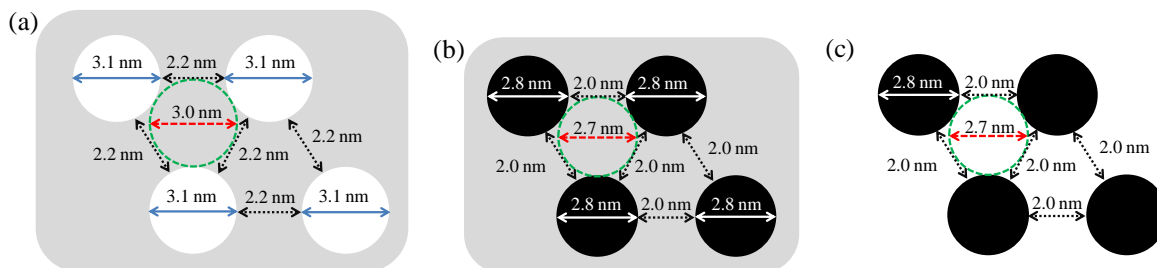


Figure 5.5. (a) Schematic of cross-sectional dimension of the pores (white circles) and pore walls of hexagonal mesoporous silica (HMS, grey), used as template for the synthesis of ordered mesoporous carbons (OMCs) [49, 132]. (b) Schematic of cross-sectional dimension of the HMS pores filled with carbon nano-strings (black circles), after the carbon precursor-filled HMS (a) has been heat-treated at high temperature (900 °C). (c) Schematic of cross-sectional dimension of the pores of OMCs after removal of silica from (b). Dashed green circle (a-c) is tangential to the three circles surrounding it, representing the thickness of silica walls (a-b) or the pore size among three adjacent carbon nano-strings (c), while arrows (a-c) represent the diameter of a circle or the gap distance between the edges of two circles.

As seen in Figure 5.3b, OMC-A has more secondary pores ($5 \text{ nm} < \text{pore size} < 50 \text{ nm}$) than OMC-S does, which is also seen in Figure 5.2f. This may arise from the incomplete

infiltration of all of the HMS pores (Figure 5.5a) by carbonized anthracene during OMC synthesis. For example, assuming that a particular HMS pore remains empty and that the six pores surrounding it are filled with carbonized anthracene (Figure 5.6a, top left corner), this would result in a 6.8 nm cylindrical pore surrounded by six carbon nano-strings after the removal of silica (Figure 5.6b, top left corner).

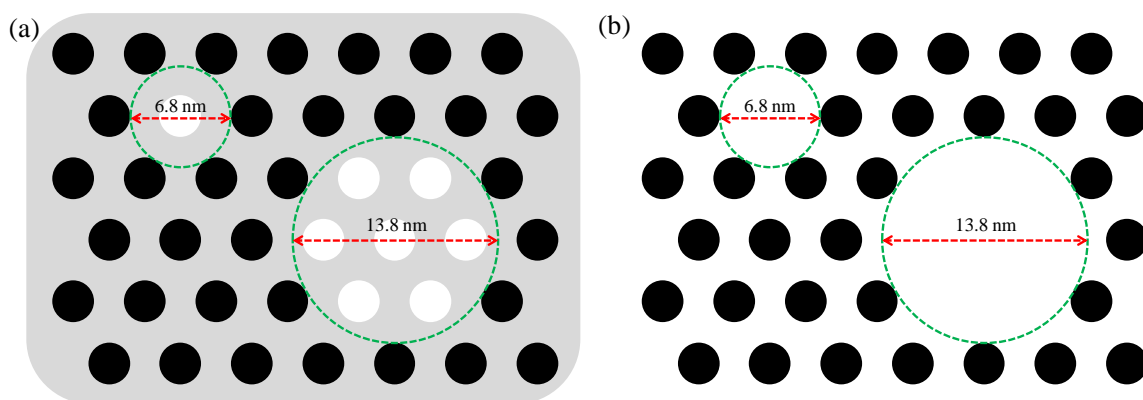


Figure 5.6. Schematic of the cross-sectional dimensions of (a) the carbon/HMS composite after heating at 900 °C and before the removal of silica, with the circles (black: carbon strings, white: non-filled pores) having the same dimensions as those in Figure 4b. The dashed circles represent the cylindrical pores surrounded by the carbon strings after the removal of silica, as shown in (b).

If additional adjacent HMS pores remain unfilled, such as the seven empty pores shown in Figure 5.6a (lower right corner, surrounded by the larger circle), the resultant pores in the OMC should have a diameter larger than 6.8 nm (consistent with the 13.8 nm pore size in Figure 5.6b, corresponding to the seven empty HMS pores in Figure 5.6a). Assuming that each pore in the HMS template can only be filled or non-filled by the carbon precursor, there should be no OMC pores having a size between 2.7 nm and 6.8 nm. This could explain why there is a minimum volume for the pores with a diameter of ca. 6 nm for OMC-A, between

the two peaks (2.2 nm and 9.7 nm) in Figure 5.3b. The peak at ca. 9.7 nm could result from bundles of the HMS mesopores remaining unfilled by carbonized anthracene during the synthesis. Again, it is noteworthy that these pore diameters were calculated by considering that the pores are cylindrical (worm-hole) in shape, according to the assumptions of the BJH gas sorption data analysis method [135, 172].

Compared to OMC-A, OMC-S has significantly fewer secondary mesopores (width ~ 10 nm, Figure 5.3b), suggesting that the mixture of sucrose and H_2SO_4 has filled the HMS pores more completely than did anthracene/sulfuric acid during the synthesis. This may be due to the high polarity of sucrose, resulting in good solubility in the H_2SO_4 solution and a high affinity for the polar HMS pore surfaces. Consistent with this hypothesis, after pyrolysis (or polymerization, catalyzed by H_2SO_4) and carbonization of sucrose, and after the removal of the silica template, OMC-S exhibits a high proportion of mesopores around 2.3 nm, showing a single peak in Figure 5.3b.

In contrast, anthracene has a low solubility in H_2SO_4 and thus these two components may experience partial phase separation after the evaporation of the acetone solvent when mixing with HMS powder at room temperature. Due to its higher affinity, H_2SO_4 may rapidly fill the HMS pores, possibly preventing anthracene from fully accessing them (Figure 5.7). During heat treatment at 160 °C in air, anthracene may polymerize to form polycyclic aromatic oligomers or pitch (tar, or its oxides) under acid catalysis [204, 205]. The pitch and H_2SO_4 may also not mix well and thus not infiltrate the HMS pores homogeneously. H_2SO_4 will then evaporate (its boiling point is 337 °C) during heating to 900 °C, leaving some of the HMS pores empty (Figures 5.7 and 5.6a), thus producing an OMC-A structure with larger mesopores (Figures 5.3b and 5.6b). The empty HMS pores in Figure 5.6a may also be

caused by the evaporation of non-polymerized (or non-stabilized) anthracene, by the decomposition of the anthracene-derived pitch during the carbonization process, or by the incomplete imprinting of HMS by the anthracene-derived pitch, as occurs in the CIC synthesis discussed in Chapter 4.

Therefore, only the HMS pores filled with both anthracene and the H_2SO_4 catalyst or infiltrated by anthracene-derived pitch would have produced ordered carbon nano-strings after carbonization (Figure 5.7), resulting in many secondary mesopores around 10 nm in diameter (Figure 5.3b). These larger mesopores would then take up almost 50% of the total pore volume of OMC-A, both before and after heat-treatment (OMC-A-HT), as reflected by the nitrogen sorption hysteresis seen in Figure 5.3a.

For better comparison, the corresponding structural properties of the carbon samples are given in Table 5.2. The specific surface area was obtained using the Brunauer-Emmett-Teller (BET) analysis in the range of $0.05 < P/P_o < 0.30$, where P and P_o are the equilibrium pressure and the vapour-saturated pressure of nitrogen at 77 K, respectively. Because all of the OMCs exhibited significant nitrogen sorption at partial pressures of ca. 0.2, attributed to N_2 condensation in the 2-2.5 nm pores, the conventional t -plot analysis method (layer-by-layer adsorption, $0.2 < P/P_o < 0.5$, employed in Chapter 4) is not suitable for the estimation of the external surface areas (including the internal surface of the mesopores) of the OMCs, either before or after heat treatment. The BJH surface areas (S_{BJH}) and BJH pore volumes (V_{BJH}) are listed in Table 5.2, where the surface area and the volume arising from the micropores were obtained by subtracting S_{BJH} from the BET surface area (S_{BET}), and V_{BJH} from the pore volume (V_{NSI} , nitrogen sorption isotherms (NSI) at $P/P_o = 0.98$ in Figure 5.3a).

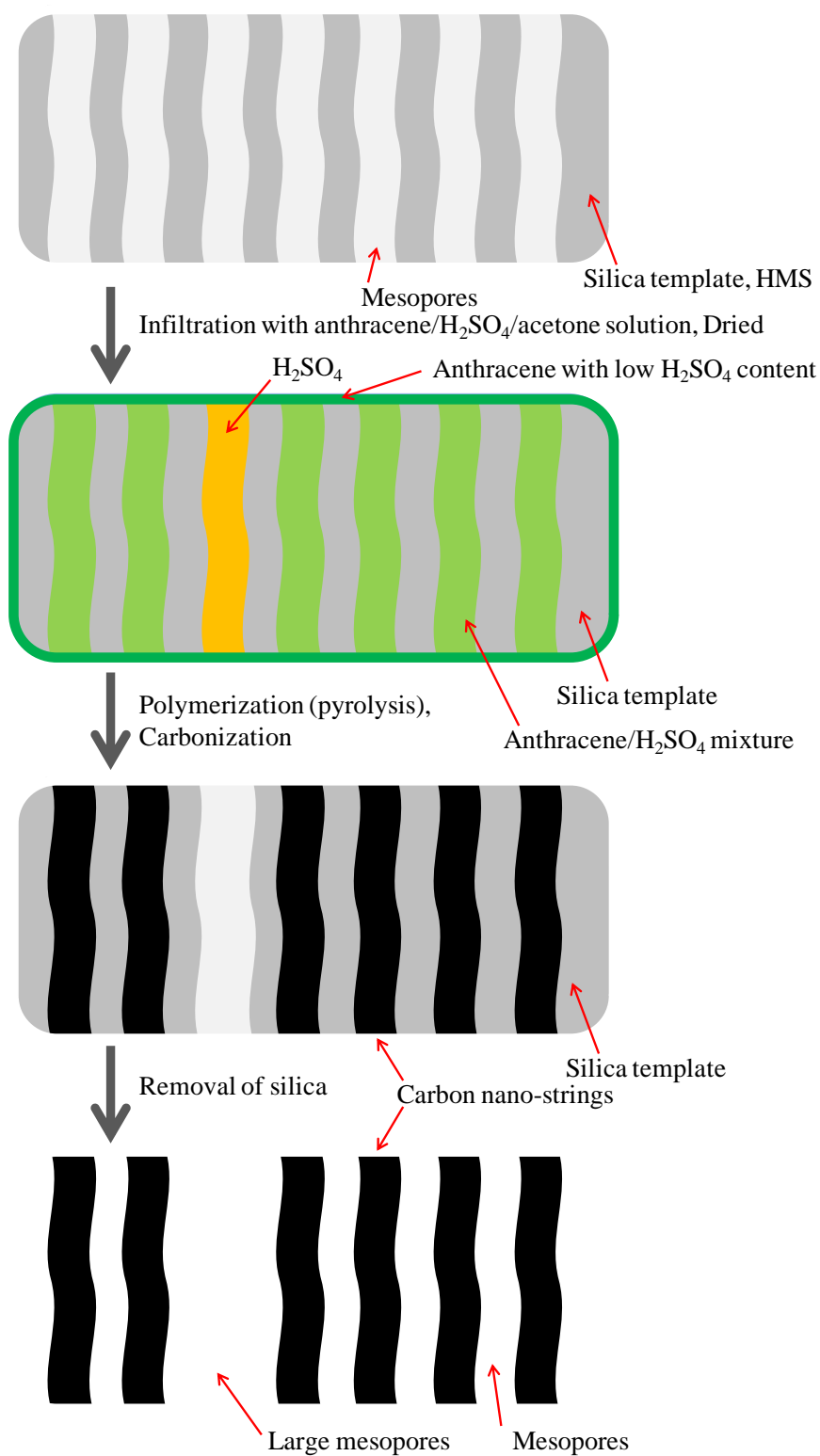


Figure 5.7. Cartoon showing a possible mechanism of the development of the microstructure of anthracene-based ordered mesoporous carbon (OMC-A).

Table 5.2 Structural properties of OMCs before and after heat-treatment ^a

Sample	Pore size (nm) ^b	S_{BET} (m ² /g) ^c	S_{BJH} (m ² /g) ^d	S_{micro} (m ² /g) ^e	$S_{\text{micro}}/S_{\text{BET}}$ (%)	V_{NSI} (mL/g) ^f	V_{BJH} (mL/g) ^g	V_{micro} (mL/g) ^h	$V_{\text{micro}}/V_{\text{NSI}}$ (%)
OMC-S	2.3	1400	1090	310	22	1.03	0.89	0.13	13
OMC-S-HT	2.2	1380	960	420	30	1.14	0.95	0.20	17
OMC-A	2.2, 9.7	920	770	150	16	1.15	1.11	0.04	4
OMC-A-HT	2.1, 8.4	940	640	300	32	1.20	1.08	0.12	10

^a Heat treated at 1500 °C for 2 h under a N₂ atmosphere.

^b Pore size obtained from the maximum in the pore size distribution plots in Figure 5.3b.

^c S_{BET} = total surface area, obtained using the Brunauer-Emmett-Teller (BET) plot in the partial pressure range of $0.05 < P/P_0 < 0.30$.

^d S_{BJH} = surface area obtained by integrating the surface area of pores with a size from 2 nm to 300 nm, estimated by applying the BJH method on the adsorption branch of the N₂ sorption isotherms in Figure 5.3a.

^e S_{micro} = micropore surface area, obtained by subtracting the BJH adsorption cumulative surface area (S_{BJH}) from the total surface area (S_{BET}).

^f V_{NSI} = pore volume, acquired from the N₂ sorption isotherms (NSI) at $P/P_0 = 0.98$ (Figure 5.3a).

^g V_{BJH} = pore volume estimated by integrating the volume of the pores with a size from 2 nm to 100 nm, as seen in Figure 5.3b.

^h V_{micro} = micropore volume, obtained by subtracting the BJH adsorption cumulative volume (V_{BJH}) from the total surface area (V_{NSI}).

As previously reported [49], the higher surface area (S_{BET} , Table 5.2) of OMC-S vs. OMC-A is due to the higher fraction of micropores within the sucrose-derived OMC, reflected by its higher $S_{\text{micro}}/S_{\text{BET}}$ and $V_{\text{micro}}/V_{\text{NSI}}$ values in Table 5.2. This is because the carbohydrate (sucrose) releases more volatiles than does the aromatic molecule (anthracene) during the polymerization and carbonization processes [49, 132], resulting in more pore surfaces formed within the carbon nano-strings (carbon frame-work) for OMC-S. The pore surfaces include both micropores and external surfaces, as OMC-S exhibits higher S_{micro} and S_{BJH} values than does OMC-A (Table 5.2). For OMC-A, the presence of more pores having a

width larger than 5 nm (Figure 5.3b) results in its significantly lower $V_{\text{micro}}/V_{\text{NSI}}$ value (4 %), when compared to OMC-S (13 %).

Heat treatment did not significantly alter the total surface area (S_{BET} , Table 5.2) of either OMC-S or OMC-A, but it did increase the micropore surface area and volume of both OMC-A and OMC-S ($S_{\text{micro}}/S_{\text{BET}}$ and $V_{\text{micro}}/V_{\text{NSI}}$, Table 5.2). Similar to the colloid-imprinted carbons (CICs), reported in Chapter 4, heat treatment at 1500 °C resulted in the removal of oxygen-containing functional groups from the OMC surfaces (Table 5.1), without significantly changing the total surface area (S_{BET} , Table 5.2). This confirms that the OMC nano-strings are connected three-dimensionally [49, 132], preventing the structures from complete collapse during heat treatment.

However, due to the sintering of the nano-strings, heat treatment may still have led to the shrinkage of the 2-2.5 nm pores of the OMCs to a certain extent, forming pores smaller than 2 nm, i.e., micropores. This would result in a decrease in the volume of the 2-2.5 nm pores for both of the OMCs (Figure 5.3b) after heat treatment. The more significant increase (2 times) of the $S_{\text{micro}}/S_{\text{BET}}$ and $V_{\text{micro}}/V_{\text{NSI}}$ ratios for OMC-A vs. OMC-S may be due to the fact that it has less cross-linkage between its nano-strings than does OMC-S.

5.4 Wettability of OMCs before and after heat treatment

In the previous section, it was shown that both OMC-S and OMC-A experienced little change in their pore structure after heat treatment (Figures 5.2 and 5.3, and Table 5.2). However, both OMCs showed a significant change in their elemental composition as a result of heat treatment (Table 5.1). In order to better understand these results, wettability studies,

including the use of both contact angle kinetics (CAK) and water vapor sorption (WVS) methods, were carried out on these carbons before and after heat-treatment.

5.4.1 Contact angle kinetics (CAK) study

Figure 5.8 shows a selection of sequential images (down each column) of water droplets on the various compressed OMC powder pellets, as well as the time (last row) taken for the water droplet to be completely absorbed by the OMC pellet. It is seen that a water droplet deposited on the OMC-S surface behaves quite differently from that on OMC-A, taking much longer for it to be absorbed. Water droplets on the heat-treated OMCs also behave differently from those on the as-synthesized samples, requiring much longer for the droplet to be absorbed.

In this work, the water droplets all had the same volume ($\sim 10 \mu\text{L}$) and were released from the same height ($\sim 1 \text{ mm}$) above the pellets. Therefore, the difference in the behavior of the water droplets (Figure 5.8) depends only on the differences in the surface properties of the OMC pellets. For example, in Figure 5.8, a water droplet deposited on OMC-S exhibits a high contact angle in the early stages of contact ($t \leq 100 \text{ ms}$), rebounding from the surface at $t = 25 \text{ ms}$, but it then ($t > 100 \text{ ms}$) shows a slow decrease in both volume and contact angle. After ca. 6 s, the water droplet was fully absorbed by the OMC-S pellet. This is attributed to the intrinsically hydrophilic nature of the OMC-S and its porous structure.

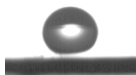
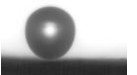
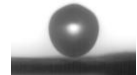
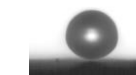
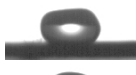
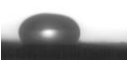
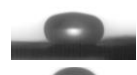

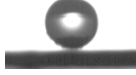
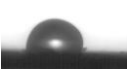
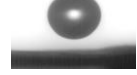
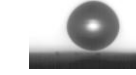
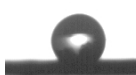

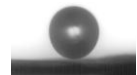
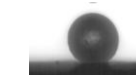






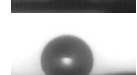

Time (ms)	OMC-S	OMC-A	OMC-S-HT	OMC-A-HT
0				
8				
25				
100				
1000				
2500				
Time to 100% dryness	6.0 s	0.6 s	> 10 min	~ 2 min

Figure 5.8. Sequential images of water droplets (diameter ≈ 2.7 mm) deposited on compressed OMC pellets, before and after heat-treatment at 1500 °C under a N₂ atmosphere, showing the contact angle kinetic (CAK) behavior of water on the pellet surfaces. The time to 100% dryness refers to the time it takes for the pellet to fully absorb the water droplet deposited on it.

Compared to what was seen for a fresh OMC-S pellet, the water droplet contacting the as-synthesized OMC-A pellet exhibits much smaller contact angles at the early stages of impact ($t \leq 100$ ms, Figure 5.8) and is absorbed by the pellet in a very short time (0.6 s). In general, the rapid up-take of water suggests that OMC-A is extremely hydrophilic, much more so than OMC-S. After heat treatment, the OMCs exhibit a significantly higher water contact angle ($> 90^\circ$) for a longer time period than before (Figure 5.8), suggesting that the heat-treated OMCs are very hydrophobic. At the same time, OMC-A-HT requires a much shorter time to absorb the water droplet than does OMC-S-HT, indicating that OMC-A-HT is more hydrophilic than OMC-S-HT.

In order to examine the wetting kinetics of water droplets on the OMC pellets in more detail, in Figure 5.9, we also plot the contact angles of the water droplets vs. time, after depositing them onto the carbon surfaces, using the data shown in Figure 5.8. Each plot has a standard deviation in the contact angles of about $\pm 8^\circ$ for the fresh OMCs, and ca. $\pm 4^\circ$ for the heat-treated OMCs, after averaging at least three independent measurements. A contact angle of 180° indicates that the water droplet has completely rebounded from the carbon surface, as seen at $t = 25$ ms in Figure 5.8 for OMC-S and for the OMC-HT samples, suggesting that these surfaces are both hydrophobic in appearance. The longer the contact angle remains at 180° , the more hydrophobic the corresponding sample surface is. Therefore, OMC-S-HT is the most hydrophobic of these samples, according to Figure 5.9.

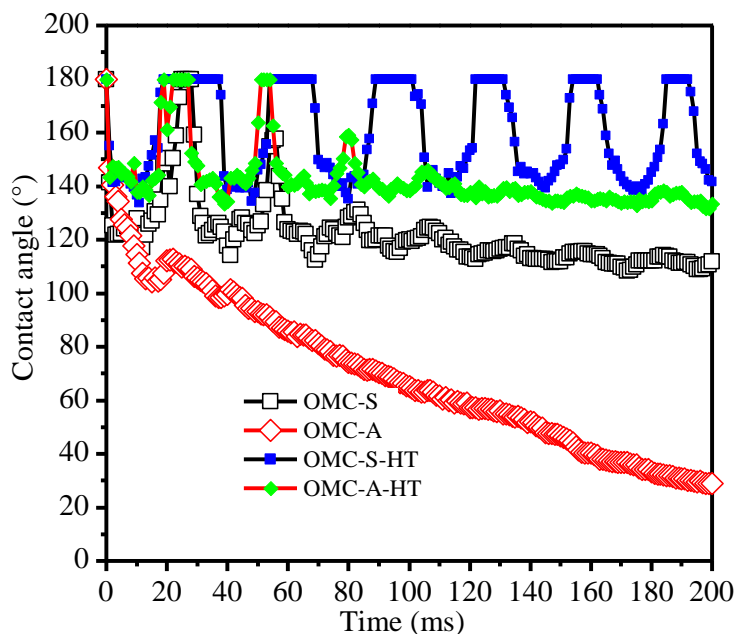


Figure 5.9. Contact angle kinetics (CAK) of water droplets deposited onto the OMC pellets, before and after heat-treatment at 1500°C under a N_2 atmosphere (data from Figure 5.8).

It is seen that the water droplets on OMC-S (Figure 5.9) exhibit a declining contact angle, but with dissipating oscillations, within the first 200 ms of contact. As discussed in Chapter 4, these types of oscillations arise from the balance between the hydrodynamic energy and the surface energy of the water droplets, and the dissipation is due to the viscosity of water and the interfacial force (or hydrophilicity) of carbon to water. The fewer number of cycles of the oscillations (Figure 5.9), the more hydrophilic the carbon pellet is.

Based on the relative values of the contact angles and the number of oscillation cycles of the water droplets in Figure 5.9, it can be concluded that the OMC pellets have the following sequence of hydrophilicity: $\text{OMC-S-HT} < \text{OMC-A-HT} < \text{OMC-S} \ll \text{OMC-A}$. Because all of the OMC and OMC-HT samples have a similar particle size (Figure 5.2), the surface roughness of the pellets should be similar, as explained in Chapter 4. Thus, the contribution of the surface roughness to the wettability should be the same, and the relative intrinsic surface hydrophilicity of these sample particles should follow the same trend seen above, i.e., $\text{OMC-S-HT} < \text{OMC-A-HT} < \text{OMC-S} \ll \text{OMC-A}$.

5.4.2 Water vapor sorption (WVS) study

As described above, the OMC-A particles exhibit a different surface morphology from OMC-S (Figures 5.2f vs. 5.2b), i.e., there are more mesopores seen in the SEM images of the OMC-A particles. This may contribute to the differences observed in the wettability of OMC-A and OMC-S, as seen in the CAK experiments. Differences are also seen when comparing OMC-S-HT and OMC-A-HT (Figures 5.8 and 5.9). Water vapor sorption (WVS) was thus examined to determine the relative hydrophilicity of the OMCs, before and after heat-treatment, in order to verify the conclusions derived from the CAK results (Figures 5.8 and 5.9).

Figure 5.10 shows the WVS results as a function of the exposure time of dry, non-heat-treated and heat-treated OMC samples to water vapor. The volume of water vapor sorbed by the carbons was obtained from the mass increase of the samples during their exposure to water vapor at room temperature, with an error of ca. ± 0.01 mL/g. Since all of the OMC and OMC-HT samples were placed in the same chamber at the same time and thus exposed to the same water vapor partial pressure, their sorption data (Figure 5.10) should be directly comparable with each other.

It can be seen in Figure 5.10 that OMC-A has the ability to sorb a much larger amount of water vapor than OMC-S does. After heat-treatment, the amount of water vapor sorbed on both OMCs decreases, with the decrease for OMC-A being more significant, but OMC-A-HT is still seen to sorb more water than OMC-S-HT at steady state. These results are in good agreement with the contact angle data shown in Figures 5.8 and 5.9, confirming the relative capability of the OMCs vs. the OMCs-HT to take up water. However, OMC-A-HT sorbs less water than either OMC-S or OMC-S-HT at the start of the experiment and then gradually sorbs more water than both OMC-S and OMC-S-HT. Therefore, a deeper analysis of the data is required to understand the intrinsic relative hydrophilicity of these carbons.

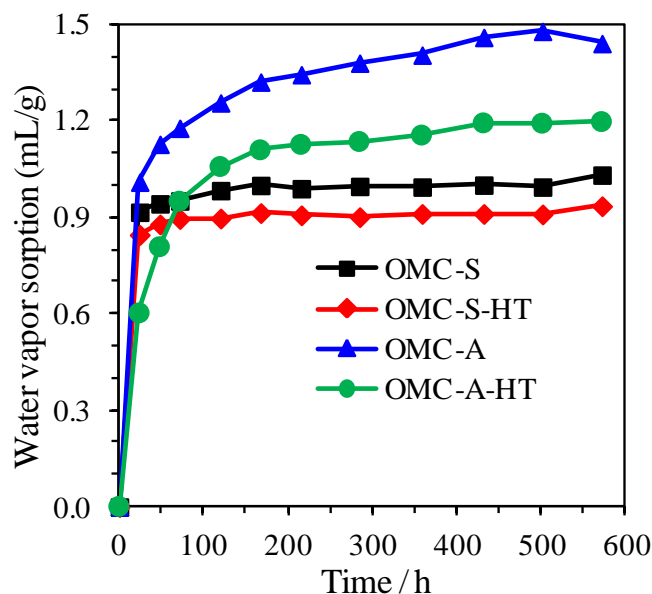


Figure 5.10. Water vapor sorption (V_{WVS}) data for OMCs, before and after heat-treatment at 1500 °C under a N_2 atmosphere, all at room temperature.

As discussed in Chapter 4, the rate and amount of water vapor sorbed by a porous sample depends mainly on its surface area, pore size, pore volume, and surface wettability. In order to compare their relative wettability, the WVS data (Figure 5.10) of these carbons were thus normalized to their corresponding surface area and pore volume ($V_{\text{WVS}}/V_{\text{mono}}$ and $V_{\text{WVS}}/V_{\text{NSI}}$, Figure 5.11), obtained from the nitrogen sorption isotherms (NSI, Figure 5.3a and Table 5.2). Here, the surface area was replaced by the volume of one monolayer of water (V_{mono}) adsorbed on an extremely hydrophilic surface (e.g., hydrolyzed silica) having the same surface area, assuming that the water molecules are closely packed, as was also assumed in Chapter 4. The differences in the $V_{\text{WVS}}/V_{\text{mono}}$ ratios should therefore reflect the relative capability of the surfaces to adsorb water (based on their polarity or wettability), if the samples have a similar microstructure and were exposed to the same vapor conditions.

It is seen in Figure 5.11a that OMC-S and OMC-S-HT each sorbed a similar amount (2.3-2.6 vs. 2.2-2.4 layers) of water on their surfaces, while OMC-A-HT took up the same number of layers (2.3) of water in a 24-hour exposure and then sorbed significantly more after that. A common characteristic of these three samples is that they contain mesopores of the same size, 2.1-2.3 nm (Table 5.2, giving an average of 2.2 nm), obtained by using the BJH method and assuming that the pores are cylindrical in nature. Assuming also that a cylindrical pore (diameter d) with an infinite length (l) is completely filled with water, the corresponding area-specific thickness (t_{ads}) of water covering the surface can be estimated by Equation 5.1:

$$t_{\text{ads}} = \frac{\frac{1}{4} \pi d^2 l}{\pi d l} = \frac{d}{4} \quad (5.1)$$

Similar to Chapter 4, assuming that each water monolayer is about 0.25 nm in thickness [186, 187], a 2.2 nm cylindrical pore can take up about 2.2 monolayers of water ($t_{\text{ads}} = 0.55$ nm, Equation 5.1). This is very close to the $V_{\text{WVS}}/V_{\text{mono}}$ values obtained for these carbon samples at $t = 24$ h (Figure 5.11a), except for OMC-A, which exhibited a much higher $V_{\text{WVS}}/V_{\text{mono}}$ ratio at this stage. It should be noted that the surface area (S_{BET}) used in the calculation of V_{mono} includes the surface area of the micropores, which take up 20-30 % of the total surface area ($S_{\text{micro}}/S_{\text{BET}}$, Table 5.2), as well as the surface area of pores larger than 2.3 nm in diameter. In other words, the $V_{\text{WVS}}/V_{\text{mono}}$ value of 2.3 ($t = 24$ h, Figure 5.11a) suggests that all of the 2-2.5 nm pores seen in Figure 5.3b were completely filled by water in the 24 h of exposure to water vapor in this work.

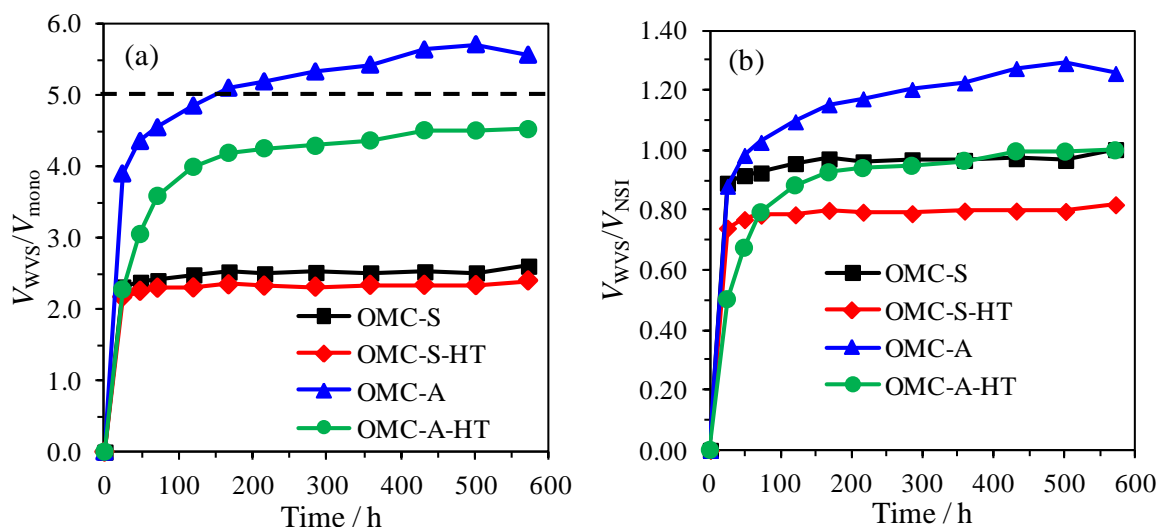


Figure 5.11. Water vapor sorption data (V_{WVS} , from Figure 5.10) of OMCs (a) before and (b) after heat-treatment at 1500 °C under a N_2 atmosphere, normalized to their corresponding (a) surface area and (b) pore volume (Tables 5.2), obtained from nitrogen sorption isotherms (Figure 5.3a).

Note: (a) V_{mono} = volume of one monolayer of water molecules closely packed on a sample surface, obtained using the equation: $V_{mono} = S_{BET} M_{H_2O} / \sigma_{H_2O} N_A \rho_{H_2O}$, where S_{BET} is the specific surface area of the sample (Table 5.2), M_{H_2O} = molar mass of water, σ_{H_2O} = cross-sectional area of water molecules (0.106 nm²) [184, 185], N_A = Avogadro's constant, and ρ_{H_2O} = water density at 23 °C. (b) V_{NSI} = Total pore volume obtained from the nitrogen sorption isotherms, as shown in Table 5.2.

The continuing increase in water up-take by OMC-A-HT in Figure 5.11a suggests that water vapor is also condensing in pores larger than 2.1 nm in diameter (Table 5.2), e.g., those that are 10-20 nm in size (Figure 5.3b). This is consistent with the results in Chapter 4, which showed that the ca. 17 nm pores present in heat-treated colloid-imprinted carbon (CIC) samples favor water vapor condensation, but that pores ≥ 24 nm in diameter do not, where the CICs were heat treated and then tested using the same conditions as used for the OMCs in this chapter. These results also indicate that these mesoporous carbon surfaces have an intrinsic water contact angle of $< 90^\circ$, favoring water condensation within the pores, based on the Kelvin equation (4.1).

Both OMC-S and OMC-S-HT almost reached a steady-state in their water up-take after 1 day of exposure (Figure 5.11a), which indicates that water may fill only the ~ 2.3 nm mesopores (Figure 5.3b). In turn, this suggests that the outer surface of OMC-S may be equally hydrophobic as in its heat-treated form. As a V_{WVS}/V_{mono} ratio of about 4 was obtained by OMC-A after the first day of exposure to water vapor ($t = 24$ h, Figure 5.11a), this indicates that both the 2.3 nm and the larger pores of OMC-A were filled by condensed water. This suggests that OMC-A has a much more hydrophilic surface than do OMC-S, OMC-S-HT and OMC-A-HT, consistent with the CAK results (Figures 5.8 and 5.9)

According to Figure 5.11b, OMC-A reaches a steady-state V_{WVS}/V_{NSI} value that is > 1 , indicating that water vapor has filled all of the pores smaller than ~ 100 nm in size, as well as the larger pores, such as textural pores, as discussed for the CICs in Chapter 4. OMC-S and OMC-A-HT have a similar V_{WVS}/V_{NSI} ratio of about 1 at the end of the experiment, suggesting that water condensed only in pores smaller than 100 nm and that the outer surface of OMC-S has a similar hydrophobicity to heat-treated OMC-A. OMC-S-HT exhibits an even smaller V_{WVS}/V_{NSI} ratio, suggesting that water condensed only in pores that are even smaller than those in OMC-S.

Importantly, the significant decrease in the V_{WVS}/V_{NSI} ratio from OMC-A to OMC-A-HT, as well as from OMC-S to OMC-S-HT, demonstrates that heat treatment made the OMC samples significantly more hydrophobic. This is fully consistent with the literature for other types of carbons [67, 167, 206] and with the conclusions reached in Chapter 4, i.e., that heat treatment made the colloid-imprinted carbons much more hydrophobic. Despite this, however, OMC-A-HT exhibits a smaller V_{WVS}/V_{NSI} ratio than OMC-S-HT in the first 50 h

(Figure 5.11b), after which its V_{WVS}/V_{NSI} ratio is higher than OMC-S-HT, so it is difficult to judge which of these two carbons is more hydrophilic.

In order to more precisely explain what size of pores has been filled by condensed water at each stage of the experiment in Figure 5.10, we have compared Figure 5.10 with Figure 5.3a to obtain the partial pressure required to condense N_2 into the same volume of pores at each stage in Figure 5.10, with the results shown in Figure 5.12a. Using these data, we have estimated the size of the pores that have been fully filled with water, as shown in Figure 5.12b, assuming that all pore surfaces have the same intrinsic wettability ($\theta = \text{constant}$ and $< 90^\circ$) for each carbon and that water tends to fill the smallest pores first. The pore size estimation is based on the rearrangement of the Kelvin equation (4.1),

$$r_k = \frac{-2\gamma V_m}{\ln(P/P_o)RT} \quad (5.2)$$

where r_k is Kelvin radius [172], P/P_o is the partial pressure of N_2 , γ is the surface tension (8.88 mJ/m²) of liquid nitrogen at $T = 77$ K [188], V_m is the molar volume (34.68 cm³/mol) of liquid nitrogen, R is the universal gas constant, and the statistical layer thickness (t_f) of an adsorbed N_2 film on a carbon black surface being:

$$t_f = 0.88(P_o/P)^2 + 6.45(P_o/P) + 2.98 \quad (5.3)$$

where t_f has units of Å. Thus, the size of the pores (d) filled with nitrogen is estimated as $d = 2(r_k + t_f)$.

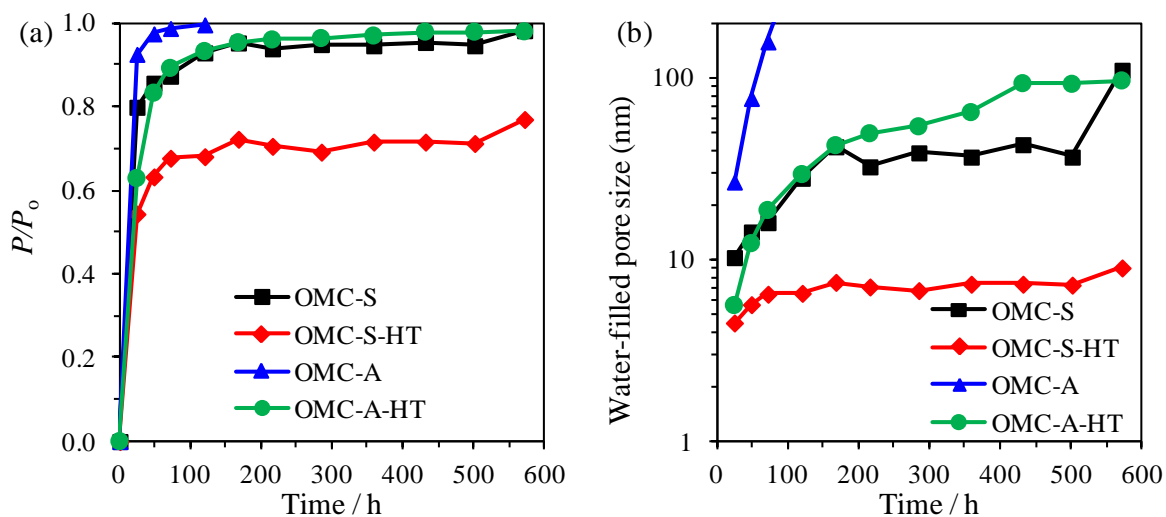


Figure 5.12. (a) Partial pressure (P/P_0) required to condense N_2 (Figure 5.3a) to fill the same pore volume as water vapor did at each stage in Figure 5.10. (b) Estimated size of the pores that have been fully filled by water with time, corresponding to the points in Figure 5.10, calculated using the Kelvin equation (5.2) and the statistical thickness of an adsorbed N_2 film on a carbon black surface (Equation 5.3) [172].

This estimation is based on the knowledge that liquid N_2 is able to completely wet all surfaces ($\theta = 0^\circ$ in Equation 4.1). If a surface can adsorb water vapor in the same way as it does N_2 , the surface must be extremely hydrophilic ($\theta = 0^\circ$). Therefore, the estimated size of the water-filled pores (Figure 5.12b) reflects the relative wettability of the OMC surface, instead of the real extent of water vapor condensation in the OMC pores.

Based on Figure 5.12b, it is seen that, at $t = 24$ h, condensed water has filled all pores smaller than 4 nm in size, for all of the carbons (Figure 5.3b), suggesting that these pores are very hydrophilic. The size of the water-filled pores at $t = 24$ h follows the trend of OMC-A \gg OMC-S $>$ OMC-A-HT $>$ OMC-S-HT. Thus, the relative hydrophilicity of the OMCs should follow the same trend, which is also in agreement with the CAK results (Figures 5.8 and 5.9).

According to the literature [207, 208], a ~ 2.2 nm graphitic cylindrical pore or carbon nanotube can easily take up water vapor at room conditions. This is consistent with our WVS results for both the as-synthesized and the heat-treated OMCs, as the < 4 nm diameter pores of all of the OMC samples investigated here were filled with water at $t = 24$ h, according to Figures 5.11a and 5.12b. However, it is not possible to determine the relative wettability of the small mesopores in the OMCs simply by relying on the WVS results in this work, largely because of the limited precision of this method.

After 24 h, compared to the rapid increase in the plot of OMC-A in Figure 5.12b, OMC-S shows behavior that is very similar to that of OMC-A-HT, suggesting that the surface of the larger OMC-S pores (> 10 nm, and including the outer surfaces of the particles) has a similar hydrophobicity as does heat-treated OMC-A. The difference between OMC-S and OMC-A-HT after 150 h in Figure 5.12b is due mainly to error in the WVS measurements. In other words, OMC-A definitely contains more hydrophilic pores that are larger than 10 nm in size, when compared to OMC-S. After ca. 50 h, water has condensed in all of the OMC-A pores < 100 nm in size (Figure 5.12b), showing that they are very hydrophilic.

After reaching a steady-state ($t > 100$ h, Figure 5.12b), only pores smaller than 10 nm in diameter in OMC-S-HT have been filled by condensed water. This suggests that the larger OMC-S-HT mesopores (> 10 nm) are more hydrophobic than those of OMC-A-HT. This, in turn, also confirms that the larger mesopores (> 10 nm) of OMC-S were originally different from those of OMC-A, as reflected by the lower water-filled pore sizes for OMC-S than OMC-A in Figure 5.12b. For OMC-S, the pores that are > 10 nm in diameter, including the textural pores, only contribute a small portion (15 %, Figure 5.3b) of the total N_2 sorption

determined pore volume (V_{NSI}). Since these larger pores cannot easily be wetted by water, the outer surface of the OMC-S particles must be hydrophobic (at least as hydrophobic as heat-treated OMC-A). Contrary to this, for OMC-A, pores larger than 10 nm in size contribute to ca. 50 % of its total volume (V_{NSI}), and these large pores have been shown above to be hydrophilic.

Collectively, it is clear that OMC-A has a very hydrophilic surface and that heat treatment makes this carbon surface more hydrophobic, as seen from both the WVS and CAK results. The WVS data ($t > 24$ h, Figure 5.12b) suggest that the surface of the large pores (> 10 nm) in the OMC-S particles, including their outer surfaces, are as hydrophobic as the surface of the larger pores (> 10 nm) in heat-treated OMC-A. This can explain the high contact angles ($> 90^\circ$) seen for water droplets in the first second after contacting the OMC-S pellet surface, as seen in Figures 5.8 and 5.9. However, the OMC-S pellet takes much less time to fully absorb the water droplet than does OMC-A-HT (Figure 5.8), suggesting that OMC-S has a very hydrophilic surface inside its 2-2.5 nm pores (Figure 5.3b). This is confirmed by the larger size of the water-filled pores of OMC-S vs. OMC-A-HT at $t = 24$ h in Figure 5.12b. Overall, the ~ 2.3 nm diameter pores of OMC-S are very hydrophilic, whereas the surface of the larger pores (width > 10 nm, including outer surface) is quite hydrophobic.

5.5 Electrochemical analysis of the wettability differences of OMC-S and OMC-A

Figure 5.13 shows the cyclic voltammetric (CV) response of the OMCs, before and after heat treatment. Similar to the CICs studied in Chapter 4, it is seen that both OMC-S and OMC-A show a pair of pseudo-capacitive peaks centered at ca. 0.55 V, suggesting the

presence of oxygen groups on the OMC surfaces [137], which would contribute to the hydrophilicity of the as-synthesized samples. After heat treatment, however, the pseudo-capacitive peaks of both OMCs disappeared, confirming the loss of surface oxygen groups from the OMCs at 1500 °C in a N₂ atmosphere (Table 5.1), consistent with the enhanced hydrophobicity of both OMCs after heat treatment. In turn, this also proves that the hydrophilicity of the OMCs is related to the presence of oxygen groups on their surfaces. In addition to the disappearance of the pseudo-capacitive peaks at ca. 0.55 V, heat treatment also decreased the double-layer capacitance (currents) of both OMCs over the full potential range, normally associated with a loss surface area. As the BET-determined surface area did not decrease significantly after heat-treatment (Table 5.2), the reason for this decrease in the CV currents is not yet understood.

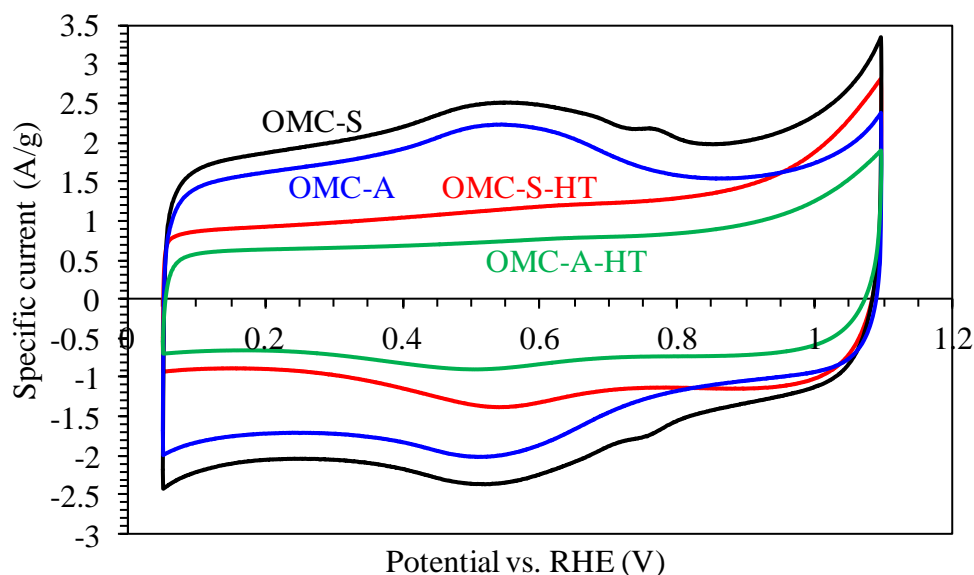


Figure 5.13. Cyclic voltammograms (CVs) of OMCs, before and after heat treatment, in N₂-saturated 0.5 M H₂SO₄ at a scan rate of 10 mV/s.

In our previous report [137], OMC-S was shown to have a gravimetric capacitance only 10 % higher than does OMC-A (156 F/g vs. 137 F/g), obtained from the CV of the corresponding carbon samples also in N₂-saturated 0.5 M H₂SO₄ at a scan rate of 10 mV/s , although OMC-S has a surface area 50 % higher than OMC-A (Table 5.2). This difference was attributed to the higher hydrophobicity of OMC-S than OMC-A, which resulted in a lower electrolyte-accessible surface area for OMC-S than OMC-A [137]. In the present work, an improved method was used for the preparation of the working electrode [137], involving the addition of sulfuric acid during ink preparation (Section 2.7). Compared to our previous work [137], both OMC-S and OMC-A exhibit a higher gravimetric capacitance (177 F/g and 145 F/g, respectively), which was also obtained from the CVs of the corresponding carbon samples (Figure 5.13). This suggests that the new method of ink preparation has improved the electrolyte accessibility to the hydrophobic pores in the OMCs.

However, OMC-S still exhibits a gravimetric capacitance only ~ 20 % higher than does OMC-A (177 F/g vs. 145 F/g), which is lower than the 50 % difference in surface area between these two carbons (Table 5.2). This may be attributed to the fact that the hydrophobic surface of OMC-S may show a different electrochemical response from that of the hydrophilic surface of OMC-A. After heat treatment, OMC-S has a gravimetric capacitance about 50 % higher than does OMC-A (103 F/g vs. 67 F/g, obtained from Figure 5.13), which is consistent with their ca. 50% difference in BET surface area (OMC-S-HT vs. OMC-A-HT, Table 6.1). This suggests that OMC-S-HT and OMC-A-HT may have a similar surface electrochemistry and also confirms that the new method of ink preparation has improved the electrolyte accessibility to the hydrophobic pores during the CV analysis.

5.6 Discussion of OMC-A and OMC-S wettability

In order to better understand the differences seen in the surface wettability of OMC-S and OMC-A (e.g., Figure 5.8), it is necessary to take into consideration their microstructure formation mechanisms. In Section 5.3, we explained the origin of the ~ 2.3 nm pores of both OMC-S and OMC-A and also the possible origin of the secondary mesopores (~ 10 nm, Figure 5.3b) found in OMC-A. All of these mesopores are equivalent to the gaps between the OMC nano-strings (Figures 5.5 and 5.6). Since the surfaces of the larger mesopores (> 10 nm) in OMC-A are very hydrophilic (Figure 5.12b), the 2.3 nm pore surfaces of OMC-A must also be very hydrophilic. Similarly, as discussed above, the 2.3 nm pore surfaces of OMC-S are also hydrophilic.

This very hydrophilic character of the OMC-S and OMC-A nano-strings may be attributable to the presence of some silica residue on the nano-string surfaces [199], or possibly due to retained oxygen groups. The carbon surfaces that were in direct contact with SiO_2 during the polymerization/carbonization stage of OMC synthesis may have formed a C-O-Si bond. After the removal of the silica with aqueous NaOH, some C-OH groups may have been left on the carbon surfaces, providing the observed hydrophilicity (Figure 5.12b) and the electrochemical pseudo-capacitive peaks (Figure 5.13). Further studies related to understanding this mechanism are still underway.

As discussed in Section 5.3, during OMC-A synthesis, anthracene was polymerized and formed pitch, catalyzed by H_2SO_4 at 160°C in air. Similar to the mesophase pitch (MP) imprinting of colloidal silica during CIC synthesis (Chapter 4), the anthracene-derived pitch is expected to infiltrate the HMS pores at elevated temperatures and will then be carbonized at temperatures up to 900°C in a N_2 atmosphere. Therefore, after the removal of silica, the

resultant OMC-A should contain open pores and show high hydrophilicity, as do the CICs. Figure 5.7 showed a possible model for the formation of OMC-A. However, it should be noted that the formation mechanism of OMC-A is still not fully understood due to the complexity of anthracene pyrolysis, and more research needs to be undertaken to elucidate this process more fully. OMC-A should be composed mainly of carbon nano-strings, as shown in the accepted OMC formation model in Figure 5.1, but it also contains some larger mesopores due to the incomplete infiltration of the HMS pores, as explained in Section 5.3. Figure 5.14a shows a schematic of the possible cross-sectional structure of OMC-A, modified from that in Figure 5.7.

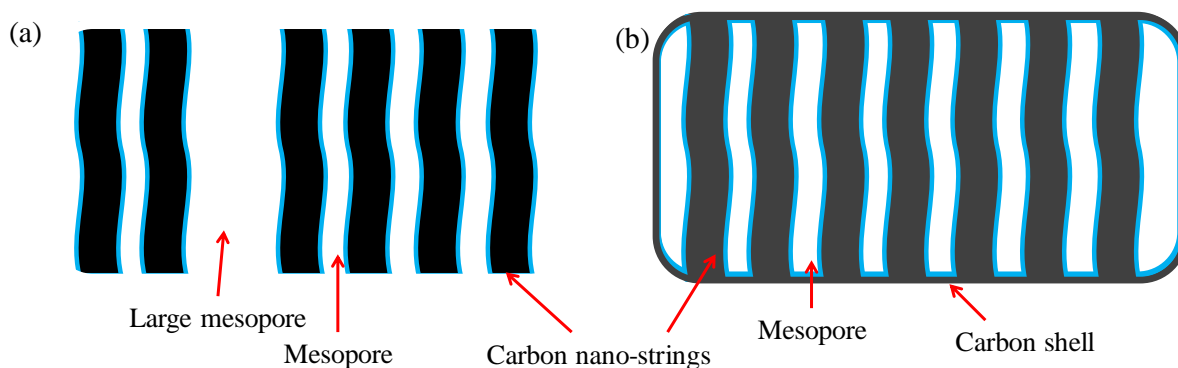


Figure 5.14. Cartoon of the cross-sectional microstructure of (a) OMC-A and (b) OMC-S. The curved black bands represent the OMC nano-strings, and the black rectangle in (b) represent a layer of carbon (or a carbon shell) surrounding the OMC-S nano-strings. The blue layers represent polar or hydrophilic carbon surfaces. Both the carbon shells and the OMC-S nano-strings contain more micropores than do the OMC-A nano-strings (Table 5.2). The large mesopore in OMC-A (a) corresponds to the 6.8 nm pore shown schematically in Figure 5.6b.

According to Figure 5.1, the OMC-S particles are also composed of carbon nano-strings, but should contain fewer large mesopores than OMC-A, as explained in Section 5.3. As concluded above, these carbon nano-strings are hydrophilic, so OMC-S should be as

hydrophilic as OMC-A. However, it was shown that the larger pores (including the textural pores) and the outer surface of the OMC-S particles are hydrophobic, similar to heat-treated OMC-A.

To explain this, we propose that the OMC-S particles may have a very thin layer of carbon covering the hydrophilic nano-strings, perhaps in the form of a thin shell (Figure 5.14b). The carbon shell is suggested to have a relatively hydrophobic outer surface, thus resulting in the more hydrophobic nature of OMC-S than OMC-A, as seen in the CAK and WVS results (Figures 5.8 and 5.12b).

Here, we attribute the possible formation of the thin carbon layers/shells surrounding the OMC-S nano-strings to the high polarity of sucrose combined with the high viscosity of the concentrated sucrose/H₂SO₄ solution. A cartoon showing this model of formation for the OMC-S is shown in Figure 5.15. During OMC-S synthesis, the mixture of sucrose and H₂SO₄ not only fills the mesopores of the HMS template, but also covers the external surface of the HMS particles. After sucrose polymerization (including cross-linking and stabilization at low temperatures, such as 160 °C, in air) and carbonization, and then the removal of the silica, the outer layer of sucrose forms a porous carbon shell, connected to the carbon nano-strings (Figure 5.14b). The outer surface of the carbon shells would have been exposed to the inert atmosphere (N₂) during the carbonization process at 900 °C, which is sufficient to remove any polar groups that were present, thereby making it hydrophobic.

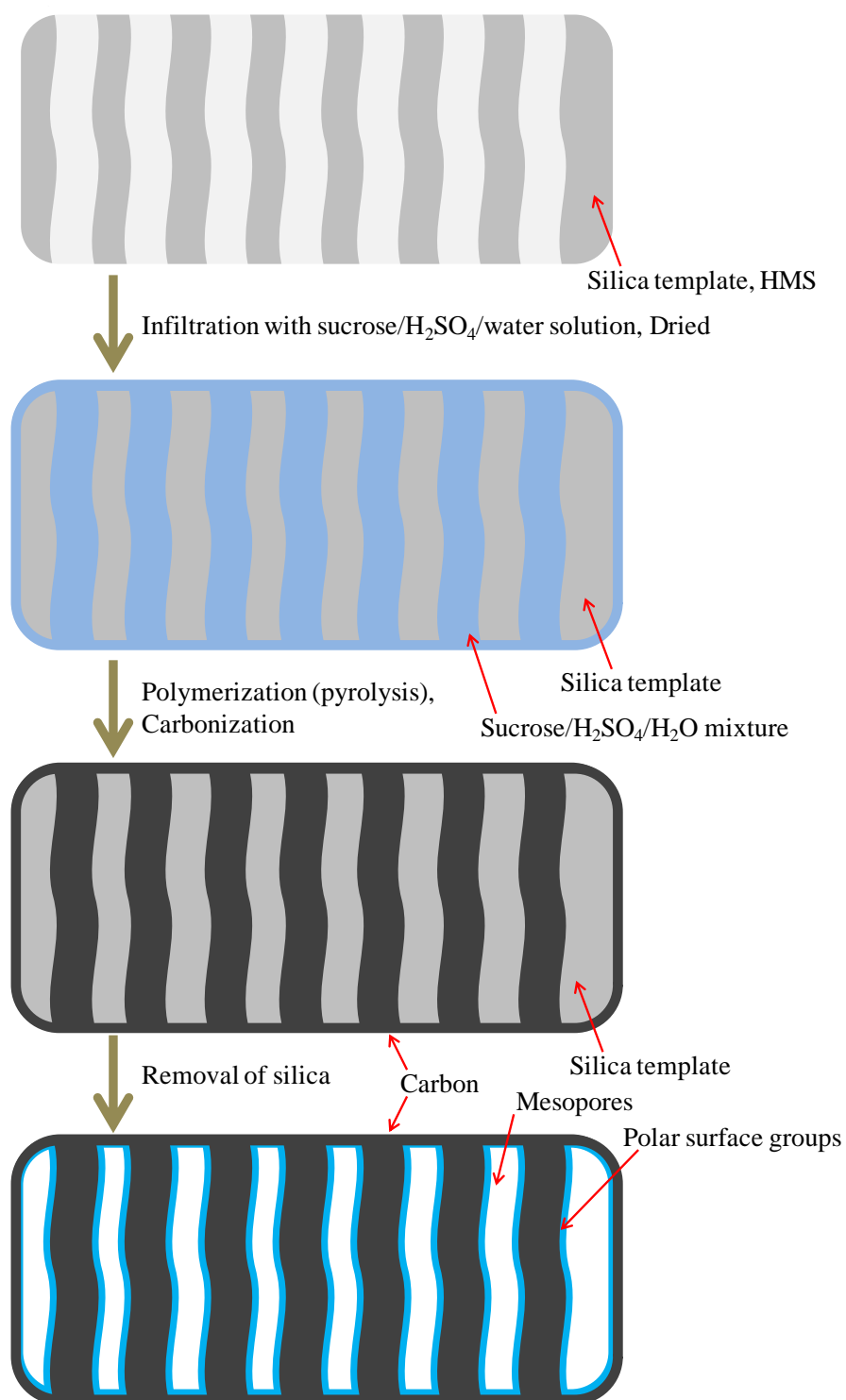


Figure 5.15. Cartoon showing a possible mechanism of the development of the microstructure of sucrose-based ordered mesoporous carbon (OMC-S).

Similar to the carbon nano-strings, the inner surface of the carbon shells surrounding the OMC-S particles, which was in direct contact with the outer surface of the silica particles, is also expected to be very hydrophilic/polar (Figure 5.14b). As mentioned above, heat-treatment at 900 °C removes the polar groups of the outer surface of the sucrose-derived carbon shell, leaving its outer surface with a lower coverage of the oxygen groups than the carbon nano-strings. This may be the reason why OMC-S has a lower oxygen content than OMC-A (Table 5.1).

It should be noted that the carbon shell may not coat the OMC particles completely, due to incomplete coverage of the HMS particles by sucrose, surface cracking during polymerization and carbonization, or due to the fragmentation of the OMC-S particles. It should also be noted that we have not been able to obtain any direct evidence for the presence of the carbon shell on the surface of the OMC-S particles by scanning electron microscopy (SEM, Figure 5.2) or, in previous work, by transmission electron microscopy (TEM) analysis [49]. However, high-resolution TEM (HR-TEM) did show what seems to be a carbon shell on OMC particles that were synthesized using chemical vapor deposition (CVD) by Su, et al. [209]. In contrast, Ryoo, et al. synthesized an OMC (CMK-1) using sucrose as the carbon precursor, but using mesoporous silica molecular sieves (MCM-48) as the hard template, and a carbon film on the OMC particle surface was not seen [210]. Vinu, et al., however, synthesized OMC samples (CMK-3, with SBA-15 as the template) with a range of sucrose and silica template mass ratios, and they observed (via SEM and HR-TEM) that some extra carbon (disordered particle clusters) was present on the external surface of the OMC particles when a high sucrose/silica mass ratio (5:1) was used [211]. However, they did not claim that this additional carbon was present in the form of a shell structure

encompassing the OMC particles. As such, further work should be conducted in order to seek evidence for a layer of carbon covering the OMC-S nano-strings.

As reported previously [49], we also prepared another OMC using the same method as used for OMC-A, but using naphthalene (N) as the aromatic precursor, forming OMC-N. We did not include the OMC-N results here, as almost all of the same physical and chemical properties of OMC-A were seen with OMC-N, especially the high hydrophilicity. OMC-N must therefore have been formed by the same mechanism as OMC-A (e.g., Figure 5.7) and must also possess a similar microstructure.

The difference in the microstructures of the sucrose- and anthracene-based OMCs should result in different effects on mass transport when used as a cathode support material in PEM fuel cells. Specifically, the presence of larger mesopores in OMC-A (Figures 5.2 and 5.3b, Table 5.2) should facilitate mass transport. This may be one of the reasons why Pt-loaded OMC-A (Pt/OMC-A) exhibited a higher current density for the oxygen reduction reaction (ORR) than Pt-loaded OMC-S (Pt/OMC-S), when they both had the same Pt loading and a similar Pt nanoparticles size and were tested under the same conditions [49]. If present on the surface of the OMC-S particles, the carbon shells, as proposed above (Figure 5.14b), may serve as a barrier for the transport of oxygen molecules and protons to the Pt nanoparticles that are inside the pores, resulting in a lower reaction rate than at Pt/OMC-A.

Ambrosio, et al. synthesized an OMC (CMK3) using sucrose as the carbon precursor and SBA-15 as the template, subsequently loading it with Pt nanoparticles and using it in the cathode catalyst layer of a PEMFC. The authors found that the catalyst exhibited a poorer performance than carbon black (Vulcan carbon and E-Tek) supported Pt catalysts [212, 213], as the sucrose-based OMC support caused a resistance loss and mass loss at high current

density. This may have been caused by the presence of a carbon shell on the surface of the sucrose-based OMC particles, or to the higher electronic resistance of sucrose-derived carbon nano-strings, as suggested earlier [49].

As discussed in Chapter 1, it was found that the high surface area of OMCs enhances the dispersion of Pt nanoparticles [49] for use in PEMFCs. The high polarity (or hydrophilicity) of the OMCs, found in this work, should also help to disperse/stabilize the Pt nanoparticles, whereas the high hydrophilicity of the OMCs could cause flooding problems in the catalyst layer, resulting in poorer PEMFC performance, such as seen in the literature [212, 213]. Heat treatment increases the hydrophobicity of the OMCs, but the mesopores that are < 4 nm in size still can take up water easily at high relative humidity (Figure 5.12b). For this reason, a low relative humidity would be required in a PEMFC if OMC-HT samples were used as the catalyst support in cathode layers. Even so, the OMCs may have advantageous properties in other applications, such as super-capacitors, adsorbents, and so on.

5.7 Summary

With hexagonal mesoporous silica (HMS) as the hard template, sucrose (S) and anthracene (A) were used as carbon precursors to synthesize ordered mesoporous carbons (OMCs), named OMC-S and OMC-A, respectively. The OMC synthesis followed the typical method reported in the literature, where sulfuric acid was used as the catalyst for the polymerization of the carbon precursors. Both of the as-synthesized OMCs were heat treated at 1500°C in a N_2 atmosphere in order to enhance their degree of carbonization. Elemental analysis

confirmed this expectation and also showed that OMC-A has a higher oxygen content than OMC-S.

Scanning electron microscopy (SEM) images and nitrogen sorption isotherms (NSI) of the OMCs, before and after heat treatment, were collected and analyzed, showing that both of the OMCs contain primary mesopores 2-3 nm in diameter, but that OMC-A contains more larger mesopores (5~50 nm) than OMC-S. This was attributed to the low solubility of anthracene in H_2SO_4 and the high affinity of HMS to H_2SO_4 , resulting in the inhomogeneous infiltration of the anthracene (or anthracene-derived pitch) and H_2SO_4 mixture into the HMS pores, thus producing larger mesopores in OMC-A.

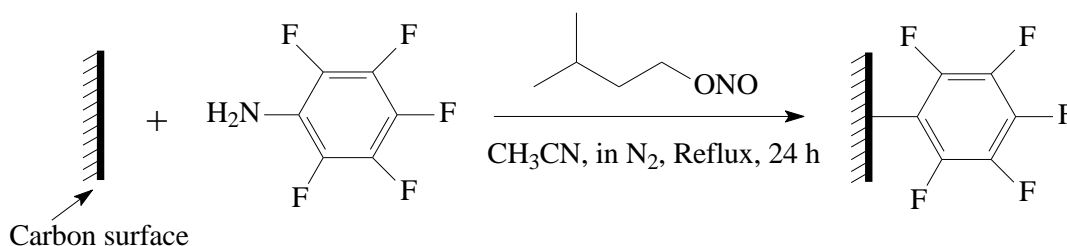
Both contact angle kinetics (CAK) and water vapor sorption (WVS) methods were employed to study the wettability of the carbon samples, showing that OMC-S is less hydrophilic than OMC-A and that heat treatment made both OMCs more hydrophobic. Heat treated OMC-S is more hydrophobic than heat-treated OMC-A, while the outer surface of OMC-S is as hydrophobic as heat-treated OMC-A, although the internal pores of OMC-S are very hydrophilic. These wettability differences were attributed to the possible presence of a thin carbon shell on the OMC-S particle surface, formed during synthesis. The formation of the carbon shells on the OMC-S surface may be attributed to the high affinity of silica to sucrose, which would coat the outer surface of the HMS particles, producing a carbon shell after carbonization. These microstructural differences, arising from the use of different carbon precursors, may also be present in other porous carbons, synthesized using a hard templating method.

Chapter Six: Wettability of High Surface Area Carbon Powders after Surface-Modification with Pentafluorophenyl Groups

This work is not published yet.

6.1 Introduction

In the discussion in Chapter 4, it was shown that colloid-imprinted carbons (CICs) have a much more hydrophilic surface than does commercial carbon black, e.g., Vulcan carbon (VC). It is thus anticipated to be challenging to use CICs in their as-synthesized state as catalyst supports in PEMFCs, because the hydrophilic CIC surface could potentially cause flooding problems [8, 32, 77], especially in the cathode catalyst layer where water is generated during the oxygen reduction reaction (ORR, Reaction 1.2). In addition to the thermal treatment method presented in Chapter 4, this chapter will demonstrate a second approach to increase the hydrophobicity of carbon surfaces. This can be realized by attaching pentafluorophenyl (-PhF₅) groups to the carbon surfaces via the *in-situ* diazonium reduction reaction (Scheme 6.1), as reported in the literature for the functionalization of other carbon surfaces [74, 214]. This surface modification is also expected to increase the resistance of the carbons to electrochemical corrosion when used as catalyst supports in PEMFCs because of the enhancement in surface hydrophobicity [63], due to the high electronegativity and low polarizability of fluorine [215].



Scheme 6.1. Functionalization of carbon surfaces with pentafluorophenyl (-PhF₅) groups.

Since Chapter 4 has shown that CICs with different pore sizes have very similar surface properties (polarity and thus wettability), this chapter is focused only on CIC-22 (22 nm is the size of colloidal silica used in the imprinting stage (Section 2.1.1)) as a typical example. VC was used as the reference material, as it has a significantly less polar surface than the CICs (Chapter 4). It should also be noted that the CIC-22 material investigated in this chapter was from a different batch than studied in Chapter 4, and thus slightly different values were obtained for some of its properties, e.g., the specific surface area.

Although the high surface area ordered mesoporous carbons (OMCs), discussed in Chapter 5, can also be used as catalyst supports in PEMFCs, their hydrophilic mesopores are already too small (2-3 nm) to accommodate both catalytic Pt nanoparticles (2-5 nm) and the Nafion clusters (1-3 nm) needed for proton conductivity. Surface functionalization of the OMC pores, if even achievable, will further decrease the pore size, and thus further inhibit the mass transport of H^+ , H_2O , H_2 or O_2 through the pores, resulting in a PEMFC with low performance. Therefore, surface modification of OMCs with fluorine groups was not carried out in this project, and only CIC-22 and VC were surface modified here.

6.2 Porous structure of carbons before and after surface functionalization

The N_2 adsorption/desorption isotherms of VC and CIC-22, before and after surface functionalization, were obtained in order to track any change in their porous structure due to surface modification (Figure 6.1). After surface modification, the amount of adsorbed N_2 on VC decreased, as seen over a wide range of partial pressures ($P/P_o < 0.9$), while CIC-22 does not exhibit any significant decrease in the amount of adsorbed N_2 at $P/P_o < 0.8$. This suggests

that $-\text{PhF}_5$ functionalization results in a significant decrease in the surface area of VC, but not CIC-22. However, the adsorption-desorption hysteresis seen at CIC-22, at P/P_0 around 0.8, did shift to lower pressures after surface functionalization, suggesting a slight shrinkage in the average pore size of CIC-22.

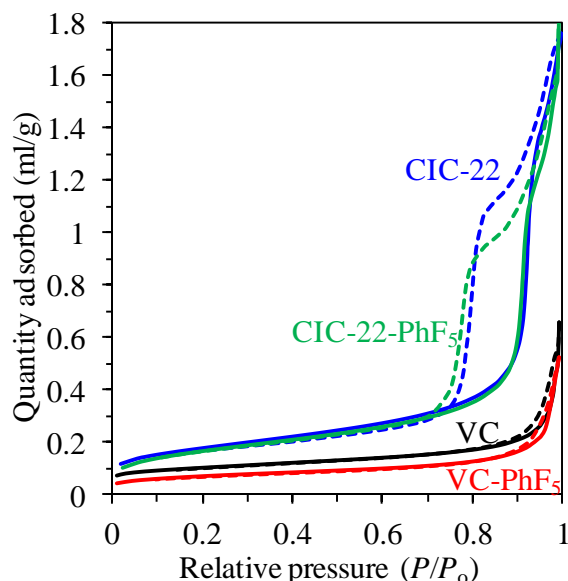


Figure 6.1. N_2 adsorption (solid line) and desorption (dashed line) isotherms for VC and CIC-22, before and after surface functionalization with pentafluorophenyl ($-\text{PhF}_5$) groups using the diazonium reduction reaction (Scheme 6.1).

In order to obtain the pore sizes of these carbons, the Barrett-Joyner-Halenda (BJH) method was applied to analyze both the N_2 adsorption and desorption branches of the isotherms of the carbons, with the results shown in Figure 6.2. As explained in Chapter 4, the pore size derived from the adsorption branch of the CIC isotherms (Figure 6.2a) reflects the diameter of the spherical pores, which is directly related to the diameter of the colloidal imprinting particles, while that obtained from the desorption branch (Figure 6.2b) reflects the size of the necks (or connecting pores) between adjacent spherical pores.

Figures 6.2a and 6.2b show that surface functionalization decreased the average pore size of CIC-22 by ca. 3 nm (Table 6.1), while it decreased the size of the CIC-22 pore necks by 1 nm, from 10 to 9 nm. Surface functionalization also narrowed the pore size distribution of CIC-22, as seen in both figures. These changes confirm the successful attachment of the -PhF₅ groups, which have a diameter of ca. 0.7 nm (similar to hexafluorobenzene, C₆F₆ [216]), onto the inner surface of the CIC pores. The majority of the VC pores are < 2 nm in diameter (micropores). However, Figure 6.2a show that a broad distribution of pores larger than 2 nm in size are present in VC, arising from textural porosity between VC particles. Figure 6.2a also shows that VC, after functionalization, has fewer pores that are < 15 nm in size but more that are > 20 nm in size than VC before functionalization.

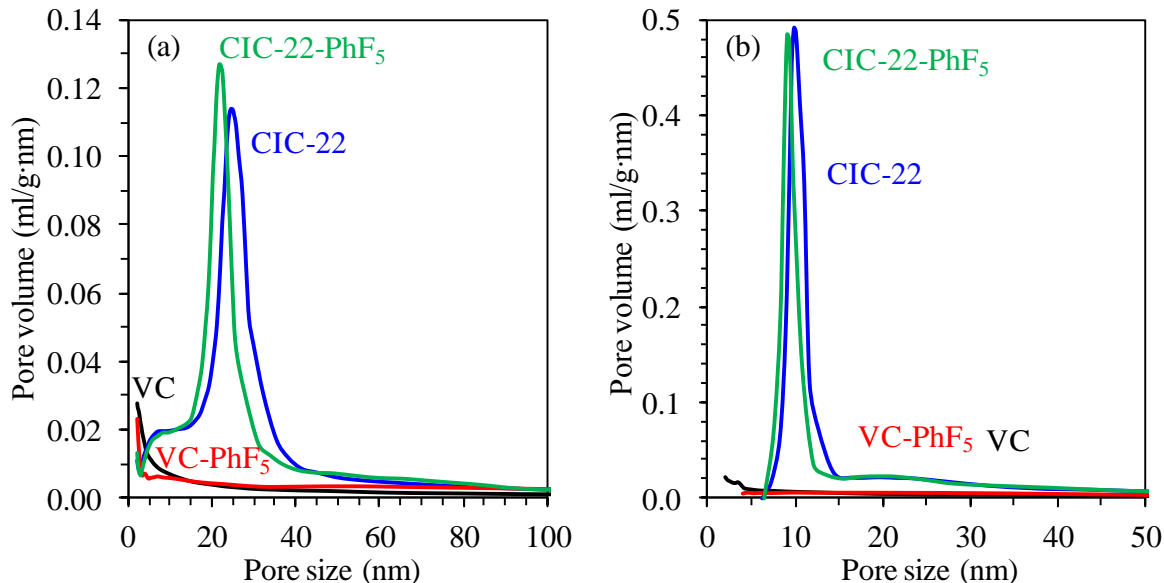


Figure 6.2. Pore size distribution of carbons before and after surface functionalization, calculated from the (a) adsorption and (b) desorption branches of the N₂ sorption isotherms (Figure 6.1) using the Barrett-Joyner-Halenda (BJH) method, with the *t*-curve of carbon black used as the standard to determine the statistical thickness of the adsorbed nitrogen film [172].

Theoretically, if the pore surface of CIC-22 is completely covered by one monolayer of the functional groups, the pore diameter and the pore neck width of CIC-22 should both decrease by 1.4 nm. Since it is unlikely that a second -PhF₅ group can be bonded to an already attached -PhF₅ group (forming more than one monolayer of attached -PhF₅) because of the high electronegativity of fluorine, the larger decrease in pore diameter (3 nm vs. 1.4 nm) obtained from the BJH fitting (Figure 6.2a, Table 6.1) is attributed to the limited precision of the testing system of nitrogen sorption isotherms (NSI) at high partial pressures ($P/P_0 \sim 0.92$ for 25 nm pores vs. ~ 0.91 for 22 nm pores, Figure 6.1). Even so, the 1 nm decrease in the CIC-22 pore neck width ($P/P_0 \sim 0.79$ for 10 nm pores vs. ~ 0.77 for 9 nm pores, seen from the desorption branches in Figure 6.1) is more realistic than the 3 nm decrease in pore size obtained from the adsorption branch for the two samples.

As discussed in Chapter 4, VC is composed of ~ 30 nm particles (Figure 4.2a) containing only micropores (< 2 nm in diameter) [217]. As seen in Figure 4.2a, the VC particles are connected together to form agglomerates or aggregates, with a wide range of mesopores (textural pores, 2-50 nm) present between the VC particles [217]. In Figure 6.2a, it is shown that surface functionalization has led to a decrease in the total volume of VC pores that are smaller than 15 nm in diameter, and that VC-PhF₅ has more pores that are > 20 nm than does VC, suggesting that the functionalization chemistry is affecting primarily inter-particle VC properties. Similar phenomena have also been observed when VC was surface modified with other functional groups [218]. This may be caused by the aggregation of VC particles/agglomerates during the surface functionalization process [219], decreasing the number of pores smaller than 15 nm and forming more textural mesopores (> 20 nm) between the particles [217], as seen in Figure 6.2a.

For better comparison, the properties of the carbons, with and without surface functionalization, are shown in Table 6.1. Similar to Chapter 4, the t -plot method was used to determine the external surface area (S_{external}) and total micropore volume (V_{micro}) of these carbons, and thus their micropore surface area (S_{micro}) was obtained by subtracting S_{external} from the total surface area (S_{BET}). The total pore volume (V_{NSI} , Table 6.1) was obtained from the nitrogen sorption isotherms (NSI) at a partial pressure of 0.98, which is the total volume of the pores that are < 100 nm in size, as explained in Chapter 4.

Table 6.1 Structural properties of VC and CIC-22 before and after surface functionalization ^a

Sample ^b	Pore size (nm) ^c	S_{BET} (m ² /g) ^d	S_{external} (m ² /g) ^e	S_{micro} (m ² /g) ^f	$S_{\text{micro}}/S_{\text{BET}}$ (%)	V_{NSI} (mL/g) ^g	V_{micro} (mL/g) ^e	$V_{\text{micro}}/V_{\text{NSI}}$ (%)
VC	< 2	220	130	90	40	0.38	0.05	12.0
VC-PhF ₅	< 2	160	100	60	40	0.41	0.03	6.7
CIC-22	25	400	320	80	20	1.6	0.04	2.4
CIC-22-PhF ₅	22	390	310	80	20	1.5	0.04	2.3

^a Surface modified with pentafluorophenyl (-PhF₅) groups.

^b The “22” in the sample names is the particle size (in nanometers) of the colloidal silica template used in the colloid-imprinted carbon (CIC) synthesis.

^c Pore size obtained from the maximum in the pore size distribution plots in Figure 6.1a.

^d S_{BET} = total surface area, obtained using the Brunauer-Emmett-Teller (BET) plot in the partial pressure range of $0.05 < P/P_o < 0.30$.

^e S_{external} = external surface area and V_{micro} = micropore volume, both obtained using the t -plot method in the partial pressure range of $0.2 < P/P_o < 0.5$, with carbon black used as the reference material [172].

^f S_{micro} = micropore surface area, obtained by subtracting the external surface area (S_{external}) from the total surface area (S_{BET}).

^g V_{NSI} = pore volume, acquired from the N₂ sorption isotherms (NSI) at $P/P_o = 0.98$ (Figure 6.1).

Table 6.1 confirms that surface functionalization results in a significant decrease in the total surface area (S_{BET}) of VC and only a small increase in its total pore volume (V_{NSI}). As discussed above, the decrease in surface area may be attributed to the blockage of the

entrance of many of the VC micropores (< 2 nm) [218] by the $-\text{PhF}_5$ groups (~ 0.7 nm) and may also be due to some aggregation of the VC nanoparticles/agglomerates. This would result in a net decrease in both the micropore surface area (S_{micro}) and external surface area (S_{external}). As the same time, the aggregation of VC particles/agglomerates may result in the formation of new textural mesopores, as mentioned above, resulting in an overall only minor change in the VC pore volume (V_{NSI}) (0.41 mL/g vs. 0.38 mL/g, Table 6.1) and thus a significant decrease in $V_{\text{micro}}/V_{\text{NSI}}$ for VC (6.7 % vs. 12.0%, Table 6.1), after functionalization.

Compared to VC, the surface functionalization of CIC-22 with $-\text{PhF}_5$ groups has led to only a minor decrease in total surface area and pore volume. This is likely due to the larger pore size of CIC-22 as well as its more robust pore walls than VC, as concluded in Chapter 4, which prevent the collapse of the internal pores of CIC-22 during the functionalization process. The PhF_5 groups are too small in size to block the large CIC-22 pores in any way, leaving the mesopore surfaces fully accessible to the adsorbate (N_2) and having little effect on the mass transport of N_2 through the pores. The average size of the CIC-22 particles is about 10 μm (Chapter 4), so the outer surface of the particles contributes little to their total surface area, when compared to the large number of ca. 25 nm pores (Table 6.1) inside the CIC particles. Therefore, any aggregation of the CIC-22 particles will not significantly affect their total surface area (S_{BET} , Table 6.1). These are the main reasons why surface modification has much less influence on the surface area of CIC-22 than VC.

It is interesting to note that the attachment of $-\text{PhF}_5$ groups to the surfaces of both VC and CIC-22 did not significantly change the percentage of micropore surface area for either of the two carbons ($S_{\text{micro}}/S_{\text{BET}}$, Table 6.1), suggesting that surface modification does not

significantly change the internal atomic structure of the VC or CIC-22 pore walls, in contrast to what was seen after heat-treatment (Chapter 4). This is also reflected by the only small change in volume percentage of micropores in CIC-22 after functionalization ($V_{\text{micro}}/V_{\text{NSI}}$, Table 6.1). In comparison, heat treatment at 1500 °C in a N₂ atmosphere can significantly decrease both the $S_{\text{micro}}/S_{\text{BET}}$ and $V_{\text{micro}}/V_{\text{NSI}}$ ratios of VC and the CICs (Table 4.2), as discussed in Chapter 4.

6.3 Elemental composition of carbons before and after surface functionalization

The elemental composition of the synthesized colloid-imprinted carbon (CIC-22) and Vulcan carbon (VC), before and after functionalization with the -PhF₅ groups, was evaluated to determine the concentration of fluorine groups grafted onto the carbon surfaces, with the results shown in Table 6.2. As expected, the introduction of fluorine resulted in a decrease in the carbon content, with more functional groups apparently on the CIC-22 vs. VC surface, perhaps because of the higher CIC-22 surface area.

The functional group surface coverage of these carbons in Table 6.2 was then estimated by normalizing the number of moles of bonded -PhF₅ to the external surface area of the pre-functionalized carbons (S_{external}), excluding the micropores (Table 6.1). This calculation was based on the assumption that the -PhF₅ groups will not form in the micropores, but are covalently bonded to the surface of all other pores that are > 2 nm in size, due to steric hindrances. This assumption is reasonable, since the conditions of the surface functionalization reaction (Scheme 6.1) are quite moderate so that it is difficult to break the C-F bond of the pentafluoroaniline (F₅Ph-NH₂) molecule, and also because the samples had been thoroughly washed to remove any residue or by-products. Due to the steric effect, it is

difficult for the $-\text{PhF}_5$ groups to attach to micropore surfaces, and thus only the external surface area was used for the coverage calculation.

Table 6.2 Element content (wt. %) of VC and CIC-22 before and after functionalization ^a

Sample	C (%) ^b	H (%) ^b	N (%) ^b	F (%) ^c	Solid residue (%) ^d	O (%) ^e	Coverage of $-\text{PhF}_5$ groups ($\mu\text{mol}/\text{m}^2$) ^f
VC	98.4	0.8	0.1	-	-	0.7 ± 0.5	
VC- PhF_5	92.4	1.0	0.8	3.7	-	2.1 ± 0.6	3.2
CIC-22	93.0	1.0	0.0	-	1.8	4.1 ± 2.1	
CIC-22- PhF_5	85.3	1.1	1.0	7.6	1.2	3.7 ± 2.1	2.9

^a Carbon samples were surface-functionalized with pentafluorophenyl ($-\text{PhF}_5$) groups.

^b The carbon, hydrogen and nitrogen contents were obtained by combustion analysis, with an error of ca. ± 0.3 % for each element.

^c The fluorine content was determined using potentiometric titration with $\text{La}(\text{NO}_3)_3$, with an error of ca. ± 0.3 %.

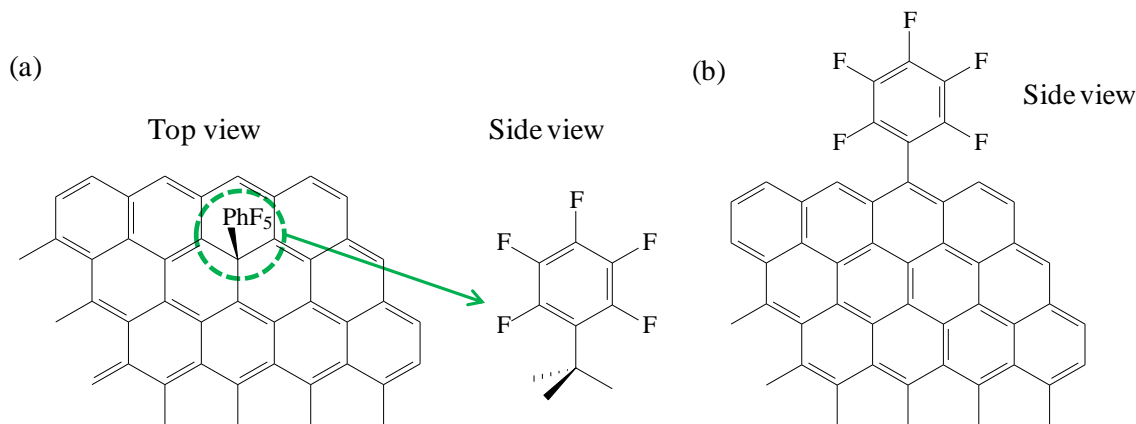
^d The solid residues in the CICs were obtained via thermogravimetric analysis (TGA) in air, with an estimated error of ± 2.0 %.

^e Obtained assuming that $\text{O}\% = 100\% - (\text{C}\% + \text{H}\% + \text{N}\% + \text{F}\% + \text{solid residue } \%)$.

^f The coverage of $-\text{PhF}_5$ groups on the functionalized carbon surfaces was obtained by normalizing the fluorine content to the external surface area (S_{external} , Table 6.1) of the corresponding carbon before functionalization, assuming that $-\text{PhF}_5$ groups were only grafted onto the surface of pores that are > 2 nm in diameter.

Table 6.2 shows that both VC- PhF_5 and CIC-22- PhF_5 have a similar surface coverage of the $-\text{PhF}_5$ functional groups, 3.2 and $2.9 \mu\text{mol}/\text{m}^2$, respectively. This similarity is indirect evidence that the analysis is being done correctly, since both carbons were functionalized under the same conditions. If the $-\text{PhF}_5$ group covalently bonds to a carbon surface via a C-C single bond (e.g., Scheme 6.2), the groups should be oriented perpendicularly to the carbon surface and thus will turn freely along the axis of the single bond. Assuming that a freely-rotating $-\text{PhF}_5$ group takes up a surface area of ca. 50 \AA^2 , the same as the cross-sectional area of flat-oriented hexafluorobenzene (C_6F_6) [216], the maximum coverage (one monolayer) of

the -PhF_5 groups on a carbon surface would be $3.4 \mu\text{mol/m}^2$. If the -PhF_5 groups are oriented perpendicularly to the carbon surface and are closely packed, the maximum coverage is about $10 \mu\text{mol/m}^2$, assuming that the cross-sectional area of a -PhF_5 group is the same as that of a C_6F_6 molecule (16 \AA^2) [216]. However, due to electronic and steric effects (e.g., in the case of Scheme 6.2b) of the functionalization reactions, the latter alignment is unlikely. Therefore, the observed coverage of $\sim 3 \mu\text{mol/m}^2$ of VC- PhF_5 and CIC-22- PhF_5 (Table 6.2) suggests that the -PhF_5 groups cover about ca. 90% of the external surface of the accessible carbon surface, which is very reasonable.



Scheme 6.2. Suggested C-C single bonds between -PhF_5 groups and carbon surfaces: (a) a planar graphene surface and (b) a surface composed of graphene edges (top side).

In Table 6.2, it is also seen that surface functionalization leads to a significant increase in the nitrogen content for both VC and CIC-22, and an increase in the oxygen content of VC. The N atoms in the surface-modified carbons may be present in the form of pentafluorophenyl-azo ($\text{PhF}_5\text{-N=N-}$) groups [218], covalently bonded to the carbon surfaces, since $\text{PhF}_5\text{-N=N-O-C}_5\text{H}_9$ and $\text{PhF}_5\text{-N}\equiv\text{N}^+$ are the important intermediates during the

functionalization reaction [220, 221]. The N atoms can also be present in other chemical forms, some of which may contain oxygen, as will be addressed in the following sections.

6.4 Wettability of carbons before and after surface functionalization

It was shown above that surface functionalization using $-\text{PhF}_5$ groups changed some of the characteristics of both VC and CIC-22 (Table 6.1), as well as their elemental composition (Table 6.2). As was done for the heat-treated CICs and OMCs in Chapters 4 and 5, both contact angle kinetics (CAK) and water vapor sorption (WVS) methods were used here to confirm the anticipated increased hydrophobicity of the carbons after surface functionalization, and to better understand the surface chemistry of the carbons after modification.

6.4.1 Contact angle kinetics (CAK) study

Figure 6.3 shows both the sequential images of water droplet kinetics on various carbon pellets and the time when the water droplet was fully taken up by the pellet, while Figure 6.4 shows the contact angle kinetics of the water droplets in the first 200 ms of contact with the carbon pellets. As shown in Chapter 4, water droplets have a higher contact angle on CIC-22 than on VC at short times ($t < 200$ ms, Figures 6.3 and 6.4), but water is fully absorbed in a much shorter time by the CIC pellet than the VC pellet (0.8 vs. 10.7 s, Figure 6.3). As explained in Chapter 4, the higher initial contact angles seen on as-synthesized CIC-22 are attributed mainly to its larger particle size (rougher pellet surface), while its shorter water-uptake time is due to its very hydrophilic mesopore surfaces when compared to VC. Any differences seen between Figure 4.6 and Figure 6.3 in terms of contact

angles (vs. time) of VC and CIC-22 are attributed to small variances in the experimental conditions, such as room temperature and sample batch.


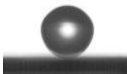
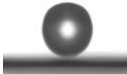
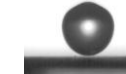

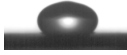
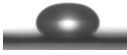






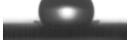














Time (ms)	VC	CIC-22	VC-PhF ₅	CIC-22-PhF ₅
0				
8				
25				
50				
100				
200				
1000				
Time to 100% dryness	10.7 s	0.8 s	> 10 min	> 10 min

Figure 6.3. Sequential images of water droplets deposited on carbon pellets before and after surface functionalization with pentafluorophenyl groups. The time to 100% dryness (last row) refers to the time that it takes for the pellet to fully absorb the water droplet deposited on it.

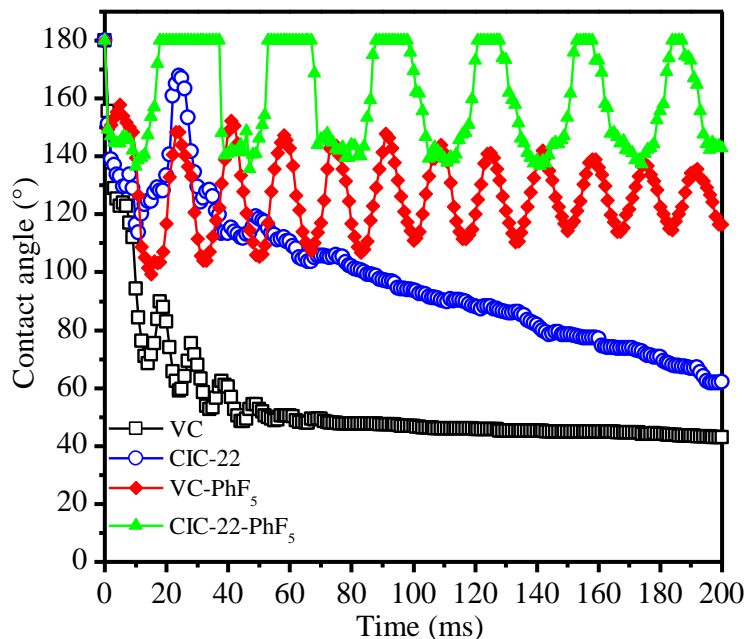


Figure 6.4. Contact angle kinetics (CAK) of water droplets after deposition onto carbon pellets before and after surface modification with $-\text{PhF}_5$ groups. A contact angle of 180° indicates that the water droplet has fully rebounded from the sample surface (e.g., as on CIC-22- PhF_5 at $t = 25$ ms in Figure 6.3).

Compared to VC, a water droplet deposited on a VC- PhF_5 pellet shows much higher contact angles at all times (Figure 6.4) and exhibits a static contact angle of ca. 120° on VC- PhF_5 ($t = 1$ s, Figure 6.3), suggesting significantly enhanced hydrophobicity. A high static contact angle of water has also been reported for other fluorinated carbon powders [73, 222]. The long time to 100% dryness (> 10 min) indicates that the water droplet cannot be absorbed by the VC- PhF_5 pellet, and thus it finally evaporates, which also reflects the high hydrophobicity of the VC- PhF_5 surface. It should be noted that the high contact angle of water on VC- PhF_5 , shown in Figures 6.3 and 6.4, is not only due to the hydrophobic carbon surface, but also to the roughness of the pellets, as explained in Chapter 4. However, compared to heat-treated VC (Figures 4.4 and 4.5), VC- PhF_5 exhibits a much higher contact

angle, which suggests that surface modification with -PhF_5 groups makes VC even more hydrophobic, as expected.

In terms of CIC-22, it is seen to be much more hydrophobic after functionalization than before, as shown by the high contact angle of water on the CIC-22- PhF_5 pellet and the long time to 100% dryness (Figures 6.3 and 6.4). A water droplet deposited on the CIC-22- PhF_5 pellet surface even rebounds from the surface, reflecting superhydrophobicity of the surface, a combined resultant phenomenon of intrinsic surface hydrophobicity and surface roughness, as explained in Chapter 3. As compared to heat-treated CIC-22 (Figures 4.6 and 4.7), CIC-22- PhF_5 exhibits a higher contact angle, which suggests that surface modification with -PhF_5 groups also makes this carbon even more hydrophobic.

Similar to the heat-treated carbons in Chapter 4, the significant difference in the dynamic/static contact angle of water on VC- PhF_5 and CIC-22- PhF_5 should be due primarily to their different particle sizes (~ 30 nm vs. ~ 10 μm). Here, it is believed that surface modification did not change the carbon particle size, as concluded in Section 6.2. (Note: This does not refer to the size of agglomerates, which could be changed during the functionalization process or at the die-pressing stage of pellet preparation.) However, based on these CAK results, it is still not clear which surface, VC- PhF_5 or CIC-22- PhF_5 , is intrinsically more hydrophobic.

6.4.2 Water vapor sorption (WVS) study

Water vapor sorption (WVS) at carbons with/without surface functionalization was also studied to confirm the wettability results obtained from the contract angle kinetic measurements (Figures 6.3 and 6.4). Figure 6.5 shows the WVS results with time, where the

volume of water sorbed on the carbons was calculated from the mass increase of the samples in a water vapor environment at room temperature. As found in Chapter 4, the CICs have the ability to sorb a larger amount of water than VC does, and the volume of water sorbed by CIC-22 is close to the pore volume obtained from the nitrogen sorption isotherms (Table 6.1). After surface functionalization, however, the amount of water sorbed by CIC-22-PhF₅ decreases significantly (Figure 6.5), consistent with Figure 6.3.

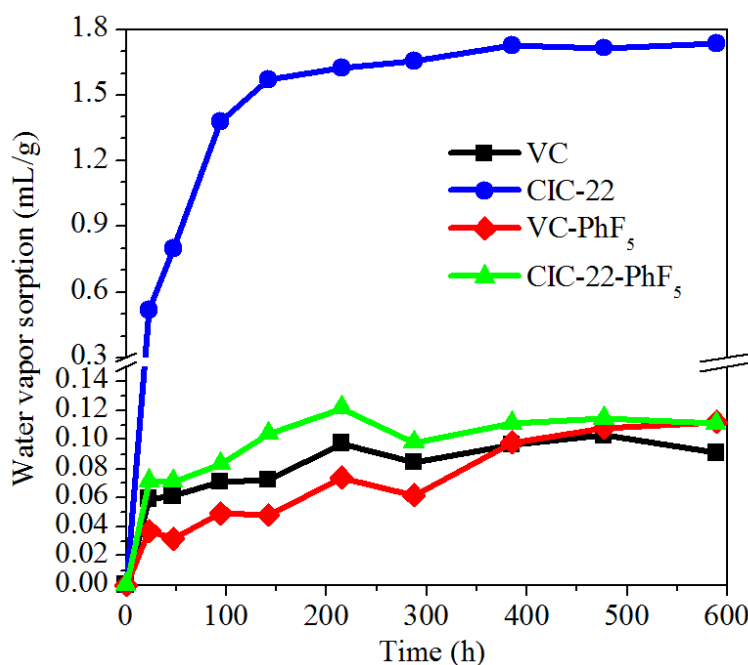


Figure 6.5. Water vapor sorption (WVS) data of VC and CIC-22, before and after surface functionalization with pentafluorophenyl (-PhF₅) groups, in a water vapor atmosphere at room temperature.

Compared to the fresh VC, VC-PhF₅ takes up less water in the beginning of the experiment ($t < 300$ h, Figure 6.5), as expected, but then unexpectedly sorbs more than VC did after longer time exposure to water vapor ($t > 500$ h, Figure 6.5). Since all of the samples

in Figure 6.5 were placed in the same chamber, i.e., exposed to the same water vapor environment, the data are fully comparable with each other.

As pointed out in Chapters 4 and 5, the raw WVS data cannot correctly give the relative wettability of the carbons because the surface area and pore volume of a sample can limit the maximum WVS. Thus, the WVS mass (Figure 6.5), normalized to the surface area and pore volume of the corresponding carbon samples (S_{BET} and V_{NSI} , Table 6.1), are plotted in Figure 6.6 to better gauge the relative wettability of the carbons. In Figure 6.6, V_{mono} is the volume of one monolayer of water closely packed on the surface with an area of S_{BET} , assuming the surface is sufficiently hydrophilic, as explained in Chapter 4. The $V_{\text{WVS}}/V_{\text{mono}}$ values (Figure 6.6a) can be considered as reflective of the number of layers of water sorbed on the sample surface. Although this may not be the real case, it can still reflect the ability of the sample to sorb water, i.e., the relative wettability (Chapter 4). The $V_{\text{WVS}}/V_{\text{NSI}}$ ratios (Figure 6.6b) thus indicate the fraction of the pores (≤ 100 nm in size) that are filled by condensed water, which should also be related to the relative wettability of the sample, as explained in Chapter 4.

The $V_{\text{WVS}}/V_{\text{mono}}$ and $V_{\text{WVS}}/V_{\text{NSI}}$ ratios obtained for CIC-22 and VC in Figure 6.6 are not exactly the same as obtained in Chapter 4 (Figure 4.9). This is caused by the different conditions of these two experiments, such as the temperature and the time interval used to track the sample mass. Even so, as mentioned above, the samples shown in Figure 6.6 can be compared directly, since the samples were placed in the same dessicator and tested under the identical conditions (temperature and relative humidity).

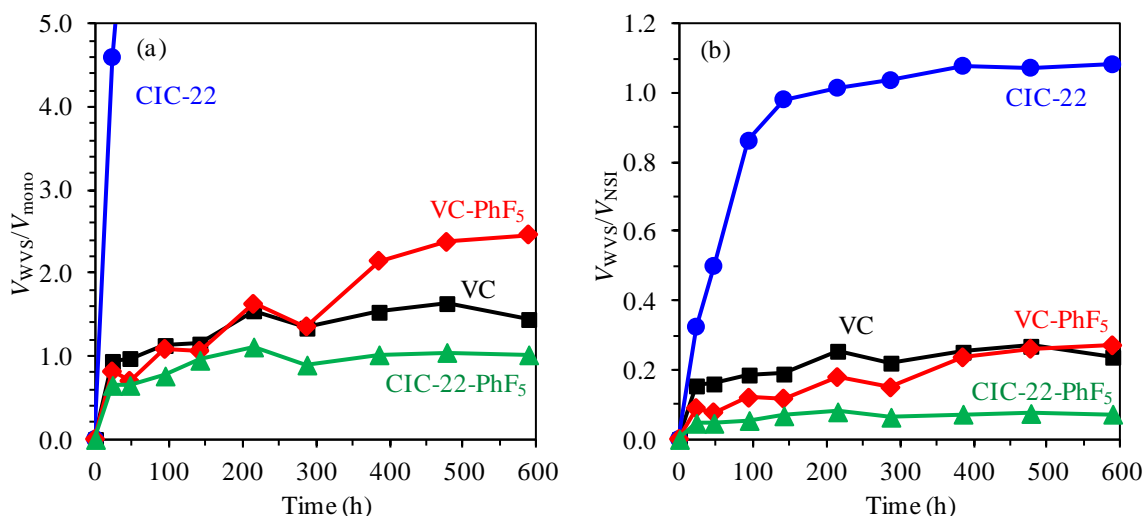


Figure 6.6. Water vapor sorption data (V_{WVS} , from Figure 6.5) of VC and CIC-22 before and after surface functionalization, normalized to their corresponding (a) surface area and (b) pore volume (S_{BET} and S_{NSI} in Table 6.1, respectively), obtained from nitrogen sorption isotherms (Figure 6.1).

Note: (a) V_{mono} = one monolayer of water molecules closely packed on sample surfaces, using the equation: $V_{mono} = S_{BET} M_{H_2O} / \sigma_{H_2O} N_A \rho_{H_2O}$, where S_{BET} is the specific surface area of samples shown in Table 6.1, M_{H_2O} = molar mass of water, σ_{H_2O} = cross-sectional area of water molecules (0.106 nm^2) [184, 185], N_A = Avogadro's constant, and ρ_{H_2O} = water density at 23°C . (b) V_{NSI} = Pore volume, as shown in Table 6.1.

As seen in Figure 6.6, non-functionalized CIC-22 exhibits much higher V_{WVS}/V_{mono} and V_{WVS}/V_{NSI} ratios than the other samples do, reflecting its very hydrophilic surface, which is consistent with the conclusions reached in Chapter 4. Surface functionalization with the fluorine groups made the CIC-22 the most hydrophobic (CIC-22-PhF₅) among these samples, as seen from their lowest V_{WVS}/V_{mono} and V_{WVS}/V_{NSI} ratios over the full time range. This is also fully consistent with what was seen in the CAK experiments for these samples (Figures 6.3 and 6.4).

However, the VC-PhF₅ sample exhibits V_{WVS}/V_{mono} ratios that are almost the same as for VC in the first 300 h of exposure to water vapor, and then, unexpectedly, VC-PhF₅ is still

seen to sorb more water than does VC. The fact that more water is sorbed per unit surface area of VC-PhF₅ than VC after 350 h of exposure to water vapor suggests that VC-PhF₅ is a bit more hydrophilic than VC, which is very different from what was concluded from the CAK results (Figures 6.3 and 6.4). This will be explained in more detail in Section 6.5.

As seen in Figure 6.6b, VC-PhF₅ exhibits lower V_{WVS}/V_{NSI} values in the first 300 h of exposure to water vapor than VC, and it then has similar V_{WVS}/V_{NSI} values after 300 h. This is quite different from the hydrophobicity trend suggested by the V_{WVS}/V_{mono} ratios above (Figure 6.6a). This may be caused by the different pore size distributions of VC-PhF₅ vs. VC (Figure 6.2a), and thus the V_{WVS}/V_{NSI} ratios of these two samples may not be a good indicator of their relative hydrophobicity. Therefore, the WVS data of the carbon samples in Figure 6.5 were compared with their nitrogen sorption isotherms (NSI) in Figure 6.1, using the method described in Chapter 5, with the results shown in Figure 6.7. Here, it is assumed that water vapor adsorbs on the sample surfaces in the same way as nitrogen does [172]. Figure 6.7a shows the partial pressure (Figure 6.1) required to sorb the same volume of N₂ as water vapor in Figure 6.5. Using the partial pressure in Figure 6.7a, the size of the pores filled by condensed water vapor can be estimated (Figure 6.7b) by using the Kelvin equation (5.2) and Equation (5.3) of the thickness of an adsorbed N₂ film on carbon surface. Figure 6.7b is expected to be more reliable than Figure 6.6b in terms of assessing the relative wettability of these carbons, as it includes the pore size distribution within these carbons.

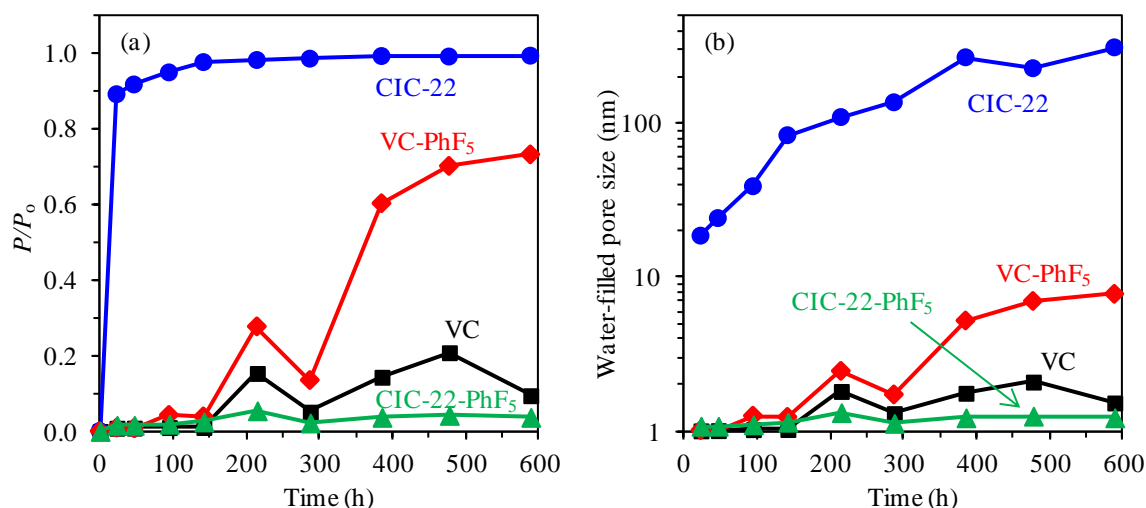


Figure 6.7. (a) Partial pressure (P/P_0) required to condense N₂ (Figure 6.1) to fill the same pore volume as water vapor did at each stage in Figure 6.5. (b) Estimated size of the pores that have been filled by water with time, corresponding to the points in Figure 6.5, obtained by using the Kelvin equation (5.2) and the statistical thickness of an adsorbed N₂ film on a carbon black surface (Equation 5.3) [172] at the corresponding partial pressures in (a), as described in Chapter 5.

Overall, it is very clear that CIC-22 has the most water-filled pores among these carbon samples, as seen in Figure 6.7b, suggesting again that it has the most hydrophilic surface and that its relatively large mesopores are easily accessible to water vapor. After functionalization, CIC-22-PhF₅ exhibits the most hydrophobic surface, as suggested by Figure 6.7b, which is consistent with the results shown in Figure 6.6a and also indicates that the CIC pore surfaces were fully functionalized by the PhF₅ groups.

Because the results in Figure 6.7b were acquired based on the numerous assumptions described above, the size of the water-filled pores may not be realistic. Even so, all the trends are likely correct and should still reflect the polarity or relative wettability of these samples, as discussed in Chapter 5. In Figure 6.7b, the apparently larger water-filled pores of VC-PhF₅ vs. VC (at $t > 350$ h) may just indicate that VC-PhF₅ takes up more water than VC, which is

consistent with the conclusion drawn from the comparison of their $V_{\text{WVS}}/V_{\text{mono}}$ ratios ($t > 350$ h in Figure 6.6a). However, this conclusion still disagrees with the CAK results, which showed that VC-PhF₅ is more hydrophobic than VC. Therefore, Section 6.5 is focused on understanding these conflicting results.

6.5 Further understanding of –PhF₅ functionalized carbon surfaces

The contradiction between the relative wettability of VC vs. VC-PhF₅, obtained by the CAK and WVS methods, can perhaps be understood by taking into account the different wetting processes involved in the two methods. After water droplet deposition on a sample surface in the CAK experiments, the contact angle will depend mainly on the distribution of hydrophobic sites, such as the fluorinated surface groups in the case of VC-PhF₅ and CIC-22-PhF₅, as well as void space (air is considered to be hydrophobic). If the hydrophobic sites dominate the surface, even if some hydrophilic domains (polar groups) are present, this will prevent the water droplet from spreading on the surface, seen as a high contact angle. A similar discussion was presented in Chapter 3 to explain the wetting of Nafion films by an impacting water droplet.

Thus, the likely high coverage of hydrophobic -PhF₅ groups attached to the VC particle surfaces (~ 95 % coverage, when calculated based on the external surface area (textural porosity)) and the void space between the particles must dominate the observed surface wettability of the VC-PhF₅ pellets in the CAK experiments, hindering the water droplets from spreading and thus exhibiting high contact angles (Figures 6.3 and 6.4). In comparison, the fresh VC particle surfaces are more hydrophilic ($\theta < 90^\circ$), as explained in Chapters 3 and 4, and thus do not prevent the water droplets from spreading. Therefore, VC

shows a smaller contact angle than does VC-PhF₅ in the CAK measurements, as fully expected (Figures 6.3 and 6.4).

In contrast, however, in the WVS experiments, when the samples are exposed to water vapour, any polar groups present on the surface (e.g., C-OH and COOH on CIC-22), even at low concentrations, could nucleate water condensation, as explained in Chapter 4. Therefore, the WVS results will depend on the area-specific density of polar and non-polar groups, i.e., a surface with a higher polar group density will take up more water vapour per unit area of surface (i.e., a higher V_{WVS}/V_{mono} ratio) than a surface with a lower polar group density.

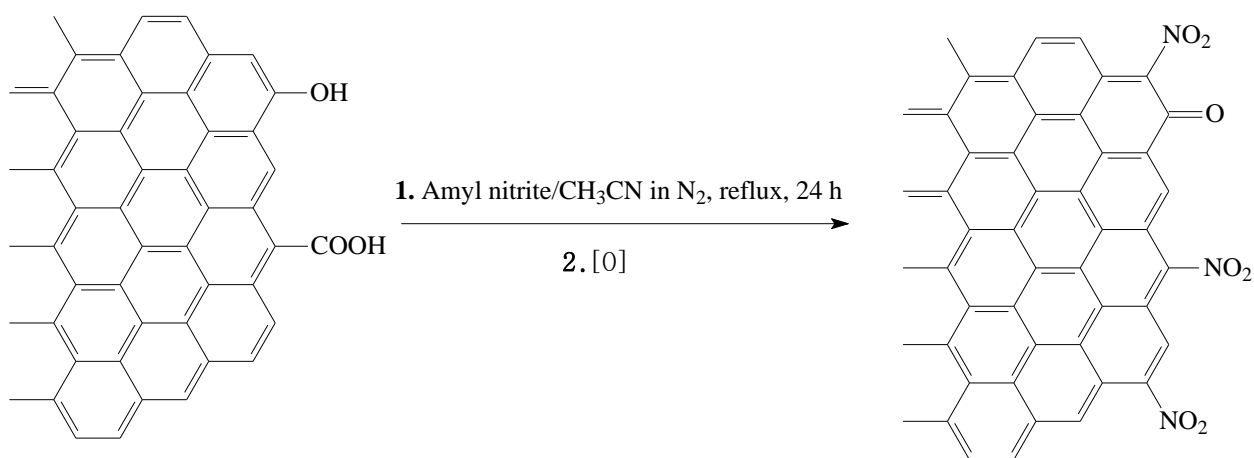
In the WVS experiments, a micropore in a carbon structure could be considered to be a surface polar group, since it can quickly take up water vapor [207, 208], as explained above. Although VC and VC-PhF₅ both have a similar micropore density ($S_{micro}/S_{BET} \sim 40\%$, Table 6.1), VC-PhF₅ has a higher nitrogen and oxygen surface content than does VC (Table 6.2) and a lower surface area (160 m²/g vs. 220 m²/g, Table 6.1). This means that VC-PhF₅ must have a higher density of surface polar groups than VC (area-specific density of oxygen atoms: 8.2 μmol/m² vs. 2.1 μmol/m², in average). Since the presence of -PhF₅ groups (~ 95 % coverage on the external surface) cannot prevent water vapor from nucleating around the polar groups on the VC-PhF₅ surface, the higher density of surface polar groups could be the reason why VC-PhF₅ takes up more water vapor than VC (Figures 6.6a and 6.7b).

For this explanation, it is of interest to better understand the origin and nature of the polar surface groups, containing nitrogen and oxygen (Table 6.2), on the VC-PhF₅ surfaces. As mentioned in Section 6.3, nitrogen may be present in the form of azo (-N=N-PhF₅)

groups, but this would not explain the significant increase in the oxygen content of VC after surface functionalization (Table 6.2)

Considering the instability of the amyl nitrite reagent used in the diazonium reduction reaction (Scheme 6.1), it may have reacted directly with the carbon surface during the functionalization process, following the proposed reactions in Scheme 6.3. At high temperatures (82 °C, boiling point of acetonitrile), amyl nitrite dissociates [220, 221], which is accelerated by protic agents (such as C-OH or COOH groups), forming $\cdot\text{NO}$ radicals or $[\text{NO}]^+$ ions. The radicals and ions can react with the carbon surface to form nitroso groups, which will be oxidized by oxygen when exposed to air at high temperatures (100 °C, used to dry the sample after washing) [223, 224], forming nitro groups ($-\text{NO}_2$, Scheme 6.3). Due to steric hindrance, the further conversion of the surface to $-\text{PhF}_5$ could well have been hindered inside the VC micropores, leaving the micropore surfaces more likely coated with the nitro groups (area-specific density of oxygen atoms on VC- PhF_5 vs. VC is $8.2 \mu\text{mol}/\text{m}^2$ vs. $2.1 \mu\text{mol}/\text{m}^2$, respectively), resulting in a higher degree of water uptake for VC- PhF_5 vs. VC (Figures 6.6a and 6.7b).

Along with the diazonium reduction reaction (Scheme 6.1), these side reactions (e.g., Scheme 6.3) will remove groups having a high polarity (e.g., COOH groups [218]), present on the non-functionalized CIC-22 (Chapter 4), and add groups with lower polarity (e.g., $-\text{NO}_2$ groups), or will oxidize the C-OH groups to form less polar C=O groups [225]. In addition to the attachment of $-\text{PhF}_5$ groups, all of the reactions above should also decrease the hydrophilicity of CIC-22. This is likely the reason why surface functionalization does not increase the oxygen content of CIC-22 (vs. VC, Table 6.2) and why CIC-22- PhF_5 does not have a higher $V_{\text{WVS}}/V_{\text{mono}}$ ratio than VC- PhF_5 (Figure 6.6a).



Scheme 6.3. Possible reactions of carbon surfaces with amyl nitrite during the functionalization reaction (Scheme 6.1).

In order to verify the presence of -NO_2 groups on the -PhF_5 functionalized carbon surfaces, we obtained the cyclic voltammetry (CV) response of VC- PhF_5 and CIC-22- PhF_5 , using non-surface modified VC and CIC-22 as the reference states, as shown in Figure 6.8. The CV response of carbon is a very useful method to confirm its surface chemistry. For example, CIC-22 exhibits a pair of much larger pseudo-capacitance peaks at ~ 0.55 V than VC does (Figures 6.8c vs. 6.8a), reflecting its higher density of surface oxygen groups, as explained in Chapter 4.

Compared to VC, VC- PhF_5 exhibits a higher cathodic current at < 0.4 V in the initial few cycles, and it also has some very small pseudo-capacitive peaks at ca. 0.55 V. VC- PhF_5 also shows a more significant increase in the cathodic pseudo-capacitive peak, at ca. 0.55 V, between the first and second cycles, when compared to VC. CIC-22- PhF_5 shows similar electrochemical responses to VC- PhF_5 . The additional cathodic current at < 0.4 V and the

increase in the size of the pseudo-capacitive peaks from the first cycle to the second at ca. 0.55 V were not observed for the non-functionalized carbons (Figures 6.8d vs. 6.8c).

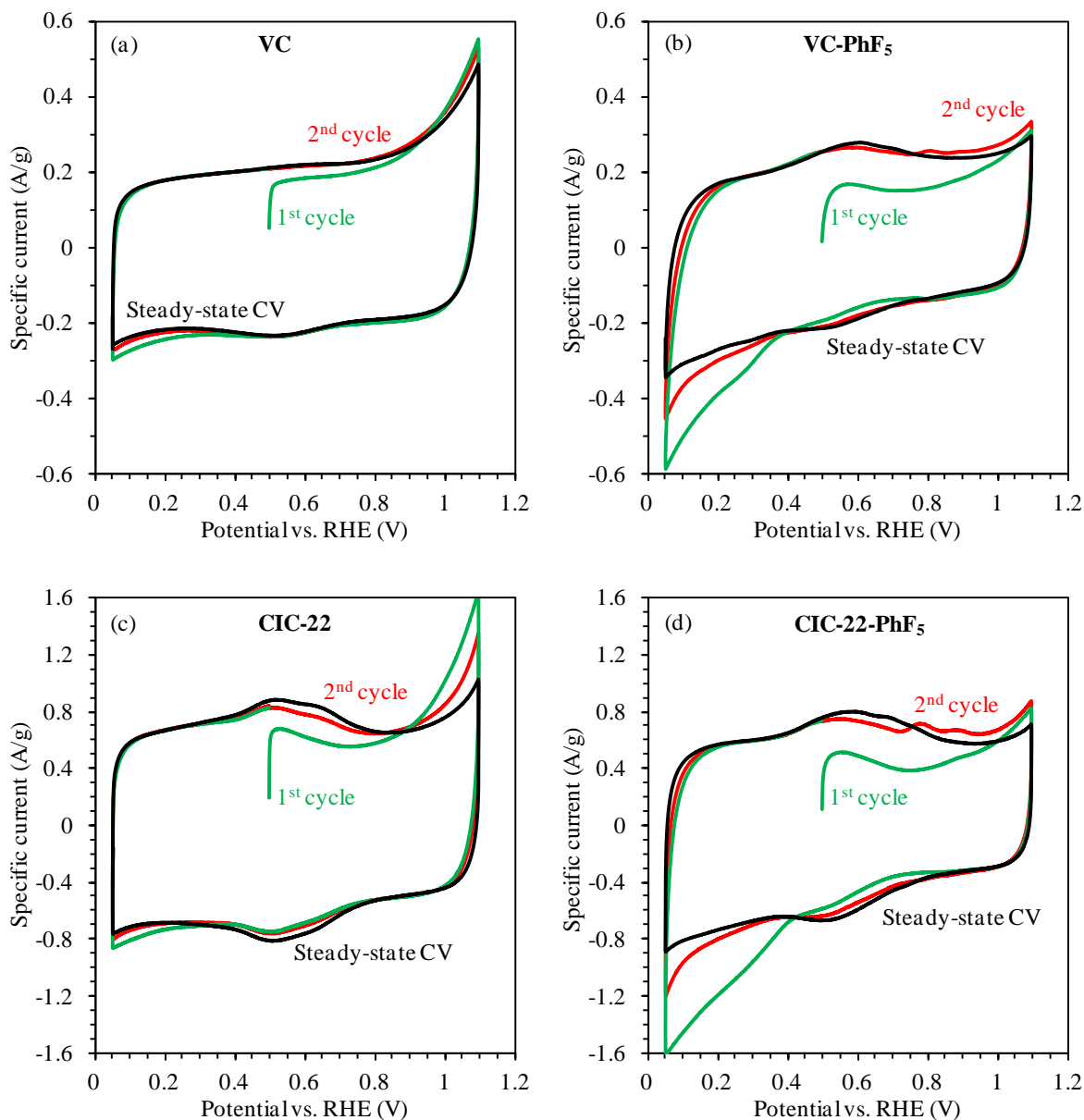
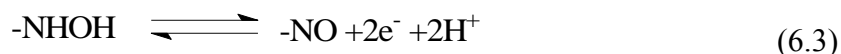
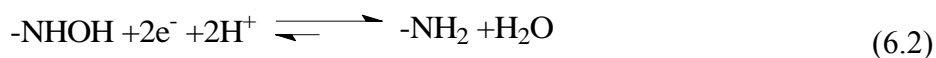
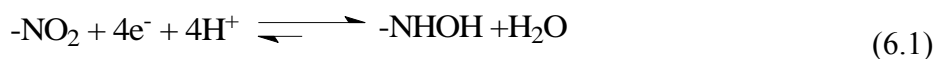


Figure 6.8. Cyclic voltammograms (CVs) of (a) VC, (b) VC- PhF_5 , (c) CIC-22, and (d) CIC-22- PhF_5 in N_2 -saturated 0.5 M H_2SO_4 solution at a scan rate of 10 mV/s.

According to the literature [226-230], the presence of $-\text{NO}_2$ groups on a carbon surface will be seen by a large cathodic current at < 0.4 V, attributed to the irreversible reduction of $-\text{NO}_2$ to $-\text{NHOH}$ (Reaction 6.1) or even further to $-\text{NH}_2$ (Reaction 6.2). The CVs subsequently show a pair of reversible pseudo-capacitance peaks at around 0.55 V, due to the electrochemical reaction involving the $-\text{NHOH}$ and $-\text{NO}$ groups (Reaction 6.3), in addition to the reaction between hydroquinone and quinone (Reaction 4.2).



This is exactly what is observed in the CV responses of VC- PhF_5 and CIC-22- PhF_5 (Figure 6.8). In the first negative scan, $-\text{NO}_2$ is reduced at < 0.4 V to form $-\text{NHOH}$ or $-\text{NH}_2$. The newly generated $-\text{NHOH}$ gives a higher cathodic current in the second vs. first CV cycle at 0.55 V for both of the functionalized carbons (Figures 6.8b and 6.8d). Therefore, the difference between the CV response of VC and VC- PhF_5 and that of CIC-22 and CIC-22- PhF_5 confirms the presence of the $-\text{NO}_2$ groups on the $-\text{PhF}_5$ functionalized carbon surfaces.

The reason why the first CV was started at 0.5 V and then taken positively was to avoid the reduction of $-\text{NO}_2$ and also to observe any change in the cathodic pseudo-capacitance peak at 0.55 V from the first to second cycle (Figure 6.8). It is also seen in the first cycle that VC- PhF_5 has an obviously larger pseudo-capacitance peak than VC at 0.55 V (Figures 6.8b vs. 6.8a), which may be due to newly generated hydroquinone/quinone (Reaction 4.2) or hydroxylamine/nitroso (Reaction 6.3) groups. However, it is still not clear from Figures 6.8b and 6.8d which electroactive groups are associated with the small anodic

peaks at 0.8 V and 0.9 V seen in the subsequent cycles for both of the functionalized carbons, then disappearing after a long time of potential cycling.

Overall, surface functionalization using the method shown in Scheme 6.1 has successfully added -PhF₅ groups onto the VC and CIC-22 surfaces but it also left other polar groups (e.g., -NO₂) on the surfaces from the functionalization reagents. These polar groups, which may be located primarily in the VC micropores, make these VC surfaces more hydrophilic to water vapor than expected, as suggested by the WVS results (Figures 6.6a and 6.7b). At the macroscopic scale, the presence of the -PhF₅ groups on the outer VC particle surfaces makes the VC surface more hydrophobic by preventing the spreading of water droplets on VC-PhF₅ surface, as seen in the CAK results (Figure 6.3).

As mentioned at the end of Section 6.4.1, the significant difference in the particle sizes of VC-PhF₅ and CIC-22-PhF₅ (~30 nm vs. ~ 10 μ m) makes it difficult to judge which of these two surface modified carbons is intrinsically more hydrophobic, based on the CAK results (Figures 6.3 and 6.4). The WVS data (Figures 6.6 and 6.7) suggest that VC-PhF₅ takes up more water vapour than CIC-22-PhF₅, which may be related to the higher coverage of nitro groups, likely inside the VC micropores that were not able to be PhF₅-modified, due to steric hindrances. As stated above, the micropores are more easily accessible to \cdot NO radicals (due to the dissociation of amyl nitrite) than \cdot PhF₅ radicals (from the diazonium reaction (Scheme 6.1)), which would place the majority of the -NO₂ groups inside the micropores and -PhF₅ on the external surface. Compared to CIC-22-PhF₅, VC-PhF₅ has more micropores ($S_{\text{micro}}/S_{\text{BET}}$, 40 % vs. 20 %, Table 6.1) filled with the polar -NO₂ groups, thus resulting in more water uptake, as seen in Figures 6.6a and 6.7b.

6.6. Summary

In this study, VC and CIC-22 were surface modified with $-\text{PhF}_5$ groups by using an *in-situ* diazonium reduction reaction. The analysis of the microstructure shows that surface modification resulted in a significant decrease ($\sim 30\%$) in the surface area of VC but less significantly for CIC-22. The reaction decreased the CIC-22 pore size by 1-3 nm, but no significant size change was observed for VC due to the functionalization. The elemental analysis of both carbons confirms the successful bonding of the fluorinate groups, with a coverage of ca. 90% on their external surfaces, and it also shows that there was a significant increase in the nitrogen and oxygen contents after modification.

The wettability of the functionalized carbons was examined by using both contact angle kinetics (CAK) and water vapor sorption (WVS) methods, with the as-received VC and as-synthesized CIC-22 used as benchmarks. The CAK results show that the $-\text{PhF}_5$ groups makes both carbons become much more hydrophobic, as expected. While the WVS results confirm the high hydrophobicity of CIC-22- PhF_5 , the data show that VC- PhF_5 takes up more water vapour than VC alone. One possible explanation is that the $-\text{PhF}_5$ groups have deposited primarily on the outer surface of the VC particles, while nitro groups, formed during the surface modification, have been mainly retained inside the VC micropores which are too small to complete $-\text{PhF}_5$ attachment. The CAK experiments will be influenced most by the chemistry of the outer VC particle surfaces, showing hydrophobic behaviour, while water vapour will also condense in the more hydrophilic micropores. The presence of nitro groups on the VC surfaces has been confirmed by cyclic voltammetry studies of the functionalized vs. non-functionalized carbons.

Chapter Seven: Conclusions and Suggested Future Work

7.1 Conclusions

Because of their good electric conductivity, tunable pore sizes and surface properties, and low preparation cost, high surface area carbon powders are of interest as catalyst supports in polymer electrolyte membrane fuel cells (PEMFCs). As a catalyst support, the wettability of carbon powders is directly related to the water balance in the catalyst layers (CLs) and is also believed to play an important role in the stability of the carbons and catalyst materials. These factors are critical for the performance and durability of PEMFCs. Therefore, the main goal of this thesis was to understand and control the wettability of high surface area carbon powders, primarily to produce PEMFCs with high performance and long lifetimes.

This thesis has demonstrated the preparation, surface modification, and evaluation of the wettability of several carbon samples, including a commercial, microporous carbon black (Vulcan carbon, VC) and several recently developed mesoporous carbons. VC was selected as a benchmark for the wettability study in this project, as it has been widely studied and used. Colloid-imprinted carbons (CICs) and ordered mesoporous carbons (OMCs) were also synthesized in-house and then examined for their wettability, as well as their porosity and elemental composition. These carbons were then heat treated at 1500 °C in a N₂ atmosphere for 2 hours to increase their crystallinity and carbonaceous nature, which, in turn, was expected to enhance their resistance to oxidation in practice. The VC and CIC surfaces were also chemically modified with pentafluorophenyl (-PhF₅) groups and then all of these modified carbons were evaluated for their wetting characteristics.

7.1.1 Effect of Nafion on the wettability of carbon/Nafion composites

In Chapter 3, the first-time use of the water droplet impacting (DI) method to determine the wettability of 100% Nafion films, as a benchmark, and then of VC/Nafion composite films, both deposited by spin-coating on glass substrates, was demonstrated. Pure Nafion films, shown by SEM analysis to have a nano-channeled structure, were shown to be initially hydrophobic, but become hydrophilic as the water droplet spreads, likely due to re-orientation of the sulfonic acid groups towards the deposited water, thus showing heterogeneity in its wettability. This is attributed to the unique molecular structure of Nafion, possessing both hydrophobic polymer chains and hydrophilic sulfonic groups.

The wettability of VC/Nafion composite films was shown to depend significantly on the VC/Nafion mass ratios, even though Nafion is believed to be preferentially oriented (sulfonate groups toward VC) in all cases. At low VC contents, a significant water droplet contact angle hysteresis was seen, similar to what was observed with pure Nafion films, while at higher VC contents ($> 30\%$), the films became hydrophobic, also sometimes exhibiting superhydrophobicity, with surface roughness playing a significant role. At $> 80\%$ VC, the surfaces became wettable again, as there is insufficient Nafion loading present to fully cover the carbon surface. This allowed us to calculate the Nafion:carbon ratio required to achieve full coverage of carbon by Nafion, i.e., ~ 1.9 mg of Nafion per m^2 of carbon surface.

7.1.2 Wettability of synthesized and heat-treated carbons

In Chapters 4 and 5, CICs with different pore sizes (15 - 50 nm) and OMCs (primarily 2 - 3 nm diameter pores, but also containing 5 - 50 nm pores), derived from different carbon precursors, were examined first-time with both contact angle kinetics (CAK) and water vapor sorption (WVS) experiments to determine their wettability. The results showed that both of these carbons are much more hydrophilic than commercial carbon black (VC). The high hydrophilicity of both the CICs and OMCs is likely due to their high surface-specific oxygen atomic density (5 - 10 $\mu\text{mol}/\text{m}^2$). Heat treatment not only enhances the degree of carbonization of both groups of carbons, but also removes their oxygen groups, causing a significant decrease in their hydrophilicity. The loss of oxygen groups of these carbons after heat treatment was reflected by their cyclic voltammetric (CV) response in acidic solutions.

7.1.3 Microstructure of mesoporous carbons and effect on wettability

In this work, it was found that CICs have a narrow pore size distribution and dense carbon pore walls, which survive the heat treatment, as reflected by their porosity properties obtained from nitrogen sorption isotherms (NSI) analysis. The OMCs were also examined using the same method, showing that their surface area and porosity also experienced little change after heat treatment. This allowed us to examine the relative wettability of these carbons, before and after heat treatment, without any significant change to their microstructure.

If only considering the primary pores (2 - 3 nm in diameter) of OMCs, this study showed that in-house synthesized carbons (OMCs and CICs) with smaller pore diameters are

more wettable, following common capillary theory. After heat treatment, the wettability of the mesopores of these carbons also obeys this theory, meaning that the intrinsic water contact angle of these pore surfaces is smaller than 90 °.

Interestingly, CICs with different pore sizes do not show any significant differences in their intrinsic wettability. However, the OMCs derived from the different precursors do have different microstructures and also exhibit differences in wettability, although the same silica template was used in for each OMC. The anthracene-derived OMC (OMC-A) contains more secondary mesopores (~ 10 nm) than the sucrose-based OMC (OMC-S), and these larger OMC-A mesopores as well as their primary pores (size: 2-3 nm) are all quite hydrophilic. In contrast, OMC-S exhibits a hydrophobic outer surface, which is attributed to the possible formation of a very thin carbon shell on the OMC-S particle surface, formed during synthesis. This is explained, for the first time, as resulting from the fact that sucrose is polar and thus miscible with the H₂SO₄, used as the catalyst, while anthracene is non-polar and insoluble in H₂SO₄. This is proposed to be the reason for the different resulting microstructures of OMC-S and OMC-A, also influencing their wettability.

7.1.4 Surface functionalization of carbons and effect on wettability

VC and CIC-22 (22 nm diameter colloidal silica used for CIC synthesis) were surface modified with pentafluorophenyl (-PhF₅) groups, for the first time in the case of the highly promising CICs studied in this thesis work, using an *in-situ* diazonium reduction reaction. CAK measurements showed that surface functionalization enhances the hydrophobicity of both carbons, as expected. However, the WVS results showed that the fluorinated VC also contains a high density of polar groups, higher than the fresh VC surface. This was attributed

to the introduction of polar N and O containing groups (e.g., nitro), most likely on the micropore surfaces during the surface modification process, as confirmed from the CV studies. These groups are also present on the fluorinated CIC-22 surfaces, perhaps in micropores within the CIC-22 walls, as shown from its elemental content and CV response.

7.1.5 Conclusions related to wettability of carbons for PEMFC applications

In this thesis, it was shown that the DI, CAK, and WVS methods and the related data analysis approaches used here are suitable for the determination of the relative wettability of carbon powders and carbon/Nafion composites. They also can be used to determine the wettability of other carbons, Pt-loaded carbons, Nafion and Pt-loaded carbon composites, materials of direct application in PEMFCs.

It was demonstrated that VC, a commercial carbon black, is more hydrophobic than the carbons synthesized in-house using hard templating methods, but it can still be wetted by water, as shown in Chapter 4. Because of this, as well as the limitations of its microporous structure (Chapter 1), VC is not the best choice as a catalyst support material for use in PEMFCs.

As discussed in Chapter 5 and Section 6.1, the OMCs are very hydrophilic, so that they could potentially be used in a PEMFC operated at low relative humidity to avoid flooding problems. Heat treatment of the OMCs could also reduce cathode layer flooding problem. However, the mesopores of the OMCs, both before and after heat treatment, are too small (2-3 nm) to accommodate both Pt nanoparticles (2-6 nm) and Nafion clusters (1-3 nm) and to provide enough room for gas transfer through them. Further, the possible presence of a carbon shell around OMC-S could further inhibit mass transport from/to the Pt

nanoparticles inside the OMC-S particles. Overall, it appears that the OMCs may not be very suitable for use as catalyst supports in PEMFC cathode layers.

On the other hand, the CICs seem to be much more promising, due to their larger pores and more robust pore walls. However, this work has shown that they have hydrophilic surfaces, which would be good for the dispersion of Pt nanoparticles within their mesopores, but could again cause flooding problems at the cathode. To remedy this, heat treatment does make the CICs more hydrophobic, while retaining the pore structure. Also, surface fluorine groups can be attached on the full CIC pore surface, thus lowering their hydrophilicity without significantly lowering pore diameter. Therefore, a fluorinated and/or heat-treated CIC may be the optimum choice as a catalyst support for use in PEMFCs.

7.2 Overview of novel contributions of this thesis work

Overall, the novel findings of this work include the following:

1. There is a significant influence of Nafion on the wettability of carbon/Nafion composites, determined using the droplet impacting (DI) method (Chapter 3).
2. The supposition regarding Nafion orientation on carbon surfaces, proposed by other researchers prior to this work, has been confirmed (Chapter 3).
3. Sulfuric acid was added to the carbon/Nafion composites for the electrochemical testing of carbon powders, where Nafion was used as a binder (Chapter 4-6), resulting in a significant improvement in the reproducibility/reliability of the electrochemical performance of the carbons in sulfuric acid solutions.

4. Both the CAK and WVS methods have been shown to indicate the wettability of high surface area carbon powders, but only when reasonable criteria are used for the analysis of the results (Chapters 4-6).
5. The intrinsically hydrophilic nature of the mesopores of both CICs and OMCs (Chapters 4 and 5) was demonstrated, and a possible origin of the hydrophilicity was suggested (Chapter 5).
6. The more hydrophobic nature of the sucrose-based OMC than the anthracene-based OMC (Chapter 5) was demonstrated and explained.
7. This work has verified that surface functionalization with $-\text{PhF}_5$ groups makes carbon powders more hydrophobic (Chapter 6).
8. It was discovered that surface functionalization using the *in-situ* diazonium reduction reaction also introduces $-\text{NO}_2$ groups on to the carbon surfaces (Chapter 6), thus adding some hydrophilicity.

7.3 Suggestions for future work

Although the results presented in this thesis have helped us to understand the relative wettability of the carbons before and after various treatments, including heat treatment, surface modification by $-\text{PhF}_5$ groups, and the addition of Nafion, there is still more work needed, as follows:

1. Other functional groups ($-\text{NO}_2$, $-\text{NH}_2$, $-\text{SO}_3\text{H}$, etc.) could be grafted on to the carbon surfaces in order to further modify the hydrophobicity or hydrophilicity of the surfaces. For these surface-modified samples, the CAK and WVS methods should be used to characterize their wettability. The DI method could also be used to determine

the wettability of composites of Nafion and these newly surface-modified carbons in order to determine how these surface groups affect the orientation of Nafion molecules.

2. The presence of Pt nanoparticles on the carbon powder surface is important in influencing the wettability of carbons (both before and after surface functionalization). Thus, the same studies as described in this thesis should be carried out, using the CAK and WVS methods, but with the addition of various loadings of Pt nanoparticles, thus making these results more applicable to PEMFCs.
3. In this work, it has been shown that silica is a residue after CIC and OMC synthesis, but the properties and amount of silica present remains uncertain. Also, it would be of interest to determine the effect of silica on the hydrophilicity of these carbons.
4. In this thesis work, the hydrophilicity of the CICs and OMCs was attributed mainly to the presence of C-OH, COOH and other polar groups on the carbon surfaces, and the CVs of these carbons helped to verify the presence of these electrochemically active surface groups. It would be of interest to determine the mechanism of the formation of these groups on the carbon surfaces and elaborate on the mechanism proposed in Chapter 5.
5. It would be desirable to prove that there is a thin layer of carbon surrounding the OMC-S particles, thus making this material more hydrophobic than OMC-A. This could be done by varying the mass ratio of sucrose to the silica template, with verification achieved by TEM analysis.
6. As discussed in Chapter 6, the *in-situ* diazonium reduction reaction (Scheme 6.1) used in carbon surface functionalization involves the grafting of $-\text{NO}_2$ groups onto

the carbon surfaces, but several side reactions also likely occur. It would be of interest to investigate these side reactions in more depth, including their kinetics and particularly their influence on the surface wettability of the carbons, without the interference of $-\text{PhF}_5$ groups. This could result in a more facile functionalization method than involved in the diazonium reduction reaction [218].

7. In another direction, electrochemical grafting of $-\text{PhF}_5$ groups to carbon surfaces by using *ex-situ* synthesized pentafluorophenyl diazonium salts could potentially avoid the addition of $-\text{NO}_2$ groups onto the surfaces. This may also result in a different fluorinated carbon surfaces (e.g., surface coverage of fluorine groups) and thus the surface wettability may also be different.
8. As discussed in this thesis, the gaps between carbon particles, or surface roughness, affect the phenomenological wetting behavior of carbon or its composites. Therefore, it would be of interest to carry out wetting studies of a continuous colloid imprinted carbon monolith (films or pellets) containing only uniform mesopores. This would allow the study of the surface properties, especially wettability, as well as the mass transport of electrolytes, gases, and water through the nano-porous structures.
9. More information may be obtained from the WVS measurements (Section 2.6.2) if a hygrometer were to be placed in the dessicator (Figure 2.3a) to monitor the real-time relative humidity inside the chamber during the experiment.
10. As mentioned in Section 4.6, an alternative system to collect the water vapor isotherm data (vs. P/P_0 instead of vs. time, as done this work) for powder/porous samples should be developed. The water vapor isotherms could then be compared directly to

nitrogen sorption isotherms to obtain more information about the surface polarity of the samples, as shown in the literature [102, 115, 121].

11. A long term research goal would be to apply the methods and findings of this thesis to determining the wetting properties of catalyst layers of real PEMFCs, including Pt/carbon/Nafion composites, and to determine the relationship between the wettability and the performance of PEMFCs.
12. Cost evaluation related to the synthesis, heat treatment, and surface modification of the carbons should be carried out in the future in order to employ the materials and techniques discussed above in PEMFC manufacturing.

References

- [1] Bureau USC. U.S. and World Population Clock 2015 [cited 2015 January 27]; Available from: <http://www.census.gov/popclock/>
- [2] Worldometers. Current world population. 2015 [cited 2015 January 27]; Available from: <http://www.worldometers.info/world-population/>
- [3] Assembly UNG. Report of the world commission on environment and development: Our common future 1987.
- [4] Hiesgen R, Wehl I, Aleksandrova E, Roduner E, Bauder A, Friedrich KA. Nanoscale properties of polymer fuel cell materials-A selected review. *International Journal of Energy Research* 2010;34(14):1223-38.
- [5] Borup RL, Davey JR, Garzon FH, Wood DL, Inbody MA. PEM fuel cell electrocatalyst durability measurements. *Journal of Power Sources* 2006;163(1):76-81.
- [6] Mehta V, Cooper JS. Review and analysis of PEM fuel cell design and manufacturing. *Journal of Power Sources* 2003;114(1):32-53.
- [7] Wang Y, Chen KS, Mishler J, Cho SC, Adroher XC. A review of polymer electrolyte membrane fuel cells: Technology, applications, and needs on fundamental research. *Applied Energy* 2011;88(4):981-1007.
- [8] Li H, Tang Y, Wang Z, Shi Z, Wu S, Song D, et al. A review of water flooding issues in the proton exchange membrane fuel cell. *Journal of Power Sources* 2008;178(1):103-17.
- [9] Carrette L, Friedrich KA, Stimming U. Fuel cells – fundamentals and applications. *Fuel Cells* 2001;1(1):5-39.
- [10] Liu Z, Gan LM, Hong L, Chen W, Lee JY. Carbon-supported Pt nanoparticles as catalysts for proton exchange membrane fuel cells. *Journal of Power Sources* 2005;139(1-2):73-8.
- [11] Moreira J, del Angel P, Ocampo AL, Sebastián PJ, Montoya JA, Castellanos RH. Synthesis, characterization and application of a Pd/Vulcan and Pd/C catalyst in a PEM fuel cell. *International Journal of Hydrogen Energy* 2004;29(9):915-20.
- [12] Litster S, McLean G. PEM fuel cell electrodes. *Journal of Power Sources* 2004;130(1-2):61-76.
- [13] Chen Z, Higgins D, Yu A, Zhang L, Zhang J. A review on non-precious metal electrocatalysts for PEM fuel cells. *Energy & Environmental Science* 2011;4(9):3167-92.
- [14] Hayashi A, Notsu H, Kimijima Ki, Miyamoto J, Yagi I. Preparation of Pt/mesoporous carbon (MC) electrode catalyst and its reactivity toward oxygen reduction. *Electrochimica Acta* 2008;53(21):6117-25.
- [15] Ticianelli EA, Derouin CR, Redondo A, Srinivasan S. Methods to advance technology of proton-exchange membrane fuel-cells. *Journal of the Electrochemical Society* 1988;135(9):2209-14.
- [16] Do J-S, Liou B-C. A mixture design approach to optimizing the cathodic compositions of proton exchange membrane fuel cell. *Journal of Power Sources* 2011;196(4):1864-71.

- [17] Gode P, Jaouen F, Lindbergh G, Lundblad A, Sundholm G. Influence of the composition on the structure and electrochemical characteristics of the PEFC cathode. *Electrochimica Acta* 2003;48(28):4175-87.
- [18] Passalacqua E, Lufrano F, Squadrito G, Patti A, Giorgi L. Nafion content in the catalyst layer of polymer electrolyte fuel cells: effects on structure and performance. *Electrochimica Acta* 2001;46(6):799-805.
- [19] Wang QP, Eikerling M, Song DT, Liu ZS. Structure and performance of different types of agglomerates in cathode catalyst layers of PEM fuel cells. *Journal of Electroanalytical Chemistry* 2004;573(1):61-9.
- [20] O'Hayre R, Cha S-W, Colella W, Prinz FB. *Fuel cell fundamentals*. 2nd ed. New York: John Wiley & Sons; 2009.
- [21] Borup R, Meyers J, Pivovar B, Kim YS, Mukundan R, Garland N, et al. Scientific aspects of polymer electrolyte fuel cell durability and degradation. *Chemical reviews* 2007;107(10):3904-51.
- [22] Ramaswamy P, Wong NE, Shimizu GKH. MOFs as proton conductors - challenges and opportunities. *Chemical Society Reviews* 2014;43(16):5913-32.
- [23] Hurd JA, Vaidhyanathan R, Thangadurai V, Ratcliffe CI, Moudrakovski IL, Shimizu GKH. Anhydrous proton conduction at 150 °C in a crystalline metal-organic framework. *Nat Chem* 2009;1(9):705-10.
- [24] Cindrella L, Kannan AM, Lin JF, Saminathan K, Ho Y, Lin CW, et al. Gas diffusion layer for proton exchange membrane fuel cells-A review. *Journal of Power Sources* 2009;194(1):146-60.
- [25] Benziger J, Nehlsen J, Blackwell D, Brennan T, Itescu J. Water flow in the gas diffusion layer of PEM fuel cells. *Journal of Membrane Science* 2005;261(1-2):98-106.
- [26] Dai W, Wang H, Yuan X-Z, Martin JJ, Yang D, Qiao J, et al. A review on water balance in the membrane electrode assembly of proton exchange membrane fuel cells. *International Journal of Hydrogen Energy* 2009;34(23):9461-78.
- [27] Middelmann E, Kout W, Vogelaar B, Lenssen J, de Waal E. Bipolar plates for PEM fuel cells. *Journal of Power Sources* 2003;118(1-2):44-6.
- [28] Li XG, Sabir M. Review of bipolar plates in PEM fuel cells: Flow-field designs. *International Journal of Hydrogen Energy* 2005;30(4):359-71.
- [29] Wu J, Yuan XZ, Martin JJ, Wang H, Zhang J, Shen J, et al. A review of PEM fuel cell durability: Degradation mechanisms and mitigation strategies. *Journal of Power Sources* 2008;184(1):104-19.
- [30] de Bruijn FA, Dam VAT, Janssen GJM. Review: Durability and degradation Issues of PEM fuel cell components. *Fuel Cells* 2008;8(1):3-22.
- [31] Bi W, Gray GE, Fuller TF. PEM fuel cell Pt/C dissolution and deposition in nafion electrolyte. *Electrochemical and Solid State Letters* 2007;10(5):B101-B4.
- [32] Das PK, Li X, Liu Z-S. Analysis of liquid water transport in cathode catalyst layer of PEM fuel cells. *International Journal of Hydrogen Energy* 2010;35(6):2403-16.
- [33] Li A, Chan SH, Nguyen N-t. Anti-flooding cathode catalyst layer for high performance PEM fuel cell. *Electrochemistry Communications* 2009;11(4):897-900.
- [34] Lim C, Wang CY. Effects of hydrophobic polymer content in GDL on power performance of a PEM fuel cell. *Electrochimica Acta* 2004;49(24):4149-56.

- [35] Lin GY, Van Nguyen T. Effect of thickness and hydrophobic polymer content of the gas diffusion layer on electrode flooding level in a PEMFC. *Journal of the Electrochemical Society* 2005;152(10):A1942-A8.
- [36] Stevens DA, Hicks MT, Haugen GM, Dahn JR. Ex situ and in situ stability studies of PEMFC catalysts. *Journal of the Electrochemical Society* 2005;152(12):A2309-A15.
- [37] Gasteiger HA, Kocha SS, Sompalli B, Wagner FT. Activity benchmarks and requirements for Pt, Pt-alloy, and non-Pt oxygen reduction catalysts for PEMFCs. *Applied Catalysis B: Environmental* 2005;56(1–2):9-35.
- [38] US-DRIVE. Fuel cell technical team roadmap June 2013 [cited 2014 03-22]; Available from: http://energy.gov/sites/prod/files/2014/02/f8/fctt_roadmap_june2013.pdf
- [39] Jha N, Ramesh P, Bekyarova E, Tian X, Wang F, Itkis ME, et al. Functionalized single-walled carbon nanotube-based fuel cell benchmarked against US DOE 2017 technical targets. *Sci Rep* 2013;3.
- [40] Shao Y, Wang J, Kou R, Engelhard M, Liu J, Wang Y, et al. The corrosion of PEM fuel cell catalyst supports and its implications for developing durable catalysts. *Electrochimica Acta* 2009;54(11):3109-14.
- [41] Shao Y, Yin G, Gao Y. Understanding and approaches for the durability issues of Pt-based catalysts for PEM fuel cell. *Journal of Power Sources* 2007;171(2):558-66.
- [42] Antolini E. Carbon supports for low-temperature fuel cell catalysts. *Applied Catalysis B: Environmental* 2009;88(1–2):1-24.
- [43] Banham D, Feng F, Fürstenthaupt T, Pei K, Ye S, Birss V. Effect of Pt-loaded carbon support nanostructure on oxygen reduction catalysis. *Journal of Power Sources* 2011;196(13):5438-45.
- [44] Chang H, Joo SH, Pak C. Synthesis and characterization of mesoporous carbon for fuel cell applications. *Journal of Materials Chemistry* 2007;17(30):3078-88.
- [45] Wang X, Li W, Chen Z, Waje M, Yan Y. Durability investigation of carbon nanotube as catalyst support for proton exchange membrane fuel cell. *Journal of Power Sources* 2006;158(1):154-9.
- [46] Zhang W, Sherrell P, Minett AI, Razal JM, Chen J. Carbon nanotube architectures as catalyst supports for proton exchange membrane fuel cells. *Energy & Environmental Science* 2010;3(9):1286-93.
- [47] Joo SH, Choi SJ, Oh I, Kwak J, Liu Z, Terasaki O, et al. Ordered nanoporous arrays of carbon supporting high dispersions of platinum nanoparticles. *Nature* 2001;412(6843):169-72.
- [48] Pei K, Banham D, Feng F, Fuerstenthaupt T, Ye S, Birss V. Oxygen reduction activity dependence on the mesoporous structure of imprinted carbon supports. *Electrochemistry Communications* 2010;12(11):1666-9.
- [49] Banham D, Feng F, Pei K, Ye S, Birss V. Effect of carbon support nanostructure on the oxygen reduction activity of Pt/C catalysts. *Journal of Materials Chemistry A* 2013;1(8):2812-20.
- [50] Lee J, Kim J, Hyeon T. Recent progress in the synthesis of porous carbon materials. *Adv Mater* 2006;18(16):2073-94.
- [51] Liang C, Li Z, Dai S. Mesoporous carbon materials: Synthesis and modification. *Angewandte Chemie International Edition* 2008;47(20):3696-717.

- [52] Chuenchom L, Kraehnert R, Smarsly BM. Recent progress in soft-templating of porous carbon materials. *Soft Matter* 2012;8(42):10801-12.
- [53] Lee J, Han S, Hyeon T. Synthesis of new nanoporous carbon materials using nanostructured silica materials as templates. *Journal of Materials Chemistry* 2004;14(4):478-86.
- [54] Li ZJ, Jaroniec M. Colloidal imprinting: A novel approach to the synthesis of mesoporous carbons. *Journal of the American Chemical Society* 2001;123(37):9208-9.
- [55] Matsumoto T. Mesophase pitch and its carbon-fibers. *Pure Appl Chem* 1985;57(11):1553-62.
- [56] Fang B, Kim JH, Yu J-S. Colloid-imprinted carbon with superb nanostructure as an efficient cathode electrocatalyst support in proton exchange membrane fuel cell. *Electrochemistry Communications* 2008;10(4):659-62.
- [57] Fang B, Kim M, Hwang S, Yu J-S. Colloid-imprinted carbon with tailored nanostructure as an unique anode electrocatalyst support for formic acid oxidation. *Carbon* 2008;46(6):876-83.
- [58] Banham D, Feng F, Furstenhaupt T, Ye S, Birss V. First time investigation of Pt nanocatalysts deposited inside carbon mesopores of controlled length and diameter. *Journal of Materials Chemistry* 2012;22(15):7164-71.
- [59] Banham DWH. Design and optimization of nanoporous carbon for electrochemical applications. The University of Calgary, PhD thesis, 2012.
- [60] Lee K, Zhang J, Wang H, Wilkinson DP. Progress in the synthesis of carbon nanotube- and nanofiber-supported Pt electrocatalysts for PEM fuel cell catalysis. *J Appl Electrochem* 2006;36(5):507-22.
- [61] Sharma S, Pollet BG. Support materials for PEMFC and DMFC electrocatalysts—A review. *Journal of Power Sources* 2012;208(0):96-119.
- [62] Huang S-Y, Ganesan P, Park S, Popov BN. Development of a titanium dioxide-supported platinum catalyst with ultrahigh stability for polymer electrolyte membrane fuel cell applications. *Journal of the American Chemical Society* 2009;131(39):13898-9.
- [63] Yu X, Ye S. Recent advances in activity and durability enhancement of Pt/C catalytic cathode in PEMFC: Part II: Degradation mechanism and durability enhancement of carbon supported platinum catalyst. *Journal of Power Sources* 2007;172(1):145-54.
- [64] Yu X, Ye S. Recent advances in activity and durability enhancement of Pt/C catalytic cathode in PEMFC: Part I. Physico-chemical and electronic interaction between Pt and carbon support, and activity enhancement of Pt/C catalyst. *Journal of Power Sources* 2007;172(1):133-44.
- [65] Shao Y, Liu J, Wang Y, Lin Y. Novel catalyst support materials for PEM fuel cells: current status and future prospects. *Journal of Materials Chemistry* 2009;19(1):46-59.
- [66] Lei M, Wang ZB, Li JS, Tang HL, Liu WJ, Wang YG. CeO₂ nanocubes-graphene oxide as durable and highly active catalyst support for proton exchange membrane fuel cell. *Sci Rep* 2014;4.
- [67] Shao Y, Zhang S, Kou R, Wang X, Wang C, Dai S, et al. Noncovalently functionalized graphitic mesoporous carbon as a stable support of Pt nanoparticles for oxygen reduction. *Journal of Power Sources* 2010;195(7):1805-11.

- [68] Shanahan PV, Xu L, Liang C, Waje M, Dai S, Yan YS. Graphitic mesoporous carbon as a durable fuel cell catalyst support. *Journal of Power Sources* 2008;185(1):423-7.
- [69] Lv H, Cheng N, Mu S, Pan M. Heat-treated multi-walled carbon nanotubes as durable supports for PEM fuel cell catalysts. *Electrochimica Acta* 2011;58(0):736-42.
- [70] Ndamanisha JC, Guo L-p. Ordered mesoporous carbon for electrochemical sensing: A review. *Analytica Chimica Acta* 2012;747(0):19-28.
- [71] Lu AH, Schüth F. Nanocasting: A versatile strategy for creating nanostructured porous materials. *Adv Mater* 2006;18(14):1793-805.
- [72] Boehm HP. Carbon surface chemistry. In: Pierre D, ed. *Graphite and precursors*. France: Gordon and Breach Science Publishers 2001, p. 169-70.
- [73] Sansotera M, Bianchi CL, Lecardi G, Marchionni G, Metrangolo P, Resnati G, et al. Highly hydrophobic carbon black obtained by covalent linkage of perfluorocarbon and perfluoropolyether chains on the carbon surface. *Chemistry of Materials* 2009;21(19):4498-504.
- [74] Xu Z, Qi Z, Kaufman A. Hydrophobization of carbon-supported catalysts with 2,3,4,5,6-pentafluorophenyl moieties for fuel cells. *Electrochemical and Solid-State Letters* 2005;8(10):A492-A4.
- [75] Jiao K, Zhou B. Effects of electrode wettabilities on liquid water behaviours in PEM fuel cell cathode. *Journal of Power Sources* 2008;175(1):106-19.
- [76] Kandlikar SG, Garofalo ML, Lu Z. Water management in a PEMFC: Water transport mechanism and material degradation in gas diffusion layers. *Fuel Cells* 2011;11(6):814-23.
- [77] Ji M, Wei Z. A review of water management in polymer electrolyte membrane fuel cells. *Energies* 2009;2(4):1057-106.
- [78] Chiu KF, Wang KW. Hydrophobic coatings on carbon electrodes for proton exchange membrane fuel cells. *Surface & Coatings Technology* 2007;202(4-7):1231-5.
- [79] Banham DW, Soderberg JN, Birss VI. Pt/carbon catalyst layer microstructural effects on measured and predicted tafel slopes for the oxygen reduction reaction. *Journal of Physical Chemistry C* 2009;113(23):10103-11.
- [80] Bewig KW, Zisman WA. Wetting of gold and platinum by water. *Journal of Physical Chemistry* 1965;69(12):4238-42.
- [81] Bass M, Berman A, Singh A, Konovalov O, Freger V. Surface structure of Nafion in vapor and liquid. *Journal of Physical Chemistry B* 2010;114(11):3784-90.
- [82] Goswami S, Klaus S, Benziger J. Wetting and absorption of water drops on nafion films. *Langmuir* 2008;24(16):8627-33.
- [83] Liu C, Liang X, Liu X, Wang Q, Teng N, Zhan L, et al. Wettability modification of pitch-based spherical activated carbon by air oxidation and its effects on phenol adsorption. *Applied Surface Science* 2008;254(9):2659-65.
- [84] Weissmann M, Baranton S, Clacens J-M, Coutanceau C. Modification of hydrophobic/hydrophilic properties of Vulcan XG72 carbon powder by grafting of trifluoromethylphenyl and phenylsulfonic acid groups. *Carbon* 2010;48(10):2755-64.
- [85] Zawodzinski TA, Gottesfeld S, Shoichet S, McCarthy TJ. The contact-angle between water and the surface of perfluorosulfonic acid membranes. *J Appl Electrochem* 1993;23(1):86-8.

- [86] Nagai T, Nakanishi S, Nakato Y. Water molecules adsorbed at electrode surfaces determine the macroscopic contact angles. *ChemPhysChem* 2007;8(7):1016-8.
- [87] Yan A, Xiao X, Külaots I, Sheldon BW, Hurt RH. Controlling water contact angle on carbon surfaces from 5° to 167°. *Carbon* 2006;44(14):3116-20.
- [88] Wood DL, Chlistunoff J, Majewski J, Borup RL. Nafion structural phenomena at platinum and carbon interfaces. *Journal of the American Chemical Society* 2009;131(50):18096-104.
- [89] Volfkovich YM, Sosenkin VE, Bagotsky VS. Structural and wetting properties of fuel cell components. *Journal of Power Sources* 2010;195(17):5429-41.
- [90] Volfkovich YM, Sosenkin VE, Nikol'skaya NF. Hydrophilic-hydrophobic and sorption properties of the catalyst layers of electrodes in a proton-exchange membrane fuel cell: A stage-by-stage study. *Russian Journal of Electrochemistry* 2010;46(4):438-49.
- [91] Yu HM, Ziegler C, Oszcipok M, Zobel M, Hebling C. Hydrophilicity and hydrophobicity study of catalyst layers in proton exchange membrane fuel cells. *Electrochimica Acta* 2006;51(7):1199-207.
- [92] Mashio T, Malek K, Eikerling M, Ohma A, Kanesaka H, Shinohara K. Molecular dynamics study of ionomer and water adsorption at carbon support materials. *The Journal of Physical Chemistry C* 2010;114(32):13739-45.
- [93] Lopez-Haro M, Guétaz L, Printemps T, Morin A, Escribano S, Jouneau PH, et al. Three-dimensional analysis of Nafion layers in fuel cell electrodes. *Nat Commun* 2014;5.
- [94] Andersen SM, Borghei M, Dhiman R, Ruiz V, Kauppinen E, Skou E. Adsorption behavior of perfluorinated sulfonic acid ionomer on highly graphitized carbon nanofibers and their thermal stabilities. *The Journal of Physical Chemistry C* 2014;118(20):10814-23.
- [95] Fletcher AJ, Yüzak Y, Thomas KM. Adsorption and desorption kinetics for hydrophilic and hydrophobic vapors on activated carbon. *Carbon* 2006;44(5):989-1004.
- [96] Li X, Feng F, Zhang K, Ye S, Kwok DY, Birss V. Wettability of Nafion and Nafion/Vulcan carbon composite films. *Langmuir* 2012;28(16):6698-705.
- [97] Good RJ. Contact angle, wetting, and adhesion: a critical review. *J Adhes Sci Technol* 1992;6(12):1269-302.
- [98] Grundke K, Bogumil T, Gietzelt T, Jacobasch HJ, Kwok DY, Neumann AW. Wetting measurements on smooth, rough and porous solid surfaces. In: Jacobasch HJ, ed. *Interfaces, Surfactants and Colloids in Engineering*: Steinkopff 1996, p. 58-68.
- [99] de Gennes PG. Wetting: statics and dynamics. *Reviews of Modern Physics* 1985;57(3):827-63.
- [100] Washburn EW. The dynamics of capillary flow. *Physical Review* 1921;17(3):273-83.
- [101] Burg P, Abraham MH, Cagniant D. Methods of determining polar and non-polar sites on carbonaceous adsorbents. The contribution of the linear solvation energy relationship approach. *Carbon* 2003;41(5):867-79.
- [102] Kaneko K, Hanzawa Y, Iiyama T, Kanda T, Suzuki T. Cluster-mediated water adsorption on carbon nanopores. *Adsorption* 1999;5(1):7-13.

- [103] Soboleva T, Malek K, Xie Z, Navessin T, Holdcroft S. PEMFC catalyst layers: The role of micropores and mesopores on water sorption and fuel cell activity. *ACS Applied Materials & Interfaces* 2011;3(6):1827-37.
- [104] Kim HY, Chun JH. The recoiling of liquid droplets upon collision with solid surfaces. *Physics of Fluids* 2001;13(3):643-59.
- [105] Lee JB, Lee SH. Dynamic wetting and spreading characteristics of a liquid droplet impinging on hydrophobic textured surfaces. *Langmuir* 2011;27(11):6565-73.
- [106] Rioboo R, Marengo M, Tropea C. Time evolution of liquid drop impact onto solid, dry surfaces. *Experiments in Fluids* 2002;33(1):112-24.
- [107] Roisman IV, Rioboo R, Cameron T. Normal impact of a liquid drop on a dry surface: Model for spreading and receding. *Proceedings: Mathematical, Physical and Engineering Sciences* 2002;458(2022):1411-30.
- [108] Ukiwe C, Kwok DY. On the maximum spreading diameter of impacting droplets on well-prepared solid surfaces. *Langmuir* 2005;21(2):666-73.
- [109] Lander LM, Siewierski LM, Brittain WJ, Vogler EA. A systematic comparison of contact angle methods. *Langmuir* 1993;9(8):2237-9.
- [110] Kwok DY, Neumann AW. Contact angle measurement and contact angle interpretation. *Adv Colloid Interface Sci* 1999;81(3):167-249.
- [111] Lazghab M, Saleh K, Pezron I, Guigon P, Komunjer L. Wettability assessment of finely divided solids. *Powder Technology* 2005;157(1-3):79-91.
- [112] Buckton G, Newton JM. Assessment of the wettability of pharmaceutical powders using compressed discs. *Journal of Pharmacy and Pharmacology* 1985;37(S12):27P-P.
- [113] Meraz-Torres LS, Quintanilla-Carvajal MX, Hernandez-Sanchez H, Tellez-Medina DI, Alamilla-Beltran L, Gutierrez-Lopez GF. Assessment of the kinetics of contact angle during the wetting of maltodextrin agglomerates. *Revista Mexicana de Ingenieria Quimica* 2011;10(2):273-9.
- [114] Farris S, Introzzi L, Biagioni P, Holz T, Schiraldi A, Piergiovanni L. Wetting of biopolymer coatings: Contact angle kinetics and image analysis investigation. *Langmuir* 2011;27(12):7563-74.
- [115] Muster TH, Prestidge CA, Hayes RA. Water adsorption kinetics and contact angles of silica particles. *Colloids Surf, A* 2001;176(2-3):253-66.
- [116] Muster TH, Prestidge CA. Water adsorption kinetics and contact angles of pharmaceutical powders. *Journal of Pharmaceutical Sciences* 2005;94(4):861-72.
- [117] Do DD, Junpirom S, Do HD. A new adsorption-desorption model for water adsorption in activated carbon. *Carbon* 2009;47(6):1466-73.
- [118] Horikawa T, Sekida T, Hayashi Ji, Katoh M, Do DD. A new adsorption-desorption model for water adsorption in porous carbons. *Carbon* 2011;49(2):416-24.
- [119] Foley NJ, Thomas KM, Forshaw PL, Stanton D, Norman PR. Kinetics of water vapor adsorption on activated carbon. *Langmuir* 1997;13(7):2083-9.
- [120] Wang Y, Guan C, Wang K, Guo CX, Li CM. Nitrogen, hydrogen, carbon dioxide, and water vapor sorption properties of three-dimensional graphene. *Journal of Chemical and Engineering Data* 2011;56(3):642-5.
- [121] Narayan S, Harrison B, Liang S, Evans M, Croll L, Smith S. Sorption kinetic studies of water vapour on activated carbon beds. *Carbon* 2008;46(3):397-404.

- [122] Ng E-P, Mintova S. Nanoporous materials with enhanced hydrophilicity and high water sorption capacity. *Microporous and Mesoporous Materials* 2008;114(1–3):1-26.
- [123] Turner NH. Surface analysis: x-ray photoelectron spectroscopy and Auger electron spectroscopy. *Analytical Chemistry* 1986;58(5):153R-65R.
- [124] Kozbial A, Li Z, Sun J, Gong X, Zhou F, Wang Y, et al. Understanding the intrinsic water wettability of graphite. *Carbon* 2014;74(0):218-25.
- [125] Bezerra CWB, Zhang L, Liu H, Lee K, Marques ALB, Marques EP, et al. A review of heat-treatment effects on activity and stability of PEM fuel cell catalysts for oxygen reduction reaction. *Journal of Power Sources* 2007;173(2):891-908.
- [126] Figueiredo JL, Pereira MFR, Freitas MMA, Órfão JJM. Modification of the surface chemistry of activated carbons. *Carbon* 1999;37(9):1379-89.
- [127] Kinoshita K. *Carbon: Electrochemical and physicochemical properties*. New York, USA: John Wiley & Sons, Inc.; 1988.
- [128] Yao H, Chu C-C, Sue H-J, Nishimura R. Electrically conductive superhydrophobic octadecylamine-functionalized multiwall carbon nanotube films. *Carbon* 2013;53(0):366-73.
- [129] Li X, Banham D, Feng F, Forouzandeh F, Ye S, Kwok DY, et al. Wettability of colloid-imprinted carbons by contact angle kinetics and water vapor sorption measurements. *Carbon* 2015;87(0):44-60.
- [130] Li Z, Jaroniec M. Synthesis and adsorption properties of colloid-Imprinted carbons with surface and volume mesoporosity. *Chemistry of Materials* 2003;15(6):1327-33.
- [131] Li Z, Jaroniec M, Lee Y-J, Radovic LR. High surface area graphitized carbon with uniform mesopores synthesised by a colloidal imprinting method. *Chem Commun* 2002(13):1346-7.
- [132] Banham D, Feng F, Burt J, Alsayheen E, Birss V. Bimodal, templated mesoporous carbons for capacitor applications. *Carbon* 2010;48(4):1056-63.
- [133] Bebeskko GI, Karpov YA. Determination of fluorine in inorganic substances (Overview). *Inorg Mater* 2012;48(15):1335-40.
- [134] Brunauer S, Emmett PH, Teller E. Adsorption of gases in multimolecular layers. *Journal of the American Chemical Society* 1938;60(2):309-19.
- [135] Barrett EP, Joyner LG, Halenda PP. The determination of pore volume and area distributions in porous substances. I. Computations from nitrogen isotherms. *Journal of the American Chemical Society* 1951;73(1):373-80.
- [136] Frank CW, Rao V, Despotopoulou MM, Pease RFW, Hinsberg WD, Miller RD, et al. Structure in thin and ultrathin spin-cast polymer films. *Science* 1996;273(5277):912-5.
- [137] Forouzandeh F, Banham D, Feng F, Li X, Ye S, Birss V. Corrosion study of mesoporous carbon supports for use in PEM fuel cells. *ECS Transactions* 2013;58(1):1739-49.
- [138] Kwok DY, Gietzelt T, Grundke K, Jacobasch HJ, Neumann AW. Contact angle measurements and contact angle interpretation .1. Contact angle measurements by axisymmetric drop shape analysis and a goniometer sessile drop technique. *Langmuir* 1997;13(10):2880-94.
- [139] Rubatat L, Rollet AL, Gebel G, Diat O. Evidence of elongated polymeric aggregates in Nafion. *Macromolecules* 2002;35(10):4050-5.

- [140] Schmidt-Rohr K, Chen Q. Parallel cylindrical water nanochannels in Nafion fuel-cell membranes. *Nature Materials* 2008;7(1):75-83.
- [141] Aleksandrova E, Hiesgen R, Friedrich KA, Roduner E. Electrochemical atomic force microscopy study of proton conductivity in a Nafion membrane. *Physical Chemistry Chemical Physics* 2007;9(21):2735-43.
- [142] Affoune AM, Yamada A, Umeda M. Surface observation of solvent-impregnated Nafion membrane with atomic force microscopy. *Langmuir* 2004;20(17):6965-8.
- [143] Bussian DA, O'Dea JR, Metiu H, Buratto SK. Nanoscale current imaging of the conducting channels in proton exchange membrane fuel cells. *Nano Letters* 2007;7(2):227-32.
- [144] Umemura K, Wang T, Hara M, Kuroda R, Uchida O, Nagai M. Nanocharacterization and nanofabrication of a Nafion thin film in liquids by atomic force microscopy. *Langmuir* 2006;22(7):3306-12.
- [145] Luo C, Zuo X, Wang L, Wang E, Song S, Wang J, et al. Flexible carbon nanotube-polymer composite films with high conductivity and superhydrophobicity made by solution process. *Nano Letters* 2008;8(12):4454-8.
- [146] Malek K, Eikerling M, Wang Q, Navessin T, Liu Z. Self-organization in catalyst layers of polymer electrolyte fuel cells. *Journal of Physical Chemistry C* 2007;111(36):13627-34.
- [147] Malek K, Mashio T, Eikerling M. Microstructure of catalyst layers in PEM fuel cells redefined: A computational approach. *Electrocatalysis* 2011;2(2):141-57.
- [148] Zook LA, Leddy J. Density and solubility of nafion: Recast, annealed, and commercial films. *Analytical Chemistry* 1996;68(21):3793-6.
- [149] Barthlott W, Neinhuis C. Purity of the sacred lotus, or escape from contamination in biological surfaces. *Planta* 1997;202(1):1-8.
- [150] Furstner R, Barthlott W, Neinhuis C, Walzel P. Wetting and self-cleaning properties of artificial superhydrophobic surfaces. *Langmuir* 2005;21(3):956-61.
- [151] Lafuma A, Quere D. Superhydrophobic states. *Nature Materials* 2003;2(7):457-60.
- [152] Rioboo R, Voue M, Vaillant A, De Coninck J. Drop impact on porous superhydrophobic polymer surfaces. *Langmuir* 2008;24(24):14074-7.
- [153] Sun MH, Luo CX, Xu LP, Ji H, OuYang Q, Yu DP, et al. Artificial lotus leaf by nanocasting. *Langmuir* 2005;21(19):8978-81.
- [154] Wang S, Jiang L. Definition of superhydrophobic states. *Adv Mater* 2007;19(21):3423-4.
- [155] Ignaszak A, Ye S, Gyenge E. A study of the catalytic interface for O₂ electroreduction on Pt: The interaction between carbon support meso/microstructure and ionomer (Nafion) distribution. *Journal of Physical Chemistry C* 2009;113(1):298-307.
- [156] Ahn M, Cho Y-H, Cho Y-H, Kim J, Jung N, Sung Y-E. Influence of hydrophilicity in micro-porous layer for polymer electrolyte membrane fuel cells. *Electrochimica Acta* 2011;56(5):2450-7.
- [157] Li Z, Jaroniec M. Silica gel-templated mesoporous carbons prepared from mesophase pitch and polyacrylonitrile. *Carbon* 2001;39(13):2080-2.
- [158] Ji X, Lee KT, Nazar LF. A highly ordered nanostructured carbon-sulphur cathode for lithium-sulphur batteries. *Nature Materials* 2009;8(6):500-6.

- [159] Yang W, Ratinac KR, Ringer SP, Thordarson P, Gooding JJ, Braet F. Carbon nanomaterials in biosensors: should you use nanotubes or graphene? *Angewandte Chemie International Edition* 2010;49(12):2114-38.
- [160] Simon P, Gogotsi Y. Materials for electrochemical capacitors. *Nature Materials* 2008;7(11):845-54.
- [161] Horikawa T, Sakao N, Do DD. Effects of temperature on water adsorption on controlled microporous and mesoporous carbonaceous solids. *Carbon* 2013;56(0):183-92.
- [162] Akter T, Hu K, Lian K. Investigations of multilayer polyoxometalates-modified carbon nanotubes for electrochemical capacitors. *Electrochimica Acta* 2011;56(14):4966-71.
- [163] Vix-Guterl C, Ehrburger P. Effect of the properties of a carbon substrate on its reaction with silica for silicon carbide formation. *Carbon* 1997;35(10-11):1587-92.
- [164] Sharma A, Kyotani T, Tomita A. Comparison of structural parameters of PF carbon from XRD and HRTEM techniques. *Carbon* 2000;38(14):1977-84.
- [165] Zhi LJ, Wu JS, Li JX, Kolb U, Mullen K. Carbonization of disclike molecules in porous alumina membranes: Toward carbon nanotubes with controlled graphene-layer orientation. *Angewandte Chemie International Edition* 2005;44(14):2120-3.
- [166] Jian K, Truong TC, Hoffman WP, Hurt RH. Mesoporous carbons with self-assembled surfaces of defined crystal orientation. *Microporous and Mesoporous Materials* 2008;108(1-3):143-51.
- [167] Jian K, Yan A, Kulaots I, Crawford GP, Hurt RH. Reconstruction and hydrophobicity of nanocarbon surfaces composed solely of graphene edges. *Carbon* 2006;44(10):2102-6.
- [168] Jian KQ, Shim HS, Schwartzman A, Crawford GP, Hurt RH. Orthogonal carbon nanofibers by template-mediated assembly of discotic mesophase pitch. *Adv Mater* 2003;15(2):164-7.
- [169] Hurt R, Krammer G, Crawford G, Jian K, Rulison C. Polyaromatic assembly mechanisms and structure selection in carbon materials. *Chemistry of Materials* 2002;14(11):4558-65.
- [170] Yang H, Yan, Liu Y, Zhang F, Zhang R, YanMeng Y, et al. A simple melt impregnation method to synthesize ordered mesoporous carbon and carbon nanofiber bundles with graphitized structure from pitches. *The Journal of Physical Chemistry B* 2004;108(45):17320-8.
- [171] Sing KSW, Everett DH, Haul RAW, Moscou L, Pierotti RA, Rouquerol J, et al. Reporting physisorption data for gas/solid systems with special reference to the determination of surface area and porosity (Recommendations 1984). *Pure Appl Chem* 1985;57(4):603-19.
- [172] Lowell S, Shields JE, Thomas MA, Thommes M. Characterization of porous solids and powders: Surface area, pore size and density. Dordrecht, The Netherlands: Kluwer Academic Publishers; 2004.
- [173] Haynes JM. Pore size analysis according to the Kelvin equation. *Mat Constr* 1973;6(3):209-13.

- [174] Yoon SB, Chai GS, Kang SK, Yu J-S, Gierszal KP, Jaroniec M. Graphitized pitch-based carbons with ordered nanopores synthesized by using colloidal crystals as templates. *Journal of the American Chemical Society* 2005;127(12):4188-9.
- [175] Wang S, Zhang Y, Abidi N, Cabrales L. Wettability and surface free energy of graphene films. *Langmuir* 2009;25(18):11078-81.
- [176] Taherian F, Marcon V, van der Vegt NFA, Leroy F. What is the contact angle of water on graphene? *Langmuir* 2013;29(5):1457-65.
- [177] Li Z, Wang Y, Kozbial A, Shenoy G, Zhou F, McGinley R, et al. Effect of airborne contaminants on the wettability of supported graphene and graphite. *Nature Materials* 2013;12(10):925-31.
- [178] Liu Y, Zhou J, Zhu E, Tang J, Liu X, Tang W. Covalently intercalated graphene oxide for oil–water separation. *Carbon* 2015;82(0):264-72.
- [179] Xu X, Zhou J, Jiang L, Lubineau G, Payne SA, Gutschmidt D. Lignin-based carbon fibers: Carbon nanotube decoration and superior thermal stability. *Carbon* 2014;80(0):91-102.
- [180] Wang HZ, Huang ZP, Cai QJ, Kulkarni K, Chen CL, Carnahan D, et al. Reversible transformation of hydrophobicity and hydrophilicity of aligned carbon nanotube arrays and buckypapers by dry processes. *Carbon* 2010;48(3):868-75.
- [181] Müller EA, Rull LF, Vega LF, Gubbins KE. Adsorption of water on activated carbons: A molecular simulation study. *Journal of Physical Chemistry* 1996;100(4):1189-96.
- [182] Bray WC, Draper HD. Capillary condensation and adsorption. *Proceedings of the National Academy of Sciences* 1926;12(5):295-9.
- [183] Evans R, Marconi UMB, Tarazona P. Capillary condensation and adsorption in cylindrical and slit-like pores. *Journal of the Chemical Society, Faraday Transactions 2: Molecular and Chemical Physics* 1986;82(10):1763-87.
- [184] Livingston HK. Cross-sectional areas of molecules adsorbed on solid surfaces. *Journal of the American Chemical Society* 1944;66(4):569-73.
- [185] McClellan AL, Harnsberger HF. Cross-sectional areas of molecules adsorbed on solid surfaces. *Journal of Colloid and Interface Science* 1967;23(4):577-99.
- [186] Antognozzi M, Humphris ADL, Miles MJ. Observation of molecular layering in a confined water film and study of the layers viscoelastic properties. *Appl Phys Lett* 2001;78(3):300-2.
- [187] Israelachvili JN, Pashley RM. Molecular layering of water at surfaces and origin of repulsive hydration forces. *Nature* 1983;306(5940):249-50.
- [188] Naono H, Hakuman M, Shiono T. Analysis of nitrogen adsorption isotherms for a series of porous silicas with uniform and cylindrical pores: A new method of calculating pore size distribution of pore radius 1–2 nm. *Journal of Colloid and Interface Science* 1997;186(2):360-8.
- [189] Frackowiak E, Béguin F. Carbon materials for the electrochemical storage of energy in capacitors. *Carbon* 2001;39(6):937-50.
- [190] Kangasniemi KH, Condit DA, Jarvi TD. Characterization of vulcan electrochemically oxidized under simulated PEM fuel cell conditions. *Journal of the Electrochemical Society* 2004;151(4):E125-E32.

- [191] Boehm HP. Carbon surface chemistry. In: Pierre D, ed. Graphite and precursors. France: Gordon and Breach Science Publishers 2001, p. 146.
- [192] Boehm HP. Some aspects of the surface chemistry of carbon blacks and other carbons. Carbon 1994;32(5):759-69.
- [193] Goertzen SL, Thériault KD, Oickle AM, Tarasuk AC, Andreas HA. Standardization of the Boehm titration. Part I. CO₂ expulsion and endpoint determination. Carbon 2010;48(4):1252-61.
- [194] Ma T-Y, Liu L, Yuan Z-Y. Direct synthesis of ordered mesoporous carbons. Chemical Society Reviews 2013;42(9):3977-4003.
- [195] Yang H, Zhao D. Synthesis of replica mesostructures by the nanocasting strategy. Journal of Materials Chemistry 2005;15(12):1217-31.
- [196] Zhai Y, Wan Y, Cheng Y, Shi Y, Zhang F, Tu B, et al. The influence of carbon source on the wall structure of ordered mesoporous carbons. J Porous Mater 2008;15(5):601-11.
- [197] Kim CH, Lee D-K, Pinnavaia TJ. Graphitic mesostructured carbon prepared from aromatic precursors. Langmuir 2004;20(13):5157-9.
- [198] Jun S, Joo SH, Ryoo R, Kruk M, Jaroniec M, Liu Z, et al. Synthesis of new, nanoporous carbon with hexagonally ordered mesostructure. Journal of the American Chemical Society 2000;122(43):10712-3.
- [199] Kruk M, Jaroniec M, Ryoo R, Joo SH. Characterization of ordered mesoporous carbons synthesized using MCM-48 silicas as templates. The Journal of Physical Chemistry B 2000;104(33):7960-8.
- [200] Gierszal KP, Jaroniec M, Kim T-W, Kim J, Ryoo R. High temperature treatment of ordered mesoporous carbons prepared by using various carbon precursors and ordered mesoporous silica templates. New Journal of Chemistry 2008;32(6):981-93.
- [201] Ravikovitch PI, Neimark AV. Experimental confirmation of different mechanisms of evaporation from ink-bottle type pores: Equilibrium, pore blocking, and cavitation. Langmuir 2002;18(25):9830-7.
- [202] Nguyen PTM, Do DD, Nicholson D. On the cavitation and pore blocking in cylindrical pores with simple connectivity. The Journal of Physical Chemistry B 2011;115(42):12160-72.
- [203] Brinker CJ. Sol-gel processing of silica. In: Bergna HE, ed. The colloid chemistry of silica. The United States of America: American Chemical Society 1994, p. 379-85.
- [204] Kim T-W, Park I-S, Ryoo R. A synthetic route to ordered mesoporous carbon materials with graphitic pore walls. Angewandte Chemie 2003;115(36):4511-5.
- [205] Hara M, Yoshida T, Takagaki A, Takata T, Kondo JN, Hayashi S, et al. A carbon material as a strong protonic acid. Angewandte Chemie International Edition 2004;43(22):2955-8.
- [206] Shin S, Jang J, Yoon SH, Mochida I. A study on the effect of heat treatment on functional groups of pitch based activated carbon fiber using FTIR. Carbon 1997;35(12):1739-43.
- [207] Kyakuno H, Matsuda K, Yahiro H, Inami Y, Fukuoka T, Miyata Y, et al. Confined water inside single-walled carbon nanotubes: Global phase diagram and effect of finite length. The Journal of Chemical Physics 2011;134(24):-.

- [208] Pascal TA, Goddard WA, Jung Y. Entropy and the driving force for the filling of carbon nanotubes with water. *Proceedings of the National Academy of Sciences* 2011;108(29):11794-8.
- [209] Su F, Zeng J, Bao X, Yu Y, Lee JY, Zhao XS. Preparation and characterization of highly ordered graphitic mesoporous carbon as a Pt catalyst support for direct methanol fuel cells. *Chemistry of Materials* 2005;17(15):3960-7.
- [210] Ryoo R, Joo SH, Jun S. Synthesis of highly ordered carbon molecular sieves via template-mediated structural transformation. *The Journal of Physical Chemistry B* 1999;103(37):7743-6.
- [211] Vinu A, Srinivasu P, Takahashi M, Mori T, Balasubramanian VV, Ariga K. Controlling the textural parameters of mesoporous carbon materials. *Microporous and Mesoporous Materials* 2007;100(1–3):20-6.
- [212] Ambrosio E, Francia C, Gerbaldi C, Penazzi N, Spinelli P, Manzoli M, et al. Mesoporous carbons as low temperature fuel cell platinum catalyst supports. *J Appl Electrochem* 2008;38(7):1019-27.
- [213] Ambrosio EP, Dumitrescu MA, Francia C, Gerbaldi C, Spinelli P. Ordered mesoporous carbons as catalyst support for PEM fuel cells. *Fuel Cells* 2009;9(3):197-200.
- [214] Bahr JL, Tour JM. Highly functionalized carbon nanotubes using in situ generated diazonium compounds. *Chemistry of Materials* 2001;13(11):3823-4.
- [215] Mao K, Kobayashi T, Wiench JW, Chen H-T, Tsai C-H, Lin VSY, et al. Conformations of silica-bound (pentafluorophenyl)propyl groups determined by solid-state NMR spectroscopy and theoretical calculations. *Journal of the American Chemical Society* 2010;132(35):12452-7.
- [216] Budarin VL, Clark JH, Hale SE, Tavener SJ, Mueller KT, Washton NM. NMR and IR study of fluorobenzene and hexafluorobenzene adsorbed on alumina. *Langmuir* 2007;23(10):5412-8.
- [217] Soboleva T, Zhao X, Malek K, Xie Z, Navessin T, Holdcroft S. On the micro-, meso-, and macroporous structures of polymer electrolyte membrane fuel cell catalyst layers. *ACS Applied Materials & Interfaces* 2010;2(2):375-84.
- [218] Toupin M, Bélanger D. Spontaneous functionalization of carbon black by reaction with 4-nitrophenyldiazonium cations. *Langmuir* 2008;24(5):1910-7.
- [219] Carmo M, Linardi M, Poco JGR. Characterization of nitric acid functionalized carbon black and its evaluation as electrocatalyst support for direct methanol fuel cell applications. *Applied Catalysis A: General* 2009;355(1–2):132-8.
- [220] Doyle MP, Dellaria JF, Siegfried B, Bishop SW. Reductive deamination of arylamines by alkyl nitrites in N,N-dimethylformamide. A direct conversion of arylamines to aromatic hydrocarbons. *The Journal of Organic Chemistry* 1977;42(22):3494-8.
- [221] Friedman L, Chlebowsky J. Aprotic diazotization of aniline in the presence of iodine. *The Journal of Organic Chemistry* 1968;33(4):1636-8.
- [222] Sansotera M, Navarrini W, Resnati G, Metrangolo P, Famulari A, Bianchi CL, et al. Preparation and characterization of superhydrophobic conductive fluorinated carbon blacks. *Carbon* 2010;48(15):4382-90.

- [223] Koley D, Colón OC, Savinov SN. Chemoselective nitration of phenols with tert-butyl nitrite in solution and on solid support. *Organic Letters* 2009;11(18):4172-5.
- [224] Maity S, Naveen T, Sharma U, Maiti D. Stereoselective nitration of olefins with tBuONO and TEMPO: Direct access to nitroolefins under metal-free conditions. *Organic Letters* 2013;15(13):3384-7.
- [225] Ershov VV, Zlobina GA. Radical reactions of alkyl nitrites with 2,4,6-trisubstituted phenols. *Russ Chem Bull* 1964;13(12):2138-40.
- [226] Cougnon C, Nguyen NH, Dabos-Seignon S, Mauzeroll J, Bélanger D. Carbon surface derivatization by electrochemical reduction of a diazonium salt in situ produced from the nitro precursor. *Journal of Electroanalytical Chemistry* 2011;661(1):13-9.
- [227] Cline KK, Baxter L, Lockwood D, Saylor R, Stalzer A. Nonaqueous synthesis and reduction of diazonium ions (without isolation) to modify glassy carbon electrodes using mild electrografting conditions. *Journal of Electroanalytical Chemistry* 2009;633(2):283-90.
- [228] Brooksby PA, Downard AJ. Electrochemical and atomic force microscopy study of carbon surface modification via diazonium reduction in aqueous and acetonitrile solutions. *Langmuir* 2004;20(12):5038-45.
- [229] Tsutsumi H, Furumoto S, Morita M, Matsuda Y. Electrochemical behavior of a 4-nitrothiophenol modified electrode prepared by the self-assembly method. *Journal of Colloid and Interface Science* 1995;171(2):505-11.
- [230] Ortiz B, Saby C, Champagne GY, Bélanger D. Electrochemical modification of a carbon electrode using aromatic diazonium salts. 2. Electrochemistry of 4-nitrophenyl modified glassy carbon electrodes in aqueous media. *Journal of Electroanalytical Chemistry* 1998;455(1-2):75-81.